frontiers | Research Topics

Methods in biosensors and biomolecular electronics

Edited by
Tatiana Fiordelisio, Mathieu Hautefeuille, Kawsar Ahmed and Francis Bui

Published in
Frontiers in Bioengineering and Biotechnology

ISSN 1664-8714
ISBN 978-2-8325-3824-1
DOI 10.3389/978-2-8325-3824-1

About Frontiers

Frontiers is more than just an open access publisher of scholarly articles: it is a pioneering approach to the world of academia, radically improving the way scholarly research is managed. The grand vision of Frontiers is a world where all people have an equal opportunity to seek, share and generate knowledge. Frontiers provides immediate and permanent online open access to all its publications, but this alone is not enough to realize our grand goals.

Frontiers journal series

The Frontiers journal series is a multi-tier and interdisciplinary set of open-access, online journals, promising a paradigm shift from the current review, selection and dissemination processes in academic publishing. All Frontiers journals are driven by researchers for researchers; therefore, they constitute a service to the scholarly community. At the same time, the *Frontiers journal series* operates on a revolutionary invention, the tiered publishing system, initially addressing specific communities of scholars, and gradually climbing up to broader public understanding, thus serving the interests of the lay society, too.

Dedication to quality

Each Frontiers article is a landmark of the highest quality, thanks to genuinely collaborative interactions between authors and review editors, who include some of the world's best academicians. Research must be certified by peers before entering a stream of knowledge that may eventually reach the public - and shape society; therefore, Frontiers only applies the most rigorous and unbiased reviews. Frontiers revolutionizes research publishing by freely delivering the most outstanding research, evaluated with no bias from both the academic and social point of view. By applying the most advanced information technologies, Frontiers is catapulting scholarly publishing into a new generation.

What are Frontiers Research Topics?

Frontiers Research Topics are very popular trademarks of the *Frontiers journals series*: they are collections of at least ten articles, all centered on a particular subject. With their unique mix of varied contributions from Original Research to Review Articles, Frontiers Research Topics unify the most influential researchers, the latest key findings and historical advances in a hot research area.

Find out more on how to host your own Frontiers Research Topic or contribute to one as an author by contacting the Frontiers editorial office: frontiersin.org/about/contact

Methods in biosensors and biomolecular electronics

Topic editors

Tatiana Fiordelisio — National Autonomous University of Mexico, Mexico

Mathieu Hautefeuille — Sorbonne Université, France

Kawsar Ahmed — Mawlana Bhashani Science and Technology University, Bangladesh

Francis Bui — University of Saskatchewan, Canada

Citation

Fiordelisio, T., Hautefeuille, M., Ahmed, K., Bui, F., eds. (2023). *Methods in biosensors and biomolecular electronics*. Lausanne: Frontiers Media SA. doi: 10.3389/978-2-8325-3824-1

Table of contents

frontiers | Frontiers in Bioengineering and Biotechnology

TYPE Editorial
PUBLISHED 17 October 2023
DOI 10.3389/fbioe.2023.1294221

OPEN ACCESS

EDITED AND REVIEWED BY
Guozhen Liu,
The Chinese University of Hong Kong, China

*CORRESPONDENCE
Tatiana Fiordelisio,
tfiorde@ciencias.unam.mx

RECEIVED 14 September 2023
ACCEPTED 06 October 2023
PUBLISHED 17 October 2023

CITATION
Fiordelisio T (2023), Editorial: Methods in biosensors and biomolecular electronics. *Front. Bioeng. Biotechnol.* 11:1294221. doi: 10.3389/fbioe.2023.1294221

Editorial: Methods in biosensors and biomolecular electronics

Tatiana Fiordelisio[1,2]*

[1]Laboratorio de Neuroendocrinología Comparada, Facultad de Ciencias, Universidad Nacional Autónoma de México, Mexico City, Mexico, [2]Laboratorio Nacional de Soluciones Biomiméticas para Diagnóstico y Terapia LaNSBioDyT, Facultad de Ciencias, Universidad Nacional Autónoma de México, Mexico City, Mexico

KEYWORDS

biosensor, point-of-care, biological detector, immunosensors, genosensors, electrochemical biosensor, optical biosensor, diagnostic assays

Editorial on the Research Topic
Methods in biosensors and biomolecular electronics

Initially, biosensors were considered to be any analytical probe that provided a quantifiable signal in a biological medium, such as pH and oxygen electrodes. Today, we define them as analytical devices that can determine the presence of biological elements or biomolecules in a sample and are capable of converting a physical or chemical signal into an optically or electrically measurable signal.

In 1962, Clark and Lyons developed the first electrochemical biosensor to measure glucose. Since then, biosensor development and popularity has grown substantially. The research areas with the highest presence are Chemistry (53.0%), Science Technology (21.4%), and Materials Science (17.5%). It is noteworthy that fields with great potential in their own right have a relatively low presence, such as Agriculture (0.5%), which is ranked 25th (Figure 1). The leading countries are the People's Republic of China (26.7%) and the United States of America (20.0%).

Biosensors can be categorized into: qualitative, semi-quantitative or quantitative, covering a wide and dynamic range of information. Any biosensor must include three units specialized in detection, translation and processing. They are able to detect a wide range of biomarkers (nucleic acids, metabolites, hormones, proteins) and are therefore often used as diagnostic or prognostic tests for medical conditions. Molecular recognition of biomarkers by the detection unit depends on the affinity and specificity that results from thermodynamic equilibrium to form stable complexes. In this sense, innovation is needed to improve the affinity and stability of such bindings.

Depending on the characteristics of the biological detector, we have immunosensors, based on antigen-antibody recognition to measure biomolecules (as developed in this Research Topic by Liang et al. for the detection of 17β-estradiol) and genosensors, based on the detection of nucleic acids, which are very useful due to their high biocompatibility and thermal stability, (which can be used in many forms of biosensing, especially for viral infections). Their coupling to nanoparticles by Wang et al. used in the development of biosensors focused on infections such as *Candida* albicans is presented in this Research Topic.

In terms of the signal translation unit, both electrochemical and optical signals are considered. The electrochemical ones have high sensitivity and specificity, are low-cost and a very simple structure; they have also been miniaturized. Within these, there are those that

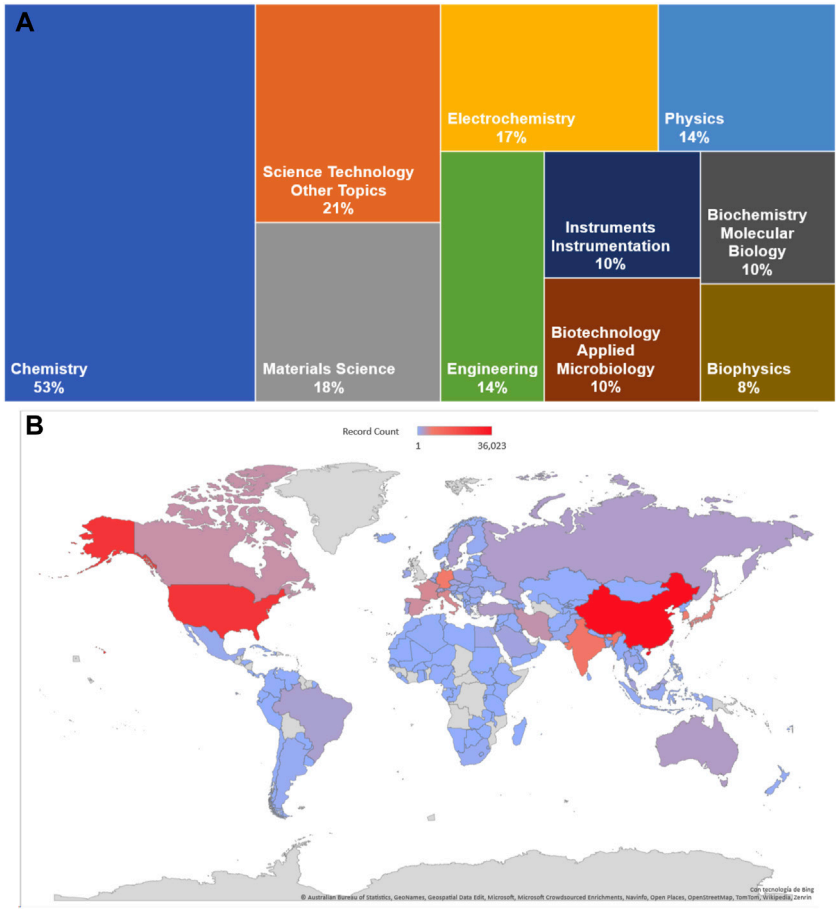

FIGURE 1
Topic search on biosensor or biomolecular electronics in Web of Science Core Research Topic (all editors 1900–2023). **(A)** Comparative graph of the percentage of developing areas in biosensors. **(B)** Heat map of the countries and its development on biosensors studies.

measure conductometry, voltammetry, potentiometry and impedance. Other uses of electrical biosensors have been applied recently, such as the work done by Abadijoo et al. in developing electrical fields to prevent cytokine storms.

Optical translation biosensors have received a lot of attention given their usefulness in clinical diagnostics, drug measurement, food quality control, and even environmental monitoring. Most of them use the evanescent field to detect and measure molecules, they can use the surface plasmon wave where a change in refractive index caused by molecular interactions is detected, and there are also waveguide interferometers based on an optical resonator and fiber optics (Chen and Wang, 2020).

There has been a boom in the development of point-of-care (PoC) biosensors for diagnostics, which aim to meet the ideal ASSURED properties: Affordable, Sensitive, Specific, User-friendly, Rapid and Robust, Equipment-free and Delivered (Mabey et al., 2004; Drain et al., 2014). The absence of amplification of both the recognition and the signal is responsible for most of these systems and the possibility of miniaturization (Ortiz and Loeffelholz, 2023). Some of these aspects are proposed by Nelson-Mora in the article "New detection method of SARS-CoV-2 antibodies towards a point-of-care biosensor". On the other hand, the search for new materials that allow miniaturized multiplex detection has been a major endeavor; the article in this Research Topic on hydrogel silk-based microarrays and molecular beacons for reagentless PoC diagnostics provides important advances in this field. While PoC biosensors have been developed for a variety of clinical diagnostic tests (Chen et al., 2020), they have also become popular in veterinary medicine because they can be used in the field and require only a small amount of sample (Stern and Camus, 2023). However, one limitation to their use is the need for improved signal transducers.

The COVID-19 pandemic greatly influenced such developments. The goal was to rapidly reduce the high transmission rate and mortality. However, detection limits and dynamic ranges are key Research Topic, as these analytical features affect clinical parameters such as sensitivity and specificity. As a result, even though most of them could be applied on a large scale, many developments had very low sensitivity, leading to false negatives. Having PoC ASSURED biosensors can make a difference in controlling a pandemic. During this time, many new biosensors for viral RNA detection were developed, including the use of CRISPR-Cas as optical biosensors (Morales-Moreno et al., 2023), lamp assays, aptamers, antigens, nanoparticles, and plasmon resonance (Mobed and Sepehri

Shafigh, 2021), and even adaptations of standardized techniques to improve the sensitivity and speed of a test, as observed in the work of Mao et al. on asymmetric stem-loop-mediated isothermal amplification of nucleic acids for DNA diagnostic assays by simple.

Measuring environmental conditions, pathogens or pests affecting agricultural crops has been the focus of few PoCs. However, because of the agricultural and global ecological implications, it is critical to pay attention to these Research Topic. The development of this line of research and innovation should be motivated by concerns for environmental sustainability, water monitoring, air quality, food quality as well as disease diagnosis and tracking. In this Research Topic, Arena-Ortiz et al. developed DNA microarrays for the identification of etiological agents, as sensors of environmental wellbeing.

The main problems that arise from research and development of biosensors have to do with relying on large, expensive equipment and requiring highly trained personnel. As well as improvement of the signal translation and measurement system so that they can be low-cost, miniaturized devices that can be used by a person at home, in a modest clinic or in the field.

This Research Topic in the series aims to highlight the latest experimental techniques and methods used to investigate fundamental questions in biosensors and biomolecular electronic research, from methods in sensors for PoC diagnostics to those in protein electronics.

Author contributions

TF: Writing–original draft.

Acknowledgments

The author thanks Diana delRio and Regina Zamora, for style and writing correction and Diego Zamarron for figure edition.

Conflict of interest

The author declares that the research was conducted in the absence of any commercial or financial relationships that could be construed as a potential conflict of interest.

Publisher's note

All claims expressed in this article are solely those of the authors and do not necessarily represent those of their affiliated organizations, or those of the publisher, the editors and the reviewers. Any product that may be evaluated in this article, or claim that may be made by its manufacturer, is not guaranteed or endorsed by the publisher.

References

Chen, C., and Wang, J. (2020). Optical biosensors: an exhaustive and comprehensive review. *Analyst* 145, 1605–1628. doi:10.1039/c9an01998g

Chen, Y. T., Lee, Y. C., Lai, Y. H., Lim, J. C., Huang, N. T., Lin, C. T., et al. (2020). Review of integrated optical biosensors for point-of-care applications. *Biosensors* 10, 209. doi:10.3390/bios10120209

Drain, P. K., Hyle, E. P., Noubary, F., Freedberg, K. A., Wilson, D., Bishai, W. R., et al. (2014). Diagnostic point-of-care tests in resource-limited settings. *Lancet Infect. Dis.* 14, 239–249. doi:10.1016/s1473-3099(13)70250-0

Mabey, D., Peeling, R. W., Ustianowski, A., and Perkins, M. D. (2004). Diagnostics for the developing world. *Nat. Rev. Microbiol.* 2, 231–240. doi:10.1038/nrmicro841

Mobed, A., and Sepehri Shafigh, E. (2021). Biosensors promising bio-device for pandemic screening COVID-19. *Microchem. J.* 164, 106094. doi:10.1016/j.microc.2021.106094

Morales-Moreno, M. D., Valdés-Galindo, E., Reza, M. M., Fiordelisio, T., Peon, J., and Hernandez-Garcia, A. (2023). Multiplex gRNAs synergically enhance detection of SARS-CoV-2 by CRISPR-Cas12a. *CRISPR J.* 6 (2), 116–126. doi:10.1089/crispr.2022.0074

Ortiz, D. A., and Loeffelholz, M. J. (2023). Practical challenges of point-of-care testing. *Clin. Lab. Med.* 43, 155–165. doi:10.1016/j.cll.2023.02.002

Stern, J. K., and Camus, M. S. (2023). Point-of-Care instruments. *Vet. Clin. North Am. Small Anim. Pract.* 53, 17–28. doi:10.1016/j.cvsm.2022.08.001

frontiers in Bioengineering and Biotechnology

ORIGINAL RESEARCH
published: 28 March 2022
doi: 10.3389/fbioe.2022.818983

Isolation of a Monoclonal Antibody and its Derived Immunosensor for Rapid and Sensitive Detection of 17β-Estradiol

Jingru Liang[1†], Hang Dong[2†], Fei Xu[1], Baowei Li[1], Haimei Li[1], Limei Chen[1], Mei Li[1], Yingchu Liu[3], Guosheng Jiang[1,4] and Jinhua Dong[1,5*]*

[1]Key Laboratory for Biological Medicine in Shandong Universities, Weifang Key Laboratory for Antibody Medicine, School of Life Science and Technology, Weifang Medical University, Weifang, China, [2]School of Clinical Medicine, Peking University, Beijing, China, [3]School of Clinical Medicine, Beijing University of Chinese Medicine, Beijing, China, [4]College of Basic Medicine, Binzhou Medical University, Yantai, China, [5]World Research Hub Initiative, Institute of Innovative Research, Tokyo Institute of Technology, Yokohama, Japan

OPEN ACCESS

Edited by:
Mathieu Hautefeuille, Sorbonne Université, France

Reviewed by:
Xiaolin Huang, Nanchang University, China
Hyung Sik Kim, Sungkyunkwan University, South Korea

***Correspondence:**
Guosheng Jiang
jiangguosh@163.com
Jinhua Dong
dongjh@wfmc.edu.cn

[†]These authors have contributed equally to this work and share first authorship

Specialty section:
This article was submitted to Biosensors and Biomolecular Electronics, a section of the journal Frontiers in Bioengineering and Biotechnology

Received: *20 November 2021*
Accepted: *14 March 2022*
Published: *28 March 2022*

Citation:
Liang J, Dong H, Xu F, Li B, Li H, Chen L, Li M, Liu Y, Jiang G and Dong J (2022) Isolation of a Monoclonal Antibody and its Derived Immunosensor for Rapid and Sensitive Detection of 17β-Estradiol. Front. Bioeng. Biotechnol. 10:818983. doi: 10.3389/fbioe.2022.818983

Estrogens are effective for stimulating several functions in living organisms and for regulating cancer development by promoting cell proliferation. Estradiol can disrupt the reproductive and endocrine systems, leading to the development of various diseases. In this study, the monoclonal antibody ESC9 was developed by immunizing mice with a 17β-estradiol (E2) conjugate, preparing an antibody phage display library, and screening monoclonal antibodies from the prepared library. An antibody with the same sequence as that of ESC9 has not been reported previously. The equilibrium dissociation constant between ESC9 and E2 was found to be 43.3 nM. Additionally, we generated an ESC9-derived immunosensor named as the ESC9 Quenchbody (Q-body), which can rapidly and sensitively detect E2. The assay can be completed within 2 min with a limit of detection of 3.9 pg/ml and half-maximal effective concentration of 154.0 ng/ml. Serum E2 levels were measured using the ESC9 Q-body without pretreatment with serum and with a high recovery rate of 83.3–126.7%. The Q-body immunosensor shows potential for clinical applications based on its excellent detection speed and sensitivity.

Keywords: estradiol, phage display, monoclonal antibody, immunosensor, rapid detection

INTRODUCTION

Estrogens effectively stimulate several functions in living organisms and regulate cancer development by promoting cell proliferation (Russo and Russo, 2006; Kumar et al., 2018). As one of the most active steroidal estrogens, 17β-estradiol (E2) has been widely examined. High or low levels of estradiol can disrupt the reproductive and endocrine systems, leading to the development of many diseases. Estradiol levels in the human serum can be used clinically to diagnose endocrine or gynecological disorders and male and female infertility, to assess male and female gonadal function and the post-menopausal status, and as a diagnostic indicator for tumors, such as ovarian and pituitary tumors (Rosenfeld et al., 2001; Schlegel, 2012; Luine, 2014; Leivo et al., 2019).

The main methods used to detect estradiol are chromatography (Asadi Atoi et al., 2019), enzyme-linked immunosorbent assay (ELISA) (Silva et al., 2013), radioimmunoassay (Saumande, 1981), chemiluminescence (Leivo et al., 2019), electrochemiluminescence (Ojeda et al., 2012) and

homogeneous enzyme immunoassay (Chiu et al., 2011). However, these assays are complex and some exhibit limited reproducibility, stability, and sensitivity. Among these methods, chromatography is a relatively sensitive assay with high accuracy; however, this assay requires several treatments of the sample in advance, costly instruments, and expert personnel. Therefore, the use of chromatography assays in clinical diagnoses is not preferred.

In contrast, Quenchbody (Q-body), a fluorescent biosensor based on antigen-antibody reactions, is simple to operate, highly specific, and can significantly improve the sensitivity and accuracy of the traditional assay. The Q-body is a recombinant antibody fragment in which the N-terminus is specifically labeled with a fluorescent dye, and the fluorescence is quenched by a tryptophan residue in the variable region of the antibody based on photo-induced electron transfer (Abe et al., 2011; Dong et al., 2020b; Dong and Ueda, 2021). Specific binding of the antigen to the antibody results in quenching of the fluorescent dye inside the antibody. The dye is displaced to the outside of the antibody, where de-quenching occurs, resulting in an antigen-dependent increase in fluorescence intensity (Dong et al., 2020a).

Monoclonal antibodies are the basis of immunoassays, and hybridoma technology (Kohler and Milstein, 1975) and molecular phage display technology (Smith, 1985) are two important methods for developing monoclonal antibodies. Phage display technology can correlate the genotype and phenotype of antibodies and can be used to rapidly develop monoclonal antibodies and evaluate antibody activity. In the present study, an anti-E2 antibody was developed by immunization of mice and the preparation and screening of a phage display antibody library. An E2 Q-body was prepared by labeling the N-terminus of an anti-E2 antibody with a fluorescent dye. A concentration-dependent increase in fluorescence intensity was detected following addition of E2, which was used to accurately determine serum E2 levels. This fluorescent biosensor, which is based on the specific binding of antigens and antibodies, can improve the accuracy of E2 detection and facilitate standardization of E2 test results.

MATERIALS AND METHODS

Materials

The strains *Escherichia coli* TG-1 used to construct the phage display antibody library and *E. coli* DH5α for gene cloning were purchased from Agilent Technologies (Santa Clara, CA, United States). *Escherichia coli* SHuffle T7 Express lysY was purchased from New England Biolabs (Ipswich, MA, United States) (Bessette et al., 1999; Levy et al., 2001). The E2 ovalbumin conjugate (E2-OVA) for immunization and E2 bovine serum albumin conjugate (E2-BSA) for antibody screening were purchased from Wuhan Huamei Biotechnology Co., Ltd (Wuhan, China). BALB/c mice were purchased from Jinan Yuepeng Experimental Animal Breeding Center (Jinan, China). The primers used in this study were synthesized by Shanghai Sangon Biotech Co. Ltd (Shanghai, China). Restriction enzymes were purchased from New England Biolabs. Unless otherwise specified, all reagents were purchased from Aladdin Industrial Corporation (Shanghai, China) or Shanghai Sangon Biotech.

Mouse Immunization

As shown in **Figure 1**, an anti-E2 antibody was obtained by immunizing BALB/c mice with the E2-OVA conjugate, preparing an antibody phage display library, and screening for monoclonal antibodies from the library. The developed monoclonal antibody was used to construct a fluorescent immunosensor for detecting E2. First, two BALB/c mice were immunized with 100 μl E2-OVA at a concentration of 100 μg/ml. Three immunizations were performed at 2-week intervals. Blood was collected from the tails of the mice at 1 week after the last antigen injection. ELISA was performed using immobilized E2-BSA to confirm the titer of anti-E2 antibodies in the blood of mice. The experimental protocol was established according to the ethical guidelines of the Declaration of Helsinki and approved by the Animal Ethics Committee of Weifang Medical University.

Construction of Phage Display Antibody Library

After confirming the presence of anti-E2 antibodies in the blood, the mice were sacrificed, and their spleens were extracted for total RNA extraction. TRIzol (Life Technologies, Carlsbad, CA, United States) was used for total RNA extraction according to the manufacturer's instructions. Reverse transcription-polymerase chain reaction (RT-PCR) was performed with 1 μl of total RNA to amplify genes in the antibody heavy chain variable region (V_H) and light chain variable region (V_L) using a PrimeScript One Step RT-PCR kit from Takara Bio (Shiga, Japan) according to the manufacturer's instructions. The murine antibody-specific primers used for this step are listed in **Supplementary Table S1**. The V_H and V_L genes were treated with the restriction enzymes *Sfi*I/*Xho*I and *Sal*I/*Not*I, respectively, and cloned into the phage display vector pDong1. The recombinant plasmids were used to transform *E. coli* TG-1 to prepare a phage display antibody library according to previously reported protocols (Dong et al., 2009).

Screening of Monoclonal Antibody

Sodium bicarbonate solution (100 μl) containing 10 μg/ml of E2-BSA was added to a 96-well microplate, which was then incubated at 4°C overnight. The next day, the cells were washed with PBS containing 0.1% Tween 20 (PBST), after which 200 μl phosphate-buffered saline (PBS) containing 2% skim milk powder (MPBS) was added to each well and incubated for 2 h to block any non-specific binding. After incubation and washing, 100 μl of phage solution containing 1×10^{10} colony forming units of phage displaying the antibody library was added to each well. After shaking for 1 h and incubating for another 1 h, the phage antibody bound to E2 was eluted with 1 mg/ml trypsin after washing. The eluted phage antibody was used to infect TG-1, and the phage display antibody library R1 was prepared at 30°C overnight. The above steps were repeated for the second and third rounds of selection and preparation of phage display antibody libraries R2 and R3, respectively. The microplates were coated with E2-BSA, and ELISA was performed to compare the E2-binding activity of the antibody libraries, including the primary phage library (R0), R1, R2, and R3. *Escherichia coli* TG-1 was infected with the phage library that exhibited the highest E2-binding activity and plated on Luria-Bertani (LB) solid medium

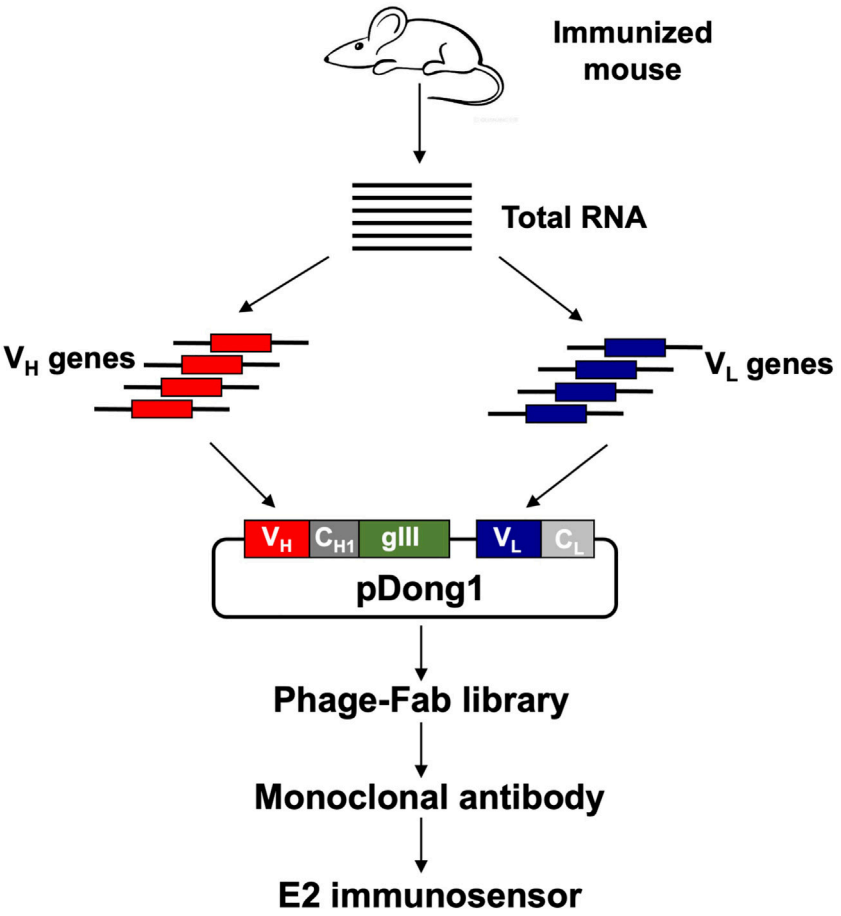

FIGURE 1 | Flow chart of antibody library construction and monoclonal antibody selection. V_H: variable region of antibody heavy chain; V_L: variable region of antibody light chain; C_{H1}: constant region 1 of heavy chain; C_L: constant region of light chain.

containing 100 μg/ml ampicillin. After overnight culture at 37°C, 96 colonies were selected to prepare phage-display antibodies. Phage ELISA was performed to select positive clones, which were further cultured for plasmid extraction and sequence analysis.

Vector Construction for Expression of Antigen-Binding Fragment (Fab)

The flowchart for constructing the vector expressing ESC9 Fab is shown in **Supplementary Figure S1**. The V_H-C_H1 and V_L genes of the selected positive clone ESC9 were amplified from pDong1-ESC9 using the primer pairs InfuAgeIESC9Vhback/OverlapEcoRvMycFor and OverlapEcoRvESC9VLback/InfuHindIIIESC9VL, respectively, followed by linking of the V_H-C_H1 and V_L genes to obtain V_H-C_H1-V_L by overlap PCR with the primers InfuAgeIESC9Vhback and InfuHindIIIESC9VL. The purified V_H-C_H1-V_L DNA fragments were then ligated and cloned into the pUQ1H (KTM219) vector (Abe et al., 2014) after double digestion with *Age*I and *Hin*dIII. The positive clone pUQ1H-ESC9 selected for the expression of ESC9 Fab was screened using colony PCR with T7 promoter and T7

TABLE 1 | Primers for preparation of Fab expression vector.

Primer name	Sequence (5′-3′)	Length (bp)
InfuAgeIESC9VHback	ACTGCTCTAATGAGACCGGTGAGGTTCAGCTGCAGCAGTCT	41
OverlapEcoRvMycFor	GTGATATCTCCTTCTAgaTTATTATGCGGCCCCATTCAGAT	42
OverlapEcoRvESC9VLback	TAGAAGGAGATATCACATGGATATTGTGATGACGCAGGCT	40
InfuHindIIIESC9VLfor	ACGTTTGATTTCaAGCTTGGTCCCAG	26
T7 promoter	TAATACGACTCACTATAGGG	20
T7 terminator	GCTAGTTATTGCTCAGCGG	19

terminator primers, followed by sequence analysis. The primers used to construct the Fab expression vectors are listed in **Table 1**.

Expression and Purification of ESC9 Fab

The successfully constructed vector was transformed into SHuffle T7 Express lysY *E. coli* cells, after which 40 µl of the transformed bacteria was spread evenly on LB solid medium containing 100 µg/ml ampicillin and incubated at 37°C overnight. Single colonies were picked and inoculated into 4 ml LB liquid medium containing 100 µg/ml ampicillin and incubated overnight at 250 rpm and 37°C. The overnight culture was transferred to 300 ml of fresh LB broth, to which 0.5 mM isopropyl β-D-thiogalactoside was added. The mixture was incubated at 220 rpm at 16°C for 20 h to induce protein expression.

The supernatant was removed by centrifugation at 8,000 × *g* for 10 min at 4°C. Thereafter, 10 ml of binding/washing buffer (50 mM phosphate, 0.3 M NaCl, 5 mM imidazole, pH 7.4) was added to resuspend the bacterial precipitate. The cells were sonicated on ice and centrifuged at 8,000 × *g* for 10 min at 4°C. The collected supernatant (10 ml) was added to an immobilized metal affinity chromatography resin, spin-bound for 1 h at 4°C, and passed through the column. After equilibrating the column with binding/washing buffer, the column was washed five times to remove heteroproteins. The target proteins were eluted by incubation with elution buffer (50 mM phosphate, 0.3 M NaCl, 500 mM imidazole, pH 7.0) for 1 min. The target protein bands were verified using sodium dodecyl sulfate-polyacrylamide gel electrophoresis (SDS-PAGE).

ELISA

BSA and E2-BSA (10 µg/ml each) were immobilized in 96-well clear polystyrene microplates and incubated overnight at 4°C. Blocking was performed with MPBS (200 µl) for 2 h, and the plates were washed three times with PBST. Thereafter, 100 µl of the anti-E2 antibody (10 µg/ml) was added, and the mixture was incubated for 1 h at 25°C, followed by three washes with PBST. Anti-6×His tag mouse antibody (100 µl) diluted by 1: 2,000 was added, and the plates were incubated at 25°C for 1 h. After three washes with PBST, 100 µl of the rabbit anti-mouse antibody coupled with horseradish peroxidase (HRP) diluted by 1:5,000 was added to the plates and incubated at 25°C for 1 h. After three washes with PBST, 100 µl of color-developing solution was added. The chromogenic solution was composed of 200 µg/ml 3,3,5,5-tetramethylbenzidine and 0.3 µl/ml hydrogen peroxide in 100 mM sodium acetate (pH 6.0). The reaction was terminated by adding 50 µl 10% H_2SO_4 to each well after 5 min of color development. Absorbance was measured at 450 nm using an iMark™ microplate reader (Bio-Rad, Hercules, CA, United States), with 630 nm as a reference.

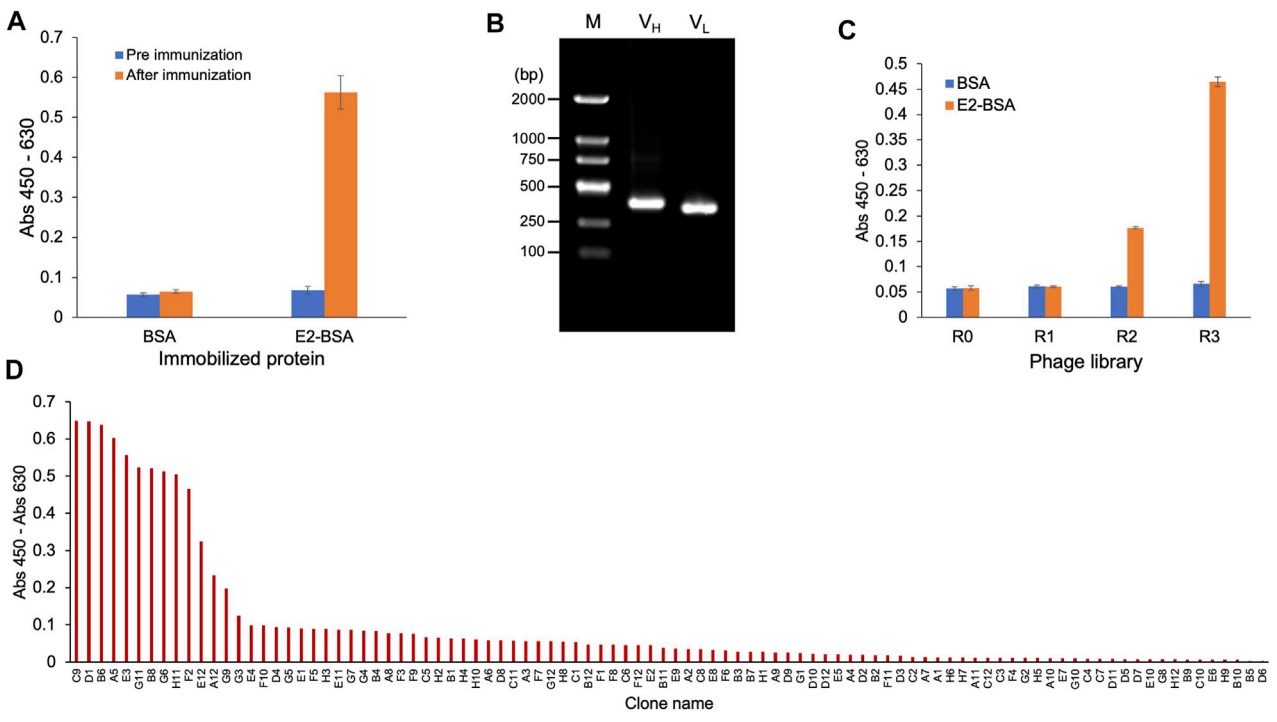

FIGURE 2 | Cloning of anti-E2 antibody. **(A)** ELISA of anti-E2 antibody in the sera of mice before and after immunization; **(B)** Gene amplification product of V_H gene (400 bp) and V_L gene (slightly smaller than V_H gene); **(C)** ELISA of phage-displayed anti-E2 antibody; **(D)** ELISA of monoclonal antibodies screened from the phage displayed antibody library. E2: 17β-estradiol; M: DNA Marker (100–2000 bp); V_H: variable regions of heavy chain; V_L: variable regions of light chain; E2-BSA: conjugate of E2 and bovine serum albumin.

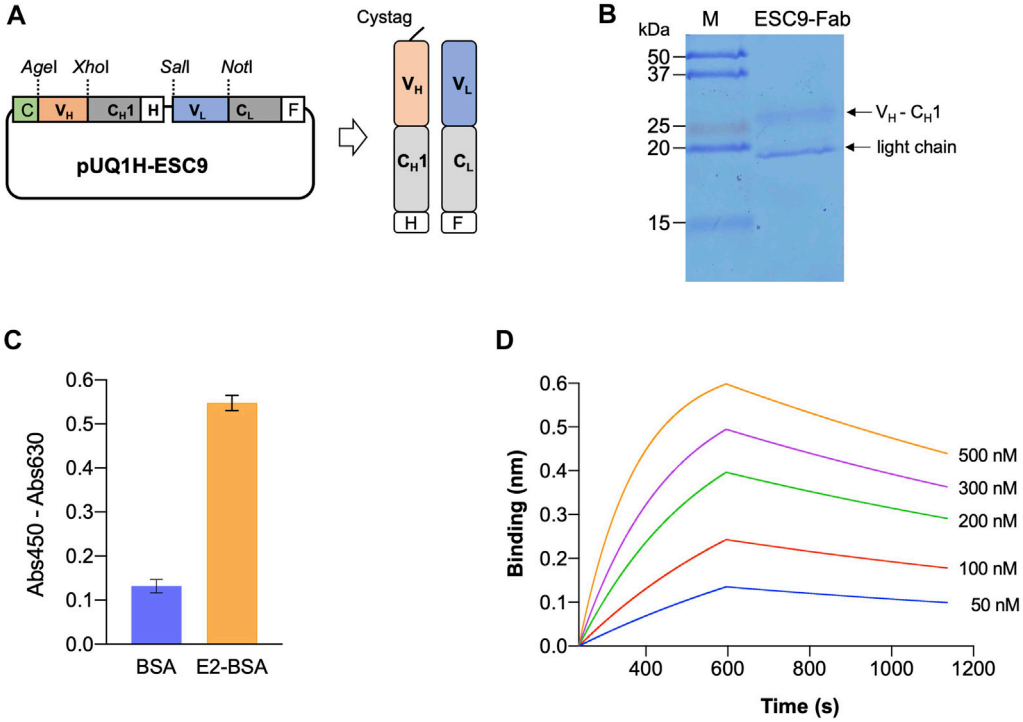

FIGURE 3 | Expression of antigen-binding fragment of ESC9 monoclonal antibody. **(A)** Construct of Fab expression vector; **(B)** SDS-PAGE analysis of purified ESC9 fragment; **(C)** ELISA of antigen-binding activity of purified Fab; **(D)** Sensorgram of bio-layer interference analysis of ESC9 Fab binding to E2. C: Cys-tag1; H: His_6-tag; F: Flag-tag; C_H1: constant region 1 of human IgG1 heavy chain; C_L: constant region of antibody light chain.

Kinetic Parameters of ESC9 Fab Binding to E2

E2-BSA was labeled with a biotinylation kit (BBI Life Sciences, Shanghai, China) according to the manufacturer's instructions to obtain E2-BSA-biotin, and the streptavidin-binding activity of E2-BSA-biotin was verified by performing the following assay: E2-BSA-biotin was coated onto a 96-well plate at 10 μg/ml and incubated at 4°C overnight. After washing and blocking the wells with PBST and MPBS, respectively, streptavidin-HRP (0.2 μg/ml) was added to each well and the plate was incubated at 25°C for 1 h. After washing with PBST, the assay was carried out based on the protocol for ELISA.

E2-BSA-biotin was fixed on a streptavidin (SA) probe, and kinetic parameters were measured using an Octet Red 96e system (FortéBio Corp., Fremont, CA, United States) based on bio-layer interference (BLI) technology. Antibody solutions with different concentrations (0, 50, 100, 200, 300, and 500 nM) were used to detect the binding rate in kinetic buffer (PBS containing 0.02% Tween 20 and 0.1% BSA). The dissociation rates of antibodies were determined. The SA probe was immersed in kinetic buffer without antibody as a negative control. The detection curve and equilibrium dissociation constant (K_D) were obtained using Data Analysis 12 HD (FortéBio).

Competitive ELISA

E2-BSA (100 μl; 10 μg/ml) was added to the wells of a microplate and incubated overnight at 4°C. The E2-BSA solution was discarded, and the microplate was blocked with 200 μl of MPBS. After washing three times with PBST, 100 μl of ESC9 Fab solution at 10 μg/ml with E2, testosterone, dehydroepiandrosterone, pregnenolone acetate, cortisol (Shanghai Macklin Biochemical Co., Ltd.), and diethylstilbestrol (Macklin) at concentrations of 0, 0.4, 2.0, 10, 50, 250, 1,000, 2000, and 20,000 ng/ml was added to the wells and incubated at 25°C. for 2 h. After washing with PBST three times, HRP-conjugated anti-His mouse antibody diluted by 1:5,000 was added and incubated for 1 h at 25°C. After washing, the assay was performed as previously described in ELISA section. The half-maximal inhibitory concentration (IC_{50}) of each competitive assay and cross-reactivity of ESC9 against E2, testosterone, dehydroepiandrosterone, pregnenolone acetate, cortisol, and diethylstilbestrol were calculated.

Preparation of E2 Q-Body

Fab solution (300 μl; 20 μM) was added to 0.5 mM tris (2-carboxyethyl) phosphine hydrochloride, and the exposed thiol groups were lightly reduced by mixing at 4°C for 20 min in the dark. Next, 2 mM 4-azidobenzoic acid was added, and the mixture was incubated on ice for 10 min. ATTO520-C2-maleimide (ATTO-TEC GmbH, Siegen, Germany) at a final concentration of 200 μM was added to the reaction solution, and the mixture was incubated at 25°C for 2 h. The protein was further purified by adding 60 μl of DYKDDDDK tag antibody-coated agarose beads (Thermo Fisher Scientific, Waltham, MA, United States) and

TABLE 2 | Kinetic parameters of ESC9 Fab and Q-body for E2-binding.

	K_{on} (1/Ms) ×10^4	K_{dis} (1/s) × 10^{-4}	K_D (nM)	R^2
ESC9-Fab	1.32 ± 0.003	5.72 ± 0.07	43.3 ± 0.1	0.9908
ESC9 Q-body	1.26 ± 0.007	7.08 ± 0.06	56.2 ± 0.5	0.9783

incubating the sample for 2 h at 4°C in the dark with stirring. Free fluorescent dye was removed by washing with PBST at 4°C, followed by centrifugation 5 times at 5,000 × *g* for 10 s each. The Q-body was obtained by adding 100 µl of 3×FLAG peptide at a concentration of 150 µg/ml and incubating the sample for 1 h at 4°C in the dark, followed by centrifugation for 1 min at 5,000 × g. SDS-PAGE was performed to verify the fluorescence modification and purity of the purified Q-body.

Denaturation Tests of ESC9 Q-Body and Detection of E2

The initial quenching of the Q-body was analyzed by comparing the fluorescence spectra obtained using PBST and PBST containing equal volumes of 7 M guanidine hydrochloride and 100 mM dithiothreitol (GdnHCl/DTT), using a Hitachi F4600 fluorescence spectrophotometer (Tokyo, Japan). The excitation and emission wavelengths of the ATTO520 dye were 520 and 545 nm, respectively. The fluorescence spectra of the ESC9 Q-body were again measured after adding E2 at final concentrations of 1.0, 5.0, 10.0, and 100 pg/ml; 1.0, 10.0, 100.0, and 500.0 ng/ml; and 1.0, 5.0, and 10.0 µg/ml followed by incubation at 25°C for 2 min. The fluorescence intensity of the Q-body at 545 nm in the presence of different concentrations of E2 was normalized by dividing the intensity by that of the Q-body without E2. Normalized values were used to draw a concentration-dependent curve for E2 detection. As shown in **Eq. 1**, a four-parameter logistic equation was used to fit the concentration-dependent relationship curve, and half-maximal effective concentration (EC_{50}) was evaluated using GraphPad Prism eight software (GraphPad, Inc., San Diego, CA, United States). The limit of detection of the assay for E2 was estimated as the antigen concentration equal to the mean blank value plus three standard deviations.

$$y = d + \frac{a - d}{1 + \left(\frac{x}{c}\right)^b} \quad (1)$$

Detection of E2 in Spiked Serum Samples

To evaluate the applicability of the ESC9 Q-body in practical assays, the E2 content in 25% serum was assayed using ESC9 Q-body. Three concentrations of E2 standards (100.0 pg/ml, 1.0 ng/ml, and 100.0 ng/ml) were added to human serum diluted to 25% with PBST and mixed with the ESC9 Q-bodies. The fluorescence intensity of prepared samples was measured at excitation and emission wavelengths of 520 and 545 nm, respectively, from which the fluorescence intensity of diluted serum was subtracted. Finally, the normalized fluorescence intensity of the Q-body probe in the serum samples was interpolated in the concentration-dependent standard curve and the E2 concentrations was calculated.

RESULTS

Screening of Monoclonal Antibodies

Venous blood was collected from the mice before and after three immunizations, and ELISA was performed. The results are shown in **Figure 2A**. After three immunization cycles, the absorbance of ELISA wells in which the serum from one mouse bound with E2-BSA was 0.58; this value was 9.7-fold higher than that of serum bound with BSA, which was only 0.06. Serum bound to BSA showed no signal difference before and after immunization, indicating that the signal difference observed in the serum bound to E2-BSA was due to the presence of specific antibodies against E2 after immunization, indicating that immunization was successful. Total RNA was extracted from the mouse spleens and used as a template to amplify the variable region genes of the antibodies. As shown in **Figure 2B**, the agarose gel electrophoresis results of PCR products with primers for the antibody V_H showed a DNA band of 400 bp, which was considered as the V_H gene. The amplified V_L gene with a slightly smaller size than that of V_H was also observed. The V_H and V_L genes were cloned into the phage display vector pDong1 and transfected into *E. coli* TG-1 to prepare a 2.1×10^6 phage display antibody library. Three rounds of biopanning against E2-BSA were conducted, and ELISA was performed to identify the E2-BSA binding activity of the original phage display antibody library (R0) and three antibody libraries (R1, R2, and R3) obtained during biopanning. As shown in **Figure 2C**, as panning progressed, the binding activity of the phage library to E2-BSA gradually increased, whereas that of the negative control (BSA) did not increase, indicating that anti-E2 antibodies were enriched in the phage display antibody library. Phage R3 was used to infect *E. coli* TG-1, 96 clones were selected after culture, monoclonal phages were prepared, and a phage ELISA was performed. As shown in **Figure 2D**, ten clones showed strong binding activity to E2. DNA sequences of these antibody genes were same and considered from the same antibody, which was named as ESC9. No antibody with the same sequence was found in the antibody database, suggesting that ESC9 is a novel antibody.

Construction of Fab Expression Vector

PCR was used to amplify the V_H-C_H1 and V_L fragments of the monoclonal antibody ESC9, and the amplicons were verified using agarose gel electrophoresis. As shown in **Supplementary Figure S2A**, for V_H-C_H1 and V_L, DNA bands were observed at 800 and 400 bp, respectively. The amplicon size was consistent with the theoretical fragment size, and the target genes were eluted. The V_H-C_H1 and V_L fragments were then linked using an overlap PCR and verified

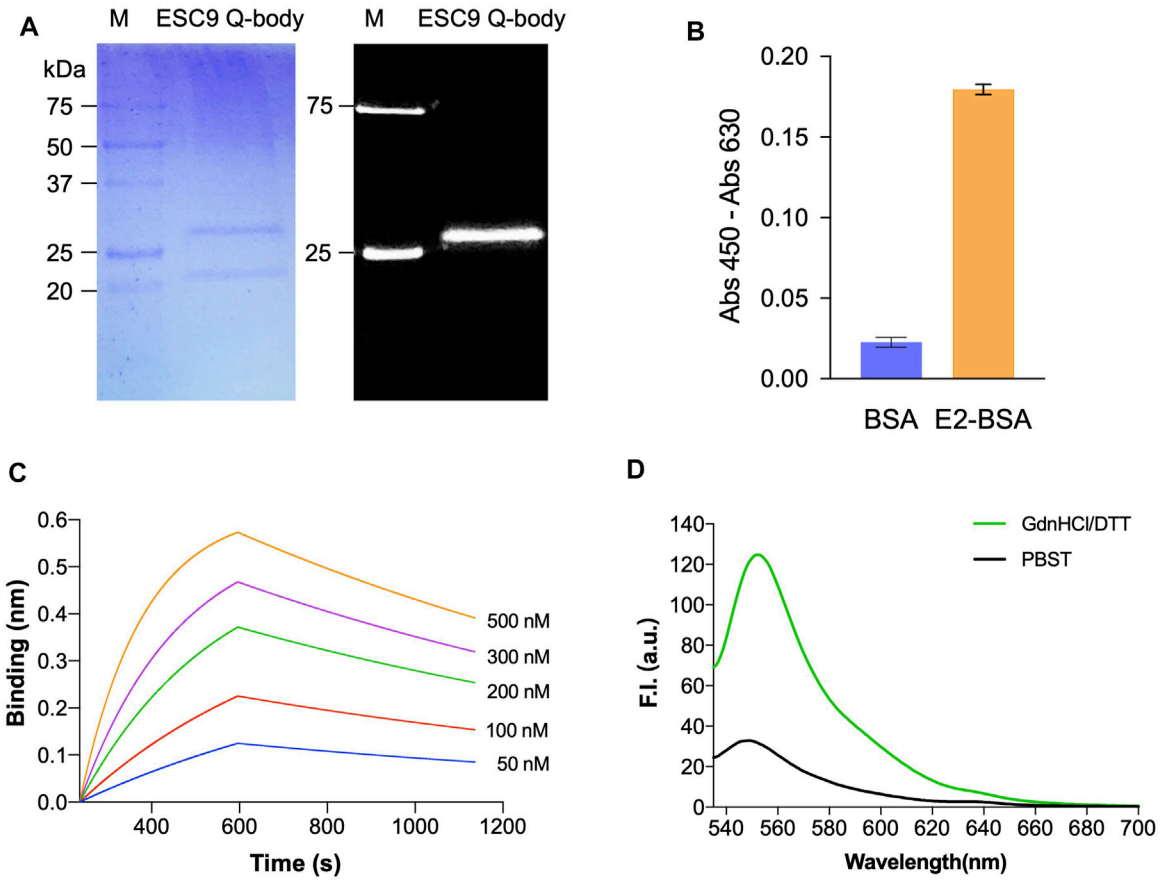

FIGURE 4 | Analysis of Q-body sensor. **(A)** Coomassie Brilliant Blue staining and fluorescent image of separated Q-body in SDS-PAGE; **(B)** ELISA of antigen-binding activity of E2 Q-body; **(C)** Sensorgram of bio-layer interference analysis of ESC9 Q-body binding to E2; **(D)** Fluorescent spectra of Q-body in PBST and denaturing reagent. M: Precision Plus Protein™ Unstained Protein Standards with 1/50 of Precision Plus Protein™ Dual-color Protein Standards (Bio-Rad); PBST: PBS containing 0.5% Tween 20; GdnHCl/DTT: 7 M guanidine hydrochloride and 100 mM dithiothreitol in PBST.

using agarose gel electrophoresis, as shown in **Supplementary Figure S2B**. The target genes were purified and inserted into the target vector, and colony PCR was performed to screen for the expression vector pUQ1H-ESC9, as shown in **Supplementary Figure S2C**. The construction of Fab Expression Vector pUQ1H-ESC9 is illustrated in **Figure 3A**. A Cys-tag peptide (MAQIEVNCSNET) was attached to the N-terminal of the heavy chain of the vector to allow for efficient expression of the Fab of the antibody and modification of the fluorescent dye, and a 6×His-tag and a FLAG-tag (DYKDDDDK) at the C-terminal end of the antibody Fd fragment (V_H-C_H1) and light chain were included to purify the antibody Fab. The vector was successfully constructed, as confirmed using sequencing analysis.

E2-Binding Affinity of ESC9-Fab

The Fab fragment of the ESC9 monoclonal antibody was purified using Ni-NTA Sefinose™ resin, and the purified Fab protein target bands was verified using SDS-PAGE. The results of Coomassie Brilliant Blue staining are shown in **Figure 3B**, where the Fd fragment of the heavy chain and light chain (V_L-C_L) of the Fab antibody were observed as two bands at 27 and 19 kDa, respectively. The size of Fd was similar to its theoretical molecular weight of 27.5 kDa, whereas its light chain was slightly smaller than the theoretical molecular weight of 24.4 kDa. This may be because we performed SDS-PAGE under non-denaturing conditions to prevent both proteins from stopping at the same position in the gel. The antigen-binding activity of ESC9-Fab was confirmed using ELISA. As shown in **Figure 3C**, purified Fab bound to E2-BSA with an absorbance of 0.57, whereas that against BSA was 0.12, indicating that purified Fab retained the antigen specificity of the original antibody. To further measure the kinetic parameters of ESC9 Fab binding to E2, E2-BSA-biotin was prepared, and its SA-binding activity was confirmed in a binding assay. As shown in **Supplementary Figure S3**, SA-HRP bound to E2-BSA-biotin but not to E2-BSA, indicating the successful preparation of E2-BSA-biotin. A sensorgram was obtained using BLI technology, as shown in **Figure 3D**, and the kinetic parameters are listed in **Table 2**. The association and dissociation rates were 1.32 ± 0.003 ×

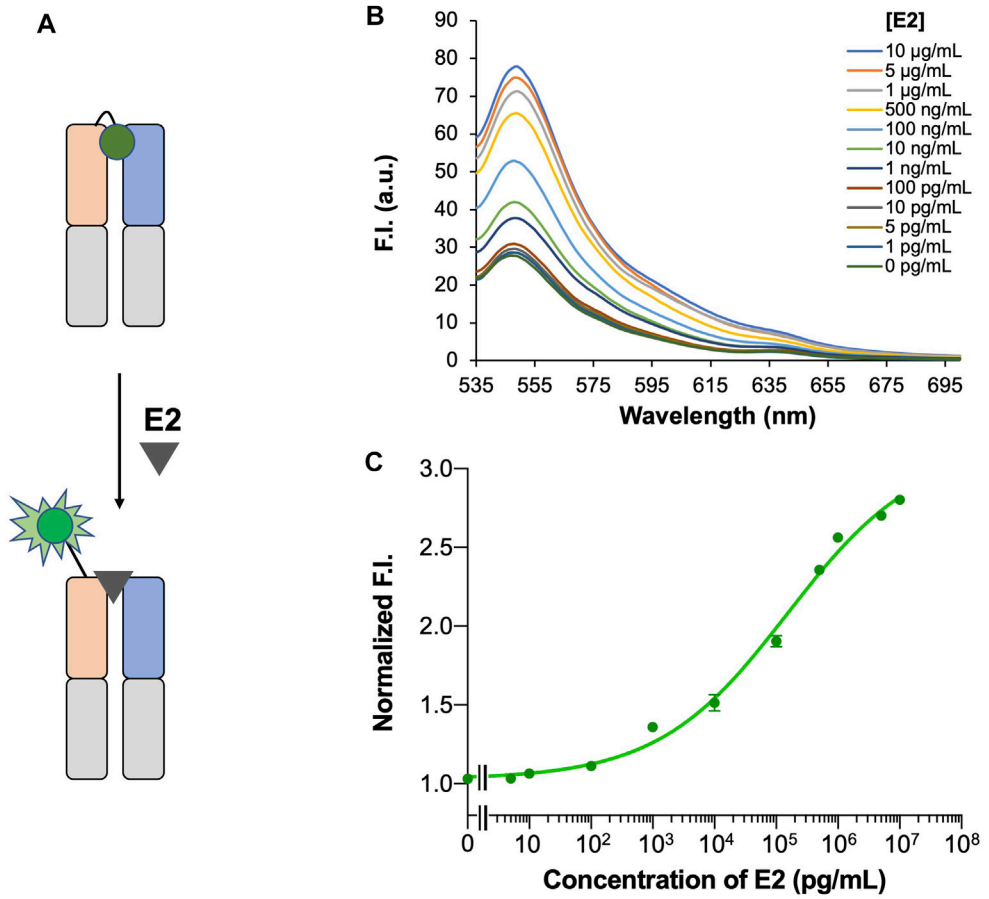

FIGURE 5 | Detection of E2 with ESC9 Q-body. **(A)** Scheme for E2 detection with the ESC9 Q-body; **(B)** Fluorescent spectrum of the ESC9 Q-body for E2 detection; **(C)** Concentration-dependent relationship curve for the detection of E2 with ESC9 Q-body.

10^4 $M^{-1}s^{-1}$ and $5.72 \pm 0.07 \times 10^{-4}$ s^{-1}, respectively, and the K_D value was calculated as 43.3 ± 0.1 nM with a coefficient of determination (R^2) of 0.9908.

Cross-Reactivity of ESC9

The IC_{50} values of the competitive assays with E2, testosterone, dehydroepiandrosterone, pregnenolone acetate, cortisol, and diethylstilbestrol were calculated by fitting the results of a standard competitive ELISA. The IC_{50} values of the assay with E2 and testosterone were 796.5 and 16,547.0 ng/ml, respectively, whereas no competition was observed with the other compounds. Based on these results, the cross-reactivity of ESC9 against TS was 4.8%, whereas no cross-reactivity was observed for dehydroepiandrosterone, pregnenolone acetate, cortisol and diethylstilbestrol.

TABLE 3 | Recovery of spiked E2 in human serum.

Spiked conc. (ng/ml)	Detected conc. (ng/ml)	Recovery (%)	
		Rate	RSD
0.1	0.083	83	6.2
1.0	1.27	127	10.3
100	105	105	11.4

Preparation of ESC9 Q-Body

ESC9 Fab was further labeled with ATTO520-C2-maleimide fluorescent dye and purified using G1 anti-DYKDDDDK beads. Fluorescent images and Coomassie Brilliant Blue staining of gels after SDS-PAGE were obtained to visualize the fluorescent modification of Q-bodies and their corresponding Fab target bands (**Figure 4A**). Two bands at 27 and 22 kDa were observed in the Coomassie Brilliant Blue-stained images and were considered to be the Fd and light chain, respectively. Only Fd was observed in the fluorescence image, suggesting that the labeling was successful. The antigen-binding activity of the ESC9 Q-body was assayed using ELISA with BSA as a negative control. The results are shown in **Figure 4B**, with an signal-to-noise value of 14.5, indicating that the fluorescence modification did not affect the antigen-binding activity of ESC9-Fab. **Figure 4C** shows the sensorgram of BLI analysis of ESC9 Q-body binding

to E2, and the association rate, dissociation rate, and K_D values of the binding were calculated as 1.26 ± 0.007 × 10^4 $M^{-1}s^{-1}$, 7.08 ± 0.06 × 10^{-4} s^{-1}, and 56.2 ± 0.5 nM, with an R^2 of 0.9783, as shown in **Table 2**.

Detection of E2 With ESC9 Q-Body

The quenching degree is an important parameter for evaluating the function of a Q-body (Ohashi et al., 2016). To evaluate the quenching degree, the fluorescence spectra of the ESC9 Q-body in PBST and denaturant GdnHCl/DTT were measured and compared. As shown in **Figure 4D**, the fluorescence intensity of the ESC9 Q-body at 545 nm was 3.8-fold higher than that of PBST, suggesting that the fluorescent dye in the ESC9 Q-body was quenched by the amino acids in the antibody. We then verified whether the fluorescence intensity increased upon E2 binding (**Figure 5A**). The fluorescence spectra of the ESC9 Q-body at different E2 concentrations are shown in **Figure 5B**. The maximum increase in fluorescence intensity was 2.8-fold at 10 μg/ml of E2; normalized fluorescence increase values at each concentration were plotted and fitted with a four-parameter to obtain an E2 concentration-dependent relationship standard curve, as shown in **Figure 5C**. Based on these results, the limit of detection of E2 and EC_{50} value were calculated as 3.9 pg/ml and 154.0 ng/ml, respectively.

E2-Spiked Serum Test and Evaluation

Three E2 standards at concentrations of 100 pg/ml, 1 ng/ml, and 100 ng/ml were added to 25% serum to verify that the Q-body probe can be used to detect E2 concentrations in blood samples. The change in fluorescence of the Q-body probe in the serum was calculated after subtracting the serum background with no sample and was calculated with the concentration-dependent curve. As shown in **Table 3**, the spiked E2 concentrations of 0.1, 1.0, and 100.0 ng/mL were detected as 0.083, 1.27, and 105 ng/mL with recovery rates of 83.0%, 127 and 105%, respectively, indicate that the Q-body probe can be used to quantitatively determine E2 levels in serum.

DISCUSSION

E2 is the most active natural estrogen among all endocrine disruptors and is often used as an important clinical indicator of gynecological diseases. Accurate quantification of serum estradiol levels is important for identifying physiological and pathological conditions in women. Moreover, E2 is commonly used as an endocrine-regulating drug in menopausal women (Adeel et al., 2017). When E2 accumulates in the human body through drinking water and food and exceeds the safety threshold, it destroys the body balance, damages human health, and endangers future generations (Singh et al., 2012; Zhang et al., 2013). Therefore, the research and development of E2 detection technology is of great significance.

In the present study, a novel monoclonal antibody against E2, ESC9, was developed by immunizing mice and constructing and biopanning a phage-display antibody library. The gene and allele symbols of the V_H of ESC9 were *IGHV1* and *IGHJ2*, respectively; those of the V_L region were *IGKV4* and *IGKJ2*. Using bio-layer interference, the affinity of ESC9 Fab was measured to be 43.3 nM, showing high affinity. Several anti-E2 antibodies have been reported previously. For example, Pajunen et al. reported three anti-estradiol-17β antibodies with Ka values of 2.2–13.4 nM (Pajunen et al., 1997). Kabayashi et al. reported an scFv antibody with an affinity of 860 nM developed by immunization with mouse and phage display technology, which was further improved to 26 nM using complementary-determining region shuffling technology (Kobayashi et al., 2008; Kobayashi et al., 2010). The affinity of our antibodies was equal to or slightly better than that of the aforementioned antibodies. In our further studies, we may perform artificial evolution of ESC9 using approaches such as molecular breeding (Oyama et al., 2013) or open-sandwich selection (Iwai et al., 2010) to further improve the affinity of the antibody and sensitivity of the assay. Although ESC9 does not cross-react with dehydroepiandrosterone, pregnenolone acetate, cortisol, and diethylstilbestrol, it does react with TS. We will artificially evolve antibodies to reduce cross-reactions and improve the antibody specificity, as reported previously (Liu et al., 2012).

By modifying the N-terminus of the ESC9 Fab fragment with a fluorescent dye, a Q-body for detecting E2 was prepared. The affinity of Q-body was measured to be 56.2 nM, which is slightly lower than that of ESC9 Fab, suggesting that fluorescent dye labeling did not greatly reduce antigen-binding activity. The Q-body assay detected E2 at concentrations as low as 3.9 pg/ml within 2 min. The Q-body assay is a homogeneous detection technology with excellent detection speed and sensitivity. Additionally, it is not necessary to remove other substances from the sample, and high-throughput automatic detection is easy to perform (Abe et al., 2011; Jeong and Ueda, 2014; Ueda and Dong, 2014). Although the detection sensitivity of our method is similar or slightly better than those of some previously reported assays mainly based on competitive immunoassays in which the detection time is generally long, and its detection range is relatively narrow. To date, only one homogeneous assay for detecting E2 has been reported (Chiu et al., 2011); however, the sensitivity was 1 nM (272 pg/ml). Compared with the traditional methods, the detection time and range were significantly improved in our assay. We also used the developed assay to successfully detect E2 in sera with excellent accuracy and recovery, indicating its potential for use in clinical applications.

DATA AVAILABILITY STATEMENT

The original contributions presented in the study are included in the article/**Supplementary Material**, further inquiries can be directed to the corresponding authors.

ETHICS STATEMENT

The animal study was reviewed and approved by The Animal Ethics Committee of Weifang Medical University.

AUTHOR CONTRIBUTIONS

JL, HD, FX, BL, HL and YL conducted experiments. LC, ML and GJ collected experimental data and performed analyses. JD obtained funds and supervised all experiments. JL and JD wrote the manuscript.

FUNDING

All sources of funding received for the research being submitted. This research was partly funded by the National Natural Science Foundation of China (Grant Number: 21775064) and Science and Technology Planning Project of Weifang City, Shandong Province, China (Grant Number: 2020YQFK014).

SUPPLEMENTARY MATERIAL

The Supplementary Material for this article can be found online at: https://www.frontiersin.org/articles/10.3389/fbioe.2022.818983/full#supplementary-material

REFERENCES

Abe, R., Ohashi, H., Iijima, I., Ihara, M., Takagi, H., Hohsaka, T., et al. (2011). "Quenchbodies": Quench-Based Antibody Probes that Show Antigen-dependent Fluorescence. *J. Am. Chem. Soc.* 133 (43), 17386–17394. doi:10.1021/ja205925j

Abe, R., Jeong, H.-J., Arakawa, D., Dong, J., Ohashi, H., Kaigome, R., et al. (2014). Ultra Q-Bodies: Quench-Based Antibody Probes that Utilize Dye-Dye Interactions with Enhanced Antigen-dependent Fluorescence. *Sci. Rep.* 4, 4640. doi:10.1038/srep04640

Adeel, M., Song, X., Wang, Y., Francis, D., and Yang, Y. (2017). Environmental Impact of Estrogens on Human, Animal and Plant Life: A Critical Review. *Environ. Int.* 99, 107–119. doi:10.1016/j.envint.2016.12.010

Asadi Atoi, P., Talebpour, Z., and Fotouhi, L. (2019). Introduction of Electropolymerization of Pyrrole as a Coating Method for Stir Bar Sorptive Extraction of Estradiol Followed by Gas Chromatography. *J. Chromatogr. A* 1604, 460478. doi:10.1016/j.chroma.2019.460478

Bessette, P. H., Åslund, F., Beckwith, J., and Georgiou, G. (1999). Efficient Folding of Proteins with Multiple Disulfide Bonds in the *Escherichia coli* Cytoplasm. *Proc. Natl. Acad. Sci. U.S.A.* 96 (24), 13703–13708. doi:10.1073/pnas.96.24.13703

Chiu, M. L., Tseng, T. T.-C., and Monbouquette, H. G. (2011). A Convenient Homogeneous Enzyme Immunoassay for Estradiol Detection. *Biotechnol. Appl. Biochem.* 58 (1), 75–82. doi:10.1002/bab.5

Dong, J., and Ueda, H. (2021). Recent Advances in Quenchbody, a Fluorescent Immunosensor. *Sensors* 21 (4), 1223. doi:10.3390/s21041223

Dong, J., Ihara, M., and Ueda, H. (2009). Antibody Fab Display System that Can Perform Open-sandwich ELISA. *Anal. Biochem.* 386 (1), 36–44. doi:10.1016/j.ab.2008.11.045

Dong, J., Miyake, C., Yasuda, T., Oyama, H., Morita, I., Tsukahara, T., et al. (2020a). PM Q-Probe: A Fluorescent Binding Protein that Converts many Antibodies to a Fluorescent Biosensor. *Biosens. Bioelectron.* 165, 112425. doi:10.1016/j.bios.2020.112425

Dong, J., Oka, Y., Jeong, H. J., Ohmuro-Matsuyama, Y., and Ueda, H. (2020b). Detection and Destruction of HER2-positive Cancer Cells by Ultra Quenchbody-siRNA Complex. *Biotechnol. Bioeng.* 117 (5), 1259–1269. doi:10.1002/bit.27302

Iwai, H., Öztürk, B., Ihara, M., and Ueda, H. (2010). Antibody Affinity Maturation *In Vitro* Using Unconjugated Peptide Antigen. *Protein Eng. Des. Sel.* 23 (4), 185–193. doi:10.1093/protein/gzp093

Jeong, H.-J., and Ueda, H. (2014). Strategy for Making a superior Quenchbody to Proteins: Effect of the Fluorophore Position. *Sensors* 14 (7), 13285–13297. doi:10.3390/s140713285

Kobayashi, N., Kato, Y., Oyama, H., Taga, S., Niwa, T., Sun, P., et al. (2008). Anti-estradiol-17β Single-Chain Fv Fragments: Generation, Characterization, Gene Randomization, and Optimized Phage Display. *Steroids* 73 (14), 1485–1499. doi:10.1016/j.steroids.2008.08.009

Kobayashi, N., Oyama, H., Kato, Y., Goto, J., Söderlind, E., and Borrebaeck, C. A. K. (2010). Two-Step *In Vitro* Antibody Affinity Maturation Enables Estradiol-17β Assays with More Than 10-Fold Higher Sensitivity. *Anal. Chem.* 82 (3), 1027–1038. doi:10.1021/ac902283n

Kohler, G., and Milstein, C. (1975). Continuous Cultures of Fused Cells Secreting Antibody of Predefined Specificity. *Nature* 256 (5517), 495–497. doi:10.1038/256495a0

Kumar, A., Banerjee, A., Singh, D., Thakur, G., Kasarpalkar, N., Gavali, S., et al. (2018). Estradiol: A Steroid with Multiple Facets. *Horm. Metab. Res.* 50 (5), 359–374. doi:10.1055/s-0044-100920

Leivo, J., Kivimäki, L., Juntunen, E., Pettersson, K., and Lamminmäki, U. (2019). Development of Anti-immunocomplex Specific Antibodies and Non-competitive Time-Resolved Fluorescence Immunoassay for the Detection of Estradiol. *Anal. Bioanal. Chem.* 411 (22), 5633–5639. doi:10.1007/s00216-019-01952-6

Levy, R., Weiss, R., Chen, G., Iverson, B. L., and Georgiou, G. (2001). Production of Correctly Folded Fab Antibody Fragment in the Cytoplasm of *Escherichia coli* trxB Gor Mutants via the Coexpression of Molecular Chaperones. *Protein Expr. Purif.* 23 (2), 338–347. doi:10.1006/prep.2001.1520

Liu, X., Eichenberger, M., Fujioka, Y., Dong, J., and Ueda, H. (2012). Improved Detection Sensitivity and Selectivity Attained by Open-sandwich Selection of an Anti-estradiol Antibody. *Anal. Sci.* 28 (9), 861–867. doi:10.2116/analsci.28.861

Luine, V. N. (2014). Estradiol and Cognitive Function: Past, Present and Future. *Horm. Behav.* 66 (4), 602–618. doi:10.1016/j.yhbeh.2014.08.011

Ohashi, H., Matsumoto, T., Jeong, H.-J., Dong, J., Abe, R., and Ueda, H. (2016). Insight into the Working Mechanism of Quenchbody: Transition of the Dye Around Antibody Variable Region that Fluoresces upon Antigen Binding. *Bioconjug. Chem.* 27 (10), 2248–2253. doi:10.1021/acs.bioconjchem.6b00217

Ojeda, I., López-Montero, J., Moreno-Guzmán, M., Janegitz, B. C., González-Cortés, A., Yáñez-Sedeño, P., et al. (2012). Electrochemical Immunosensor for Rapid and Sensitive Determination of Estradiol. *Analytica Chim. Acta* 743, 117–124. doi:10.1016/j.aca.2012.07.002

Oyama, H., Yamaguchi, S., Nakata, S., Niwa, T., and Kobayashi, N. (2013). "Breeding" Diagnostic Antibodies for Higher Assay Performance: A 250-Fold Affinity-Matured Antibody Mutant Targeting a Small Biomarker. *Anal. Chem.* 85 (10), 4930–4937. doi:10.1021/ac3037602

Pajunen, M., Saviranta, P., Jauria, P., Karp, M., Pettersson, K., Mäntsälä, P., et al. (1997). Cloning, Sequencing, Expression and Characterization of Three Anti-estradiol-17beta Fab Fragments. *Biochim. Biophys. Acta* 1351 (1-2), 192–202. doi:10.1016/s0167-4781(96)00202-3

Rosenfeld, C., Wagner, J., Roberts, R., and Lubahn, D. (2001). Intraovarian Actions of Oestrogen. *Reproduction* 122 (2), 215–226. doi:10.1530/rep.0.1220215

Russo, J., and Russo, I. H. (2006). The Role of Estrogen in the Initiation of Breast Cancer. *J. Steroid Biochem. Mol. Biol.* 102 (1-5), 89–96. doi:10.1016/j.jsbmb.2006.09.004

Saumande, J. (1981). Radioimmunoassay of Estradiol-17β in Unextracted EWE Plasma. *Steroids* 38 (4), 425–437. doi:10.1016/0039-128x(81)90077-5

Schlegel, P. N. (2012). Aromatase Inhibitors for Male Infertility. *Fertil. Sterility* 98 (6), 1359–1362. doi:10.1016/j.fertnstert.2012.10.023

Silva, C. P., Lima, D. L. D., Schneider, R. J., Otero, M., and Esteves, V. I. (2013). Development of ELISA Methodologies for the Direct Determination of

17β-Estradiol and 17α-Ethinylestradiol in Complex Aqueous Matrices. *J. Environ. Manage.* 124, 121–127. doi:10.1016/j.jenvman.2013.03.041

Singh, K. P., Treas, J., Tyagi, T., and Gao, W. (2012). DNA Demethylation by 5-Aza-2-Deoxycytidine Treatment Abrogates 17 Beta-Estradiol-Induced Cell Growth and Restores Expression of DNA Repair Genes in Human Breast Cancer Cells. *Cancer Lett.* 316 (1), 62–69. doi:10.1016/j.canlet.2011.10.022

Smith, G. P. (1985). Filamentous Fusion Phage: Novel Expression Vectors that Display Cloned Antigens on the Virion Surface. *Science* 228 (4705), 1315–1317. doi:10.1126/science.4001944

Ueda, H., and Dong, J. (2014). From Fluorescence Polarization to Quenchbody: Recent Progress in Fluorescent Reagentless Biosensors Based on Antibody and Other Binding Proteins. *Biochim. Biophys. Acta Proteins Proteomics* 1844 (11), 1951–1959. doi:10.1016/j.bbapap.2014.06.005

Zhang, X., Tworoger, S. S., Eliassen, A. H., and Hankinson, S. E. (2013). Postmenopausal Plasma Sex Hormone Levels and Breast Cancer Risk over 20 Years of Follow-Up. *Breast Cancer Res. Treat.* 137 (3), 883–892. doi:10.1007/s10549-012-2391-z

Conflict of Interest: The authors declare that the research was conducted in the absence of any commercial or financial relationships that could be construed as a potential conflict of interest.

Publisher's Note: All claims expressed in this article are solely those of the authors and do not necessarily represent those of their affiliated organizations or those of the publisher, the editors, and the reviewers. Any product that may be evaluated in this article, or claim that may be made by its manufacturer, is not guaranteed or endorsed by the publisher.

frontiers | Frontiers in Bioengineering and Biotechnology

ORIGINAL RESEARCH
published: 02 June 2022
doi: 10.3389/fbioe.2022.850571

Healing Field: Using Alternating Electric Fields to Prevent Cytokine Storm by Suppressing Clonal Expansion of the Activated Lymphocytes in the Blood Sample of the COVID-19 Patients

Hamed Abadijoo[1,2,3,4†], *Mohammad Ali Khayamian*[1,2,3,4*†], *Mahsa Faramarzpour*[1,2,3,4], *Mohammadreza Ghaderinia*[1,2,3,4], *Hossein Simaee*[1,2,3,4], *Shahriar Shalileh*[1,2,3,4], *Seyed Mojtaba Yazdanparast*[1,2,3,4], *Bahman Ghabraie*[1,2,3,4], *Jalil Makarem*[4], *Ramin Sarrami-Forooshani*[5,6] *and Mohammad Abdolahad*[1,2,3,4*†]

[1]Nano Electronic Center of Excellence, Nano Bio Electronic Devices Lab, School of Electrical and Computer Engineering, University of Tehran, Tehran, Iran, [2]Nano Electronic Center of Excellence, Thin Film and Nano Electronics Lab, School of Electrical and Computer Engineering, University of Tehran, Tehran, Iran, [3]Institute of Cancer, Imam Khomeini Hospital, Tehran University of Medical Sciences, Tehran, Iran, [4]UT and TUMS Cancer Electronics Research Center, Tehran University of Medical Sciences, Tehran, Iran, [5]ATMP Department, Breast Cancer Research Center, Motamed Cancer Institute, ACECR, Tehran, Iran, [6]Department of Experimental Immunology, Amsterdam Infection and Immunity Institute, Amsterdam University Medical Centers, University of Amsterdam, Amsterdam, Netherlands

In the case of the COVID-19 early diagnosis, numerous tech innovations have been introduced, and many are currently employed worldwide. But, all of the medical procedures for the treatment of this disease, up to now, are just limited to chemical drugs. All of the scientists believe that the major challenge toward the mortality of the COVID-19 patients is the out-of-control immune system activation and the subsequent cytokine production. During this process, the adaptive immune system is highly activated, and many of the lymphocytes start to clonally expand; hence many cytokines are also released. So, any attempt to harness this cytokine storm and calm down the immune outrage is appreciated. While the battleground for the immune hyperactivation is the lung ambient of the infected patients, the only medical treatment for suppressing the hypercytokinemia is based on the immunosuppressor drugs that systemically dampen the immunity with many unavoidable side effects. Here, we applied the alternating electric field to suppress the expansion of the highly activated lymphocytes, and by reducing the number of the renewed cells, the produced cytokines were also decreased. Applying this method to the blood of the COVID-19 patients *in vitro* showed ~33% reduction in the average concentration of the three main cytokines after 4 days of stimulation. This method could carefully be utilized to locally suppress the hyperactivated immune cells in the lung of the COVID-19 patients without any need for systemic suppression of the immune system by the chemical drugs.

Keywords: COVID-19, cytokine storm, clonal expansion, lymphocyte, alternating electric fields, mitosis suppression, inflammation

OPEN ACCESS

Edited by:
Tatiana Fiordelisio, National Autonomous University of Mexico, Mexico

Reviewed by:
Pradipta Ranjan Rauta, Asian Institute of Public Health, India
Sumit Ghosh, The Research Institute at Nationwide Children's Hospital, United States

***Correspondence:**
Mohammad Ali Khayamian
m.a.khayamian@ut.ac.ir
m.a.khayamian@gmail.com
Mohammad Abdolahad
m.abdolahad@ut.ac.ir
abdolahad@tums.ac.ir

[†]*These authors have contributed equally to this work*

Specialty section:
This article was submitted to Biosensors and Biomolecular Electronics, a section of the journal Frontiers in Bioengineering and Biotechnology

Received: *07 January 2022*
Accepted: *02 May 2022*
Published: *02 June 2022*

Citation:
Abadijoo H, Khayamian MA, Faramarzpour M, Ghaderinia M, Simaee H, Shalileh S, Yazdanparast SM, Ghabraie B, Makarem J, Sarrami-Forooshani R and Abdolahad M (2022) Healing Field: Using Alternating Electric Fields to Prevent Cytokine Storm by Suppressing Clonal Expansion of the Activated Lymphocytes in the Blood Sample of the COVID-19 Patients. Front. Bioeng. Biotechnol. 10:850571. doi: 10.3389/fbioe.2022.850571

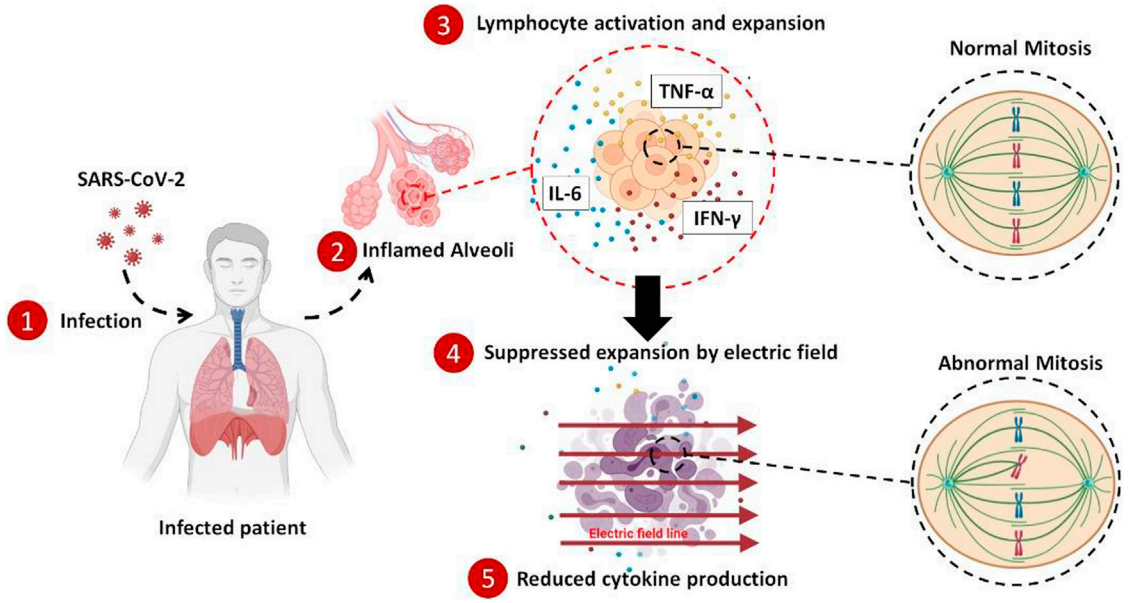

Graphical Abstract |

INTRODUCTION

More than 200 million infections with at least four million mortalities (World Health Organization, 2021) worldwide are just a small part of the consequences that a 100 nm coronavirus (Zhu et al., 2020) has imposed on the world community since its emergence in China in 2019 (Phelan et al., 2020). After infection and commencement of the disease's immunological phase, many clinical manifestations would arise, but acute respiratory distress syndrome (ARDS) is the most lethal feature of the COVID-19 (Gibson et al., 2020; Ragab et al., 2020). Numerous pieces of evidence suggest that the severity of the disease and ARDS is highly correlated with the proinflammatory cytokine levels in the bloodstream and the intensity of the immune cell hyperactivation caused by the virus (Mangalmurti and Hunter, 2020; Mehta et al., 2020; Vaninov, 2020; Khayamian et al., 2021).

Out-of-control secretion of cytokine proteins with subsequent immune system hyper-activation causes severe systemic damages to the tissues and organs throughout the body, such as pulmonary dysfunction and renal failure (Bhaskar et al., 2020; Rabb, 2020; Sun et al., 2020). To prevent exacerbation and progression of the disease in such patients, a broad range of immunosuppressor drugs such as corticosteroids, JAK inhibitors, etc., are used as a general treatment (Abdin et al., 2020; Kolilekas et al., 2020; Sharun et al., 2020; Ye et al., 2020; Hu et al., 2021). For instance, dexamethasone therapy has shown promising results in reducing the severity of the infection and suppressing cytokine storm and the consequent hyperinflammation phase of the disease (Chen et al., 2006; Lammers et al., 2020; Group et al., 2021; Noreen et al., 2021). One major effect of the immunosuppressor drugs such as dexamethasone is their antiproliferative effect. In fact, dexamethasone impairs the proliferation of the lymphocytes such as T cells during their clonal expansion (Creed et al., 2009; Maślanka, 2013; Maślanka and Jaroszewski, 2013; Giles et al., 2018). Although many benefits are associated with the administration of dexamethasone for suppression of severe inflammations, many serious side effects (Alessi et al., 2020; Langarizadeh et al., 2021), such as the increased risk of sepsis (Bendel et al., 2002; Pera et al., 2002), calcium metabolism (Caniggia et al., 1981; Kusuda et al., 2019), kidney disorders (McKay and Cidlowski, 2003; de Vries et al., 2010), etc., (Russell et al., 2020; Hu et al., 2021), are also inevitable.

Cytokines, as the signaling proteins and mediators of the immune response to the inflammation, are secreted by a variety of the cells, including lymphocytes, granulocytes, macrophages, endothelial cells, fibroblasts, etc., among which T cell lymphocytes are the dominant agents that level up the released cytokines in the bloodstream (Zhang and An, 2007). Part of the cytokine secretion by the lymphocytes is attributed to their clonal expansion, a phenomenon by which activated lymphocytes produce more of themselves through mitosis division with the same antigen against a specific pathogen (Condotta and Richer, 2017; Adams et al., 2020; Gutierrez et al., 2020; Liao et al., 2020). Hence, controlling such mitosis would be of interest in the suppression of immune hyperactivation in COVID-19 patients.

Alternating electric field (AEF) therapy, mostly called tumor-treating fields (TTF), is a safe treatment of highly proliferative cancer cells by delivering the low intensity and intermediate frequency electric field (Carrieri et al., 1991; Hottinger et al., 2016). The method disrupts the mitotic spindle assembly of the dividing cells (Kirson et al., 2007). The abnormally divided cells with prolonged mitosis phase (during their cell cycle) finally

undergo apoptosis. Since the AEF has an antimitotic mechanism, the most affected cells are highly proliferative ones, such as rapid growing cancer cells, while the healthy cells with a low division rate are not damaged during this stimulation (Kirson et al., 2004; Giladi et al., 2015).

On this basis, AEF could safely be applied for each patient to suppress the highly activated and expanding lymphocytes and consequently reduce the amount of the released cytokines into the blood. As previously mentioned, such a procedure is currently implemented using the systemic administration of the immunosuppressor drugs that debilitate the entire immune system (Mehta et al., 2020). AEF stimulation just impacts the highly expanding lymphocytes in the lung ambient without any effect on the other immune cells, contrary to the immunosuppressor drugs that impair all of the immune cells.

Here, we investigated the possibility of using the AEF modality to suppress the clonal expansion of highly activated and proliferative lymphocytes and the consequent reduction in the cytokines released by these cells, suitable as an anti-inflammation technique for COVID-19 patients. For this purpose, the peripheral blood mononuclear cells (PBMCs) were isolated from healthy donors, followed by artificially being activated using the lymphocyte expansion kits. Then, the effect of the AEF on suppressing the expansion of the lymphocytes was evaluated by time-lapse imaging, viability, and apoptosis assays as well as flow cytometry technique. Moreover, the amount of three major cytokines (TNF-alpha, INF-gamma, IL-6) after AEF stimulation was also measured using the ELISA method. Then, the proposed method was verified by *in vitro* stimulating the WBCs derived from the COVID-19 patients with severe inflammation and cytokine storm. Based on the results, an average of ~33% in cytokine reduction was achieved after 1 week of AEF stimulation on the immune cells of the blood. In the case of artificially activated immune cells by lymphocyte expansion kits, this number was about ~26%. We believe that the proposed electrical method with promising results by local suppression of the cytokine storm could be a safe substitute for the immunosuppressor drugs with their systemic effects.

MATERIALS AND METHODS

Alternating Electric Field Stimulation Set-Up

The glass substrate was cleaned using piranha solution (H_2SO_4: H_2O_2 with a volume ratio of 2:1, respectively). Then the substrate was deposited with Cr and Au layers using RF sputtering procedure. The 20 nm Cr layer was used in order to enhance the 100 nm Au layer adhesion to the glass substrate. Using standard photolithography (Jahangiri et al., 2019; 2020), the eight electrodes were patterned on the surface of Au coated glass. The patterned electrodes were passivated using a 4 μm layer of PDMS by spin coating at 6000 rpm for 5 min. The biochip contains eight electrodes designed in a circular pattern with an inner radius of 2 cm to attain symmetrical electric field distribution in four directions of electric field stimulation. Finally, the biochip was inserted into the set-up and connected to the RF function generator for AEF stimulation (100 kHz sinusoid of 3 V/cm electric field amplitude).

Electric Field Simulation

Potential and electric field distributions were studied using electrostatics physics of COMSOL Multiphysics 5.5 to investigate the electric field distribution in the biochip. The applied electric field was calibrated to obtain the highest area percentage covered by the electric field intensity in the range of AEF stimulation.

Peripheral Blood Mononuclear Cells Activation and Expansion Protocol

Human PBMC isolation was performed using the density gradient centrifugation method. The isolated PBMCs were diluted to 10^6 cells/ml in Dulbecco's Modified Eagle Medium (Cat number: 10566016, Gibco, United States) containing 10% fetal bovine serum (Cat number: 10082139, Gibco, United States) and 1% penicillin-streptomycin (Cat number: 15070063, Gibco, United States). 10^6 cells were seeded in 6-well plates per well. 3 mls of the cell culture medium were added to each well. To obtain the lymphocyte activation, Human T cell activator (Cat number: 10,970, Stemcell Technologies, Canada) and B cell expansion kit (Cat number: 100-0645, Stemcell Technologies, Canada) were added to the culture medium with concentrations of 25 μl/ml and 20 μl/ml respectively. The cells were incubated at 37°C and 5% CO_2 in a humidified incubator for 5 days.

Peripheral Blood Mononuclear Cells Isolation

PBMCs were isolated from freshly drawn blood stored in Heparin capped tubes for 15 min at 37°C. At first, the blood was diluted using PBS (1:1) and then gently layered over Ficoll (Cat number: F4375, Merck, Germany) (4:3) in a centrifuge tube. The whole sample was then centrifuged for 20 min at 2000 rpm. After this process, four layers were formed. The uppermost layer contained diluted blood plasma, and the second layer contained PBMCs. This layer was then gently removed and was added to fresh PBS (1:3) for another two rounds of centrifugation for 10 min at 2000 and 1500 rpm to wash out any remained platelets. Then the PBMCs were diluted in 1 cc of PBS and counted using Trypan blue staining in the Neubauer chamber.

Immunofluorescence Microscopy

CD8 and CD19 expression in PBMCs was assessed using inverted fluorescence microscopy. As previously reported by our group (Ansaryan et al., 2019; Khayamian et al., 2019), the PBMCs were first fixed in 3.7% formaldehyde for 15 min and permeabilized with Triton X-100 in PBS for 5–10 min (with a concentration of 1%) at room temperature. The cells were then washed with PBS and then treated with a blocking buffer (1% BSA in PBS) for 40 min at room temperature. Then, all samples were washed and stained with the Anti-CD8 Antibody (ab217344-abcam) as the primary antibody, followed by incubation for 18 h, and again stained with Goat anti-rabbit secondary antibody conjugated with Alexa Fluor 488 (A21424-Invitrogen) for 4 h. The samples were also stained for CD19 (ab134114-abcam) with the same procedure. For Acridine

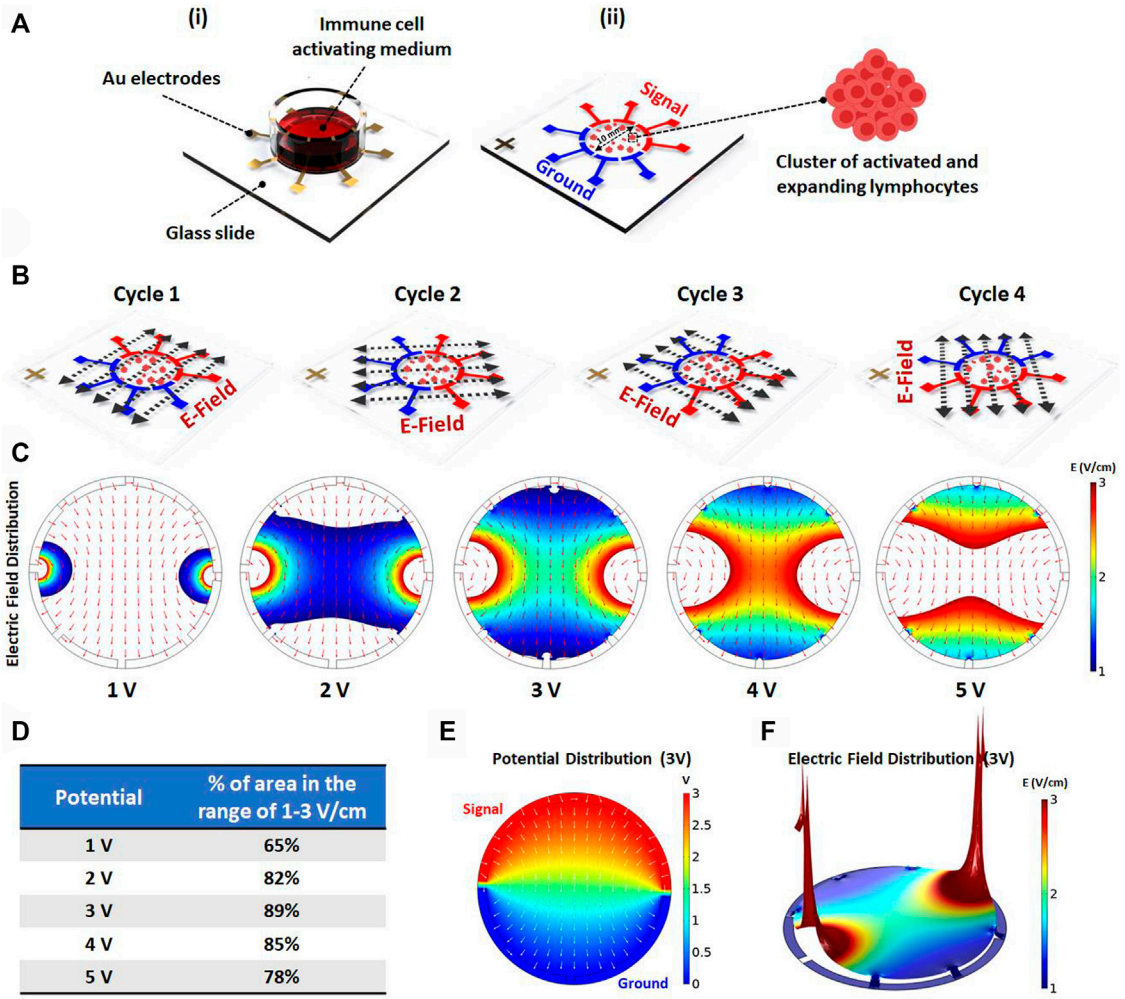

Potential	% of area in the range of 1-3 V/cm
1 V	65%
2 V	82%
3 V	89%
4 V	85%
5 V	78%

FIGURE 1 | (A_i) Schematics showing the electric field stimulation set-up. The set-up structure consists of Au patterned electrodes on a glass slide to generate alternating electric fields in four directions. The PBMCs are cultured inside the immune cell activation medium, which is placed on Au patterned electrodes. **(A_{ii})** The 100 kHz alternating voltage is applied to two groups of electrodes (each group containing four electrodes) in order to obtain uniform electric field distribution inside the immune-cell activation medium containing clusters of activated and expanding lymphocytes. **(B)** The electric field stimulation system was designed to periodically change the electric field direction in four cycles (each cycle lasts for one second) to increase the chance of parallelism between the electric field direction and the axis of cell division. **(C)** The electric field distribution inside the immune cell activation medium was studied using COMSOL Multiphysics AC/DC module. The simulation was performed for different applied voltages to evaluate the area percentage stimulated with preferred electric field intensity (1–3 V/cm) for each voltage. **(D)** The area percentage stimulated with preferred electric field intensity was quantified for each voltage. The simulation demonstrates that the highest area percentage is obtained by 3 (Volts) stimulation voltage amplitude. **(E)** The surface plot shows the electric potential distribution corresponding to the optimum applied voltage. The normalized arrow surface plot demonstrates the electric field directional distribution. **(F)** The color range-limited 3D plot illustrates the electric field intensity distribution inside the activation medium corresponding to the optimum applied voltage. (*$p < 0.05$, **$p < 0.01$, ***$p < 0.001$, and ****$p < 0.0001$, t-test).

Orange (AO), Propidium Iodide (PI), and DAPI staining, the cells were first incubated in the desired dye for 10 min and then washed 2 times using PBS.

Apoptosis Assay by Flow Cytometry Analysis

Apoptosis assay was measured using Annexin V-FITC Apoptosis Detection Kit (ab14085, Abcam, Cambridge, United Kingdom). After AEF stimulation of each sample, PBMCs were collected by centrifugation and resuspended in 500 µl of binding buffer. After this process, 5 µl of Annexin V-FITC and 5 µl of Propidium Iodide (PI 50 µg/ml) were added to the samples, and after incubation at room temperature for 5 min dark, the fluorescent intensity was measured by the Flow cytometry (FACScan Becton Dickinson, Mountain View, CA).

The PBMCs were also stained with CD4 Tx red, CD8 APC, and CD19 PE for further analysis using flow cytometry.

Cytokine Measurement by ELISA

Using Cytokine ELISA Kits allowed to accurately measure the levels of three cytokines including IL-6 (Cat number: D6050,

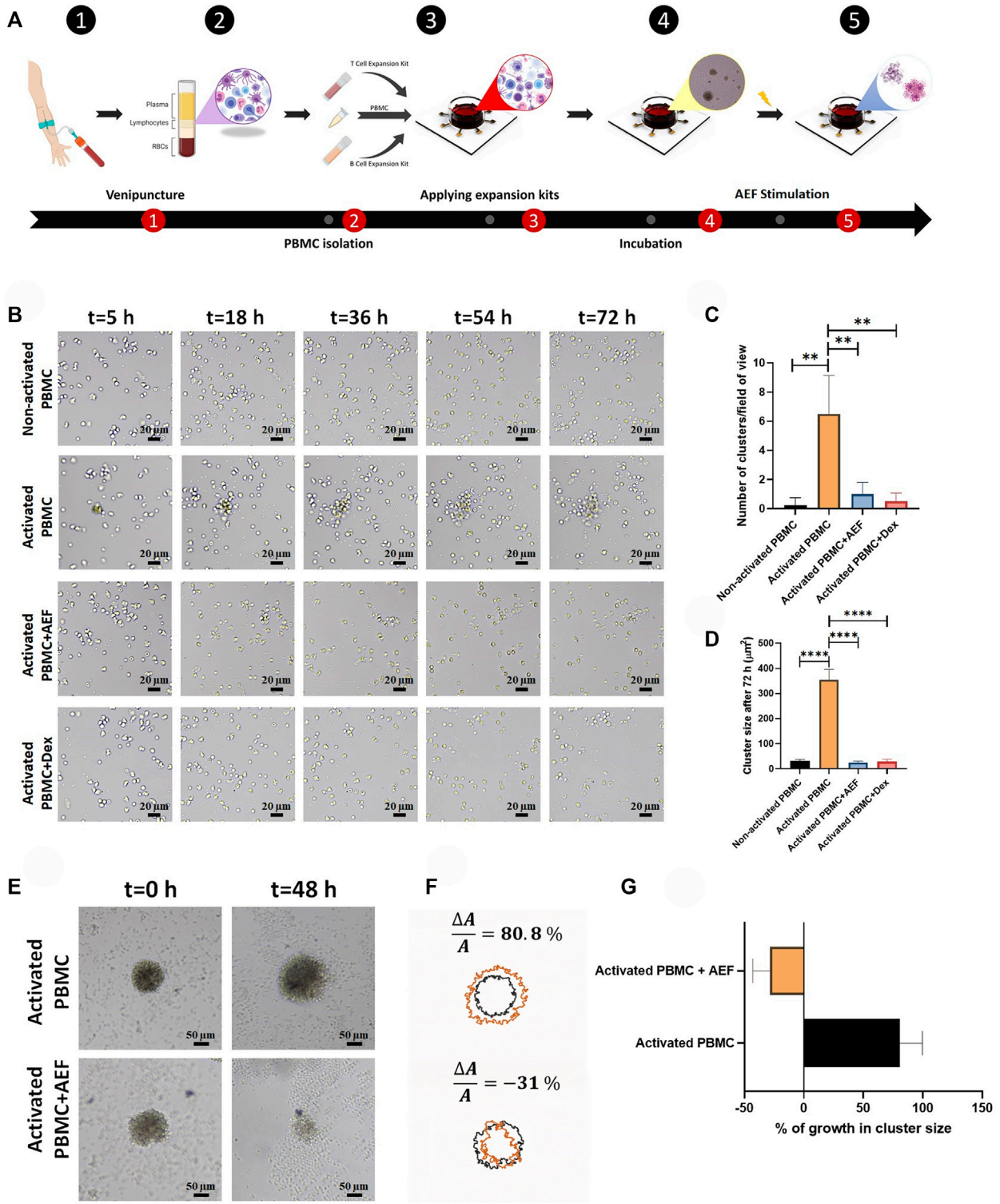

FIGURE 2 | (A) The whole blood was obtained through the venipuncture technique. The PBMCs were isolated from the whole blood using density gradient centrifugation. Isolated PBMCs were cultured inside the cell culture medium and their lymphocytes were activated by the use of expansion kits. The whole set-up was incubated for 5 days to ensure lymphocytes activation. The system was stimulated using the alternating electric field for 48 h which caused apoptosis in clusters of activated lymphocytes during cell division. **(B)** Lymphocyte cluster formation inside the immune cell activation medium was evaluated *via* time-lapse imaging. No sign of cluster formation was observed in non-activated PBMCs, while clustering was confirmed in activated PBMCs. Alternating electric field stimulation and the use of dexamethasone (4 mg/ml) similarly inhibited cluster formation in activated PBMCs. **(C, D)** The highest number of clusters were observed in activated PBMCs. These

(*Continued*)

FIGURE 2 | clusters were moderately larger in comparison with clusters formed in three other groups. **(E, F)** Activated lymphocyte clusters were stimulated using the alternating electric field for 48 h, and their size was monitored *via* time-lapse microscopy. The results demonstrated 80.8% growth in the size of activated lymphocyte clusters, whereas the size of the clusters undergoing AEF was reduced by 31%. **(G)** Percentage of growth in cluster size of activated PBMCs in control and AEF stimulated groups. (*$p < 0.05$, **$p < 0.01$, ***$p < 0.001$, and ****$p < 0.0001$, t-test).

R&D Systems, United States), TNF-α (Cat number: QK210, R&D Systems, United States), and IFN-γ (Cat number: DIF50, R&D Systems, United States) measured with an enzyme-linked immunosorbent assay. Specific concentrations of recombinant human IL-6, TNF-α, and IFN-γ along with the experimental samples were added and incubated in polystyrene microtiter plates coated with an antibody against the appointed cytokine, then incubated with an enzyme-linked polyclonal antibody directed to the cytokine. In the next step, a substrate solution for the enzyme was added, and the color development was stopped by adding 2N H2SO4. The absorbance was measured with a microplate spectrophotometer. The amount of IL-6, TNF-α, and IFN-γ in each sample was measured through a standard curve generated in each assay and expressed as picograms per milliliter. The sensitivity of the enzyme-linked immunosorbent assay for IL-6, TNF-α, and INF-γ is 0.70 pg/ml, 1.88 pg/ml, and 8 pg/ml, respectively. The reproducibility of all measurements was within 10% in our laboratory.

Blood Sampling From COVID-19 Patients

The blood samples were drawn from covid-19 patients who signed the written consent.

Ethics Statement

Each and every blood sample used in this research was obtained from donors who signed the written consent. Consents were obtained for all participants conscious of the planned experiment and the subsequent publication and all of the experiments were conducted following relevant guidelines.

Statistical Methods and Data Analysis

All the collected data were analyzed by GraphPad Prism software version 8.3.0 (GraphPad Software, Inc. La Jolla, CA, United States), and each data point represents the mean value of three independent measurements.

RESULTS

Alternating Electric Field Stimulation Set-Up and Electric Field Simulation

To investigate the effect of AEF on the expansion of the activated lymphocytes, an array of eight electrodes in a circular shape were patterned on top of a glass slide (**Figure 1A$_i$**). The cells were cultured on the center of the stimulating chip, and the electric field was applied by the use of surrounding electrodes. For better uniformity of the electric field distribution all over the chamber, each pole consists of four electrodes with a face-to-face array and in a symmetrical pattern (**Figure 1A$_{ii}$**).

Mitotic arrest induced by the AEF only occurs for the cells whose mitotic spindle is aligned in the electric field direction, while the cells with unaligned spindle would not be affected. Therefore, to impact all of the expanding cells with different spindle alignment, the signal (sine wave with an amplitude of 3 V and frequency of 100 kHz) is switched every second (0.25 Hz) between the electrodes to apply the electric field in all of the directions (**Figure 1B**).

Based on works of literature, the safe and effective intensity of AEF stimulation for suppressing the mitosis of the proliferative cells is in the range of 1–3 V/cm (Giladi et al., 2015). Hence, the applying voltage was optimized in a way that most of the cells experience the electric field in the mentioned range. For this purpose, the field intensity over the surface of the chip was calculated using the AC/DC physics of COMSOL Multiphysics simulation software. The applied voltage to the electrodes (**Figure 1C**) was swept in different ranges to extract the optimized electric field. Based on the results (**Figure 1D**), the electric potential of 3 V was selected as the optimum applied voltage because the most cell seeding area was observed in the range of 1–3 V/cm. **Figures 1E,F** demonstrate the electric potential and 3D electric field distribution for the applied voltage of 3 V.

Mimicking the Clonal Expansion by Activating the Peripheral Blood Mononuclear Cells

Lymphocytes are one of the subsets of white blood cells with mitosis capability (Oliaro et al., 2010). When these cells are activated by external physicochemical signals, they form a cluster of cells and then are expanded (Jevnikar et al., 2008; Zumwalde et al., 2013; Cheung et al., 2018). In the case of T and B lymphocytes, such a phenomenon is called clonal expansion in which the first activated cell produces many copies of itself with the same antigen properties (Adams et al., 2020).

In order to mimic the expansion of the WBCs, the T and B activation kits (Cat number: 10,970, Cat number: 100-0645, Stemcell Technologies, Canada) were utilized to artificially trigger the expansion of the lymphocytes in the PBMCs of blood *in vitro*. As could be deduced from **Figure 2A**, 4 days after PBMC activation, many of the clusters were formed in different sizes with increasing rates by the time. The bigger size of the cluster demonstrates the greater number of activated and expanding lymphocytes.

Time-Lapse Imaging to Investigate the Effect of Alternating Electric Field on Activated-Peripheral Blood Mononuclear Cells

Time-lapse imaging was used from the PBMCs at different times to investigate the ability of the AEF stimulation to suppress the

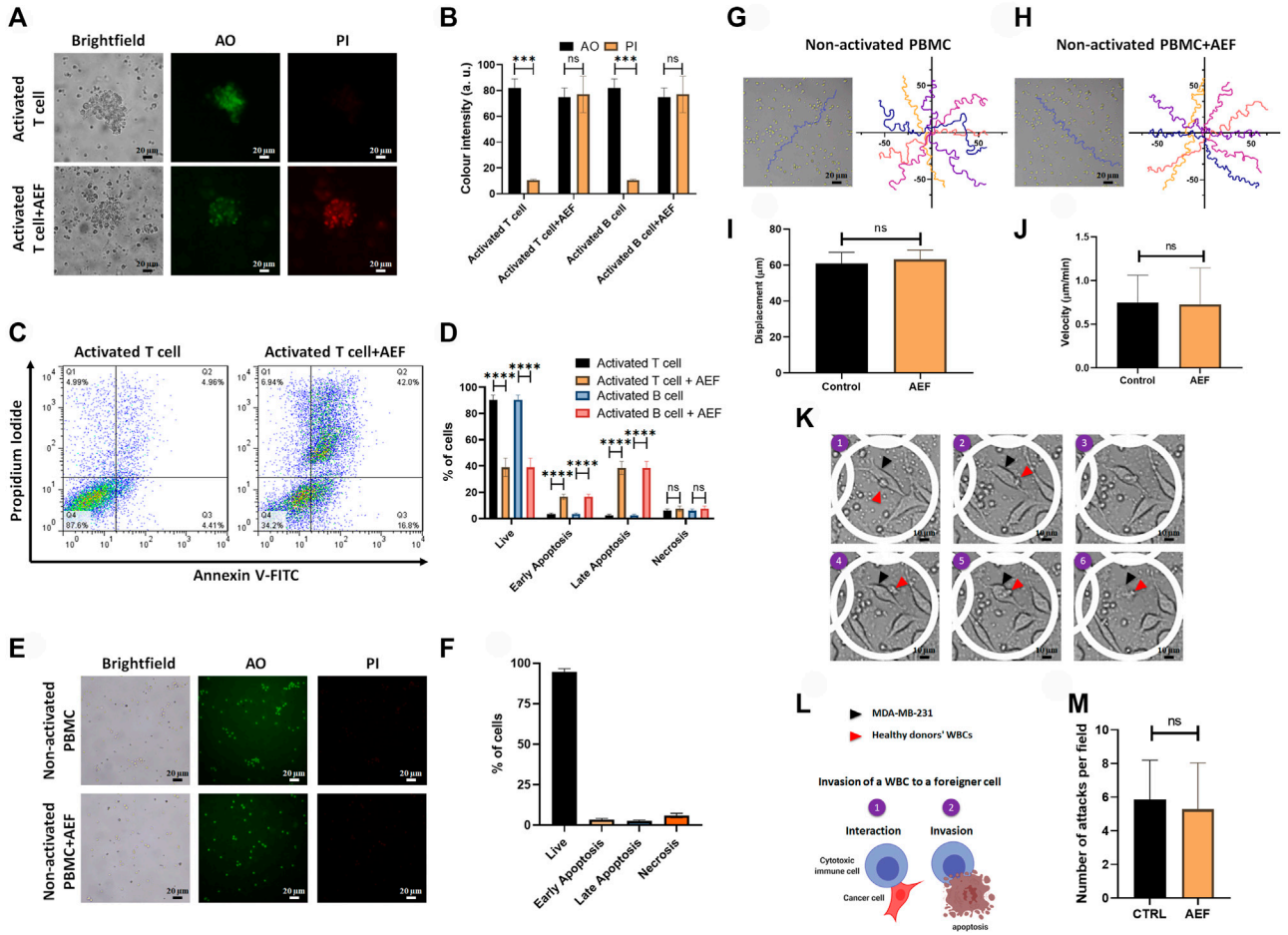

FIGURE 3 | (A, B) Immunofluorescence imaging shows elevation of PI uptake in activated lymphocytes by 48 h of AEF stimulation. PI uptake in the control group is negligible. **(C, D)** Annexin V/PI assay demonstrated the increase in the percentage of activated lymphocytes in the apoptosis phase caused by AEF. A negligible difference was observed in cells undergoing necrosis in both groups. **(E, F)** Immunofluorescence imaging demonstrates negligible PI uptake in both groups of control and AEF-stimulated non-activated PBMCs due to the effectiveness of AEF on dividing cells. **(G, H)** Cell trajectories were plotted for non-activated PBMCs in control and AEF-stimulated groups. **(I, J)** No significant difference was observed between displacements and velocities in these two groups. **(K)** Time-lapse imaging on the interaction of the electrically stimulated WBCs from a human donor with MDA-MB-231 cancer cell line. **(L)** Schematic representation of the WBC invasion to a foreigner MDA-MB-231 cell **(M)** Number of attacks by the WBCs to the foreigner MDA-MB-231 cells for the control and stimulated WBCs. (*$p < 0.05$, **$p < 0.01$, ***$p < 0.001$, and ****$p < 0.0001$, t-test).

proliferation of the activated lymphocytes. For this purpose, the PBMCs were isolated from the normal donors by density gradient centrifugation (DGC) method and then divided into four groups: 1) Non-activated PBMC--without any external stimulation (intact WBCs are imaged as the control group), 2) Activated PBMC--the WBCs are begun to expand by the commercial activating kits for T and B cells, 3) Activated PBMC + AEF and 4) Activated PBMC + Dexamethasone (4 mg/ml). In this regard, the effect of AEF in suppressing clonal expansion would also be compared to dexamethasone (conventional immunosuppressor drug).

As shown in **Figure 2B**, in the case of intact WBCs (Non-activated PBMC), no cluster formation could be seen after 72 h as all cells are moving alone. But, in the group of activated PBMCs, small immune cell aggregations could be tracked, rapidly growing in colony size and covering the whole surface after 20 h confirming the clonal expansion of the activated lymphocytes (**Figures 2C, D**).

Interestingly, when the cells are simultaneously treated with the alternating electric field (AEF), no growth of the cell clusters could be seen, which shows that even the activated cells were not able to be expanded. Such antiproliferative immunosuppressing result could also be tracked in the Activated PBMC + Dexamethasone group. This outcome corroborates that both AEF and Dexamethasone have a similar function in suppressing the mitosis process of the activated lymphocytes.

For more elaboration, the AEF stimulation was applied on the activated immune cells after 5 days. During these 5 days, the clonal expansion clusters of immune cells were formed **Figure 2E**. Then, cluster size and their abundance were imaged and analyzed after 48 h of AEF treatment. Contrary to the continuous growth of cell clusters in the cohort of activated PBMC, the proliferation

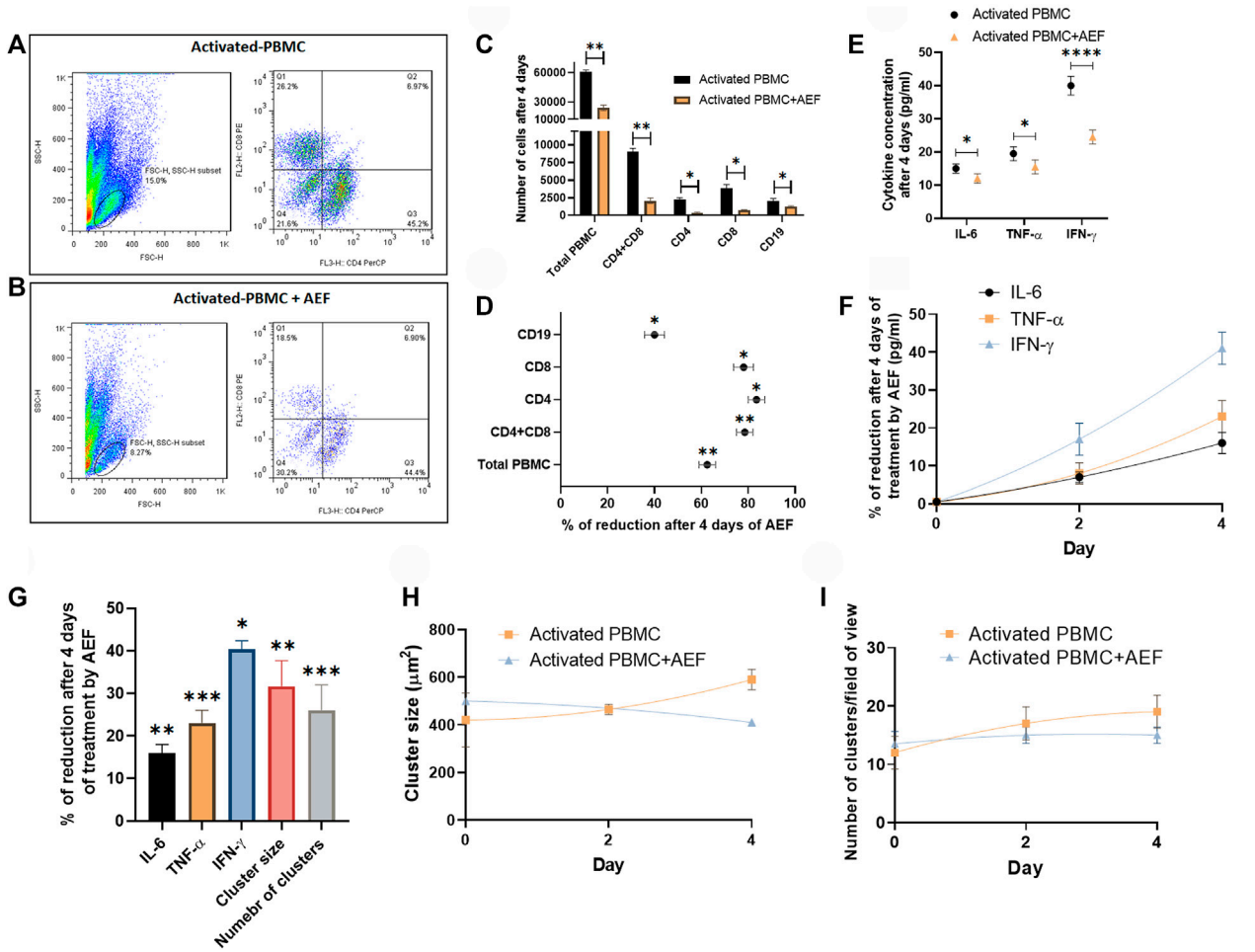

FIGURE 4 | (A, B) Flowcytometry analysis confirmed the reduction of activated PBMCs exposed to AEF for 4 days compared to their control group. **(C, D)** Comparison between the number of cells for each group of lymphocytes in PBMC and their percentage of reduction. **(E, F)** The decline in the concentration of inflammatory cytokines in PBMCs caused by AEF stimulation and the daily percentage of reduction for each cytokine. **(G)** Percentage of reduction in the concentration of the inflammatory cytokines, the cluster size and the number of clusters in the activated PBMCs after 4 days of the AEF treatment. **(H, I)** comparison between the daily amount of the cluster size and the number of clusters per field of view for the activated PBMCs in control and AEF-stimulated groups. (*$p < 0.05$, **$p < 0.01$, ***$p < 0.001$, and ****$p < 0.0001$, t-test).

and expansion of the activated PBMC were strongly suppressed by the AEF stimulation. As presented in **Figures 2F,G**, the average cluster size shows an increase of about ~81% after 48 h for the non-AEF treated group, while the growth of clusters in the electrically stimulated group has been dropped to ~ −31%. These results confirm that the suppressive effect of AEF stimulation, which had been confirmed on the proliferative cancer cells (Giladi et al., 2015; Kessler et al., 2018), is also applicable for the expanding activated lymphocytes.

Viability of the Stimulated Clusters and the Non-activated WBCs

AO/PI staining as well as apoptosis assay by Annexin V/PI flow cytometry technique was carried out to find the correlation between the cellular viability and the size reduction of the treated clusters. For more clarification, the viability and apoptosis assays were performed separately on lymphocytes, including B and T cells. Based on the image analysis, all of the two WBC subsets after AEF stimulation show a noticeable increase in the expression of the PI dye, which is an indicator of the membrane rupture and cell death (Khayamian et al., 2018) (**Figures 3A,B**). No PI uptake could be tracked in the control groups representing the viability of the cells. In harmony with the results of the AO/PI, flow cytometry results also show a significant reduction in the fraction of the live cells for the AEF treated group in which most of the cells entered into the early and late apoptosis phase (**Figures 3C,D**). As presented in **Figure 3D**, it is noteworthy to say that the necrosis portion of the cells is roughly the same before and after the electric field treatment. This phenomenon corroborates the non-necrosis induction of AEF on the expanding immune cells because based on the AEF mechanism, the cells undergo apoptosis, and sudden death or necrosis does not happen.

In the next step of the study, the effect of the AEF on the non-activated white blood cells was evaluated by live/dead staining and apoptosis assay. There is no sign of the cell clustering on the CTRL group since the cells are intact and no activating kit was used (**Figure 3E**). As presented in **Figure 3E**, no PI uptake could be traced in the CTRL WBCs before or after the electrical stimulation. This evidence corroborates the fact that the AEF only impacts the proliferative cells. In harmony with the AO/PI assay, the results of the Annexin V/PI test also show no apoptosis in the non-activated immune cells (**Figure 3F**) after 48 h of AEF treatment. The trajectory of the WBCs (**Figures 3G,H**) as well as their displacement and velocity (Ghaderinia et al., 2021) were also analyzed for non-activated WBCs in the presence and absence of AEF. As shown in **Figures 3I,J**, no difference could be inferred in their natural moving behavior. For further clarification, the effect of the electric field on the invasive function of the WBCs toward pathological threats was assessed. Time-lapse imaging (**Figure 3K**) was utilized to inspect the interaction of the WBCs with the foreigner MDA-MB-231 cells. Due to the HLA mismatch between the MDA-MB-231 cells and the donor WBCs, it is supposed that the cytotoxic T cells (CTLs), as well as natural killer cells (NK cells), are activated and invade the cells (**Figure 3L**) (Martínez-Lostao et al., 2015; Shenouda et al., 2017; Cerignoli et al., 2018). Based on the results, there is no significant alteration in the number of attacks by the immune cells to the MDA-MB-231 cells, which corroborates the safety of the AEF on the normal function of the immune cells (**Figure 3M**).

Details of the Affected Lymphocyte Subsets by Flow Cytometry Analysis

Flow cytometry technique was employed to investigate the detailed effect of alternating electric field on each subset of the lymphocytes. For this purpose, both of the B and T cell activation and expansion kits were simultaneously applied to the blood of a healthy donor. The cells (after 5 days) were then treated with the AEF stimulation for 4 days, and the number of CD8 and CD4 positive cells (T cell markers) and CD19 cells (B cell marker) were counted by the flow cytometer. The results were compared with the activated but non-AEF treated cells as the control group. Based on the results (**Figures 4A,B**), the population of all pre-activated lymphocyte subsets was drastically reduced after the AEF treatment (**Figure 4C**). For instance, the T lymphocytes, including $CD8^+$ and $CD4^+$ cells, have lost about ~80% of their population after AEF stimulation and this fraction for B cells is about ~40% (**Figure 4D**). The results are in harmony with the expectation that the proliferation of the expanding cells was suppressed by the AEF stimulation. When the activated cells lose their ability to expand and are arrested in the mitosis phase of their cell cycle due to an abnormal division, they enter the apoptosis phase. Therefore, the number of cells in the AEF treated group becomes lower than the control activated and expanding cells. Moreover, T cells, including $CD4^+$ and $CD8^+$ cells, are more affected by the electric field treatment. This is due to the fact that T cells expand faster than the B cells, and as a result, the AEF stimulation has more suppressing impact on their division.

Inspecting the Cytokine Reduction After Electric Field Treatment

Finally, the cytokine production by the immune cells was studied in both groups of activated control and AEF-treated cells. The cells at first were activated for 5 days, and then the experiment was carried out for all of the groups. In the activated PBMC + AEF group, the cells were under AEF stimulation for about 4 days. During these 4 days, the non-AEF treated group was just kept in an incubator. At the end of the experiment, the solution medium of both groups was collected and analyzed by the ELISA method.

Although many cytokines are produced and play functional roles in the post-activated immune cells, there are three main cytokines, including IL-6, TNF-α, and IFN-γ that are produced by the lymphocytes and play the main role especially in the COVID-19 disease (Chen et al., 2020; Lammers et al., 2020; McGonagle et al., 2020; Mehta et al., 2020). Based on the results, all three major cytokines have shown a considerable reduction after 4 days of the electric field stimulation (**Figures 4E,F**). As presented in **Figure 4G**, the most cytokine reduction was attributed to the IFN-γ with ~40% and the least for the IL-6 with ~16% (~25% for TNF-α). We extremely believe that this decrease is associated with the reduced number of immune cells after the suppression of their proliferation by the AEF. Hence, the number of the clusters, as well as their size, was assessed for the two groups at the end of the study. As shown in **Figures 4H,I** and in harmony with the results of the cytokine profiling, a reductive trend could be observed in the case of cluster size and abundance by 32 and 26% (**Figure 4G**), respectively.

Effect of Alternating Electric Field on Suppressing Clonal Expansion and Cytokine Production in COVID-19 Patients

Human blood samples were collected from the five patients with COVID-19 disease to assess the efficacy of the alternating electric field on suppressing the activation and expansion of immune cells and the consequent reduction in cytokine production. The patients had not received any medication prior to blood sampling. After blood sampling and isolation of the WBCs, the cells were divided into two cohorts of control (without electrical treatment) and the group of electrically stimulated cells. Both groups were under study for 4 days.

The time-lapse imaging from the samples of the patients reveals that the lymphocyte clusters are formed (**Figure 5A**) in the samples of the patients due to cytokine storm. The size of the produced clusters was analyzed after AEF stimulation, and similar to the previous results, the electrical stimulation halted the growth of the clusters in the blood sample of each patient (**Figure 5B**), and also their average number was also decreased by ~30% (**Figure 5C**).

As presented in **Figures 5D,G**, all of the three major cytokines in the blood sample of all five patients were reduced after 4 days of AEF stimulation, even though the amount of reduction is different for each patient. Also, a major difference in concentration of the all of the three inflammatory cytokines could be observed compared to their initial values (**Figure 5H**). **Figure 5I** displays the average

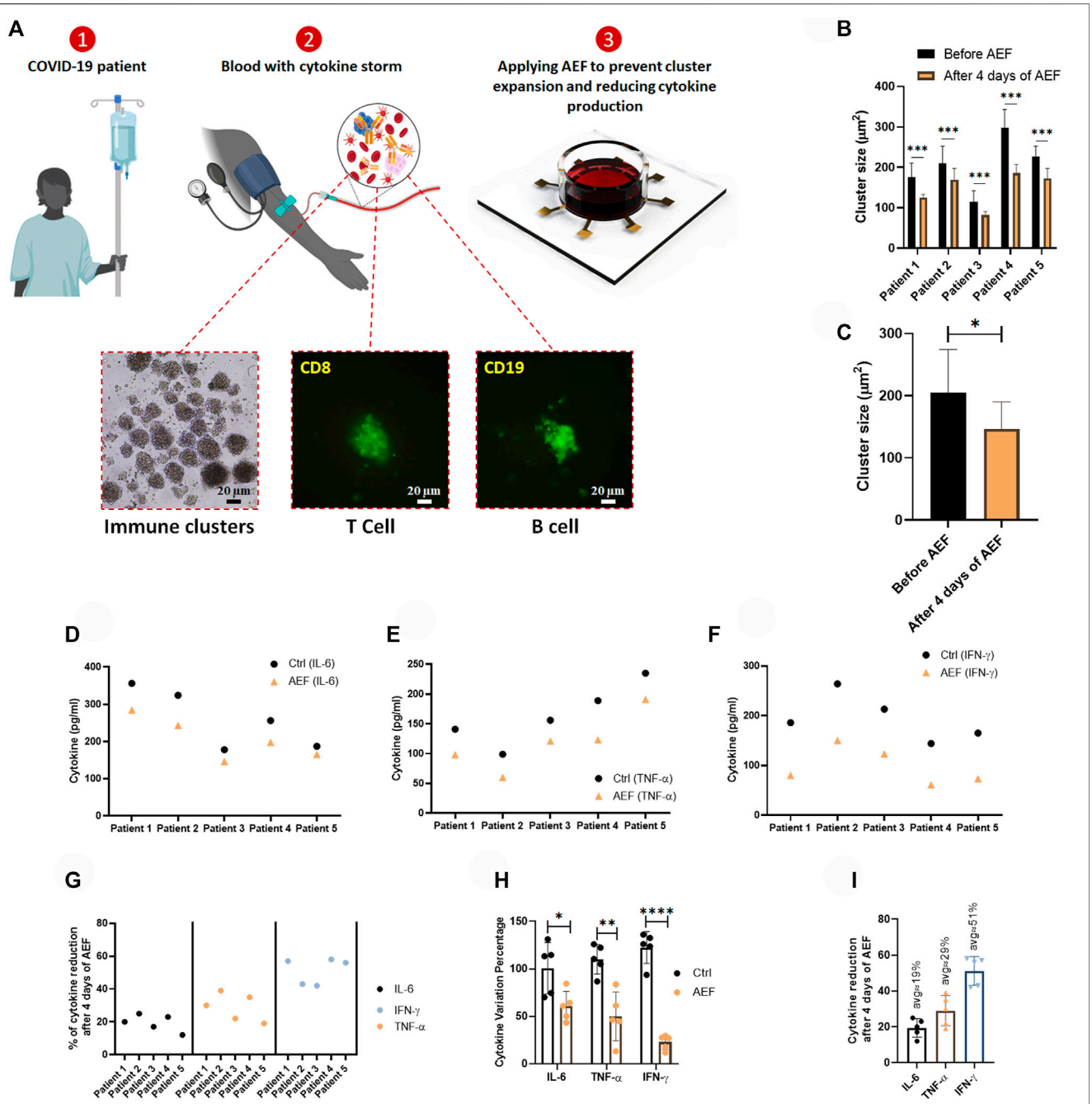

FIGURE 5 | (A) The whole blood sample was obtained from COVID-19 patients, and the PBMCs were isolated using the density gradient centrifugation method. Immunofluorescence imaging confirms the activation and the expansion of lymphocytes in these blood samples. The lymphocytes were cultured in blood serums and were stimulated by AEF for 4 days. **(B, C)** Significant differences were observed in the size of lymphocyte clusters after 4 days of AEF stimulation for COVID-19 patients' PBMCs. **(D–F)** The concentration of inflammatory cytokines in COVID-19 patients' blood serum, which their PBMCs were cultured, for control and AEF exposed groups. **(G)** Percentage of cytokine reduction in COVID-19 patients' blood serum caused by AEF stimulation. **(H)** Comparing the cytokine variation percentage for the three cytokines of IL-6, TNF-α and IFN-γ after 4 days of incubation for both groups of control and AEF with respect to the primary sample. **(I)** The average percentage of cytokine reduction in COVID-19 patients' blood serum after 4 days of exposure to AEF. (*$p < 0.05$, **$p < 0.01$, ***$p < 0.001$, and ****$p < 0.0001$, t-test).

amount of cytokine reduction after electric field treatment of the patients' PBMCs. Based on the results, the most cytokine reduction is related to the IFN-γ by ~51%, while this number for TNF-α and IL-6 is ~29 and ~19%, respectively.

Similar to the previous results obtained by the AEF treatment of the artificially activated PBMCs, we hypothesize that the decrease in the production of the cytokines in the samples of the COVID-19 patients is due to the suppressed clonal expansion

of the lymphocytes. In fact, when the lymphocytes are confronted with the SARS-CoV-2 virus antigens, they become activated and then start to expand (Gutierrez et al., 2020). But here, we have suppressed their proliferation by the AEF method as a substitute to the prevalent immunosuppressor drugs such a dexamethasone.

DISCUSSION

The most challenge attributed to the positive COVID-19 cases that puts the lives of the patients in danger is the hyperactivation of the immune cells and their consequent high cytokine releasement into the bloodstream or the so-called cytokine storm (Huang et al., 2020; Pearce et al., 2020). Currently, the typical remedy for harnessing such an imposed lethal storm is using immunosuppressor drugs, e.g., dexamethasone, which entirely damps the immune system in the body. Although immunosuppressors subside the hyperactivation of the immune system, their various and serious side effects have always been a challenge and limited their prescription. Hence, any other safe and effective treatment that controls cytokine production with less or no side effects is highly appreciated.

Since part of the cytokine storm in the COVID-19 disease is due to the hyperactivation of the lymphocytes and their uncontrolled growth, We, for the first time, have introduced AEF (a known procedure in brain tumor treatment (Fabian et al., 2019)) on electrical stimulation of the lymphocytes to suppress their clonal expansion (**Figure 2**). Subsequently, the cytokine storm is also reduced due to the reduction of the number of cytokine-producing cells (**Figure 4** and **Figure 5**).

Based on the obtained results (**Figure 3**), the AEF method had no harmful effects on the viability and function of the non-expanding and non-activated immune cells and other blood cells. The electrical stimulation just perturbs the expansion of the highly proliferating lymphocytes formed as a cluster. This suppression in lymphocyte expansion is followed by a noticeable reduction in the amount of the produced cytokines.

We believe that this method can safely take the place of the current immunosuppressor drugs such as dexamethasone, which is regularly used for cytokine storm treatment that represses the whole immune system all over the body with severe side effects. In the future trend, the electric field could safely be delivered to the lung of the patients to locally suppress the highly proliferating cytokine-producing lymphocytes as a complementary method.

DATA AVAILABILITY STATEMENT

The original contributions presented in the study are included in the article/Supplementary Material, further inquiries can be directed to the corresponding authors.

ETHICS STATEMENT

Ethical review and approval was not required for the study on human participants in accordance with the local legislation and institutional requirements. The patients/participants provided their written informed consent to participate in this study.

AUTHOR CONTRIBUTIONS

HA: data curation, formal analysis, software, validation, investigation, methodology MK: conceptualization, data curation, formal analysis, methodology, investigation, writing—original draft MF: validation, investigation, data curation, formal analysis MG: validation, investigation, data curation, formal analysis HS: validation, investigation, data curation, formal analysis SS: investigation SY: investigation BG: software JM: resources RS-F: resources MA: conceptualization, formal analysis, supervision, project administration, writing—review and editing.

REFERENCES

Abdin, S. M., Elgendy, S. M., Alyammahi, S. K., Alhamad, D. W., and Omar, H. A. (2020). Tackling the Cytokine Storm in COVID-19, Challenges and Hopes. *Life Sci.* 257, 118054. doi:10.1016/j.lfs.2020.118054

Adams, N. M., Grassmann, S., and Sun, J. C. (2020). Clonal Expansion of Innate and Adaptive Lymphocytes. *Nat. Rev. Immunol.* 20 (11), 694–707. doi:10.1038/s41577-020-0307-4

Alessi, J., de Oliveira, G. B., Schaan, B. D., and Telo, G. H. (2020). Dexamethasone in the Era of COVID-19: Friend or Foe? an Essay on the Effects of Dexamethasone and the Potential Risks of its Inadvertent Use in Patients with Diabetes. *Diabetol. Metab. Syndr.* 12 (1), 80. doi:10.1186/s13098-020-00583-7

Ansaryan, S., Khayamian, M. A., Saghafi, M., Shalileh, S., Nikshoar, M. S., Abbasvandi, F., et al. (2019). Stretch Induces Invasive Phenotypes in Breast Cells Due to Activation of Aerobic-Glycolysis-Related Pathways. *Adv. Biosys.*, 3 (7), 1800294. doi:10.1002/adbi.201800294

Bendel, C. M., Wiesner, S. M., Garni, R. M., Cebelinski, E., and Wells, C. L. (2002). Cecal Colonization and Systemic Spread of Candida Albicans in Mice Treated with Antibiotics and Dexamethasone. *Pediatr. Res.* 51 (3), 290–295. doi:10.1203/00006450-200203000-00005

Bhaskar, S., Sinha, A., Banach, M., Mittoo, S., Weissert, R., Kass, J. S., et al. (2020). Cytokine Storm in COVID-19-Immunopathological Mechanisms, Clinical Considerations, and Therapeutic Approaches: The REPROGRAM Consortium Position Paper. *Front. Immunol.* 2020, 11. doi:10.3389/fimmu.2020.01648

Caniggia, A., Nuti, R., Lore, F., and Vattimo, A. (1981). Pathophysiology of the Adverse Effects of Glucoactive Corticosteroids on Calcium Metabolism in Man. *J. Steroid Biochem.*, 15, 153–161. doi:10.1016/0022-4731(81)90270-3

Carrieri, F. A., Smack, C., Siddiqui, I., Kleinberg, L. R., and Tran, P. T. (1991). Tumor Treating Fields: At the Crossroads between Physics and Biology for Cancer Treatment. *Front. Oncol.* 10, 10. doi:10.3389/fonc.2020.575992

Cerignoli, F., Abassi, Y. A., Lamarche, B. J., Guenther, G., Santa Ana, D., Guimet, D., et al. (2018). *In Vitro* immunotherapy Potency Assays Using Real-Time Cell Analysis. *PloS one* 13 (3), e0193498. doi:10.1371/journal.pone.0193498

Chen, G., Wu, D., Guo, W., Cao, Y., Huang, D., Wang, H., et al. (2020). Clinical and Immunological Features of Severe and Moderate Coronavirus Disease 2019. *J. Clin. investigation* 130 (5), 2620–2629. doi:10.1172/jci137244

Chen, R.-c., Tang, X.-p., Tan, S.-y., Liang, B.-l., Wan, Z.-y., Fang, J.-q., et al. (2006). Treatment of Severe Acute Respiratory Syndrome with Glucosteroids. *Chest*, 129 (6), 1441–1452. doi:10.1378/chest.129.6.1441

Cheung, A. S., Zhang, D. K. Y., Koshy, S. T., and Mooney, D. J. (2018). Scaffolds that Mimic Antigen-Presenting Cells Enable *Ex Vivo* Expansion of Primary T Cells. *Nat. Biotechnol.* 36 (2), 160–169. doi:10.1038/nbt.4047

Condotta, S. A., and Richer, M. J. (2017). The Immune Battlefield: The Impact of Inflammatory Cytokines on CD8+ T-Cell Immunity. *PLoS Pathog.* 13 (10). e1006618. doi:10.1371/journal.ppat.1006618

Creed, T. J., Lee, R. W., Newcomb, P. V., di Mambro, A. J., Raju, M., and Dayan, C. M. (2009). The Effects of Cytokines on Suppression of Lymphocyte Proliferation by Dexamethasone. *J. Immunol.* 183 (1), 164–171. doi:10.4049/jimmunol.0801998

de Vries, W. B., van den Borne, P., Goldschmeding, R., de Weger, R. A., Bal, M. P., van Bel, F., et al. (2010). Neonatal Dexamethasone Treatment in the Rat Leads to Kidney Damage in Adulthood. *Pediatr. Res.* 67 (1), 72–76. doi:10.1203/PDR.0b013e3181bf570d

Fabian, D., Guillermo Prieto Eibl, M., Alnahhas, I., Sebastian, N., Giglio, P., Puduvalli, V., et al. (2019). Treatment of Glioblastoma (GBM) with the Addition of Tumor-Treating Fields (TTF): A Review. *Cancers* 11 (2), 174. doi:10.3390/cancers11020174

Ghaderinia, M., Khayamian, M. A., Abadijoo, H., Shalileh, S., Faramarzpour, M., Zandi, A., et al. (2021). Capture-free Deactivation of CTCs in the Bloodstream; a Metastasis Suppression Method by Electrostatic Stimulation of the Peripheral Blood. *Biosens. Bioelectron.*, 183, 113194. doi:10.1016/j.bios.2021.113194

Gibson, P. G., Qin, L., and Puah, S. H. (2020). COVID -19 Acute Respiratory Distress Syndrome (ARDS): Clinical Features and Differences from Typical Pre- COVID -19 ARDS. *Med. J. Aust.*, 213 (2), 54–56. doi:10.5694/mja2.50674

Giladi, M., Schneiderman, R. S., Voloshin, T., Porat, Y., Munster, M., Blat, R., et al. (2015). Mitotic Spindle Disruption by Alternating Electric Fields Leads to Improper Chromosome Segregation and Mitotic Catastrophe in Cancer Cells. *Sci. Rep.* 5 (1). 18046. doi:10.1038/srep18046

Giles, A. J., Hutchinson, M.-K. N. D., Sonnemann, H. M., Jung, J., Fecci, P. E., Ratnam, N. M., et al. (2018). Dexamethasone-induced Immunosuppression: Mechanisms and Implications for Immunotherapy. *J. Immunother. cancer* 6 (1), 51. doi:10.1186/s40425-018-0371-5

Group, R. C., Horby, P., Lim, W. S., Emberson, J. R., Mafham, M., Bell, J. L., et al. (2021). *N. Engl. J. Med.* 384 (8), 693–704. doi:10.1056/NEJMoa2021436

Gutierrez, L., Beckford, J., and Alachkar, H. (2020). Deciphering the TCR Repertoire to Solve the COVID-19 Mystery. *Trends Pharmacol. Sci.* 41 (8), 518–530. doi:10.1016/j.tips.2020.06.001

Hottinger, A. F., Pacheco, P., and Stupp, R. (2016). Tumor Treating Fields: a Novel Treatment Modality and its Use in Brain Tumors. *Neuonc* 18 (10), 1338–1349. doi:10.1093/neuonc/now182

Hu, B., Huang, S., and Yin, L. (2021). The Cytokine Storm and COVID-19. *J. Med. Virol.* 93 (1), 250–256. doi:10.1002/jmv.26232

Huang, Q., Wu, X., Zheng, X., Luo, S., Xu, S., and Weng, J. (2020). Targeting Inflammation and Cytokine Storm in COVID-19. *Pharmacol. Res.* 159. 105051. doi:10.1016/j.phrs.2020.105051

Jahangiri, M., Khosravi, S., Moghtaderi, H., Ranjbar, M., Abadijoo, H., Sarmadi, S., et al. (2019). Microfluidic Platform With Integrated Electrical Actuator to Enrich and Locating Atypical/Cancer Cells From Liquid Cytology Samples. *Sens. Actuators B Chem.* 297. 126733. doi:10.1016/j.snb.2019.126733

Jahangiri, M., Ranjbar-Torkamani, M., Abadijoo, H., Ghaderinia, M., Ghafari, H., Mamdouh, A., et al. (2020). Low Frequency Stimulation Induces Polarization-Based Capturing of Normal, Cancerous and White Blood Cells: A New Separation Method for Circulating Tumor Cell Enrichment or Phenotypic Cell Sorting. *Analyst* 145. 7636–7645. doi:10.1039/D0AN01033B

Jevnikar, Z., Obermajer, N., Bogyo, M., and Kos, J. (2008). The Role of Cathepsin X in the Migration and Invasiveness of T Lymphocytes. *J. Cell Sci.* 121 (16), 2652–2661. doi:10.1242/jcs.023721

Kessler, A. F., Frömbling, G. E., Gross, F., Hahn, M., Dzokou, W., Ernestus, R.-I., et al. (2018). Effects of Tumor Treating Fields (TTFields) on Glioblastoma Cells Are Augmented by Mitotic Checkpoint Inhibition. *Cell Death Discov.* 4 (1), 77. doi:10.1038/s41420-018-0079-9

Khayamian, M. A., Ansaryan, S., Moghtaderi, H., and Abdolahad, M. (2018). Applying VHB Acrylic Elastomer as a Cell Culture and Stretchable Substrate. *Int. J. Polym. Mater. Polym. Biomaterials* 67 (18), 1096–1104. doi:10.1080/00914037.2017.1419244

Khayamian, M. A., Parizi, M. S., Ghaderinia, M., Abadijoo, H., Vanaei, S., Simaee, H., et al. (2021). A Label-free Graphene-Based Impedimetric Biosensor for Real-Time Tracing of the Cytokine Storm in Blood Serum; Suitable for Screening COVID-19 Patients. *RSC Adv.* 11 (55). 34503. doi:10.1039/D1RA04298J

Khayamian, M. A., Shalileh, S., Vanaei, S., Salemizadeh Parizi, M., Ansaryan, S., Saghafi, M., et al. (2019). Electrochemical Generation of Microbubbles by Carbon Nanotube Interdigital Electrodes to Increase the Permeability and Material Uptakes of Cancer Cells. *Drug Deliv.* 26 (1), 928–934. doi:10.1080/10717544.2019.1662514

Kirson, E. D., Dbalý, V., Tovaryš, F., Vymazal, J., Soustiel, J. F., Itzhaki, A., et al. (2007). Alternating Electric Fields Arrest Cell Proliferation in Animal Tumor Models and Human Brain Tumors. *Proc. Natl. Acad. Sci. U.S.A.* 104 (24). 10152. doi:10.1073/pnas.0702916104

Kirson, E. D., Gurvich, Z., Schneiderman, R., Dekel, E., Itzhaki, A., Wasserman, Y., et al. (2004). Disruption of Cancer Cell Replication by Alternating Electric Fields. *Cancer Res.* 64 (9), 3288–3295. doi:10.1158/0008-5472.CAN-04-0083

Kolilekas, L., Loverdos, K., Giannakaki, S., Vlassi, L., Levounets, A., Zervas, E., et al. (2020). Can Steroids Reverse the Severe COVID-19 Induced "cytokine Storm"? *J. Med. Virol.* 92 (11), 2866–2869. doi:10.1002/jmv.26165

Kusuda, Y., Kondo, Y., Miyagi, Y., Munemasa, T., Hori, Y., Aonuma, F., et al. (2019). Long-term Dexamethasone Treatment Diminishes Store-Operated Ca2+ Entry in Salivary Acinar Cells. *Int. J. Oral Sci.* 11 (1), 1. doi:10.1038/s41368-018-0031-0

Lammers, T., Sofias, A. M., van der Meel, R., Schiffelers, R., Storm, G., Tacke, F., et al. (2020). Dexamethasone Nanomedicines for COVID-19. *Nat. Nanotechnol.* 15 (8), 622–624. doi:10.1038/s41565-020-0752-z

Langarizadeh, M. A., Tavakoli, M. R., Abiri, A., Ghasempour, A., Rezaei, M., and Ameri, A. (2021). A review on function and side effects of systemic corticosteroids used in high-grade COVID-19 to prevent cytokine storms. *EXCLI Journal*, 20, 339. doi:10.17179/excli2020-3196

Liao, M., Liu, Y., Yuan, J., Wen, Y., Xu, G., Zhao, J., et al. (2020). Single-cell Landscape of Bronchoalveolar Immune Cells in Patients with COVID-19. *Nat. Med.* 26 (6), 842–844. doi:10.1038/s41591-020-0901-9

Mangalmurti, N., and Hunter, C. A. (2020). Cytokine Storms: Understanding COVID-19. *Immunity*. 53, 19. doi:10.1016/j.immuni.2020.06.017

Martínez-Lostao, L., Anel, A., and Pardo, J. (2015). How Do Cytotoxic Lymphocytes Kill Cancer Cells? *Clin. Cancer Res.* 21 (22), 5047–5056. doi:10.1158/1078-0432.ccr-15-0685

Maślanka, T. (2013). Dexamethasone Inhibits and Meloxicam Promotes Proliferation of Bovine NK Cells. *Immunopharmacol. Immunotoxicol.* 35 (2), 225–234. doi:10.3109/08923973.2013.764504

Maślanka, T., and Jaroszewski, J. (2013). Dexamethasone, but not meloxicam, suppresses proliferation of bovine CD25+ CD4+ and CD25- CD4+ T cells. *Pol J Vet Sci*. 16, 219. doi:10.2478/pjvs-2013-0031

McGonagle, D., Sharif, K., O'Regan, A., and Bridgewood, C., (2020). The Role of Cytokines Including Interleukin-6 in COVID-19 Induced Pneumonia and Macrophage Activation Syndrome-like Disease. *Autoimmun. Rev.* 19 (6), 102537. doi:10.1016/j.autrev.2020.102537

McKay, L., and Cidlowski, J. (2003). *Holland-frei Cancer Medicine*, New Jersey, NJ, USA: Wiley.

Mehta, P., McAuley, D. F., Brown, M., Sanchez, E., Tattersall, R. S., and Manson, J. J. (2020). COVID-19: Consider Cytokine Storm Syndromes and Immunosuppression. *lancet* 395 (10229), 1033–1034. doi:10.1016/s0140-6736(20)30628-0

Noreen, S., Maqbool, I., and Madni, A., 2021, Dexamethasone: Therapeutic Potential, Risks, and Future Projection during COVID-19 Pandemic, *Eur. J. Pharmacol.* 2021, 173854. doi:10.1016/j.ejphar.2021.173854

Oliaro, J., Van Ham, V., Sacirbegovic, F., Pasam, A., Bomzon, Z. e., Pham, K., et al. (2010). Asymmetric Cell Division of T Cells upon Antigen Presentation Uses Multiple Conserved Mechanisms. *J. Immunol.* 185 (1), 367–375. doi:10.4049/jimmunol.0903627

World Health Organization, 2021. WHO Coronavirus (COVID-19) Dashboard. Available at: https://covid19.who.int (accessed 20 August 2021).

Pearce, L., Davidson, S. M., and Yellon, D. M. (2020). The Cytokine Storm of COVID-19: a Spotlight on Prevention and Protection. *Expert Opin. Ther. Targets* 24 (8), 723–730. doi:10.1080/14728222.2020.1783243

Pera, A., Byun, A., Gribar, S., Schwartz, R., Kumar, D., and Parimi, P. (2002). Dexamethasone Therapy and Candida Sepsis in Neonates Less Than 1250 Grams. *J. Perinatol.* 22 (3), 204–208. doi:10.1038/sj.jp.7210699

Phelan, A. L., Katz, R., and Gostin, L. O. (2020). The Novel Coronavirus Originating in Wuhan, China. *Jama* 323 (8), 709–710. doi:10.1001/jama.2020.1097

Rabb, H. (2020). Kidney Diseases in the Time of COVID-19: Major Challenges to Patient Care. *J. Clin. investigation* 130 (6), 2749–2751. doi:10.1172/jci138871

Ragab, D., Salah Eldin, H., Taeimah, M., Khattab, R., and Salem, R. (2020). The COVID-19 Cytokine Storm; what We Know So Far. *Front. Immunol.* 2020 11. doi:10.3389/fimmu.2020.01446

Russell, C. D., Millar, J. E., and Baillie, J. K. (2020). Clinical Evidence Does Not Support Corticosteroid Treatment for 2019-nCoV Lung Injury. *Lancet* 395 (10223), 473–475. doi:10.1016/s0140-6736(20)30317-2

Sharun, K., Tiwari, R., Dhama, J., and Dhama, K. (2020). Dexamethasone to Combat Cytokine Storm in COVID-19: Clinical Trials and Preliminary Evidence. *Int. J. Surg.* 82, 179–181. doi:10.1016/j.ijsu.2020.08.038

Shenouda, M. M., Gillgrass, A., Nham, T., Hogg, R., Lee, A. J., Chew, M. V., et al. (2017). *Breast Cancer Res.* 19 (1), 1–14. doi:10.1186/s13058-017-0867-9

Sun, X., Wang, T., Cai, D., Hu, Z., Chen, J. a., Liao, H., et al. *Cytokine & Growth Factor Rev.* 2020, Cytokine Storm Intervention in the Early Stages of COVID-19 Pneumonia**,** 53, 38–42. doi:10.1016/j.cytogfr.2020.04.002

Vaninov, N. (2020). In the Eye of the COVID-19 Cytokine Storm. *Nat. Rev. Immunol.* 20 (5), 277. doi:10.1038/s41577-020-0305-6

Ye, Q., Wang, B., and Mao, J. (2020). The Pathogenesis and Treatment of the `Cytokine Storm' in COVID-19. *J. Infect.* 80 (6), 607–613. doi:10.1016/j.jinf.2020.03.037

Zhang, J.-M., and An, J. (2007). Cytokines, Inflammation, and Pain. *Int. Anesthesiol. Clin.* 45 (2), 27–37. doi:10.1097/AIA.0b013e318034194e

Zhu, N., Zhang, D., Wang, W., Li, X., Yang, B., Song, J., et al. (2020). A Novel Coronavirus from Patients with Pneumonia in China, 2019. *N. Engl. J. Med.* 382 (8), 727–733. doi:10.1056/NEJMoa2001017

Zumwalde, N. A., Domae, E., Mescher, M. F., and Shimizu, Y. (2013). ICAM-1-Dependent Homotypic Aggregates Regulate CD8 T Cell Effector Function and Differentiation during T Cell Activation. *J. Immunol.* 191 (7), 3681–3693. doi:10.4049/jimmunol.1201954

Conflict of Interest: The authors declare that the research was conducted in the absence of any commercial or financial relationships that could be construed as a potential conflict of interest.

Publisher's Note: All claims expressed in this article are solely those of the authors and do not necessarily represent those of their affiliated organizations, or those of the publisher, the editors and the reviewers. Any product that may be evaluated in this article, or claim that may be made by its manufacturer, is not guaranteed or endorsed by the publisher.

frontiers | Frontiers in Bioengineering and Biotechnology

TYPE Original Research
PUBLISHED 22 July 2022
DOI 10.3389/fbioe.2022.931770

OPEN ACCESS

EDITED BY
Tatiana Fiordelisio,
National Autonomous University of Mexico, Mexico

REVIEWED BY
Gnanavel Venkatesan,
Indian Veterinary Research Institute (IVRI), India
Pedro Fernández-Soto,
University of Salamanca, Spain

*CORRESPONDENCE
Rui Mao,
maorui@ucas.ac.cn
Ting Cai,
caiting@ucas.ac.cn

SPECIALTY SECTION
This article was submitted to Biosensors and Biomolecular Electronics, a section of the journal Frontiers in Bioengineering and Biotechnology

RECEIVED 29 April 2022
ACCEPTED 28 June 2022
PUBLISHED 22 July 2022

CITATION
Mao R, Wu X, Miao Q and Cai T (2022), Asymmetric stem-loop–mediated isothermal amplification of nucleic acids for DNA diagnostic assays by simple modification of canonical PCR primers. *Front. Bioeng. Biotechnol.* 10:931770. doi: 10.3389/fbioe.2022.931770

Asymmetric stem-loop–mediated isothermal amplification of nucleic acids for DNA diagnostic assays by simple modification of canonical PCR primers

Rui Mao[1,2]*, Xinyao Wu[1,2], Qing Miao[1,2] and Ting Cai[1,2]*

[1]Key Laboratory of Diagnosis and Treatment of Digestive System Tumors of Zhejiang Province, Hwa Mei Hospital, University of Chinese Academy of Sciences, Ningbo, China, [2]Ningbo Institute of Life and Health Industry, University of Chinese Academy of Sciences, Ningbo, China

Nucleic acid–based assays have been adopted as mainstream tools for clinical diagnostics, food safety, and environment monitoring with the merits of accuracy, rapidity, and sensitivity. Loop-mediated isothermal amplification (LAMP) is a well-established method to rapidly identify nucleic acids and has gained recognition and been developed for clinical applications in resource-limited areas. However, the needs for specifically designed primer sets and non-specific amplification hinder the development of LAMP-based nucleic acid tests. Here, a promoted method, termed asymmetric stem-loop–mediated isothermal amplification (ASLAMP) by simple modification of canonical PCR primers, was developed to attempt to overcome those drawbacks. The two primers in the ASLAMP reaction can be easily obtained by adding a stem-loop sequence part to one PCR primer at 5′-ends to get the folding primer (FP), then adding the same primer to the counter canonical PCR primer at 5′-ends to get the turn-back primer (TP). The ASLAMP method was demonstrated in detecting the H1N1 gene fragment with merits of simple primer design, short target sequence, and high amplification efficiency. In addition, the ASLAMP method showed similar efficacy compared with LAMP targeting at the same H1N1 gene sequence. Furthermore, *Shigella* detection monitored by real-time fluorescence and endpoint colorimetric approaches were taken as examples for evaluation of the practical application of the ASLAMP method, both offered 100% sensitivity and specificity. In conclusion, the novel ASLAMP method with simplicity of primer design, low requirement of equipment, efficiency, and rapidity has exhibited its great prospect for establishment of DNA isothermal amplification in point of care application.

KEYWORDS

nucleic acid detection, isothermal amplification, asymmetric stem-loop, point of care test, real-time fluorescence, endpoint colorimetric

Introduction

Nucleic acid–based assays have been adopted as mainstream tools for clinical diagnostics, food safety, and environment monitoring with the merits of accuracy, rapidity, and sensitivity. Among those approaches, polymerase chain reaction (PCR), the most practical, rapid, accessible, and accurate molecular diagnostic approach, has been developed for identification of interested targets (Saiki et al., 1985; Petralia and Conoci, 2017). In particular, PCR-based detection methods have facilitated appropriate responses to the emerging viral threats, such as, avian influenza A viruses, Ebola virus, and most recently SARS-CoV-2 pandemic (Gao, 2018; Lu et al., 2020; Valera et al., 2021). With the merits of low hardware dependence and rapid amplification of nucleic acid sequences at constant temperature, lots of isothermal amplification techniques have been invented to supplement the sophisticated PCR method (Ju et al., 2021). Recently, novel methods, such as, cross-priming amplification (CPA) (Fang et al., 2009), polymerase spiral reaction (PSR) (Liu et al., 2015), competitive annealing–mediated isothermal amplification (CAMP) (Mao et al., 2018), and closed dumbbell–mediated isothermal amplification (CDA) (Mao et al., 2022), have been extensively established and tried to apply into clinical practice. Among those well-established isothermal amplification methods, LAMP, with the advantages of robustness, rapidity, specificity, and sensitivity, has been verified in many systems for pathogen diagnosis (Zhang Y. et al., 2014; Landaverde et al., 2020; Sheikh et al., 2020; Wang T. et al., 2021; Koeck et al., 2021). However, the drawbacks of specifically designed four to six primers and non-specific amplification hindered the development of LAMP-based nucleic acid tests. (Kimura et al., 2011; Chang et al., 2013; Su et al., 2015; Newbigging et al., 2019; Nguyen et al., 2020).

The objective of this study was to offer an option to solve problems of difficult and cumbersome primer set design of LAMP and try to decrease non-specific amplification. In particular, similar isothermal amplification based on self-primed nucleic acid structure (asymmetric stem-loop or dumbbell structure–based isothermal amplification of nucleic acids, ASLAMP) was established by simple modification of canonical PCR primer. The theoretical reaction steps of ASLAMP are represented in Figure 1. When the reaction is conducted at 60–65°C, the double-stranded structure of template DNA is unstable and could unlock automatically in the presence of betaine (Fei and Ha, 2013). The F segment of the TP primer anneals to Fc in single-stranded–targeted DNA and starts strand extension (structure 2 to structure 3). The Rc sequence in the newly synthesized TP-linked complementary strand is annealed by R in FP to extend (structure 4 to structure 5), then a single chain is obtained and released (structure 6). The single-stranded nucleic acid in structure 6 (3′-Rc-Fc-R-Dc-D-5′) can form an asymmetric dumbbell-like structure, that is, a hairpin structure at

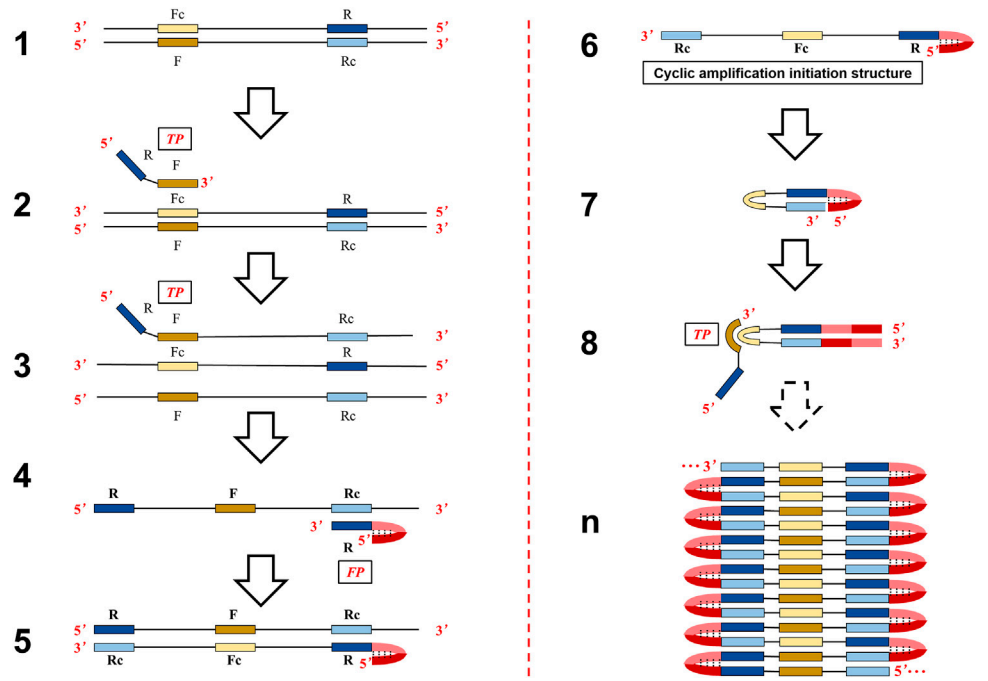

FIGURE 1
Schematic presentation of the mechanism of the ASLAMP method.

the 5′ end of the D-Dc sequence and the Rc at the 3′ end can reversely complementary to the inner R region (structure 7). The structure 7 is similar to the dumbbell-like structure which serves as a starting template to initiate self-primed DNA synthesis in LAMP (Tomita et al., 2008). Thus, the 3′ end can start DNA synthesis by the strand displacement process when the Rc region of 3′ end is annealed to the R region. At the same time, the F in the TP primer is hybridized to single-stranded Fc sequence in the loop to extend (structure 8). The cycling amplification steps of ASLAMP using self-structure as the templates to achieve nucleic acid synthesis were similar to LAMP (Supplementary Figures S1C,D depict the similarity of start structure for self-extension between LAMP and ASLAMP). Finally, similar to the self-extension and primer-aided nucleic acid synthesis procedures in LAMP, a mixture of amplification products featured by adjacent annealed DNAs are obtained (structure n) by ASLAMP. Given the mechanism described earlier, the length of the targeted DNA region required for primer design of ASLAMP can be as short as 40 bps.

The principle, performance, and non-specific reaction of the newly ASLAMP method have been investigated by amplifying the targeted H1N1 gene fragment. Also, the boost primer was designed and selected for the H1N1 gene to get a boost-ASLAMP (B-ASLAMP) reaction, which would dramatically reduce the reaction time by accelerating DNA synthesis without non-specific amplification. In addition, the amplification efficiency of ASLAMP was comparable with LAMP in detecting the same H1N1 target. Moreover, the visible onsite ASLAMP detection approach by hydroxy naphthol blue (HNB) endpoint indication was also verified. Furthermore, real-time fluorescence and HNB-based endpoint colorimetric ASLAMP detection of *Shigella* were taken as instances to obtain practical application assessment with both 100% sensitivity and specificity. In conclusion, all results suggested great potential of the developed ASLAMP method to achieve a simple, easy-to-operate, and fast nucleic acid analysis tool for the point of care diagnosis.

Materials and methods

Reagents and materials

DNA plasmids and primers were provided by BGI Biological Engineering Technology and Services Co., Ltd. (Shenzhen, China). DNA fragments of the H1N1 gene (GenBank: GQ290690.1) and *Shigella* gene (GenBank: CP055125.1) were cloned into pMV vectors to construct plasmid DNA templates. The *Bst* 2.0 WarmStart DNA polymerase and 10× ThermoPol reaction buffer (including 200 mM Tris-HCl, 100 mM KCl, 100 mM $(NH_4)_2SO_4$, 20 mM $MgSO_4$, and 1% Triton X-100) were purchased from New England BioLabs (Ipswich, MA, United States). The DNA molecular weight marker was purchased from Thermo Fisher Scientific (Waltham, MA, United States). Eva Green and GelRed were obtained from Biotium (Hayward, CA, United States). Deoxynucleotide triphosphates (dATP, dTTP, dGTP, and dCTP), restriction enzyme *EcoRV*, DNA purification kits, and DNA extraction kits were purchased from Sangon Biotech (Sangon, Shanghai, China). Other reagents, unless specified, were obtained from Sigma-Aldrich (St. Louis, MO, United States). The online DNA copy number calculator (http://cels.uri.edu/gsc/cndna.html.) was adopted to determine copy numbers of targets.

ASLAMP and B-ASLAMP reaction

The ASLAMP assays were conducted in 25 μl reaction mixtures with the following components: 8 U *Bst* 2.0 WarmStart DNA polymerase, 2.5 μl 10 × ThermoPol reaction buffer, 1 M betaine, 6 mM $MgSO_4$, 1.4 mM of each dNTP, 1.6 μM of TP and FP, and an appropriate amount of the nucleic acid sample. For the B-ASLAMP reaction, another BP (0.8 μM) was added to the mixtures. Negative control (NC) contained non-target nucleic acid samples or nuclease-free water. The reactions were generally carried out at 63°C for 60 min and heating at 85°C for 10 min to terminate.

Similar to LAMP, the by-products of insoluble magnesium pyrophosphate were produced in the process of ASLAMP amplification, and hydroxy naphthol blue (HNB, final concentration 120 μM) was added to indicate Mg^{2+} reduction in the reaction mixtures described earlier to achieve endpoint monitoring. Positive ASLAMP and B-ASLAMP colorimetric reactions are indicated by endpoint blue, while negative reactions keep violet in HNB-added reaction mixtures.

LAMP reaction

The LAMP reaction was conducted using the identical mixture applied in ASLAMP except for the primers. The LAMP and ASLAMP were performed with closely matched primer sets targeting the H1N1 gene. The primer set for LAMP consists of forward inner primer (FIP), backward inner primer (BIP), forward outer primer (F3), and forward outer primer (B3). The primers needed for the H1N1 LAMP reaction are 1.6 μM for FIP and BIP and 0.2 μM for F3 and B3 (Supplementary Table S1). For the amplification efficiency comparison, LAMP, ASLAMP, and B-ASLAMP reactions were prepared at the same time and performed at 63°C for 60 min in a Real-Time PCR detection system using identical 10^4 copies of the H1N1 plasmid gene.

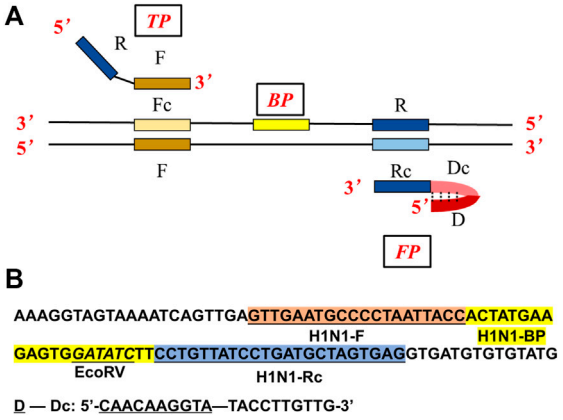

FIGURE 2
(A) Primer design of the ASLAMP method. **(B)** Localization of primers and restriction enzyme cutting site in the nucleotide sequence of the modified H1N1 gene.

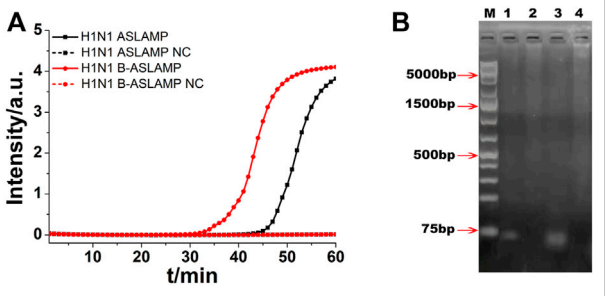

FIGURE 3
(A) ASLAMP and B-ASLAMP amplifications monitored by real-time PCR carried out at 63°C for 60 min. **(B)** Gel electrophoresis results for ASLAMP and B-ASLAMP products prior and after restriction enzyme digestion. Line M, molecular weight marker. Lane 1, H1N1 ASLAMP product that has been digested by *EcoRV*. Lane 2, ASLAMP products prior to digestion. Lane 3, B-ASLAMP product that has been digested by *EcoRV*. Lane 4, B-ASLAMP products prior to digestion. NC is the abbreviation of negative control.

Amplification product analysis

The ASLAMP reaction was real-time monitored by Eva Green which would emit fluorescence when intercalating with dsDNA. The instrument SLAN-96 Real-Time PCR detection system (Sansure biotechnology, Changsha, China) was set to measure the fluorescence intensity in every minute intervals. After ASLAMP and B-ASLAMP reaction, 5 μl products were electrophoresed at 70 V in 1% agarose gel, stained with GelRed and visualized by the ChemiDoc™ XRS Imaging System.

Restriction enzyme analysis of H1N1 gene ASLAMP products

The products of ASLAMP and B-ASLAMP methods targeting the modified H1N1 gene fragment which has a restriction enzyme recognition site for *EcoRV* (Figure 2B) were purified using commercial kits. Then, the purified products were digested with enzyme *EcoRV* at 37°C following the instruction. Then, the digested and pro-digested products by H1N1 gene ASLAMP and B-ASLAMP amplification were analyzed using 1% agarose gel electrophoresis.

Real-time and colorimetric detection of *Shigella* by ASLAMP

The ASLAMP-based *Shigella* assays by real-time fluorescence and endpoint colorimetric approaches were taken as instances of practicability investigation. For pathogen DNA preparation, single clones of the bacteria were selected from LB agar plates and cultured in 5 ml LB broth at 37°C overnight by a shaker incubator (180 rpm). For further exploration of the practical application, single clones of the standard strain of *Shigella* were mixed with pasteurized milk (5 ml) and smashed bread (5 g) in sterilized 50 ml corning tubes at room temperature overnight to mimic the natural process of infection. After incubation, the liquid cultures and artificial infections were collected and extracted using commercial DNA extraction kits or easily by boiling. The sensitivity of the developed *Shigella* ASLAMP method was evaluated using 10-fold serial dilutions of the strain ranging from 1.0×10^6 to 10 copies/μl. Also, the specificity of the *Shigella* B-ASLAMP assay was further explored using DNA samples extracted from cultured standard strains of *Escherichia coli* (CVCC 1491), *Salmonella* (CVCC1789), *L. monocytogenes* (CVCC 1597), and *Vibrio parahaemolyticus* (CGMCC 1.1997) strains (CVCC: China Veterinary Culture Collection Center, CGMCC: China General Microbiological Culture Collection Center).

Results

The principle of the ASLAMP method

Similar to LAMP, ASLAMP is dependent on auto-cycling DNA synthesis by strand displacement activity of DNA polymerase, but just needs a pair of specially designed primers (TP: turn-back primer, FP: folding primer in Figure 2A). Compared to conventional LAMP primer design (Supplementary Figure S1A), the primers can be easily designed from canonical PCR primers (typically 18–22 nts) of the targeted sequences. As depicted in Figure 2A, the sequences of F and R stands for the "forward" and "reverse" primer

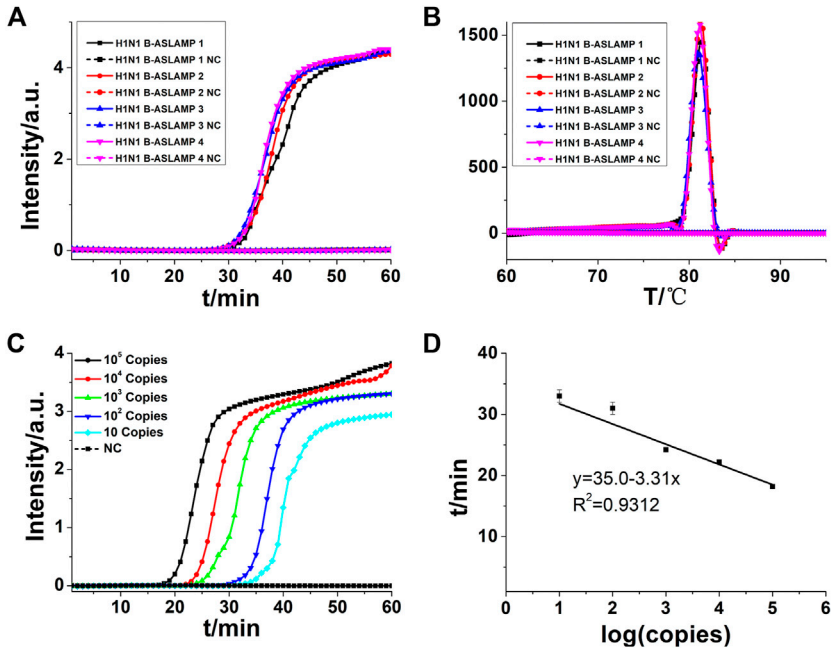

FIGURE 4
(A) B-ASLAMP amplification monitored by real-time PCR. **(B)** Melting curve analysis of B-ASLAMP products by real-time PCR. **(C)** H1N1 gene amplifications of serial dilutions of the H1N1 gene by B-ASLAMP monitored by real-time PCR carried out at 63°C for 60 min. **(D)** Standard curve generated by B-ASLAMP amplification of serial dilutions of the H1N1 gene. NC is the abbreviation of negative control.

sequences in PCR respectively, the sites with lowercase "c" represent "complementary" sites. Based on this structure, the primers of TP and FP are designed as follows. TP contains the sequence R and the sequence F. FP contains the external sequence D-Dc (D stands for non-sense) and the sequence R at the 3′ end. Boost primer is situated between F and Rc. The F sequence, R sequence, and boost sequence should be 17–24 base pairs with a GC rate of 45%~55% like the requirement of PCR reaction. We can see that the D-Dc is self-annealing and could form a hairpin structure at the 5′ end. Notably, the external sequence D-Dc is optional at any times which would offer an option to adjust theoretically and practically. So, the interaction of primers which caused non-specific amplification can be eliminated (Rolando et al., 2020).

H1N1 gene amplification by ASLAMP

To demonstrate the principle of ASLAMP, the H1N1 gene fragment modified by adding a restriction site (*EcoRV*) sequence was adopted as a model for illustration. The ASLAMP primers of the H1N1 gene are exhibited in Figure 2B and Supplementary Table S1 based on canonical H1N1 PCR primer pairs accordingly. The reactions were conducted by addition of a primer mixture of 40 μM TP and FP at constant 63°C for 60 min. The real-time fluorescence curve showed that two primers of ASLAMP successfully amplified 100 copies of the H1N1 gene fragment (Figure 3A).

After real-time fluorescence analysis, the electrophoresis of H1N1 ASLAMP products by 1% agarose gel was operated. The results showed that the amplification products were ladder-like bands with various molecular weights (lanes 1 and 2 in Figure 3B). The minimum band was consistent with the theoretical monomeric amplicons primed by TP and FP. Also, other larger bands were probably multiple-unit amplicons matched with the expected ASLAMP products. The gel electrophoresis demonstrated the correctness of the ASLAMP principle.

Optimization of H1N1 gene ASLAMP reaction

The H1N1 DNA gene was also used for the illustration of boost primer with ASLAMP (Figure 2A exhibits the location of turn-back primer, folding primer, and boost primer; Figure 2B shows the primer location targeting at H1N1 gene), termed as B-ASLAMP. The threshold time was shortened dramatically in detection of 100 copies of the H1N1 gene by B-ASLAMP compared with ASLAMP (Figure 3A), which indicated dramatic improvements in amplification efficiency. Moreover, the boost primer exhibited improvement of efficiency in

amplification of low concentration of target DNA (Figure 4C). Meanwhile, the threshold detection time by H1N1 gene B-ASLAMP amplification for 100 copies was 29.5 min, and the melting curve analysis for the products was 81.25°C as shown in Figures 4A,B. In addition, both the real-time fluorescence analysis and melting curve analysis of the H1N1 DNA gene amplification displayed the repeatability of the B-ASLAMP method (4 repeats).

To detect limitation, the cycle threshold (Ct) value of 10 copies of the H1N1 gene amplified by B-ASLAMP was about 33 min as shown in Figure 4C, demonstrating the fine sensitivity and efficiency of the novel method. In addition, the standard curve depicted by plotting the value of Ct vs. copy number (Figure 4D) indicated that the H1N1 B-ASLAMP method held a potential for semi-quantification of target DNA (R^2 = 0.9312).

Restriction enzyme analysis of ASLAMP and B-ASLAMP products

The modified H1N1 gene fragment with a restriction enzyme recognition site of *EcoRV* was used for demonstration of ASLAMP and B-ASLAMP method, and the properties of the developed methods were further explored by restriction enzyme analysis of the amplification products. The result showed that after digestion, the ASLAMP and B-ASLAMP products of various molecular weights were split into single short DNA and the theoretical digestion products were 74 bp pieces (Figure 3B, lanes 2 and 4). The specificity and principle of the boost ASLAMP (B-ASLAMP) reaction were also demonstrated by the electrophoresis and threshold time of the real-time curve of the both methods. Notably, false positive results were not observed with the addition of boost primer. Therefore, the extra addition of boost primer in the ASLAMP reaction was helpful to realize high specificity and efficiency for amplification of DNA.

Comparison of ASLAMP and LAMP in amplification of the H1N1 gene

From the amplification principle, the newly established ASLAMP method could be classified as a promoted LAMP method. Loop structures in both methods were of great importance to innate rapid accumulation of target nucleic acid signals. To obtain a primary evaluation of amplification efficiency of the developed ASLAMP assay, the same concentration of the H1N1 gene fragment was adopted to get amplified by the LAMP, ASLAMP, and B-ASLAMP assays (the sequences of primers are listed in Supplementary Table S1). The B-ASLAMP primer sets successfully amplified same 10^4 copies of the target with the lowest threshold time (Ct) compared with LAMP and the ASLAMP (Figure 5), indicating highest efficiency in H1N1 gene detection.

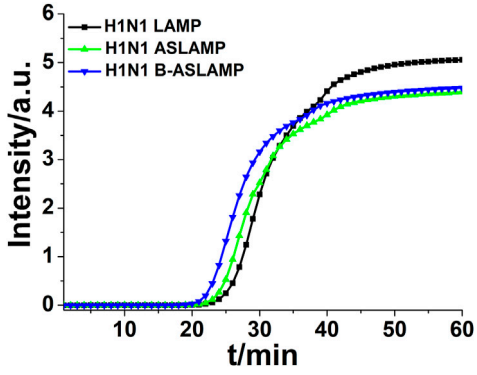

FIGURE 5
Real-time fluorescence curve of LAMP, ASLAMP, and B-ASLAMP amplification of the H1N1 gene.

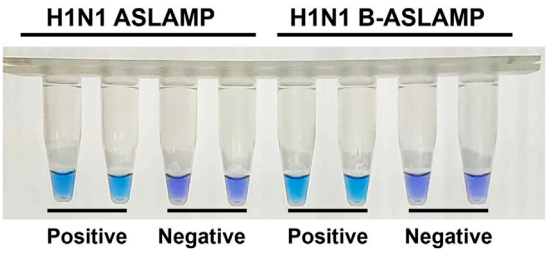

FIGURE 6
HNB-based colorimetric ASLAMP, and B-ASLAMP assays for H1N1 gene detection.

Colorimetric endpoint monitor approach of the ASLAMP method

Visual detection tools allowed us to judge the existence of interested biomarkers in low-infrastructure areas where there was lack of bulky and expensive analytical instrumentations. Various visually monitoring innovations have been developed for the well-established LAMP (Zhang X. Z. et al., 2014; Fischbach et al., 2015). To facilitate onsite ASLAMP detection similarly, the colorimetric detection method was explored. In this study, an identical endpoint visual monitoring by HNB indicated that the Mg^{2+} reduction approach was adopted for the ASLAMP reaction. As shown in Figure 6, the HNB-based H1N1 ASLAMP and B-ASLAMP colorimetric reactions conducted at 63°C for 60 min can be judged by naked eyes. Positive ASLAMP and B-ASLAMP

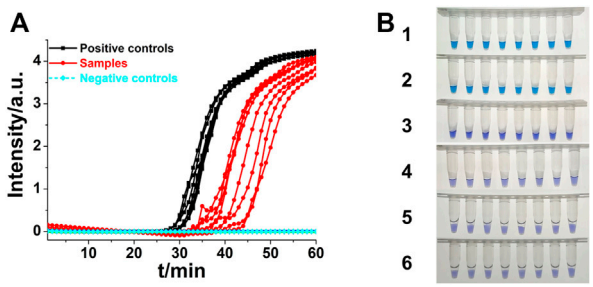

FIGURE 7
(A) Real-time B-ASLAMP for *Shigella* positive controls, samples and negative control (*E. coli*, *L. monocytogenes*, *Salmonella*, and *V. parahaemolyticus*). **(B)** Colorimetric B-ASLAMP based on HNB. Line 1, positive controls (10^5 copies of templates). Line 2, samples extracted from the standard strain of *Shigella*. Line 3, samples extracted from the standard strain of *E. coli*. Line 4, samples extracted from the standard strain of *L. monocytogenes*. Line 5, samples extracted from the standard strain of *Salmonella*. Line 6, samples extracted from the standard strain of *V. parahaemolyticus*.

colorimetric reactions are indicated by endpoint blue, while negative reactions keep violet in HNB-added reaction mixtures.

ASLAMP for *Shigella* detection

Shigella is an important foodborne pathogen that usually causes clinically severe diarrhea (Zhang et al., 2018). Real-time fluorescence and HNB-based endpoint colorimetric ASLAMP detection of *Shigella* were taken as instances to further exploration of this newly developed approach. The *Shigella* ASLAMP assays were conducted using high qualified DNA samples extracted by commercial kits and crude DNA samples prepared by simple boiling and quick centrifugation (the sequences of primers are listed in Supplementary Table S2). Real-time fluorescence curves showed that the developed *Shigella* B-ASLAMP system successfully amplified the target gene sequence of extracted genome samples including artificially contaminated samples (Figure 7A). No cross-reaction was observed when using the *Shigella* B-ASLAMP system to amplify genome DNA samples extracted by commercial kits from cultured strains of *E. coli*, *Salmonella*, *Listeria monocytogenes*, and *V. parahaemolyticus*. For endpoint colorimetric judgment by HNB-based *Shigella* B-ASLAMP assay (Figure 7B), all samples were determined correctly (100% success). The detection limitation of B-ASLAMP *Shigella* assay was 10 copies within 50 min (Supplementary Figure S2), showing good amplification efficiency. Furthermore, *Shigella* detection monitored by real-time fluorescence and endpoint colorimetric approaches both offered 100% sensitivity and specificity. (Table 1). All results proved that the developed B-ASLAMP method could detect target DNA of *Shigella* robustly and rapidly.

Discussion

Nucleic acid amplification–based techniques played critical roles in developing rapid and accurate on-site diagnosis of infectious diseases (Lee et al., 2021). Identification of specific genes of pathogens by probe-based real-time fluorescence PCR accelerated the control of the culprit SARS-CoV-2 pandemic (Valera et al., 2021). Various LAMP-based approaches were developed to achieve the point of care test of SARS-CoV-2 (Dao Thi et al., 2020; Wang R. et al., 2021; Zhang et al., 2021). However, the drawbacks of cumbersome primer design and false-positive amplification hindered the development of LAMP-based nucleic acid tests.

In this research, a novel isothermal amplification–based on self-primed nucleic acid structure (asymmetric stem-loop or dumbbell structure–based isothermal amplification of nucleic acids, ASLAMP) was established by simple modification of canonical PCR primer. This approach would offer an alternative method of LAMP for rapid isothermal detection of nucleic acids by simple

TABLE 1 Sensitivity and specificity of B-ASLAMP assay for *Shigella*.

Species	Sample number		Sensitivity	Specificity	Accuracy
	Shigella B-ASLAMP	Defined	95% CI[a]	95% CI[a]	95% CI[a]
Shigella	80	80	1.0 (95.5–100.0)	1.0 (97.2–100.0)	1.0 (98.2–100.0)
E. coli	0	32			
L. monocytogenes	0	32			
Salmonella	0	32			
V. parahaemolyticus	0	32			
Total	80	208			

[a]CI, confidence interval. Statistical analysis was carried out by the online program of "Diagnostic test evaluation calculator," https://www.medcalc.org/calc/diagnostic_test.php.

modification of canonical PCR primer. As the primer design and amplification principle demonstrated, ASLAMP should be termed as a variation of the LAMP method. The principle of ASLAMP was demonstrated by amplification of the modified H1N1 gene fragment with merits of simple and high efficiency. The study of reproducibility of B-ASLAMP was illustrated by both real-time fluorescence curve and melting curve analysis. In addition, the plot of the value of threshold time (Ct) versus copy number of the H1N1 gene plasmid indicated the developed B-ASLAMP would be applied for semi-quantification of target DNA. The results of colorimetric assays were in accordance with real-time fluorescence assays in amplification of the H1N1 gene, indicating on-site detection potential of the HNB-based ASLAMP method.

After all, the ASLAMP method showed similar amplification efficacy compared with LAMP. The ASLAMP needed a simpler primer design procedure and shorter target sequence compared with LAMP as shown in Supplementary Figures S1A,B. In addition, a similar starting structure for self-extension of LAMP and ASLAMP indicated the developed assays would obtain similar amplification efficiency in theory (Supplementary Figures S1C,D). In particular, a simple and easy primer design process of ASLAMP would achieve a convenient establishment of an isothermal amplification system from the existing PCR reaction system. Furthermore, HNB-based colorimetric B-ASLAMP would help to facilitate the development of onsite *Shigella* detection which exhibited 100% sensitivity and specificity.

In conclusion, with the advantages of simple primer design and no need of outer primer, ASLAMP has the potential to realize simple and fast nucleic acid amplification–based analysis (Liu et al., 2018; Yamanaka et al., 2018; Varona and Anderson, 2019). Single nucleotide polymorphism (SNP) identification and other applications by ASLAMP should be explored in near future (Mitani et al., 2007). It is hopeful that the established ASLAMP technique could develop into a powerful point of care DNA assays for rapid, simple, reliable, and sensitive diagnosis.

Data availability statement

The original contributions presented in the study are included in the article/Supplementary Material; further inquiries can be directed to the corresponding authors.

Author contributions

Conceptualization, RM; Methodology, RM and XW; Investigation, XW and QM; Writing—original draft preparation, RM; Writing—review and editing, XW, QM, and TC; Supervision, RM and TC; Project administration, RM and TC. All authors have read and agreed to the published version of the manuscript.

Funding

This research was funded by the Medical Scientific Research Foundation of Zhejiang Province, China, grant number 2021KY337 and the Ningbo Institute of Life and Health Industry, University of Chinese Academy of Sciences, grant numbers 2020YJY0214 and 2021YJY1008.

Conflict of interest

The authors declare that the research was conducted in the absence of any commercial or financial relationships that could be construed as a potential conflict of interest.

Publisher's note

All claims expressed in this article are solely those of the authors and do not necessarily represent those of their affiliated organizations, or those of the publisher, the editors, and the reviewers. Any product that may be evaluated in this article, or claim that may be made by its manufacturer, is not guaranteed or endorsed by the publisher.

Acknowledgments

We sincerely thank all the researchers who provided the test strains.

Supplementary material

The Supplementary Material for this article can be found online at: https://www.frontiersin.org/articles/10.3389/fbioe.2022.931770/full#supplementary-material

References

Chang, C. M., Chang, W. H., Wang, C. H., Wang, J. H., Mai, J. D., Lee, G. B., et al. (2013). Nucleic acid amplification using microfluidic systems. *Lab. Chip* 13 (7), 1225. doi:10.1039/c3lc41097h

Dao Thi, V. L., Herbst, K., Boerner, K., Meurer, M., Kremer, L. P., Kirrmaier, D., et al. (2020). A colorimetric RT-LAMP assay and LAMP-sequencing for detecting SARS-CoV-2 RNA in clinical samples. *Sci. Transl. Med.* 12 (556), eabc7075. doi:10.1126/scitranslmed.abc7075

Fang, R., Li, X., Hu, L., You, Q., Li, J., Wu, J., et al. (2009). Cross-priming amplification for rapid detection of *Mycobacterium tuberculosis* in sputum specimens. *J. Clin. Microbiol.* 47 (3), 845–847. doi:10.1128/jcm.01528-08

Fei, J., and Ha, T. (2013). Watching DNA breath one molecule at a time. *Proc. Natl. Acad. Sci. U. S. A.* 110 (43), 17173–17174. doi:10.1073/pnas.1316493110

Fischbach, J., Xander, N. C., Frohme, M., and Glokler, J. F. (2015). Shining a light on LAMP assays-A comparison of LAMP visualization methods including the novel use of berberine. *Biotechniques* 58 (4), 189–194. doi:10.2144/000114275

Gao, G. F. (2018). From "A"IV to "Z"IKV: attacks from emerging and Re-emerging pathogens. *Cell* 172 (6), 1157–1159. doi:10.1016/j.cell.2018.02.025

Ju, Y., Kim, H. Y., Ahn, J. K., and Park, H. G. (2021). Ultrasensitive version of nucleic acid sequence-based amplification (NASBA) utilizing a nicking and extension chain reaction system. *Nanoscale* 13 (24), 10785–10791. doi:10.1039/d1nr00564b

Kimura, Y., de Hoon, M. J. L., Aoki, S., Ishizu, Y., Kawai, Y., Kogo, Y., et al. (2011). Optimization of turn-back primers in isothermal amplification. *Nucleic Acids Res.* 39 (9), e59. doi:10.1093/nar/gkr041

Koeck, J., Gottschalk, C., Ulrich, S., Schwaiger, K., Gareis, M., Niessen, L., et al. (2021). Rapid and selective detection of macrocyclic trichothecene producing Stachybotrys chartarum strains by loop-mediated isothermal amplification (LAMP). *Anal. Bioanal. Chem.* 413 (19), 4801–4813. doi:10.1007/s00216-021-03436-y

Landaverde, L., Wong, W., Hernandez, G., Fan, A., and Klapperich, C. (2020). Method for the elucidation of LAMP products captured on lateral flow strips in a point of care test for HPV 16. *Anal. Bioanal. Chem.* 412 (24), 6199–6209. doi:10.1007/s00216-020-02702-9

Lee, C. Y., Degani, I., Cheong, J., Weissleder, R., Lee, J. H., Cheon, J., et al. (2021). Development of integrated systems for on-site infection detection. *Acc. Chem. Res.* 54 (21), 3991–4000. doi:10.1021/acs.accounts.1c00498

Liu, W., Dong, D. R., Yang, Z., Zou, D. Y., Chen, Z. L., Yuan, J., et al. (2015). Polymerase spiral reaction (PSR): A novel isothermal nucleic acid amplification method. *Sci. Rep.* 5, 12723. doi:10.1038/srep12723

Liu, X. N., Zhang, C., Zhao, M. Y., Liu, K. W., Li, H., Li, N. N., et al. (2018). A direct isothermal amplification system adapted for rapid SNP genotyping of multifarious sample types. *Biosens. Bioelectron. X.* 115, 70–76. doi:10.1016/j.bios.2018.05.021

Lu, R., Zhao, X., Li, J., Niu, P., Yang, B., Wu, H., et al. (2020). Genomic characterisation and epidemiology of 2019 novel coronavirus: implications for virus origins and receptor binding. *Lancet* 395 (10224), 565–574. doi:10.1016/s0140-6736(20)30251-8

Mao, R., Qi, L., Li, J., Sun, M., Wang, Z., Du, Y., et al. (2018). Competitive annealing mediated isothermal amplification of nucleic acids. *Analyst* 143 (3), 639–642. doi:10.1039/c7an01569k

Mao, R., Wang, T., Zhao, Y., Wu, X., Zhang, S., Cai, T., et al. (2022). Closed dumbbell mediated isothermal amplification of nucleic acids for DNA diagnostic assays. *Talanta* 240, 123217. doi:10.1016/j.talanta.2022.123217

Mitani, Y., Lezhava, A., Kawai, Y., Kikuchi, T., Oguchi-Katayama, A., Kogo, Y., et al. (2007). Rapid SNP diagnostics using asymmetric isothermal amplification and a new mismatch-suppression technology. *Nat. Methods* 4 (3), 257–262. doi:10.1038/nmeth1007

Newbigging, A. M., Zhang, H. Q., and Le, X. C. (2019). Beacon-mediated exponential amplification reaction (BEAR) using a single enzyme and primer. *Chem. Commun.* 55 (72), 10677–10680. doi:10.1039/c9cc04226a

Nguyen, T., Chidambara, V. A., Andreasen, S. Z., Golabi, M., Huynh, V. N., Linh, Q. T., et al. (2020). Point-of-care devices for pathogen detections: the three most important factors to realise towards commercialization. *Trends Anal. Chem.* 131, 116004. doi:10.1016/j.trac.2020.116004

Petralia, S., and Conoci, S. (2017). PCR technologies for point of care testing: progress and perspectives. *ACS Sens.* 2 (7), 876–891. doi:10.1021/acs.sensors.7b00299

Rolando, J. C., Jue, E., Barlow, J. T., and Ismagilov, R. F. (2020). Real-time kinetics and high-resolution melt curves in single-molecule digital LAMP to differentiate and study specific and non-specific amplification. *Nucleic Acids Res.* 48 (7), e42. doi:10.1093/nar/gkaa099

Saiki, R. K., Scharf, S., Faloona, F., Mullis, K. B., Horn, G. T., Erlich, H. A., et al. (1985). Enzymatic amplification of beta-globin genomic sequences and restriction site analysis for diagnosis of sickle cell anemia. *Science* 230 (4732), 1350–1354. doi:10.1126/science.2999980

Sheikh, N., Kumar, S., Sharma, H. K., Bhagyawant, S. S., and Thavaselvam, D. (2020). Development of a rapid and sensitive colorimetric loop-mediated isothermal amplification assay: a novel technology for the detection of coxiella burnetii from minimally processed clinical samples. *Front. Cell. Infect. Microbiol.* 10, 127. doi:10.3389/fcimb.2020.00127

Su, W., Gao, X., Jiang, L., and Qin, J. (2015). Microfluidic platform towards point-of-care diagnostics in infectious diseases. *J. Chromatogr. A* 1377, 13–26. doi:10.1016/j.chroma.2014.12.041

Tomita, N., Mori, Y., Kanda, H., and Notomi, T. (2008). Loop-mediated isothermal amplification (LAMP) of gene sequences and simple visual detection of products. *Nat. Protoc.* 3 (5), 877–882. doi:10.1038/nprot.2008.57

Valera, E., Jankelow, A., Lim, J., Kindratenko, V., Ganguli, A., White, K., et al. (2021). COVID-19 point-of-care diagnostics: present and future. *Acs Nano* 15 (5), 7899–7906. doi:10.1021/acsnano.1c02981

Varona, M., and Anderson, J. L. (2019). Visual detection of single-nucleotide polymorphisms using molecular beacon loop-mediated isothermal amplification with centrifuge-free DNA extraction. *Anal. Chem.* 91 (11), 6991–6995. doi:10.1021/acs.analchem.9b01762

Wang, R., Qian, C., Pang, Y., Li, M., Yang, Y., Ma, H., et al. (2021a). opvCRISPR: one-pot visual RT-LAMP-CRISPR platform for SARS-cov-2 detection. *Biosens. Bioelectron.* 172, 112766. doi:10.1016/j.bios.2020.112766

Wang, T., Ji, H., Yu, Y., Wang, X., Cheng, Y., Li, Z., et al. (2021b). Development of a loop-mediated isothermal amplification method for the rapid detection of phytopythium vexans. *Front. Microbiol.* 12, 720485. doi:10.3389/fmicb.2021.720485

Yamanaka, E. S., Tortajada-Genaro, L. A., Pastor, N., and Maquieira, A. (2018). Polymorphism genotyping based on loop-mediated isothermal amplification and smartphone detection. *Biosens. Bioelectron. X.* 109, 177–183. doi:10.1016/j.bios.2018.03.008

Zhang, X. Z., Lowe, S. B., and Gooding, J. J. (2014a). Brief review of monitoring methods for loop-mediated isothermal amplification (LAMP). *Biosens. Bioelectron. X.* 61, 491–499. doi:10.1016/j.bios.2014.05.039

Zhang, Y., Zhang, L., Sun, J., Liu, Y., Ma, X., Cui, S., et al. (2014b). Point-of-care multiplexed assays of nucleic acids using microcapillary-based loop-mediated isothermal amplification. *Anal. Chem.* 86 (14), 7057–7062. doi:10.1021/ac5014332

Zhang, L. D., Wei, Q. J., Han, Q. Q., Chen, Q., Tai, W. L., Zhang, J. Y., et al. (2018). Detection of Shigella in milk and clinical samples by magnetic immunocaptured-loop-mediated isothermal amplification assay. *Front. Microbiol.* 9, 94. doi:10.3389/fmicb.2018.00094

Zhang, L., Richards, A., Barrasa, M. I., Hughes, S. H., Young, R. A., Jaenisch, R., et al. (2021). Reverse-transcribed SARS-CoV-2 RNA can integrate into the genome of cultured human cells and can be expressed in patient-derived tissues. *Proc. Natl. Acad. Sci. U. S. A.* 118 (21), e2105968118. doi:10.1073/pnas.2105968118

frontiers | Frontiers in Bioengineering and Biotechnology

ORIGINAL RESEARCH
published: 22 July 2022
doi: 10.3389/fbioe.2022.881679

Design of Hydrogel Silk-Based Microarrays and Molecular Beacons for Reagentless Point-of-Care Diagnostics

Alicia Sampieri[1], *Ricardo Monroy-Contreras*[1], *Alexander Asanov*[2] *and Luis Vaca*[1]*

[1]Departamento de Biología Celular y del Desarrollo, Instituto de Fisiología Celular, UNAM, Ciudad Universitaria, Mexico, Mexico, [2]TIRF Labs, Cary, NC, United States

We have developed a novel microarray system based on three technologies: 1) molecular beacons designed to interact with DNA targets at room temperature (25–27°C), 2) tridimensional silk-based microarrays containing the molecular beacons immersed in the silk hydrogel, and 3) shallow angle illumination, which uses separated optical pathways for excitation and emission. Unlike conventional microarrays that exhibit reduced signal-to-background ratio, require several stages of incubation, rinsing, and stringency control, and measure only end-point results, our microarray technology provides enhanced signal-to-background ratio (achieved by separating the optical pathways for excitation and emission, resulting in reduced stray light), performs analysis rapidly in one step without the need for labeling DNA targets, and measures the entire course of association kinetics between target DNA and the molecular beacons. To illustrate the benefits of our technology, we conducted microarray assays designed for the identification of influenza viruses. We show that in a single microarray slide, we can identify the virus subtype according to the molecular beacons designed for hemagglutinin (H1, H2, and H3) and neuraminidase (N1, N2). We also show the identification of human and swine influenza using sequence-specific molecular beacons. This microarray technology can be easily implemented for reagentless point-of-care diagnostics of several contagious diseases, including coronavirus variants responsible for the current pandemic.

Keywords: molecular beacons, microarrays, silk, point-of-care diagnostics, influenza virus

OPEN ACCESS

Edited by:
Mathieu Hautefeuille, Sorbonne Université, France

Reviewed by:
Jie Wu, Nanjing University, China
Rafael Camacho-Carranza, National Autonomous University of Mexico, Mexico

***Correspondence:**
Luis Vaca
lvaca@ifc.unam.mx

Specialty section:
This article was submitted to Biosensors and Biomolecular Electronics, a section of the journal Frontiers in Bioengineering and Biotechnology

Received: *22 February 2022*
Accepted: *21 June 2022*
Published: *22 July 2022*

Citation:
Sampieri A, Monroy-Contreras R, Asanov A and Vaca L (2022) Design of Hydrogel Silk-Based Microarrays and Molecular Beacons for Reagentless Point-of-Care Diagnostics. Front. Bioeng. Biotechnol. 10:881679. doi: 10.3389/fbioe.2022.881679

INTRODUCTION

Undoubtedly, the current gold standard for molecular diagnosis is the polymerase chain reaction (PCR) (Kim, 2001). PCR, both in its traditional form and in what is known as real-time PCR, is a method widely used worldwide by clinics and hospitals for molecular diagnosis and identification of pathogens, mutations of interest, and polymorphisms (Grau-Roma et al., 2011).

The power of this diagnostic methodology is based on the fact that it is an amplification reaction, which gives it enormous sensitivity (Tong et al., 2011). PCR can detect a single nucleic acid molecule (Valasek and Repa, 2005) (Erlich et al., 1991).

However, PCR also has some problems that hinder its widespread use as a molecular diagnostic method. Below are listed some of the most important limitations of this powerful method:

1) PCR requires a thermal cycler, an expensive and bulky device that must be operated by a specialized technician.
2) The amplification reaction requires programming of the thermal cycler with heating and cooling cycles too complex to be operated by a doctor, nurse, or medical personnel. This amplification cycle is not universal and must be adapted for each DNA segment to be amplified based on the alignment and association temperatures of the oligonucleotides (known as primers) used to amplify the DNA of interest.
3) The amplification reaction (due to the temperature cycles mentioned above) takes more than 1 h to produce the result.

The ideal point-of-care diagnostics system should be one that requires very little sample preparation and handling, is portable and easy to use by any patient (Goble and Rocafort, 2017) (Ferreira et al., 2018). Many systems have been proposed during the last few years, some are easy to use and portable but require complex manipulations and labeling of the sample (Gauglitz, 2014).

One of the molecular recognition events with the highest specificity is the binding of a nucleic acid to its complement; this process has aided the exploration of gene expression and many laboratory methodologies are based on it (Chidchob and Sleiman, 2018). The potential of this technique has not been exploited efficiently for molecular diagnostics (Goble and Rocafort, 2017). To determine if a probe is hybridizing, it is necessary to label the target, immobilize the target complementary sequences on a solid surface, remove the target excess that did not hybridize, and define the number of probes to be used in the assay.

MBs are single-stranded nucleic acid molecules that form a stem-loop structure known as a hairpin (Bonnet et al., 1999; (Tyagi and Kramer, 1996; Monroy-Contreras and Vaca, 2011). The loop portion acts as a probe complementary to a predetermined target sequence (Tyagi and Kramer, 1996). The stem is formed by the union of a series of complementary bases that are located in the loop sequence (Tyagi and Kramer, 1996). The 5′ end of this molecule is covalently coupled to a quencher and the 3′end to a fluorophore. Under resting conditions (without a target), the quencher is in close proximity to the fluorophore, preventing the emission of fluorescence by a phenomenon known as FRET (Foster Resonance Energy Transfer) (Tyagi and Kramer, 1996; Bonnet et al., 1999). Upon MB-target hybridization, the stem from the MB dissociates, allowing the separation between the fluorophore and the quencher, resulting in fluorescence emission (Bonnet et al., 1999).

MBs are extremely specific and can easily discriminate target sequences that differ by a single nucleotide substitution (Vaca, 2014), and are more specific than any conventional probe. Thermodynamic analyzes reveal that this increase in specificity is due to the stem-loop (hairpin) conformation of MBs (Bonnet et al., 1999).

MB can be synthesized with different types of fluorophores, which allows simultaneous detection of different target molecules in a multiplex reaction (Monroy-Contreras and Vaca, 2011).

Because MBs are primarily used in PCR reactions, the length and the GC content of the stem sequence are designed in such a way that at the annealing temperature of the PCR, the MB remains closed and therefore non-fluorescent. This is generally ensured by choosing a stem 5–7 base pairs long that contains a high GC content (typically between 75 and 100% GC content) (Bonnet et al., 1999).

Unfortunately, this MB design prevents its use in target identification assays conducted at room (or near room) temperature. This is one of the reasons why MBs have not been employed in point-of-care diagnostics (Asanov et al., 2012).

In the present study, we have explored the length and GC content of MBs to identify the best conditions for target identification in assays conducted at room temperature (25–27°C).

DNA microarray is a multiplex technology used in molecular biology and medicine to identify DNA fragments expressed in an organism or tissue or present in fluids (Plomin and Schalkwyk, 2007). Microarrays consist of an ordered series array of hundreds or thousands of microscopic spots of DNA oligonucleotides (known as probes), each containing a few picomoles of different probes printed on top of silica slides (Gershon, 2002).

The sample is labeled using fluorescent molecules, which are later used to identify sample association with the probe printed on the silica slide (Gershon, 2002). Typical microarray spots are 100 microns in diameter, allowing the printing of thousands of spots in high-density arrays. But microarrays are not very sensitive and sample amplification is often required prior to conducting the microarray study.

Silk is a natural fiber essentially made up of two proteins: fibroin and sericin (Sutherland et al., 2010). Several insects and arthropods naturally produce silk; among them, the most commonly used is the *Bombix mori* larva, also known as the silkworm (Vepari and Kaplan, 2007). This larva produces its own silken cocoon, where it metamorphoses into a butterfly. Silk is an extraordinary product due to its properties as a biomaterial, since it can produce a wide variety of products such as sponges, gels, fibers of various diameters, and three-dimensional (Helmer, 2010; Lee, 2010; Sutherland et al., 2010). For centuries, silk has been used to produce clothing, but recently it has gained great interest because many biomaterials can be produced from it. Silk is traditionally extracted from the cocoon of the silkworm through a process of boiling and chemical extraction (Numata and Kaplan, 2010).

Silk gels are of particular interest since they have almost the same refractive index (1.34) as that ofwater (1.33). Therefore, light passes through silk gels similarly to water without any quenching (Uddayasankar and Krull, 2013; Beaucage, 2001).

The technology presented in this study utilizes MBs specifically designed to interact with their target at room temperature. The MBs are embedded in 3D microarray silk hydrogel matrices, favoring efficient fluorescence transmission and providing a friendly environment for biomolecular interactions.

We show the identification of cDNA from influenza subtype viruses, its selectivity, and its sensitivity.

MATERIALS AND METHODS

Molecular Beacons

Synthesized and purified molecular beacons and complimentary DNA oligomers were purchased from Integrated DNA Technologies (IDT, Coralville, IA, United States). All the beacons in the present study use as fluorophore 6-carboxyfluorescein (6-FAM) at the 5′end, and as quencher 4-((4-(dimethylamino)phenyl)azo)benzoic Acid (Dabcyl) at the 3′end.

Designing Molecular Beacons Used for the Analysis of GC Content and Overlap of Complementary Sequences

To explore the role of the guanine (G) cytosine (C) content in the stem of MB in the kinetics of MB-target formation, we designed MBs with 3 different percentages of GC content (40,60, and 100%). The loop section of the MBs was the same in all of them. The MB used in these experiments was

Q – 3′ – **gagagAAACCAATAGATCGACATActctc** – 5′–**F**

(40% GC content)

Q – 3′ – **aggagAAACCAATAGATCGACATActcct** – 5′–**F**

(60% GC content)

Q – 3′ – **gggggAAACCAATAGATCGACATAccccc** – 5′–**F**

(100% GC content)

In all caps is shown the sequence of the loop in the MB and in lowercase the sequence corresponding to the stem.

To explore the overlapping of the target in the loop and stem from the MB, the following target sequences were designed:

Molecular beacon	
Q-3´-gagagAAACCAATAGATCGACATActctc-5´-F	
Targets	# nt overlapping with the stem
5´-TTTGGTTATCTAGCTGTAT-3´	0
5´-cTTTGGTTATCTAGCTGTA-3´	1
5´-tcTTTGGTTATCTAGCTGT-3´	2
5´-ctcTTTGGTTATCTAGCTG-3´	3
5´-tctcTTTGGTTATCTAGCT-3´	4
5´-ctctcTTTGGTTATCTAGC-3´	5
5´-cTTTGGTTATCTAGCTGTATg-3´	2
5´-tcTTTGGTTATCTAGCTGTATga-3´	4
5´-ctcTTTGGTTATCTAGCTGTATgag-3´	6
5´-tctcTTTGGTTATCTAGCTGTATgaga-3´	8
5´-ctctcTTTGGTTATCTAGCTGTATgagag-3´	10

The sequences from the targets that are complementary to the loop from the MB are shown in all caps. Lowercase shows the sequences complementary to the stem region of the MB. The numbers to the right indicate the number of nucleotides overlapping with the stem from the MB, both unilateral (first 6 target sequences) and bilateral (five next target sequences).

Subtype	Sequence	Length (nt)
H1	ATTCGCATTCTGGGTTTCCTAAGATCCA	28
H3	CATTCCCTCCCAACCATTTTCTATGAA	27
H1s	TGAAATGGGAGGCTGGTGTTTATAGCAC	28
N1	TCTCTTATGACAAAAACATCTCC	23
N2	GAAAAAGGTGCAAATCCTGTAAT	23
N1s	TACTGTATATAGCCCATCCACTAACA	26

Designing Molecular Beacons for the Identification of Influenza Virus Subtypes

We follow a bioinformatics strategy to identify the best sequences in the different influenza genes to ensure high specificity when designing the MBs.

Influenza virus sequences were obtained from the Influenza Virus Resource: http://www.ncbi.nlm.nih.gov/genomes/FLU/FLU.html. All available sequences of the hemagglutinin HA (H1, H3) and neuraminidase NA (N1, N2) genes were downloaded from the aforementioned database and aligned using the command line version of the ClustalW program. The most conserved regions of each HA and NA subtype were selected using BioEdit software, from the previously generated alignments. Each of the conserved sequences was analyzed using the mfold server http://dinamelt.bioinfo.rpi.edu/quikfold.php; this analysis served as a filter to obtain those conserved sequences that contain a minimum secondary structure that does not interfere with the hairpin formation of the MBs. Some of these conserved sequences did not work to specifically detect each virus subtype since large regions are conserved in the gene. Due to this, it was necessary to carry out an "*in silico*" coverage analysis (Durai and Schulz, 2019), to ensure the specificity of the sequences for each of the influenza virus subtypes. The best sequences obtained after the analysis are shown in the table below:

The "*in silico*" coverage analysis help define the sensitivity and specificity of each sequence (Durai and Schulz, 2019). The results obtained are illustrated in the table below:

These sequences were used as the loop portion of the MBs, and a stem sequence was added to produce the final MBs sequences shown below (these MB sequences are protected by patent 344,352):

Underlined are the influenza genes' complementary sequences corresponding to the loop regions of the MBs.

Silk Preparation Hydrogels

There are different methods to generate silk hydrogels under controlled conditions. In the present study, we induced the hydrogel formation with methanol, as previously described (Numata et al., 2014; Numata and Kaplan, 2010). Briefly, cocoons from the silkworm *Bombyx mori* were grounded and boiled for 30 min in a 20 mM Na_2CO_3 solution and then washed with distilled water to remove sericin proteins and wax. Extracted proteins were dried and dissolved in a warm 9 M LiB solution and kept for 2 h. The silk solution was dialyzed using distilled water for 2 days using a dialysis membrane with a molecular weight cut-off of 3,500 (Thermo Fisher Scientific, Waltham, MA, United States). The ilk solution was then concentrated. To

MB ID	Sensitivity %	True positives	Number of sequences analyzed	Specificity %
H1	96.17	1,279	1,330	99.83
H3	99.5	2,458	2,583	100
H1s	100	500	500	99.72
N1	98.06	1,417	1,445	100
N2	98.8	2,880	2,915	100
N1s	99.8	499	500	100

MB ID	MB (5'--->3') Sequence	Length (nt)
H1	CGTAGCATTCGCATTCTGGGTTTCCTAAGATCCAGC**T**ACG	40
H3	CGTAGCCATTCCCTCCCAACCATTTTCTATGAAGC**T**ACG	39
H1s	CGTAGCTGAAATGGGAGGCTGGTGTTTATAGCACGC**T**ACG	40
N1	CGTAGCTCTCTTATGACAAAAACATCTCCGC**T**ACG	35
N2	CGTAGCGAAAAAGGTGCAAATCCTGTAATGC**T**ACG	35
N1s	CGTAGCTACTGTATATAGCCCATCCACTAACAGC**T**ACG	38

produce the hydrogels, an aliquot of the concentrated silk solution was introduced into a silicon cylinder and the cylinder was immersed in methanol for 12 h at room temperature (25–27°C). The resulting silk hydrogel was mixed with 1 μM of the different molecular beacons used in this study.

Printing Silk-Based Tridimensional Microarrays

The silk hydrogel containing the different molecular beacons described in the previous sections was utilized to manually print the microarrays using a Gilson P2 micropipette and the TIRF microarrayer shown below in panel A (TIRF Labs, Cary NC, United States). Typically, each microarray spot was approximately 1 mm in diameter and about 1 mm in height when dispensing 1 μl on each spot (phase contrast image from the microscope in panel B).

Reading and Analyzing the Microarrays

The microarray slides were mounted on a conventional epifluorescence inverted microscope (Nikon Instruments, Japan) using a ×10 objective. Images were acquired using an inexpensive 5 MP CCD camera from Amscope (MT5000-CCD). All microarray data were analyzed using the ImageJ line profile tool and Igor Pro v7 (WaveMetrics, Portland, OR, United States). A target was applied to the microarray slide using a Gilson micropipette.

Shallow Angle Illumination

We use an illumination device that excites the sample from a lateral pathway (TIRFLabs, Cary, NC). The device can be mounted on a conventional epifluorescence inverted microscope (Asanov et al., 2012). The use of the shallow angle illumination device results in having independent excitation and emission optical pathways, promoting reduced stray light and cross talk between the excitation and emission channels (Asanov et al., 2012). Shallow angle illumination results in the excitation of the sample only a few microns above the surface of the coverslip, preventing the excitation of the bulk solution. With each microarray spot having a height of 1 mm, with shallow angle illumination, we ensure that the excitation light is focused primarily on the microarray and not the solution above. A detailed description of the optical properties and physics behind shallow angle illumination can be found elsewhere (Asanov et al., 2012; Asanov et al., 2010).

Characterization of the Tridimensional Geometry of Silk Hydrogel Droplets

Silk hydrogel was prepared using a synthetic molecular beacon for H1 (MB_{H1}) in which the 5′ quencher was not included in order to have a MB that emits fluorescence continuously in the absence of the target. Silk hydrogel microarrays were printed with this MB and confocal microscopy experiments were conducted to reconstruct the tridimensional shape of the droplets. An Olympus FV1000 confocal microscope was utilized for the morphological characterization of the hydrogel droplets. Images of the entire microarray were obtained with a low magnification (×20) objective and a resolution of 2,048 × 2,048 pixels in the x-y plane. The z-plane optical slices were obtained every 200 nm. The entire image stack was loaded into Imaris v8.1 (Oxford Instruments, United Kingdom) for the tridimensional reconstruction and plane projections illustrated in **Supplementary Figure S1**.

RESULTS

Designing Molecular Beacons to Hybridize at Room Temperature

We use our shallow angle illumination device mounted on a conventional epifluorescence inverted microscope (material and methods) (Asanov et al., 2012). Unlike conventional microarray readers, which are basically confocal microscopes, our device utilizes a camera to acquire the fluorescence of the entire

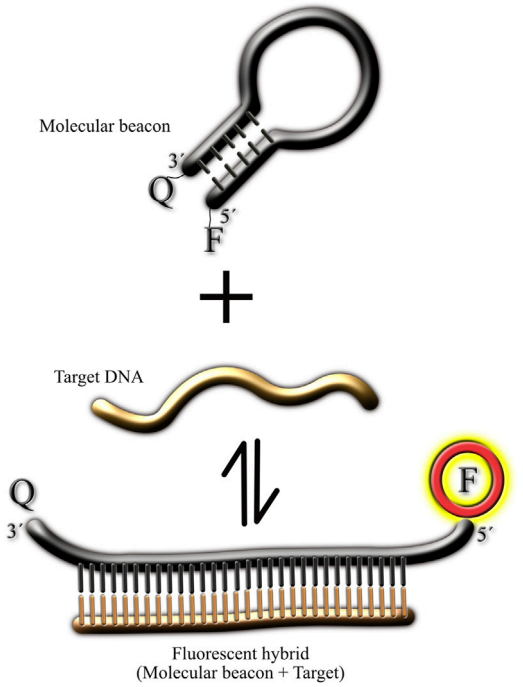

FIGURE 1 | Cartoon illustrating the different molecular conformations of molecular beacons. The figure illustrates the molecular beacon in the non-fluorescent state (hairpin) in the absence of the target. Upon target addition, the 3′ and 5′ ends of the molecular beacon separate from each other, resulting in light emission by the fluorophore. In all the MB synthesized for this study the fluorophore was at the 5′ end and the quencher at the 3′ end (Material and Methods).

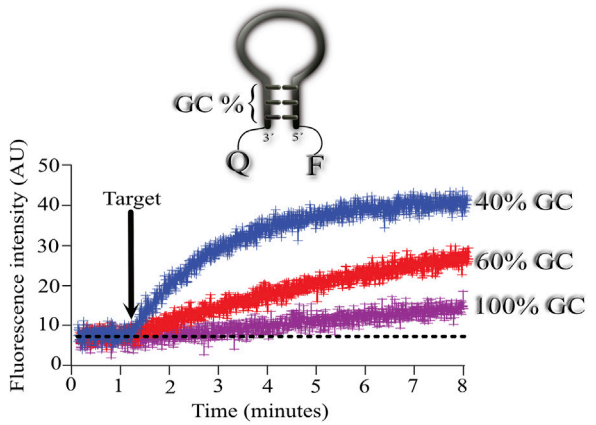

FIGURE 2 | Effect of the percentage of GC content on the hybridization kinetics of the MB-target. Mean ± standard deviation from 6 independent microarrays measuring the mean fluorescence from at least 6 spots for each microarray. Three MBs with different stems were assayed consisting of 40 (blue), 60 (red) and 100 (fuchsia) % GC content in their stem. Arrow indicates the time of target application to the microarrays. Mean fluorescence was obtained from regions of interest (ROI) using the plot profile function from ImageJ for each microarray spot and measured overtime (see **Supplementary Video S1**). Then, means from all spots measured overtime were used to calculate the final mean ± standard deviation (see **Supplementary Video S1**).

microarray in one step (conventional microarray readers read one pixel at a time). This procedure provides a time course of fluorescence increments, that reflects the interaction between the bio analyte (target) and the molecular beacon (MB).

Figure 1 illustrates the typical reaction of a MB and its target. Under resting conditions (without the presence of the target), the MB should be in the rest (non-fluorescent) state, forming a hairpin which brings together the fluorophore and its quencher, preventing light emission in this way. Upon the addition of the target, the bimolecular association MB-target is formed, resulting in the spatial separation of the fluorophore and its quencher, and therefore light emission. Ideally, the bimolecular MB-target state should be more favorable to prevent dissociation of the duo, resulting in reduced fluorescence signal. To ensure that the bimolecular state is favorable in this reaction, the stem from the MB must be carefully designed. Typically, a high GC content in the stem will prevent spontaneous separation of the fluorophore and its quencher but will also make more difficult the formation of the MB-target binomial (since the thermodynamics would favor the hairpin state). Since traditionally MBs have been used in PCR reaction, where temperature is controlled by a thermal cycler, the MBs used in PCR reactions have typically high GC content in their stems (70%–100%). This high GC content would not work in assays conducted at room temperature, and therefore is not suitable for point-of-care diagnostics using simple equipment. In fact, the thermal transition of MBs is such that at room temperature, there is basically no florescence emitted by the probe (Tyagi and Kramer, 1996).

To overcome this design, we explored the GC content usable for MB-target associations at room temperature (25–27°C). We also explored several stem lengths to identify the best combination of stem length and GC content to favor MB-target association at room temperature.

The MBs contained in our silk hydrogel were printed on the surface of silica microarray glass (1 mm thick) and the slide was mounted on the inverted microscope and fluorescence was monitored using a CCD camera (Material and Methods) and our shallow angle illumination device. Silk printed hydrogels form a tridimensional droplet of approximately 1 mm in diameter and 700–800 microns in height (**Supplementary Figure S1**). A typical fluorescence experiment is illustrated in **Supplementary Video S1**. The mean fluorescence intensity was plotted over time to illustrate the time course of association of the MB-target and its kinetics. The video shows how the area of each microarray spot was measured using a region of interest (ROI) in ImageJ (material and methods). For each microarray experiment a replica of at least six spots was measured to obtain the mean ± standard deviation. At least 5 independent microarrays were evaluated for each of the conditions explored. **Supplementary Video S2** shows the time course of fluorescence increments upon target application.

Because leakage of the MBs from the hydrogel would result in reduction in the fluorescence intensity of the microarray, we characterized the time course of MBs leakage from the hydrogel.

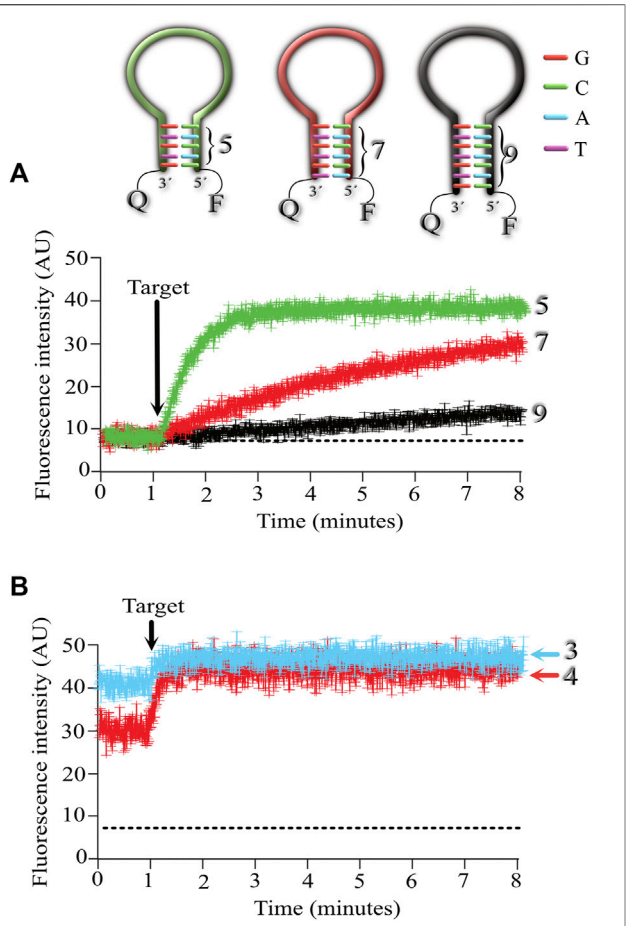

FIGURE 3 | Exploring the effect of the stem length on the association kinetics of the MB-target. Five MBs were synthesized with stem lengths of 3,4,5,7, and 9 nucleotides long. Fluorescence kinetics (Mean ± standard deviation) was measured from 6 independent microarrays, measuring the mean fluorescence from at least 6 spots for each microarray. **(A)**, kinetics of MBs with stem lengths of 5 (green), 7 (red), and 9 (black) nucleotides. **(B)**, kinetics of MBs with stem lengths of 3 and 4 nucleotides. Notice that using 3 (light blue) and 4 (red) nucleotides in the stem results in higher background fluorescence (baseline level). Arrow indicates the time of target application to the microarrays.

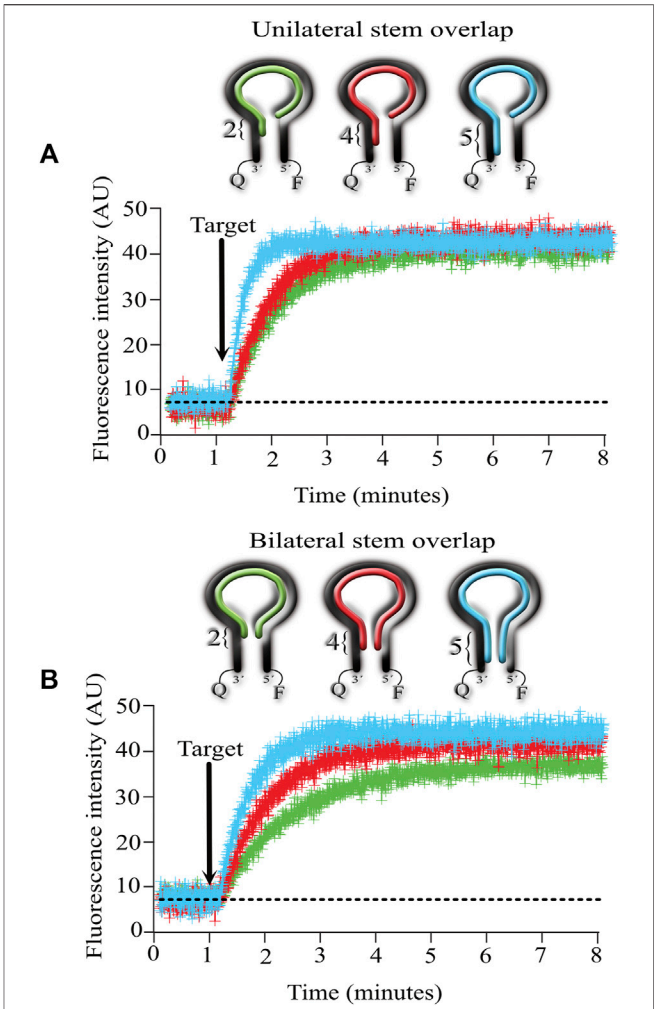

FIGURE 4 | Effect of overlapping the stem with the target complementary sequence on the kinetics of MB-targe association. **(A)**, target overlapping 2 (green), 4 (red) and 5 (light blue) nucleotides of the stem from the MB in the 3′ direction (unilateral). **(B)**, target overlapping 2 (green), 4 (red) and 5 (light blue) nucleotides of the stem from the MB in the 3′ and 5′ directions (bilateral). Values show the mean ± standard deviation from 6 independent microarrays, measuring the mean fluorescence from at least 6 spots for each microarray.

Supplementary Figure S2 (and **Supplementary Video S3**) shows that the leakage of the MBs is a very slow process that does not interfere with the fast association times of MB-target interactions.

Effect of GC Content in the Stem From the MB in the Association Constants MB-Target

To explore the effect of the GC content in the stem domain of MBs, we designed 3 MBs with different stem GC content. In all three cases, the stem length was 5 nucleotides long, and we varied the GC content from 40, 60, and 100%.

As illustrated in **Figure 2**, using a stem with 100% GC resulted in very slow association kinetics between the MB and its target (shown in fuchsia). Using the same target, we next explored the association between the MB with 60% GC content and its target (shown in red). In this case, the association kinetics were faster, with the fastest association obtained when using 40% GC in the stem (shown in blue).

Effect of the Length of the Stem From the MB in the Association Constants MB-Target

In the next series of experiments, we were interested in exploring if the length of the stem affected the association kinetics between MB and its target. For this purpose, we designed 3 MBs with stems 5, 7 and 9 nucleotides long (**Figure 3A**). Using a stem of 9 nucleotides (even when the stem contained 40% GC as in the previous experiments), the association kinetics were very slow (shown in black). Reducing the stem length to 7 nucleotides sped

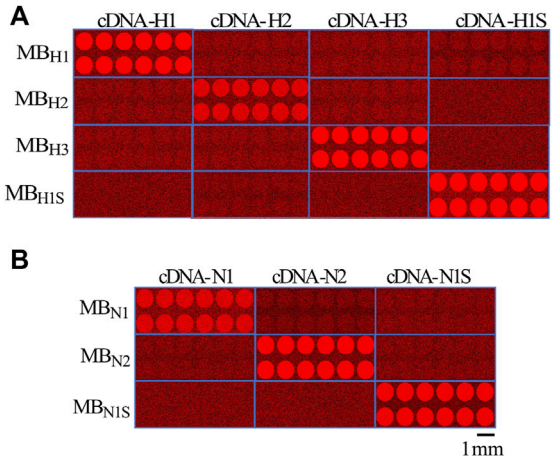

FIGURE 5 | Images from microarrays illustrating the selectivity of the MBs to identify their respective targets. **(A)**, images obtained from the microarrays illustrate the selectivity of the MBs to identify their specific target cDNA for hemagglutinin H1, H2, and H3 from human and swine H1s (each sample was printed 12 times to ensure reproducibility of the array. Microarrays were acquired separately for each gene and then combined into a single image as shown in A. **(B)**, similar procedure to the previous study in A, but in this case using the cDNA and MBs for the neuraminidase N1 and N2 from human and swine N1s. All microarray images were color mapped to red to enhance the signal to the naked eye. The spatial scale shows 1 mm.

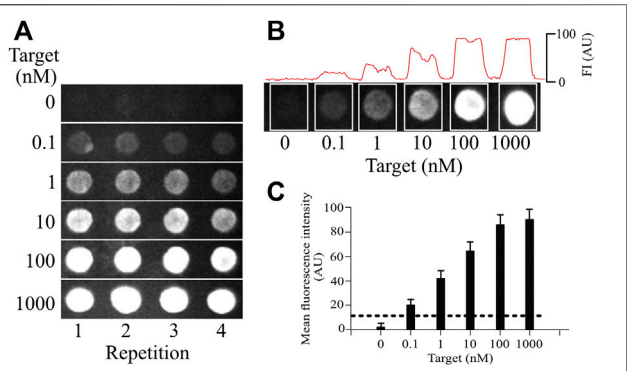

FIGURE 6 | Sensitivity of the silk-based hydrogel microarrays. **(A)**, testing different concentrations of the target to explore the sensitivity of the MB (0.1, 1, 10, 100, 1,000 nM). Each microarray row (replica) is independent. All concentrations were tested on independent microarrays (not subsequently added). **(B)**, measuring the fluorescence on each microarray spot to obtain the mean value, which was used to determine the sensitivity limit. All concentrations were tested on independent microarrays (separated by the white boxes). **(C)**, the sensitivity limit obtained from the measurements as shown in B. Each bar shows the mean ± standard deviation from at least 5 spots in the same microarray and from 6 independent microarray replicas. The dotted line shows the threshold for noise, determined as 3 standard deviations from the background signal. Above, this dotted line signal is considered different from background noise (illustrated in the 0-target concentration in A and B).

up the association kinetics between the MB and its target (shown in red), but the fastest association was obtained with MBs formed by a stem 5 nucleotides long (shown in green).

Reducing the length of the stem to 4 nucleotides resulted in increased background fluorescence in the absence of target, indicating that a portion of the MB was in the open (fluorescent) conformation (**Figure 3B**). A greater background fluorescent level was observed when using MBs with 3 nucleotide long stems (**Figure 3B**).

These results indicate that the fastest association kinetics at room temperature are obtained with MBs formed by a stem 5 nucleotides long and with a GC content of 40%. This MB configuration did not compromise the MB conformation in resting (non-florescent) conditions, which results in low background levels and reduced signal-to-noise ratios in the absence of the target.

Effect of the Overlap From the Target in the Stem From the MB in the Association Constants MB-Target

After identifying the best configuration for MBs consisting of 5 nucleotide long stems with 40% GC content, we proceeded to determine the effect of overlapping the target only in the loop region of the MB versus overlapping the loop and invading a portion of the stem.

To conduct these experiments, we designed targets that hybridize with the entire loop and with 2, 4, and 5 nucleotides from the stem on one side (unilateral, **Figure 4A**) or with the same procedure but overlapping on both sides of the stem (bilateral, **Figure 4B**).

The results obtained indicate that overlapping unilaterally or bilaterally made no difference in the association kinetics between the MB and its target. However, the number of nucleotides invading the stem did make a difference, with increasingly faster kinetics as the number of invading nucleotides augmented. Unilaterally or bilaterally, the fastest kinetics were obtained when the target complemented the entire stem sequence (5 nucleotides long, compare the blue lines in 4A and 4B).

The higher background fluorescence reported here agrees with previously published (Tsourkas et al., 2003) results indicating that MBs with stems consisting of 4 nucleotides still recognize their target but show high background fluorescence in the absence of the target.

Identifying Influenza Virus Subtypes Using MBs and Silk Microarrays

To explore the feasibility of using our MB-silk microarray technology in molecular diagnostics, we designed experiments directed at identifying cDNA sequences from different influenza virus subtypes. To design the most selective MBs for influenza we conducted in silico analysis of sequences to identify unique signatures that may serve in the design of MBs selective for each influenza virus subtype (material and methods). After all the in-silico analysis, we identified specific sequences for hemagglutinin (H1, H2 and H3) and neuraminidase (N1, N2) genes from human and two genes from swine origin (H1s and N1s). The sequences of these MBs are shown in the Material and Methods section.

Figure 5A illustrates the fluorescence changes induced after target administration for the different hemagglutinin (H1, H2,

H3 and H1s) cDNAs, and **Figure 5B** shows the results obtained for the neuraminidase (N1, N2 and N1s).

As illustrated in the figure, only the MBs designed to interact with their respective targets fluoresced upon target application. No cross-reactivity was observed between the hemagglutinin or neuraminidase MBs; they responded only to their respective targets. To demonstrate the reproducibility of the response, we printed 12 spots for each MB (**Figure 5**). The time course of the fluorescence change in the MBs is more clearly illustrated in **Supplementary Video S4**. The video also shows the selectivity of the MBs for their specific target. When the cDNA for N1 is applied, the MBs do not fluoresce since they are designed for N2. Only when N2 is applied the respective MB emit fluorescence (approximately halfway through the video sequence).

Sensitivity and Selectivity of the MBs in the Identification of Influenza Virus Subtypes

To determine the sensitivity of our microarray method, we conducted experiments aimed at identifying the smallest amount of sample that our MBs can detect (**Figure 6**).

Maintaining a constant concentration of 1 μM MB in the tridimensional silk microarray, we varied the concentration of the cDNA for the different genes of influenza. As illustrated in **Figure 6**, the minimum amount of cDNA detected under these conditions was 0.1 nM (100 p.m.). The dotted line shows 3 times the standard deviation from noise as a threshold to separate positive signals from the background. Similar values were obtained for all influenza genes explored, indicating that the sensitivity of the method was not dependent on the target to be identified but rather a property of the MB concentration and the optical properties of our silk microarray. The sensitivity of our system is higher than what has been reported for conventional microarray technology, with our microarray technology showing at least 5 times greater sensitivity (Thissen et al., 2014).

DISCUSSION

Even though many molecular tools are used daily in laboratories for research purposes, only a handful have made their way into the diagnostics area. There are many reasons why most molecular tools have not made it to clinical practice (North et al., 2010). Some of the reasons include: the complexity of the equipment used with these molecular tools, the need for a specialized technician to operate such equipment, the difficulty of analyzing the results obtained and transforming them into a diagnostic, the lack of portability of the equipment, the difficulty of standardizing the method for diagnostic procedures, the complexity of sample preparation, the need for expensive reagents, etc. (Giljohann and Mirkin, 2009).

Molecular beacons (MB) have been extensively used in research but also in molecular diagnostics in combination with real-time PCR (Abravaya et al., 2003; Broude, 2002; Fang et al., 2000; Kim et al., 2008). In fact, real-time PCR has become the gold standard for diagnostics of infectious diseases (the best example is the current coronavirus pandemic) (Floriano et al., 2020).

Some studies have reported the use of MB in reagentless experimental diagnostics (Beaucage, 2001; Brown et al., 2000). In these studies, the MBs are immobilized directly onto the glass surface of the microarray slide. Unfortunately, this procedure results in reduced fluorescence and high background levels (Teng and Libera, 2018). To prevent the quenching of the MBs by the glass surface, recently a novel method has been implemented in which the MBs are immobilized in microgels produced from polyethylene glycol (PEG) (Teng and Libera, 2018). These microgels not only localize the probes to specific surface positions but also maintain them in a waterlike environment (Teng and Libera, 2018). The microspheres used also exhibit a lensing behavior, resulting in the enhancement of the fluorescence emitted by the MBs.

In the present study, the 3D printed silk hydrogel microarray spots produce a similar lensing behavior. A geometrical lensing effect occurs in curved surfaces arising from the nature of parallel lines in spherical and hyperbolic space (Schönhöfer and Glotzer, 2022). This effect is further enhanced by the fact that the refractive index of water and silk are almost identical, and thus the entire hydrogel behaves as a homogenous material.

In the present study, we report a novel method to produce MB-based microarrays using silk hydrogel for encapsulation. This method also produces a friendly biomolecular waterlike environment. Because silk's refractive index is similar to that of water (1.3), we have observed a strong lensing behavior with light propagating properties which enhances the fluorescence emitted by the MBs upon target hybridization. The refractive index of PEG is slightly higher (1.4) than that of water (1.33) or silk (1.34). The similar refractive indexes of silk and PEG may explain the microlens effect and fluorescence enhancement observed in our study.

The use of shallow angle illumination reduces the excitation of the bulk solution and separates the excitation and emission pathways, reducing stray light and channel crossed talk, as we have previously reported (Asanov et al., 2012).

By studying the properties (length and GC content) of the stem of MBs, we were able to identify the best combination that favors association of the MB-target at room temperature. Our studies indicate that 5 nucleotides long is the minimum length to prevent background fluorescence from the MB in the absence of a target. 40% GC content in the stem is critical to accelerate the association kinetics of the MB-target complex at room temperature. Higher GC content resulted in slower association kinetics, which is not desirable for rapid point-of-care diagnostics.

This configuration of the stem length and GC content in the MB did not alter its selectivity for the specific target, as we have shown here.

Even though our microarray technology is not as sensitive as that from realtime PCR, the use of silk hydrogel in tridimensional microarrays provided higher sensitivity than previously reported obtained with conventional microarrays (Thissen et al., 2014).

One of the main disadvantage of using hydrogels is that they cannot be stored for long periods of time because they tend to

dehydrate and shrink. We have observed hydrogel dehydration and shrinkage within the first 48 h of storage at room temperature (once printed on the coverslip). Hydrogel dehydration can be prevented by keeping the microarray slides at 4°C until used.

In previous studies using MBs in hydrogels, the MBs have been immobilized in the hydrogel by chemical reactions to prevent diffusion (Teng and Libera, 2018). We have used the MBs without chemical immobilization and found that MB leakage outside the hydrogel is negligible as long as the printed microarray is maintained in a humidity-controlled environment but not immersed in water (**Supplementary Figure S2** and **Supplementary Video S3**). Target application in a water solution facilitates MB diffusion outside the hydrogel, but this phenomenon is very slow and takes several hours while the signal produced by the association MB-target takes place within minutes of target application (**Supplementary Figure S2** and **Supplementary Video S3**).

Although in the present study we used a conventional fluorescence microscope coupled to our shallow angle illumination device to capture the fluorescence emitted by the MBs in the microarray, simpler portable detectors can be easily implemented using inexpensive cMOS cameras and LEDs in combination with adequate excitation and emission filters.

DATA AVAILABILITY STATEMENT

The datasets presented in this study can be found in online repositories. The names of the repository/repositories and accession number(s) can be found at: http://www.ncbi.nlm.nih.gov/genomes/FLU/FLU.html.

AUTHOR CONTRIBUTIONS

AS, RM-C, and AA conducted experiments and prepared silk and MBs. AA and LV designed the experiments and coordinated the study. All authors contributed to the writing of this manuscript and preparation of figures.

FUNDING

This work was supported partially by grant IV200320 from Direccion General de Asuntos del Personal Academico (DGAPA) to LV. RM-C was a recipient of a scholarship from Consejo Nacional de Ciencia y Tecnologia (Conacyt).

SUPPLEMENTARY MATERIAL

The Supplementary Material for this article can be found online at: https://www.frontiersin.org/articles/10.3389/fbioe.2022.881679/full#supplementary-material

Supplementary Figure S1 | Tridimensional characterization of the geometry of silk hydrogel droplets. The molecular beacon for H1 (MB_{H1}) was synthesized without the 5′ end quencher (Material and Methods), to have a MB that emits fluorescence continuously (without the target present). Silk was prepared with this MB and droplets were printed using the microarrayer (Material and Methods). Confocal microscopy studies were conducted with the microarrays printed with this MB. Optical slices were obtained every 200 nm, and 3D images of the microarray spots (droplets) were rendered using Imaris 8.1 (Oxford Instruments). The height of the droplets is color coded to indicate the different heights of each microarray spot. Panel A shows the droplets visualized from one side. Panel B after rotating the horizontal plane 90 degrees and panel C after rotating the vertical panel 90 degrees to obtain a top view. The scale in C shows 1 millimeter (1 mm).

Supplementary Figure S2 | Leakage of the MBs from the hydrogel is a very slow process. **(A)**, examples of microarrays printed with the silk hydrogel prepared with the molecular beacon for H1 (MB_{H1}) synthesized without the 5′end quencher (Material and Methods). Notice the very small reduction in fluorescence over time that after 20 minutes amounts to a reduction in fluorescence intensity of less than 1% of the initial fluorescence values (see also **Supplementary Video S3**). **(B)** Mean ± standard deviations of the fluorescence intensity obtained from at least 8 microarray spots from 4 independent experiments. In red are shown the values for the MB leakage experiment and in green the values for a typical MB_{H1}/cDNA-H1 reaction (shown inside the gray rectangle). Notice that the leakage of the MB_{H1} is negligible during this 7-minute time window. The black dotted line shows the baseline fluorescence, and the blue dotted line shows the initial mean fluorescence value of the MB_{H1} without the quencher to highlight more clearly the amount of MB leakage during the time course of the experiment (24 min).

Supplementary Video S1 | Video illustrating the use of the procedure plot profile from ImageJ, utilized to calculate the mean fluorescence for each microarray spot. All spots were measured individually and later compounded into the mean ± standard deviation from 6 independent microarray replicas.

Supplementary Video S2 | Video illustrating the reproducibility of the microarray using multiple replicas of the same MB. The spatial scale (white line) shows 1 mm, and the time scale is in minutes. A red arrow indicates the time of target application. Notice that all 9 replicas respond to the target application with similar time courses.

Supplementary Video S3 | Time course of the leakage of MB from the silk hydrogel. A molecular beacon synthesized without the quencher was used to illustrate MB leakage from the hydrogel. Since the quencher is not present, the MB emits florescence continuously. Notice that after 25 minutes, the fluorescence inside the hydrogel remains almost intact, reflecting limited leakage of the MB. Notice that most reactions to MB-target conclude within 9 minutes after target application (video 2).

Supplementary Video S4 | The video shows 3 replicas for each of the two MBs printed, one designed to detect hemagglutinin (H1) and neuraminidase (N2). Notice that upon application of the cDNA for H1 (cDNA-H1), only the replicas containing the MB (H1) respond to the stimulus. Later in the video, the cDNA for N1 (cDNA-N1) is applied, but since the microarray contained no MB for this cDNA, no response was obtained. At the end of the video, the cDNA for N2 (cDNA-N2) is applied, to the microarray and the replicas containing the MB (N2) printed response to this application. This video illustrates the selectivity of the MBs designed for each specific target.

REFERENCES

Abravaya, K., Huff, J., Marshall, R., Merchant, B., Mullen, C., Schneider, G., et al. (2003). Molecular Beacons as Diagnostic Tools: Technology and Applications. *Clin. Chem. Lab. Med.* 41, 468–474. doi:10.1515/CCLM.2003.070

Asanov, A., Zepeda, A., and Vaca, L. (2010). A Novel Form of Total Internal Reflection Fluorescence Microscopy (LG-TIRFM) Reveals Different and Independent Lipid Raft Domains in Living Cells. *Biochimica Biophysica Acta (BBA) – Mol. Cell Biol. Lipids* 1801, 147–155. doi:10.1016/j.bbalip.2009.10.004

Asanov, A., Zepeda, A., and Vaca, L. (2012). A Platform for Combined DNA and Protein Microarrays Based on Total Internal Reflection Fluorescence. *Sensors* 12, 1800–1815. doi:10.3390/s120201800

Beaucage, S. (2001). Strategies in the Preparation of DNA Oligonucleotide Arrays for Diagnostic Applications. *Cmc* 8, 1213–1244. doi:10.2174/0929867013372463

Bonnet, G., Tyagi, S., Libchaber, A., and Kramer, F. R. (1999). Thermodynamic Basis of the Enhanced Specificity of Structured DNA Probes. *Proc. Natl. Acad. Sci. U.S.A.* 96, 6171–6176. doi:10.1073/pnas.96.11.6171

Broude, N. E. (2002). Stem-loop Oligonucleotides: a Robust Tool for Molecular Biology and Biotechnology. *Trends Biotechnol.* 20, 249–256. doi:10.1016/s0167-7799(02)01942-x

Brown, L. J., Brown, T., Cummins, J., and Hamilton, A. (2000). Molecular Beacons Attached to Glass Beads Fluoresce upon Hybridisation to Target DNA. *Chem. Commun.*, 621–622. doi:10.1039/b000389l

Chidchob, P., and Sleiman, H. F. (2018). Recent Advances in DNA Nanotechnology. *Curr. Opin. Chem. Biol.* 46, 63–70. doi:10.1016/j.cbpa.2018.04.012

Durai, D. A., and Schulz, M. H. (2019). Improving In-Silico Normalization Using Read Weights. *Sci. Rep.* 9, 5133. doi:10.1038/s41598-019-41502-9

Erlich, H. A., Gelfand, D., and Sninsky, J. J. (1991). Recent Advances in the Polymerase Chain Reaction. *Science* 252, 1643–1651. doi:10.1126/science.2047872

Fang, X., Li, J. J., Perlette, J., Tan, W., and Wang, K. (2000). Peer Reviewed: Molecular Beacons: Novel Fluorescent Probes. *Anal. Chem.* 72, A–753. doi:10.1021/ac003001i

Ferreira, C., Guerra, J., Slhessarenko, N., Scartezini, M., Franca, C., Colombini, M., et al. (2018). Point-of-Care Testing: General Aspects. *Clin. Lab.* 64, 1–9. doi:10.7754/Clin.Lab.2017.170730

Floriano, I., Silvinato, A., Bernardo, W. M., Reis, J. C., and Soledade, G. (2020). Accuracy of the Polymerase Chain Reaction (PCR) Test in the Diagnosis of Acute Respiratory Syndrome Due to Coronavirus: a Systematic Review and Meta-Analysis. *Rev. Assoc. Med. Bras.* 66, 880–888. doi:10.1590/1806-9282.66.7.880

Gauglitz, G. (2014). Point-of-care Platforms. *Annu. Rev. Anal. Chem.* 7, 297–315. doi:10.1146/annurev-anchem-071213-020332

Gershon, D. (2002). An Array of Opportunities. *Nature* 416, 887–889. doi:10.1038/416885a

Giljohann, D. A., and Mirkin, C. A. (2009). Drivers of Biodiagnostic Development. *Nature* 462, 461–464. doi:10.1038/nature08605

Goble, J. A., and Rocafort, P. T. (2017). Point-of-Care Testing. *J. Pharm. Pract.* 30, 229–237. doi:10.1177/0897190015587696

Grau-Roma, L., Fraile, L., and Segalés, J. (2011). Recent Advances in the Epidemiology, Diagnosis and Control of Diseases Caused by Porcine Circovirus Type 2. *Veterinary J.* 187, 23–32. doi:10.1016/j.tvjl.2010.01.018

Helmer, M. (2010). Dew Catchers. *Nature* 463, 618. doi:10.1038/463618a

Kim, D. W. (2001). Real Time Quantitative PCR. *Exp. Mol. Med.* 33, 101–109. doi:10.1038/emm.2001.16

Kim, Y., Sohn, D., and Tan, W. (2008). Molecular Beacons in Biomedical Detection and Clinical Diagnosis. *Int. J. Clin. Exp. Pathol.* 1, 105–116. doi:10.3342/ceo.2008.1.1.10

Lee, H. (2010). Intelligent Glue. *Nature* 465, 298–299. doi:10.1038/465298a

Monroy-Contreras, R., and Vaca, L. (2011). Molecular Beacons: Powerful Tools for Imaging RNA in Living Cells. *J. Nucleic Acids* 2011, 1–15. doi:10.4061/2011/741723

Numata, K., and Kaplan, D. L. (2010). Silk-based Delivery Systems of Bioactive Molecules. *Adv. Drug Deliv. Rev.* 62, 1497–1508. doi:10.1016/j.addr.2010.03.009

Numata, K., Yamazaki, S., Katashima, T., Chuah, J. A., Naga, N., and Sakai, T. (2014). Silk-Pectin Hydrogel with Superior Mechanical Properties, Biodegradability, and Biocompatibility. *Macromol. Biosci.* 14, 799–806. doi:10.1002/mabi.201300482

Plomin, R., and Schalkwyk, L. C. (2007). Microarrays. *Dev. Sci.* 10, 19–23. doi:10.1111/j.1467-7687.2007.00558.x

Schönhöfer, P. W. A., and Glotzer, S. C. (2022). Curvature-Controlled Geometrical Lensing Behavior in Self-Propelled Colloidal Particle Systems. *Soft Condens. Matter*. Available at: http://arxiv.org/abs/2202.09713 (Accessed 20Feb2022.

Sutherland, T. D., Young, J. H., Weisman, S., Hayashi, C. Y., and Merritt, D. J. (2010). Insect Silk: One Name, Many Materials. *Annu. Rev. Entomol.* 55, 171–188. doi:10.1146/annurev-ento-112408-085401

Teng, F., and Libera, M. (2018). Microlens Enhancement of Surface-Tethered Molecular Beacons. *Langmuir* 34, 14969–14974. doi:10.1021/acs.langmuir.8b02204

Thissen, J. B., McLoughlin, K., Gardner, S., Gu, P., Mabery, S., Slezak, T., et al. (2014). Analysis of Sensitivity and Rapid Hybridization of a Multiplexed Microbial Detection Microarray. *J. Virological Methods* 201, 73–78. doi:10.1016/j.jviromet.2014.01.024

Tong, Y., Lemieux, B., and Kong, H. (2011). Multiple Strategies to Improve Sensitivity, Speed and Robustness of Isothermal Nucleic Acid Amplification for Rapid Pathogen Detection. *BMC Biotechnol.* 11, 50. doi:10.1186/1472-6750-11-50

Tsourkas, A., Behlke, M. A., Rose, S. D., and Bao, G. (2003). Hybridization Kinetics and Thermodynamics of Molecular Beacons. *Nucleic Acids Res.* 31, 1319–1330. doi:10.1093/nar/gkg212

Tyagi, S., and Kramer, F. R. (1996). Molecular Beacons: Probes that Fluoresce upon Hybridization. *Nat. Biotechnol.* 14, 303–308. doi:10.1038/nbt0396-303

Uddayasankar, U., and Krull, U. J. (2013). Analytical Performance of Molecular Beacons on Surface Immobilized Gold Nanoparticles of Varying Size and Density. *Anal. Chim. Acta* 803, 113–122. doi:10.1016/j.aca.2013.07.059

Vaca, L. (2014). Point-of-care Diagnostic Tools to Detect Circulating MicroRNAS as Biomarkers of Disease. *Sensors* 14, 9117–9131. doi:10.3390/s140509117

Valasek, M. A., and Repa, J. J. (2005). The Power of Real-Time PCR. *Adv. Physiology Educ.* 29, 151–159. doi:10.1152/advan.00019.2005

Vepari, C., and Kaplan, D. L. (2007). Silk as a Biomaterial. *Prog. Polym. Sci.* 32, 991–1007. doi:10.1016/j.progpolymsci.2007.05.013

William G. North, W., Gao, G., Jensen, A., Memoli, V. A., and Du, J. (2010). NMDA Receptors Are Expressed by Small-Cell Lung Cancer and Are Potential Targets for Effective Treatment. *Cpaa* 2, 31–40. doi:10.2147/cpaa.s6262

Conflict of Interest: AA is the CEO of TIRF Labs. The TIRF microarrayer belongs to TIRF Labs.

The remaining authors declare that the research was conducted in the absence of any commercial or financial relationships that could be construed as a potential conflict of interest.

The reviewer RC declared a shared affiliation with the authors AS, RM-C, LV to the handling editor at the time of review.

Publisher's Note: All claims expressed in this article are solely those of the authors and do not necessarily represent those of their affiliated organizations, or those of the publisher, the editors, and the reviewers. Any product that may be evaluated in this article, or claim that may be made by its manufacturer, is not guaranteed or endorsed by the publisher.

frontiers | Frontiers in Bioengineering and Biotechnology

TYPE Original Research
PUBLISHED 15 September 2022
DOI 10.3389/fbioe.2022.1000950

OPEN ACCESS

EDITED BY
Kawsar Ahmed,
Mawlana Bhashani Science and Technology University, Bangladesh

REVIEWED BY
Md Bellal Hossain,
The University of Sydney, Australia
Shobhit K. Patel,
Marwadi University, India
Shaymaa Tahhan,
Shaymaa Riyadh Tahhan, Iraq

*CORRESPONDENCE
Li Liu,
liliu@cuhk.edu.hk
Siyu Liu,
syliu@njust.edu.cn

†These authors have contributed equally to this work

SPECIALTY SECTION
This article was submitted to Biosensors and Biomolecular Electronics, a section of the journal Frontiers in Bioengineering and Biotechnology

RECEIVED 22 July 2022
ACCEPTED 15 August 2022
PUBLISHED 15 September 2022

CITATION
Liu L, Zhao Y, Li A, Yu X, Xiao X, Liu S and Meng MQ-H (2022), A photoacoustics-enhanced drilling probe for radiation-free pedicle screw implantation in spinal surgery.
Front. Bioeng. Biotechnol. 10:1000950.
doi: 10.3389/fbioe.2022.1000950

A photoacoustics-enhanced drilling probe for radiation-free pedicle screw implantation in spinal surgery

Li Liu[1*†], Yongjian Zhao[1†], Ang Li[1], Xianghu Yu[2], Xiao Xiao[2], Siyu Liu[3*] and Max Q.-H. Meng[1,2]

[1]Department of Electronic Engineering, The Chinese University of Hong Kong, Hong Kong SAR, China, [2]Department of Electronic and Electrical Engineering, Southern University of Science and Technology, Shenzhen, China, [3]School of Science, Nanjing University of Science and Technology, Nanjing, China

This article proposes a novel intra-operative navigation and sensing system that optimizes the functional accuracy of spinal pedicle screw implantation. It does so by incorporating radiation-free and multi-scale macroscopic 3D ultrasound (US) imaging and local tissue-awareness from *in situ* photoacoustic (PA) sensing at a clinically relevant mesoscopic scale. More specifically, 3D US imaging is employed for online status updates of spinal segment posture to determine the appropriate entry point and coarse drilling path once non-negligible or relative patient motion occurs between inter-vertebral segments in the intra-operative phase. Furthermore, a sophisticated sensor-enhanced drilling probe has been developed to facilitate fine-grained local navigation that integrates a PA endoscopic imaging component for *in situ* tissue sensing. The PA signals from a sideways direction to differentiate cancellous bone from harder cortical bone, or to indicate weakened osteoporotic bone within the vertebrae. In so doing it prevents cortical breaches, strengthens implant stability, and mitigates iatrogenic injuries of the neighboring artery and nerves. To optimize this PA-enhanced endoscopic probe design, the light absorption spectrum of cortical bone and cancellous bone are measured *in vitro*, and the associated PA signals are characterized. Ultimately, a pilot study is performed on an *ex vivo* bovine spine to validate our developed multi-scale navigation and sensing system. The experimental results demonstrate the clinical feasibility, and hence the great potential, for functionally accurate screw implantation in complex spinal stabilization interventions.

KEYWORDS

multi-scale navigation and sensing, ultrasound-based surgical navigation, photoacoustic endoscopy, robotic-assisted spinal surgery, cancellous bone characterization, *in situ* tissue sensing, pedicle screw implantation

Introduction

The population is aging rapidly worldwide. Alongside population aging, the incidence of spinal degenerative pathologies (e.g., herniated discs, narrow lumbar canals) and/or vertebral osteoporotic fractures has been increasing, imposing a high socio-economic burden on eldercare and healthcare systems (Compston et al., 2019; Wang et al., 2020). Once such spine-related diseases occur, the vertebrae may no longer function properly, and, if unattended, become harmful to the surrounding nerves and tissues(Chapman, 2019). It is commonly recognized that spinal fusion surgery, which involves pedicle screw implantation to stabilize the spine, is effective in the recovery of spinal function (Germon and Hobart, 2015). During the procedure, the screws need to pierce the pedicles of the vertebrae and enter the vertebral body. Afterward, the implanted screws are attached to rods that stabilize the affected segments. Such surgery is highly challenging and technically demanding (Maria et al., 2020). First, the pedicle region is so small (around a few millimeters), it is extremely difficult to determine an accurate and safe trajectory for the drilling hole. Since the volume of the pedicle screw is relative to that of the pedicle, the margin of error needs to be within one millimeter to prevent screw misplacement or further cortical wall perforation (Lopera et al., 2010). Moreover, the lack of real-time feedback in the intra-operative phase means the success of pedicle screw implantation largely depends on subjective experience of the surgeon. To summarize, the proximity of vital neural and vascular structures, the added variability of patients, and the region-dependent morphology of the vertebrae, all contribute significantly to the difficulties with accurate screw implantation (Lonstein et al., 1999; Yamada et al., 2022). Several advanced surgical aids have previously been introduced to mitigate the associated complications and to improve accuracy. These are generally divided into two categories: global spatial navigation and local tissue sensing techniques.

The global spatial navigation technique mainly involves computer or robotics-assisted spinal surgery, navigated by macroscopic imaging modalities (Helm et al., 2015; Ahern et al., 2020). Since spinal navigation systems allow for either intra-operative imaging or pre-operative imaging with intra-operative updates, conventional navigation paradigms include intra-operative 2D fluoroscopic navigation (Foley et al., 2001), pre-operative CT with manual intra-operative registration (Nottmeier and Crosby, 2007), pre-operative CT with fluoroscopic registration and update, and intra-operative CT or CBCT (Tian et al., 2011; Dea et al., 2016; Cool et al., 2021; Zhang et al., 2021; Felix et al., 2022; Tabarestani et al., 2022). Common to these solutions is their association with X-ray-like imaging (fluoroscopy or CT-based navigation solutions featuring ionizing radiation), which can harm both patient and surgeon (Hecht et al., 2018; Ahern et al., 2020).

The other category of intelligent surgical aids is associated with local tissue sensing, also referred to as sensor-enhanced surgical instruments, that identify different tissue types and possess an integrated warning component. Intensive studies have been conducted into local tissue sensing instruments for spine-related surgeries. Li et al. (2022) proposed a surgical status perception method using an installed acceleration sensor and force sensor in robot-assisted spine surgery that mimics the surgeon's tactile sensing. Experiments have proved that the fusion of two tactile signals can significantly improve status recognition accuracy. Electromyography is another option, although not widely adopted due to its lower sensitivity (Duffy et al., 2010). Furthermore, other professionals are required to interpret these signals, for the technology fails to predict an impending cortical bone breach in advance. To date, the only commercially available product, the so-called Pedi-Guard probe instrument, is based on electrical conductivity measurement to indicate proximity to the cortical wall of the vertebra (Ovadia et al., 2011). It can distinguish different tissues by comparing electrical conductivity. However, it lacks directional information about the sensed signals (Bolger et al., 2007). In other words, when the instrument tip is close, but parallel to the cortical wall, the sensing technique issues a warning. Yet even if it correctly detects an impending cortical breach, the surgeon still has no idea in which direction the breach is about to occur, because the electrical conductivity measurement occurs in all directions simultaneously. This means that when the instrument issues a warning, the surgeon must make the next attempt without any directional input.

Endoscopic ultrasound (EUS) also holds the potential for *in situ* tissue sensing and characterization (Mujagic et al., 2008; Manbachi et al., 2014). However, experimental results have proven unreliable due to the high acoustic impedance to the US from the bone (Aly et al., 2011). For superior image quality and tissue composition imaging characteristics, photoacoustic imaging (PAI) has been introduced as an alternative (Steinberg et al., 2019; Gonzalez et al., 2021). First discovered in 1880 by Bell, the PA effect has developed as an emerging medical imaging modality, and is widely adopted in various fields (Zhou et al., 2014). The principle of PAI is as follows: once the tissue is exposed to pulsed laser beams, it absorbs the energy and converts it into heat. Simultaneously, its temperature increases locally and thermal expansion occurs (Xu and Wang, 2006). Such expansion enables the tissue to emit ultrasonic waves, which are detected by an ultrasound transducer for subsequent image reconstruction and visualization (Kruizinga et al., 2014). PAI combines the merits of both optical and ultrasound imaging, yielding high-quality images with high resolution and contrast (Xu and Wang, 2006). Furthermore, it is radiation-free, and capable of both morphological and functional imaging. It thus holds huge

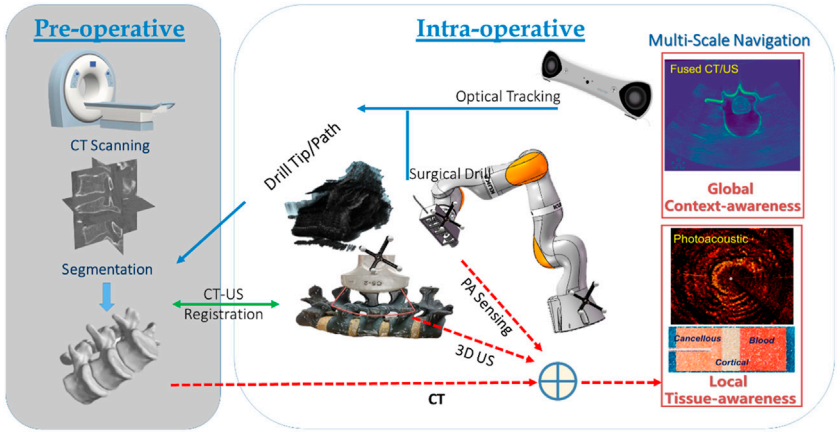

FIGURE 1
Multi-scale surgical navigation and sensing paradigm based on radiation-free intra-operative US/PA imaging.

potential for clinical translation (Beard, 2011). According to differences in excitation source and image reconstruction techniques, PAI can be categorized into different types. One of these is photoacoustic tomography (PAT), which exploits an unfocused beam for imaging (Sangha and Goergen, 2016). In general, there are several transducers, and the collected information is transferred to the computer for image reconstruction. Another type is photoacoustic microscopy (PAM), which employs a focused laser and transducer without needing a complex reconstruction algorithm (Yao and Wang, 2013). Unlike PAT, PAM has the advantage of imaging precise tissue samples and cells. The last type is photoacoustic endoscopy (PAE), a modality usually applied in invasive operations, which has a high standard in relation to the size of the probe (Joon-Mo Yang et al., 2009; Guo et al., 2020). In sum, PAI can generate images of high quality across a broad range of applications and holds huge potential in tissue sensing and characterization (Zhao et al., 2019). More recently, Gonzalez et al. (2021)developed a combined US and PAT guidance system aimed at avoiding the pedicle screw misplacement and accidental bone breaches that can lead to nerve damage. Pedicle cannulation was conducted on a human cadaver, with co-registered PAT and US images acquired at various time points during the procedure. However, the US/PAT guidance system only focuses on macroscopic anatomical navigation, without taking fine-grained local tissue characterization into consideration. To the best of our knowledge, local bone tissue sensing inside the vertebrae, based on a PAE-enhanced surgical instrument for guiding pedicle screw implantation, has not previously been studied.

In this article, we propose for the first time, a multi-scale surgical navigation and sensing system for pedicle screw insertion based on radiation-free dual-mode US/PA. More specifically, a macroscopic US imaging system achieves contextual awareness for global guidance of the drilling entry and coarse insertion path, while a mesoscopic PAE-enhanced smart probe instrument offers *in situ* tissue characterization for fine path optimization of screw insertion. Hence, in combination with US image guidance, such PAE sensing is exploited to monitor and even warn of cortical bone breaches inside the vertebrae, thereby optimizing screw implantation in complex spine-related surgeries.

Materials and methods

Radiation-free, multi-scale navigation and sensing systems for pedicle screw implantation optimization

The overall system configuration of the multi-scale surgical navigation and sensing paradigm, based on radiation-free intra-operative US/PA imaging, is presented in Figure 1:

The combination of global context-awareness via pre-operative CT and intra-operative US, along with local tissue-awareness via *in situ* PA sensing at a clinically relevant mesoscopic scale can enhance comprehensive perception for complication-free guidance of bone drill and pedicle screws through vertebrae. Specifically, a CT scan is performed and subsequently segmented to produce a 3D model of the bony surface of the spine. Once non-negligible patient movement occurs during the operation, the tracked US probe is scanned to obtain a series of 2D US images, yielding 3D volumetric data of the affected vertebral segments. In the registration phase, US-CT registration is conducted via automatic bony surface

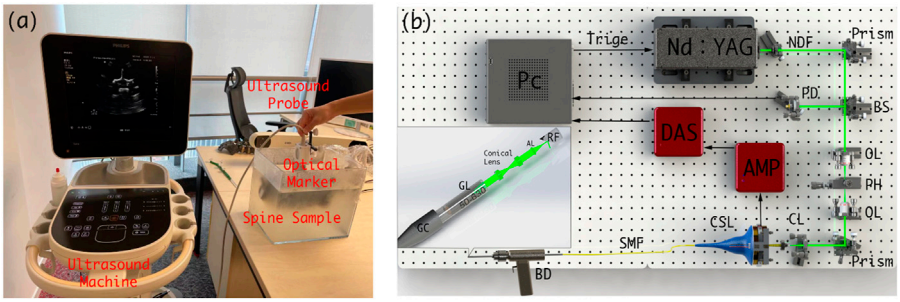

FIGURE 2
(A) Schematic diagram of the intra-operative US navigation system. **(B)** Schematic diagram of drilling probe. PC: personal computer, NDF: Neutral Density Filter, PD: Photodiode, BS: beam split, OL: object lens, PH: pin hole, CL: collimator, CSL: conductive slip, SMF: single model fiber, BD: bone drill, GC: grin collimator, GL: Grin Lens, AL: aspherical lens, RF: reflector.

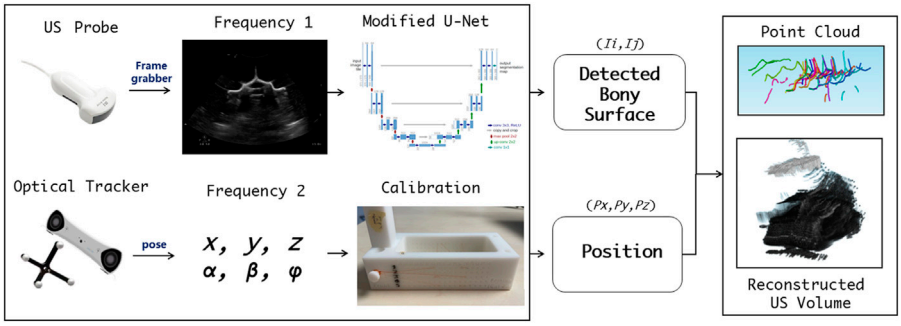

FIGURE 3
Workflow for acquisition, calibration, segmentation, compounding, and visualization of the US volume.

detection in US images, followed by Iterative Closest Point (ICP)-based point cloud registration. Afterward, the data on the drill bit, and the updated insertion path—due to any spinal segment posture variation—can be overlaid on a fused CT/US volume. Thus, with the position tracking data of the drill, the multi-scale navigation and sensing system allows for both context-aware global navigation and tissue-aware local sensing in complex spinal surgeries: 1) *Context-aware global navigation* visualizes the drill bit and insertion path from the fused CT model/US volume of the affected spine in real time. Thereafter, navigation of the drill and screw implantation, associated with an online updated insertion path, is effected based on the posture tracking data and the related US-CT registration result. 2) An embedded PAE probe inside the surgical drill is simultaneously employed for *in situ* identification of the tissue types aside of the drill bit (e.g., cortical and cancellous bones, and critical vascular/neurological structures) for optimizing fine orientation of the drilling probe in *tissue-aware local sensing*. Hence, the comprehensive fused perception serves as a multi-scale navigation and sensing paradigm enabling accurate screw implantation in complex spine-stabilization interventions.

Macroscopic 3D ultrasound-guided global contextual navigation

3D US imaging system setup

Prior to spinal surgery, a patient usually receives routine CT scanning for pre-operative examination and diagnosis. Afterward, challenging manipulations, such as pedicle screw implantations, are executed with the assistance of image-based surgical navigation in the intra-operative phase. Relative motion and deformation between the inter-vertebral segments can occur due to interactive force between the drill and the affected vertebrae. Therefore, to achieve on-the-fly status updates during the operation, a 3D US imaging system is established for continuous monitoring of the spinal segment being operated upon. Figure 2A and Figure 3 demonstrate the acquisition, calibration, segmentation, compounding, and visualization of

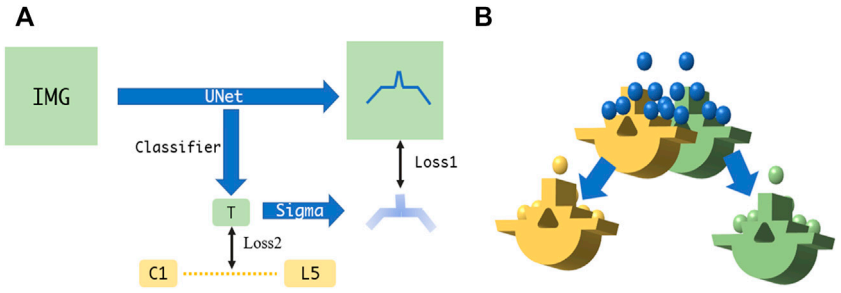

FIGURE 4
(A) Augmented U-Net using two losses for accurate bone surface detection. **(B)** Fine point cloud registration between US and CT.

the US volume. Afterward, such reconstructed US volume can be used intra-operatively in conjunction with the spinal bone surface model segmented from the pre-operative CT, together providing a global contextual perception for accurate pedicle screw implantation.

Pre-operative CT registration with intra-operative 3D US

To achieve co-registration between the reconstructed US volume and the bone surface model segmented from CT, two consecutive tasks are performed, i.e., bone surface detection of US images, followed by hierarchical coarse-fine point cloud registration.

Due to the physical nature of spinal sonography for osseous tissue imaging, only bone surface can be visualized on US images, which are highly sparse, thus making it difficult to learn via a conventional U-Net. In this study, we apply the U-Net with several modifications, i.e., employing two loss functions to ensure that the augmented U-Net is well trained (Ibtehaz and Rahman, 2020). The first loss utilizes the distance field of the bone surface as a learned target, where a heatmap-like learned target is generated via Gaussian convolution. As the learning loss reduces, the sigma of the heatmap becomes smaller to enable more accurate bone surface detection. The second loss is to estimate which level of the spine the processed US images belong to, so that the sigma of the aforementioned heatmap can be adjusted (see Figure 4A).

The overall point cloud registration is achieved in a hierarchical coarse-to-fine alignment. The coarse registration step extracts the center of the mass, plus the orientation from the bone surface point clouds detected from the US volume, such that both point clouds between the US and the CT possess the same orientation. This step is performed by decomposing both point clouds via principal component analysis (PCA) and aligning their corresponding principal axes accordingly (Jolliffe and Cadima, 2016). The subsequent fine registration step aligns the specified spine level between the CT vertebrae model and the associated US point clouds. Specifically, the US point clouds near the target spine level are automatically selected for ICP registration (Shi et al., 2006). This step selects and removes neighboring points in an iterative manner, where the criterion is to execute registration for a specified spine level based on the point clouds obtained through different radius configurations, and to eventually select the radius with the smaller MSE loss. After several radius selections, the filtered US point clouds are registered to the corresponding CT spine level model (see Figure 4B).

Mesoscopic photoacoustic-enhanced drilling probe for local tissue sensing

Cancellous bone absorption spectrum

In general, during the procedure, the surgical drill is delivered through the muscle and then reaches the outer border of the cortical bone of the lamina. It subsequently further penetrates the cancellous bone of the vertebra through an appropriate entry point on the cortical bone. As the drill advances into the vertebral body, the associated position of the drill within the vertebra provides critical information feedback for achieving the ultimate functional outcome without post-operative complications (Weiss et al., 2010). Since the pedicle structure of the vertebra is highly restricted (a minimum of approximately 3.5 mm), a safe distance between the drill bit and cortical walls (1.44 mm) must be ensured, requiring accurate differentiation between cortical and cancellous bone (An and Benoit, 1998). To this end, the optical absorption characteristics of cortical and cancellous bone should be investigated to select an appropriate laser wavelength for signal excitation. To this end, the spinal model of a bovine sacrificed less than an hour prior was prepared to expose its cancellous bone, and a tweezer was then used to carefully separate the cancellous bone from the cortical bone. The cancellous bone of approximate 2 g was first utilized for rough grinding and placed in the integrating-sphere of the testing machine. The UV spectrophotometer (UV-2600, Shimadzu [Shanghai] Global Laboratory Consumables Co., Ltd.) can

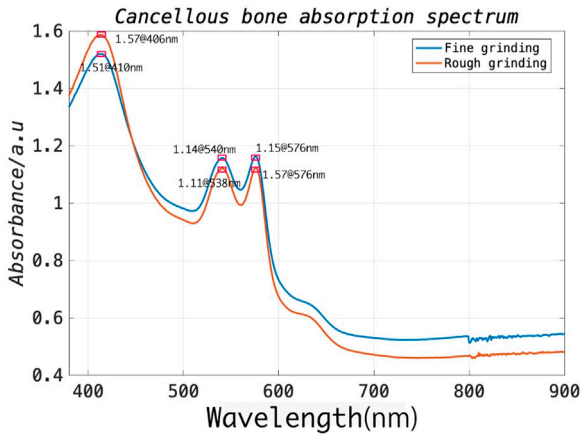

FIGURE 5
Absorption spectrum of cancellous bone.

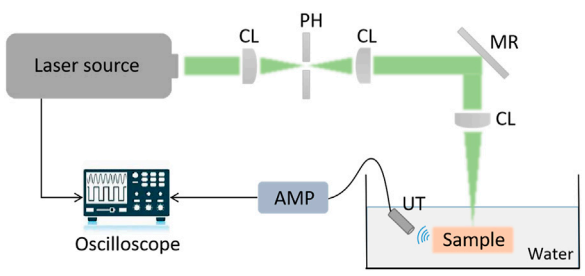

FIGURE 6
Signal acquisition and characterization of cancellous bone and cortical bone based on a single element ultrasonic transducer.

cover the wavelength range of 340–960 nm. Subsequently, the coarsely processed cancellous bone was further subjected to fine grinding. The measuring steps were then repeated. As illustrated in Figure 5, the experimental results demonstrated that the strongest absorption exists at 406 nm and stronger absorption peaks at 540 and 576 nm for the prepared bone samples. Therefore, in this study, we prefer a 532 nm pulse laser as the excitation source, which is well suited for spinal bone tissue characterization due to the overall cost considerations associated with the laser source.

PA signal acquisition and characterization

In this study, we determined an appropriate excitation wavelength as noted in the previous section by analyzing the absorption spectrum of cancellous bone and its cost. With PA imaging, differences of amplitude and frequency between the PA signals on different tissue components have significant impact on the resulting images. It was previously reported that Shubert and Lediju Bell (2018) utilized *ex vivo* photoexcitation and *in vitro* reception to qualitatively characterize cortical and cancellous bone based on PAT. However, for the PAE configuration in this study, PA signal characterization for two tissue components (cortical bone vs. cancellous bone) must present a clear distinction. In addition, there is a need to prevent PA signal interference with other tissue components, such as muscle, skin, and blood. To this end, an *ex vivo* measurement experiment using a single element ultrasonic transducer was designed for PA signal characterization of cortical bone and cancellous bone (see Figure 6).

PAE-enhanced drilling probe design

A PAE-enhanced drilling probe was developed for local tissue sensing inside the vertebrae to facilitate fine orientation adjustment for drilling path optimization. Specifically, a cannulated drill was customized for the integration of a PAE probe based on metal 3D printing. Thus, the developed PAE probe was built into a cannulated drill equipped with a mesopore, allowing for *in situ* PA imaging while perforating the vertebrae. The probe is made up of an optical unit and a single-element ultrasonic transducer. Figure 7A illustrates the optical unit, where, coupled to a single-mode fiber, the laser is collimated into a parallel beam with a diameter of approximately 1 mm, using the GRIN lens collimator (50-630-FC). The parallel beam is guided through the dual cone lenses in opposite directions, and then through the aspherical lens, forming a Bessel beam (Figure 7B). Due to the absence of diffraction, and the ability of the Bessel beam to self-restore after passing through obstacles, it is broadly adopted in measurement, calibration, precision processing, and therapies such as microscopy in particular (Li et al., 2019). After passing through a customized column refractor, the obtained Bessel beam is refracted to the sample surface. The resultant PA signals are also received via refraction from the customized circular probe. The circular single element PA probe is designed into a column to keep its overall dimensions and diameter within an acceptable range. The optical element can be inserted into the inner hole of the ultrasonic probe, which improves its compactness as well as allowing for the coaxiality and confocality of the excitation and receiving signals.

Ex vivo study design

Sample selection, processing, and fixation

To obtain experimental data for pedicle screw implantation, an intact lumbar vertebra of a bovine was chosen for *ex vivo* studies as the sample comparable to that of a human spine. This is because mammalian spines share similarities in spinal morphology and bone tissue composition. The spine of an adult bovine sacrificed within 3-h was employed for experimental validation. (Age: 3 years, gender: male, weight: 200 kg, vertebra weight: 2.5 kg). Afterward, we used a boning

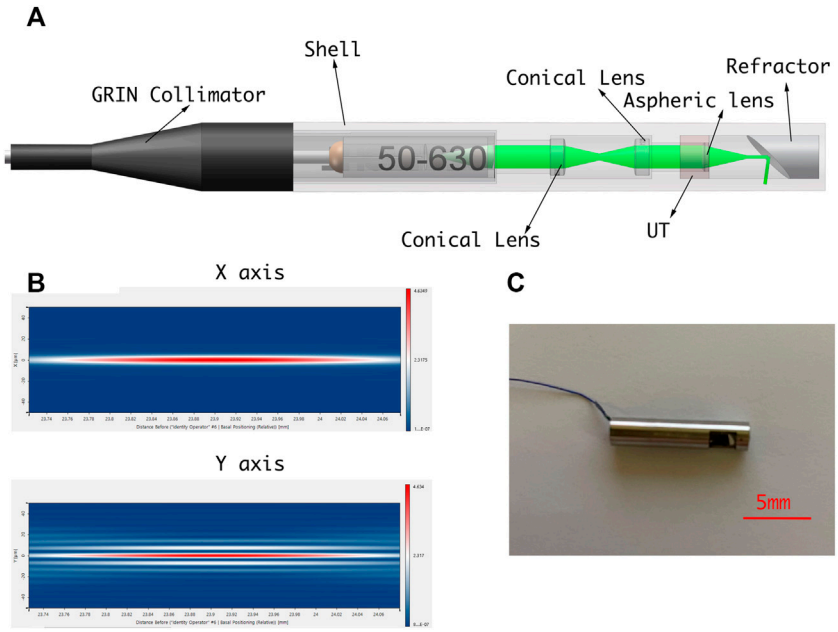

FIGURE 7
(A) Schematic diagram of PAE-enhanced drilling probe. **(B)** Simulation of Bessel beam. **(C)** PAE-enhanced drilling probe prototype.

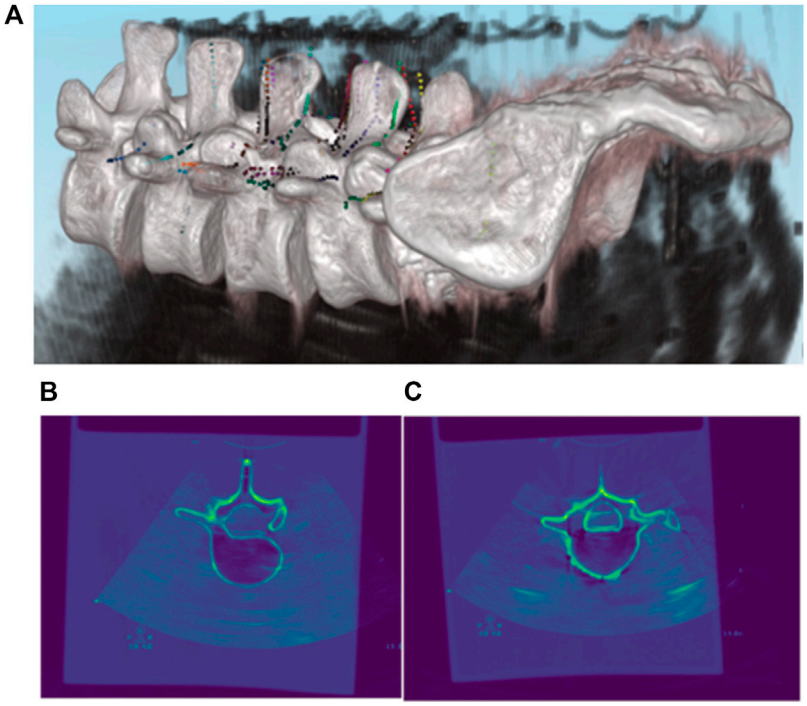

FIGURE 8
Registration results of pre-operative CT and intra-operative 3D US. **(A)** 3D Rendering of co-registered CT and US images; **(B,C)** 2D Rendering of co-registered CT and US images.

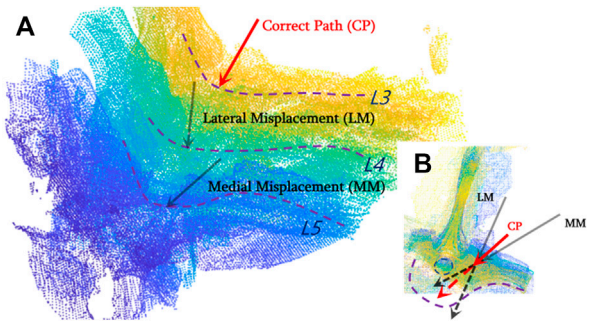

FIGURE 9
Drilling entry point determination and coarse path planning based on co-registered CT and US images for pedicle screw implantation. **(A)** Three types of screw implantation paths (correct path, lateral misplacement, and medial misplacement) are defined on co-registered CT and US images; **(B)** 2D visualization of three typical screw implantation paths.

knife to separate the muscle tissue from the spine. The purpose of this step was to make the operation field clearer, and to reduce clutter caused by light shining on the muscle tissue. The intact lumbar vertebra after bone and flesh separation is shown in Figure 8. Afterward, we performed the tissue processing by removing the lumbar vertebra for the subsequent experiments. The entire treated spine was fixed in a transparent acrylic box with glue, and the box filled with water until the tissue was completely covered, in order to significantly reduce attenuation of the PA signal.

PAE imaging experimental setup

A PAE drilling probe allows for local-scale navigation in a fine-grained manner to facilitate screw implantation more accurately and safely. A torque-enhancement unit and a PAE probe comprise the overall system. Figures 7A,C provide a schematic diagram and system prototype of the probe. After passing through the neutral-density filter (NDF), the pulse laser generated by the Q-switch laser (532 nm, 7 ns, 10 Hz, Xichanye Co., Ltd., China) is divided into two beams by the beam splitter (BS) (the beam ratio is 1:10). The photodiode receives the lower-energy beam, while the other beam is coupled into the optical fiber after being focused by a collimating filter for subsequent PAE imaging. Both signal lines are relatively thin, since the PAE probe is rotated around the main axis of the drill. As shown in Figure 2B, a mechanical torsion increasing unit was designed to prevent the signal wire from breaking during winding with the optical fibers. The outer layer of the optical fiber at the end of the drilling probe, as well as its signal line, are reinforced with a shrinkable heat tube to ensure a relatively stable connection between the outer layer and the signal line. The drill is connected to one end of the heat-shrinkable tube, and the conductive slide ring to the other. The motor's torque is transmitted to the conductive slide ring via the outer layer during rotation. Simultaneously, the signal line of the single-element ultrasonic transducer relates to the rotor of the conductive slide ring via a fiber that passes through its hollow slide ring and terminates at the end of the optical excitation unit. Since the optical fiber must be rotated as well, a rolling bearing is added at the end, enabling the optical fiber and the probe signal line to be rotated without winding. The maximum laser energy on the sample is approximately 16 mJ/cm^2, far below the ANSI (American National Standards Institute) safety standard (30 mJ/cm^2), and the calculation data from UCSB Laser Safety Manual of 19.29 mJ/cm^2 (UCSB, 2018) (Thomas et al., 2001).

Results

Registration of pre-operative CT with intra-operative 3D US

As described in the previous section, the most vital task during pedicle screw implantation is determining an appropriate drilling entry and path direction prior to entering the vertebral bone. After the US volume is generated intra-operatively, each vertebral model segmented from pre-operative CT is registered with the point clouds of the bone surface extracted from the US volume, due to the fact that the CT vertebral model can supplement the missing bone structure of the US volume caused by ultrasonic reflection and/or attenuation. As such, it offers a more comprehensive representation of the vertebral bone profile once an inter-vertebral posture variation occurs. As shown in Figure 8, CT data of the lumbar spine are overlain with the spinal sonography in 3D and 2D visualizations. Eventually, based on the co-registered CT and US images, three typical screw implantation paths (i.e., correct path, lateral misplacement, and medial misplacement) are determined (see Figure 9). Along these three coarse paths, the PAE-enhanced drilling probe is advanced for *in situ* bone tissue sensing inside the vertebra and hence for fine path optimization, which is described in the subsequent section.

PA signal characterization: Cortical bone vs. cancellous bone

The PA signals of cortical and cancellous bone are acquired and investigated by the single element ultrasonic acquisition system, as described in the previous section. It is noted that the wavelength and power of the excitation laser are constant, and multiple acquisition results are averaged to reduce crosstalk noise. Since the PA image is a composition of multiple signals with a variety of frequencies in general, the obtained images are

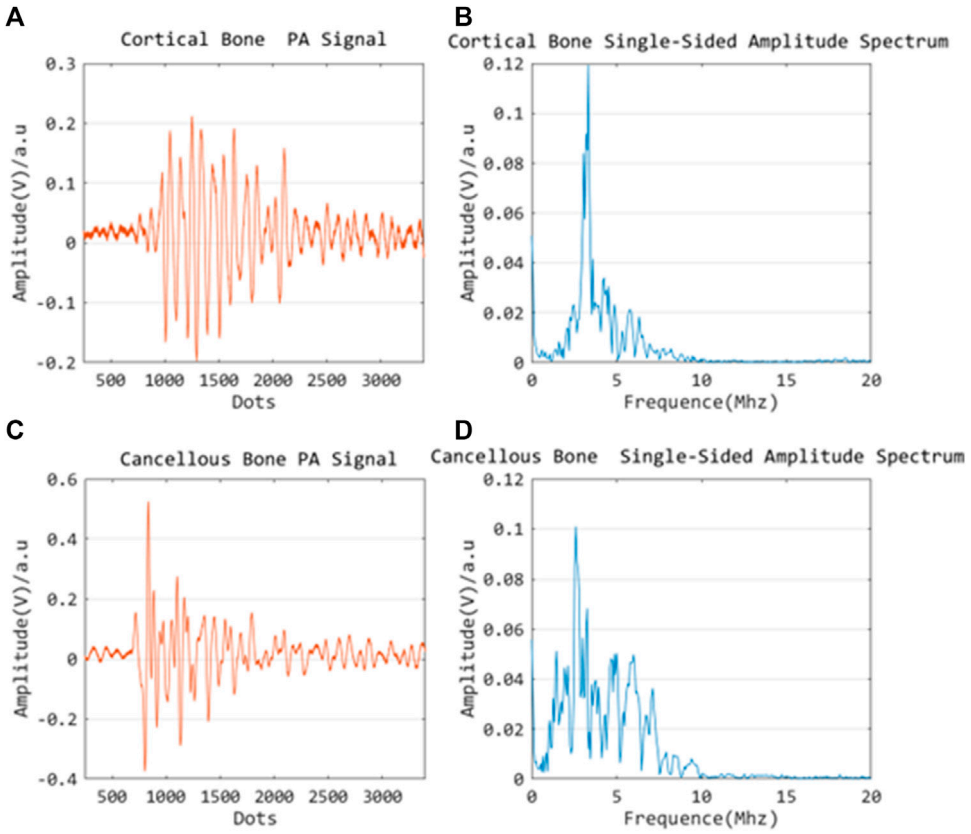

FIGURE 10
Time domain PA signal characterization of cortical bone **(A)** and cancellous bone **(C)**; Frequency domain PA signal characterization of cortical bone **(B)** and cancellous bone **(D)**.

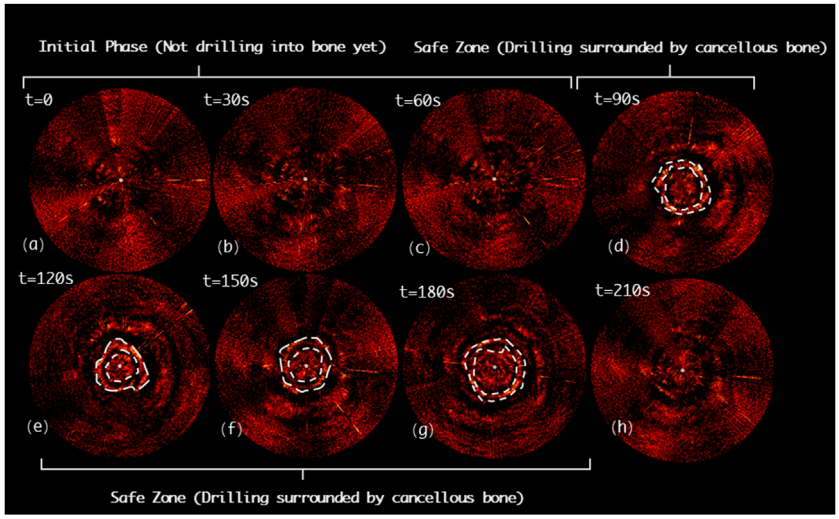

FIGURE 11
Acquired PAE images along the clinically "correct" path (CP) for *in situ* bone tissue sensing. **(A-C)** Initial phase; **(D-G)** Safe zone; **(H)** Final phase.

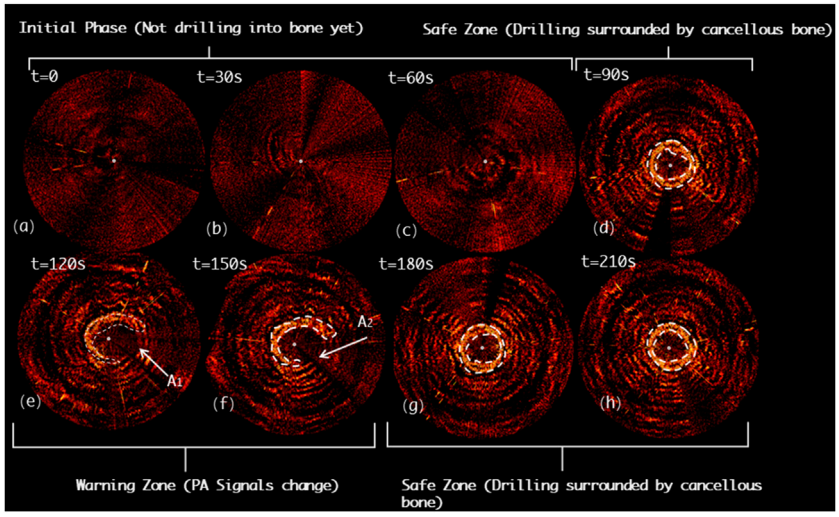

FIGURE 12
Acquired PAE images along the lateral misplacement path (LMP) for *in situ* bone tissue sensing. **(A-C)** Initial phase; **(D)** Safe zone; **(E-F)** Warning zone; **(G-H)** Safe zone.

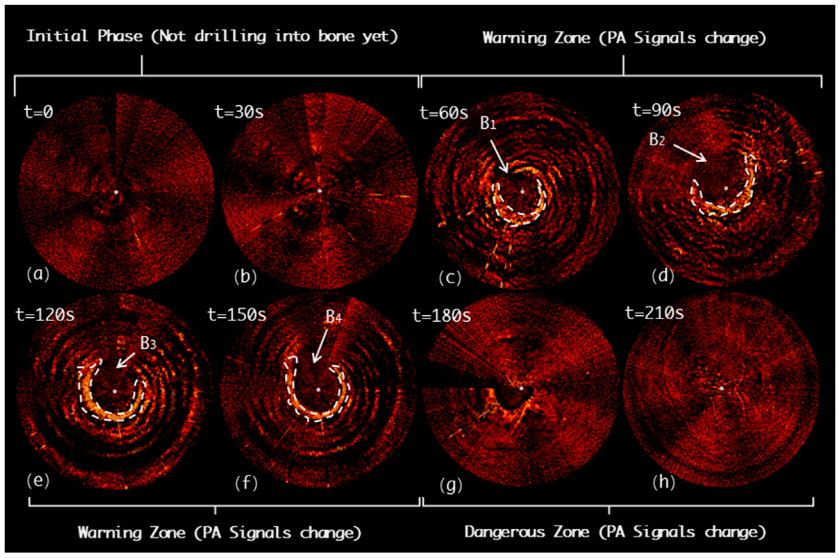

FIGURE 13
Acquired PAE images along the medial misplacement path (MMP) for *in situ* bone tissue sensing. **(A-B)** Initial phase; **(C-F)** Warning zone; (G-H) Dangerous zone.

transformed to the frequency domain using the Fourier transform for signal characterization. The experimental results are shown in the following figures: Figures 10A,C reflect the signal profile of cortical and cancellous bone in the time domain, while figures 10 B,D demonstrate the signal profile of the cortical and cancellous bone in the frequency domain. Of note, under the same laser energy excitation, the PA signal amplitude peak of cortical bone is slightly lower than that of cancellous bone, and

TABLE 1 gCNR of PAE images acquired along three typical screw implantation paths.

	(a)	(b)	(c)	(d)	(e)	(f)	(g)	(h)
CP(Figure 11)	0.13	0.14	0.13	0.37	0.41	0.48	0.53	0.12
LMP(Figure 12)	0.10	0.12	0.19	0.52	0.47	0.49	0.62	0.66
MMP(Figure 13)	0.12	0.13	0.36	0.38	0.42	0.42	0.37	0.15

continuously, the PA images obtained (see Figures 11E–G) show the PA signals yielded by the surrounding cancellous bone are still uniformly distributed near the drilling bit. From the 210th*s* on, the PA signals induced by the cancellous bone disappear; at this time the drilling probe has been removed from the vertebra (see Figure 11H).

Figure 12 shows the drilling probe insertion along the lateral misplacement path (LMP) on the *L4* segment of lumbar spine and demonstrates the acquired PAE images. Such a path often results in lateral cortical breach, thereby bringing potential harm to peripheral vessels or nerves. In the first 90s, the associated PAE images are acquired (see Figures 12A-C), and the drill has not yet been inserted into the pedicle region for bone tissue characterization. During the period of 90ths-120ths, the drilling probe enters the pedicle region. As shown in Figure 12D, the probe is evenly surrounded by cancellous bone in a safe position. During the period of 120ths-180ths, the PA signals change in the regions A_1 and A_2, as highlighted in Figures 12E,F, indicating that new PA signals, different from those of cancellous bone, have been yielded in the regions A_1 and A_2. Based on anatomical interpretation, the drill bit is thought to be approaching the interface between the cortical bone and cancellous bone within the pedicle region, indicating the drill bit is in the perforation warning zone. As shown in Figure 12G, starting from the 180th*s*, PA signals like those of the 90th*s* are observed. This reflects that the drill bit remains inside the pedicle region during insertion, only at some sites the drill bit is close to the cortical bone border of the vertebrae, requiring a warning and further correction.

Figure 13 demonstrates the drilling probe insertion along the medial misplacement path (MMP) on the *L5* segment of

TABLE 2 Comparison of a variety of navigation and sensing techniques for pedicle screw implantation.

Category	Technique	Radiation	Efficacy	Complexity	Image quality (gCNR)	Local signal direction
Global Spatial Navigation	Freehand	√ (High)	Low	Lowest	/	/
	Computer-assisted 2D fluoroscopic navigation	√ (Low)	High	High	/	/
	Computer-assisted CBCT navigation	√ (High)	High	High	/	/
	Computer-assisted CT-fluoroscopic registration	√ (Low)	High	High	/	/
	Macroscopic PAT/US	×	High	Moderate	Highest	/
Local Tissue Sensing	Electrical conductivity measurement	×	Moderate	Low	/	×
	Endoscopic US Imaging	×	Moderate	Low	Low	√
Multi-Scale Navigation and Sensing	Our proposed solution	×	High	Moderate	High	√

the signals are mostly concentrated in the high-frequency section. The signal response of cancellous bone is slightly stronger than that of cortical bone in terms of amplitude.

In situ PAE sensing via drilling probe

Based on the co-registered CT and US images, three typical screw implantation paths are determined (see Figure 9). Along these three coarse paths, the PAE-enhanced drilling probe advances for *in situ* bone tissue sensing inside the vertebra and hence for fine path optimization.

Figure 11 indicates the drilling probe insertion along the clinically "correct" implantation path (Correct Path) on the *L3* segment of lumbar spine and demonstrates the acquired PAE images. Such PAE images are obtained at 30*s* intervals. It can be noticed that in the first 90s (see Figures 11A–C), the probe has been delivered into the vertebrae, but has not yet arrived in the pedicle region. During the period of the 90ths~120ths, it can clearly be seen that the probe has penetrated the pedicle region. The PA signals yielded by the surrounding cancellous bone are presented in Figure 11D, and the cancellous bone is distributed evenly around this drilling probe. As the probe is inserted

the lumbar spine and demonstrates the acquired PAE images. Such a path frequently results in medial cortical breach, and thereafter causes complications, such as spinal cord injury. In the first 60*s*, the drill has not yet entered the pedicle region (see Figures 13A,B). As shown in Figures 13C-F, starting from the $60^{th}s$, the variation in the PA signals can be clearly detected (region B_1 and B_2), indicating that the drill bit is not surrounded by cancellous bone at this time. Subsequently, from the $120^{th}s$ to $180^{th}s$, the drill is found to be located inside a perforation warning region (B_3 and B_4), where the spinal cord may be at high risk of damage. At $210^{th}s$, no visible PA signals are detected, revealing that the drill has completely penetrated the medial cortical bone (see Figure 13H).

In order to assess the imaging quality of the PAE images quantitatively, we applied the generalized contrast-to-noise ratio (gCNR) as a metric. The gCNR is a relatively new image quality metric designed to assess the probability of lesion detectability in ultrasound images (Kempski et al., 2020). The gCNR metric is calculated from the overlap of the probability density functions (PDFs) of ROIs inside a target and background. The calculation method can be described in the following formula:

$$OVL = \int_{-\infty}^{\epsilon_0} p_i(x)dx + \int_{\epsilon_0}^{\infty} p_o(x)dx, \quad (1)$$

$$gCNR = 1 - OVL, \quad (2)$$

where $p_i(x)$ and $p_o(x)$ are the PDFs for regions inside and outside of a target, respectively, while *OVL* is the total overlap area of the two PDFs derived from photoacoustic images, and is thus the optimal threshold for minimizing the probability of misidentifying background as target and target as background. Table 1 shows the generalized contrast-to-ratio (gCNR) for the acquired PAE images along three typical screw implantation paths (CP, LMP, and MMP).

Discussion and conclusion

In this study, we developed for the first time a radiation-free and multi-scale navigation and sensing system by applying a PAE-enhanced drilling probe to facilitate pedicle screw implantation optimization. Existing studies either only consider global spatial navigation based on macroscopic anatomical imaging (fluoroscopy or CBCT with radiation; combined US/PAT without radiation) or only take *in situ* tissue sensing, using local sensor-enhanced instruments (acceleration/force sensor; electrical conductivity measurement; EUS probe), into consideration.

The main novelty of this pilot study is that we combine the advantages of global spatial navigation and local tissue sensing techniques. Specifically, the comprehensive navigation system provides global context-awareness from the macroscopic 3D US imaging. 3D US imaging was established for online status updates of the position of the spinal segment to determine an appropriate entry point and coarse drilling path once non-negligible patient motion or relative motion between inter-vertebral segments occurs intra-operatively. The PAE-enhanced drilling probe is subsequently used along the planned coarse insertion path to recognize cortical bone and cancellous bone tissue inside the vertebra near the drill bit for fine orientation correction. To the best of our knowledge, for the first time here, a PAE-enhanced drilling probe is designed, developed, and deployed for pedicle screw implantation in spinal fusion. The *ex vivo* experiment on a bovine spine demonstrates the clinical feasibility of the proposed system, which holds great potential for allowing functionally accurate screw implantation for spine stabilization in complex spine-related interventions. Table 2 demonstrates the advantages and disadvantages of a variety of existing navigation and sensing technologies for pedicle screw implantation. Compared with other state-of-the-art techniques, PA-enabled solutions (either PAT/US macroscopic dual-modal imaging, or PAE-enhanced drilling probe for *in situ* tissue sensing at clinically relevant mesoscopic scale), reveal advantages of non-radiation, high efficacy, moderate deployment complexity, better image quality (gCNR value), and local signal direction information, and hold great potential for facilitating radiation-free and minimally invasive pedicle screw placement.

However, the challenges of implementing the PAE-enhanced drilling probe for spine stabilization need to be addressed. The size of the PAE-enhanced drilling probe should be more compact, such that its application in clinical practice can meet the need of extremely deformed spine cases, where the pedicle region where the screw is to be implanted is further restricted to 1–2 mm, or even sub-millimeter. Of note, a more compact design scheme based on an optical fiber sensing solution is being investigated to replace the piezoelectrical US transducer.

In addition, the *ns*-pulse laser utilized to generate photoacoustic signals tends to be too expensive compared to other techniques, such as acceleration/force sensors, electrical conductivity measurement probes, and EUS probes. Despite this, the PAE-enhanced drilling probe still holds significant advantages over its counterparts, such as better images, more intuitive visual feedback, and local signal directional information for tissue differentiation and warning. Fortunately, many cost-effective laser sources have become commercially available. It is noted that these could offer a great opportunity to reduce the cost of the PAE-enhanced drilling probe for spinal stabilization in clinical practice.

Since it is difficult to measure the absorption spectrum of solids based on our available measuring instrument, we applied grinding to convert the solid cancellous bone into a powder-like form. We also compared the effect of the degree of grinding on the results of the absorption spectrum, which deviates from the actual absorption spectrum. In addition, the absorption spectrum of solid cortical bone could not be readily tested due to its high density and difficulty in grinding it into powder form. To solve this problem, we measured actual PA signals to distinguish between different tissues. In other

words, it elaborates the different absorption resulting from the different composition of solid tissues.

As the morphological characteristics of the cancellous bone *in vivo* are porous and blood-filled, there may be errors due to continuous reflection of the PA signal within the pores during the imaging process. Therefore, our experimental results reveal the relative deviation between the cortical and cancellous bone site in the image at the same test point, and this deviation can help us to differentiate the site. Since the rotation and feed along the axis of the PAE probe is achieved by a surgical drill, the PAE-enhanced straight drill can only accurately serve the function of detecting the safety of the drilled hole. Our future work would be to develop a steerable drilling robot that can avoid dangerous collision situations during surgery.

Data availability statement

The raw data supporting the conclusion of this article will be made available by the authors, without undue reservation.

Author contributions

All authors listed have made a substantial, direct, and intellectual contribution to the work, and approved it for publication. LL (First Author, Corresponding Author): Conceptualization, Methodology, Software, Supervision, Funding Acquisition, Writing-Original Draft; YZ (First Author): Data Curation, Methodology, Formal Analysis, Visualization, Writing-Original Draft; AL: Visualization, Software, Investigation; XY: Investigation, Validation; XX: Investigation, Validation; SL (Corresponding Author): Funding Acquisition, Resources, Supervision, Writing-Review & Editing; MM: Funding Acquisition, Resources, Supervision.

Funding

This work was supported by the National Key R&D program of China with Grant No. 2019YFB1312400; the Hong Kong Research Grants Council (RGC) Collaborative Research Fund (CRF C4026-21GF and CRF C4063-18G); the General Research Fund (GRF #14220622, GRF #14204321, and GRF#14211420); and the Natural Science Foundation of Jiangsu Province (Grant No. BK20210323).

Conflict of interest

The authors declare that the research was conducted in the absence of any commercial or financial relationships that could be construed as a potential conflict of interest.

Publisher's note

All claims expressed in this article are solely those of the authors and do not necessarily represent those of their affiliated organizations, or those of the publisher, the editors, and the reviewers. Any product that may be evaluated in this article, or claim that may be made by its manufacturer, is not guaranteed or endorsed by the publisher.

References

Ahern, D. P., Gibbons, D., Schroeder, G. D., Vaccaro, A. R., and Butler, J. S. (2020). Image-guidance, robotics, and the future of spine surgery. *Clin. Spine Surg.* 33 (5), 179–184. doi:10.1097/bsd.0000000000000809

Aly, A. H., Ginsberg, H. J., and Cobbold, R. S. C. (2011). ON ultrasound imaging for guided screw insertion in spinal FUSION surgery. *Ultrasound Med. Biol.* 37 (4), 651–664. doi:10.1016/j.ultrasmedbio.2011.01.011

An, H., and Benoit, P. (1998). Saline injection technique to confirm pedicle screw path: A cadaveric study. *Am. J. Orthop.* 27, 362–365.

Beard, P. (2011). Biomedical photoacoustic imaging. *Interface Focus* 1 (4), 602–631. doi:10.1098/rsfs.2011.0028

Bolger, C., Kelleher, M. O., McEvoy, L., Brayda-Bruno, M., Kaelin, A., Lazennec, J. Y., et al. (2007). Electrical conductivity measurement: A new technique to detect iatrogenic initial pedicle perforation. *Eur. Spine J.* 16 (11), 1919–1924. doi:10.1007/s00586-007-0409-8

Chapman, J. R. (2019). Editorial. Spinal infections: A growing problem, which deserves our urgent attention. *Neurosurg. FOCUS* 46 (1), E3. doi:10.3171/2018.10.focus18587

Compston, J. E., McClung, M. R., and Leslie, W. D. (2019). *Lancet* 393 (10169), 364–376. doi:10.1016/s0140-6736(18)32112-3

Cool, J., van Schuppen, J., de Boer, M. A., and van Royen, B. J. (2021). Accuracy assessment of pedicle screw insertion with patient specific 3D-printed guides through superimpose CT-analysis in thoracolumbar spinal deformity surgery. *Eur. Spine J.* 30 (11), 3216–3224. doi:10.1007/s00586-021-06951-9

Dea, N., Fisher, C. G., Batke, J., Strelzow, J., Mendelsohn, D., Paquette, S. J., et al. (2016). Economic evaluation comparing intraoperative cone beam CT-based navigation and conventional fluoroscopy for the placement of spinal pedicle screws: A patient-level data cost-effectiveness analysis. *Spine J.* 16 (1), 23–31. doi:10.1016/j.spinee.2015.09.062

Duffy, M. F., Phillips, J. H., Knapp, D. R., and Herrera-Soto, J. A. (2010). Usefulness of electromyography compared to computed tomography scans in pedicle screw placement. *SPINE* 35 (2), E43–E48. doi:10.1097/brs.0b013e3181b3f467

Felix, B., Kalatar, S. B., Moatz, B., Hofstetter, C., Karsy, M., Parr, R., et al. (2022). Augmented reality spine surgery navigation increasing pedicle screw insertion accuracy for both open and minimally invasive spine surgeries. *SPINE* 47 (12), 865–872. doi:10.1097/brs.0000000000004338

Foley, K. T., Simon, D. A., and Rampersaud, Y. R. (2001). Virtual fluoroscopy: Computer-assisted fluoroscopic navigation. *SPINE* 26 (4), 347–351. doi:10.1097/00007632-200102150-00009

Germon, T. J., and Hobart, J. C. (2015). Definitions, diagnosis, and decompression in spinal surgery: Problems and solution. *Spine J.* 15 (3), 5S–8S. doi:10.1016/j.spinee.2014.12.147

Gonzalez, E. A., Jain, A., and Bell, M. A. L. (2021). Combined ultrasound and photoacoustic image guidance of spinal pedicle cannulation demonstrated with intact *ex vivo* specimens. *IEEE Trans. Biomed. Eng.* 68 (8), 2479–2489. doi:10.1109/tbme.2020.3046370

Guo, H., Li, Y., Qi, W., and Xi, L. (2020). Photoacoustic endoscopy: A progress review. *J. Biophot.* 13, e202000217. doi:10.1002/jbio.202000217

Hecht, N., Yassin, H., Czabanka, M., Föhre, B., Arden, K., Liebig, T., et al. (2018). Intraoperative computed tomography versus 3D C-arm imaging for navigated spinal instrumentation. *Spine* 43 (5), 370–377. doi:10.1097/brs.0000000000002173

Helm, P. A., Teichman, R., Hartmann, S. L., and Simon, D. (2015). Spinal navigation and imaging: History, trends, and future. *IEEE Trans. Med. Imaging* 34 (8), 1738–1746. doi:10.1109/tmi.2015.2391200

Ibtehaz, N., and Rahman, M. S. (2020). MultiResUNet : Rethinking the U-Net architecture for multimodal biomedical image segmentation. *NEURAL Netw.* 121, 74–87. doi:10.1016/j.neunet.2019.08.025

Jolliffe, I. T., and Cadima, J. (2016). Principal component analysis: A review and recent developments. *PHILOSOPHICAL Trans. R. Soc. A-MATHEMATICAL Phys. Eng. Sci.* 374 (2065), 20150202. doi:10.1098/rsta.2015.0202

Joon-Mo Yang, K. M., Yang, H-C., Zhou, Q., Kirk Shung, K., and Wang, L. V. (2009). Photoacoustic endoscopy. *Opt. Lett.* 34 (10), 1591–1593. doi:10.1364/ol.34.001591

Kempski, K. M., Graham, M. T., Gubbi, M. R., Palmer, T., and Lediju Bell, M. A. (2020). Application of the generalized contrast-to-noise ratio to assess photoacoustic image quality. *Biomed. Opt. Express* 11 (7), 3684–3698. doi:10.1364/boe.391026

Kruizinga, P., van der Steen, A. F., de Jong, N., Springeling, G., Robertus, J. L., van der Lugt, A., et al. (2014). Photoacoustic imaging of carotid artery atherosclerosis. *J. Biomed. Opt.* 19 (11), 110504. doi:10.1117/1.jbo.19.11.110504

Li, Q., Du, Z., Liu, F., and Yu, H. (2022). Tactile perception for surgical status recognition in robot-assisted laminectomy. *IEEE Trans. Ind. Electron.* 69 (11), 11425–11435. doi:10.1109/tie.2021.3118387

Li, X., Xiong, K., and Yang, S. (2019). Large-depth-of-field optical-resolution colorectal photoacoustic endoscope. *Appl. Phys. Lett.* 114 (16), 163703. doi:10.1063/1.5093789

Lonstein, J. E., Denis, F., Perra, J. H., Pinto, M. R., Smith, M. D., and Winter, R. B. (1999). Complications associated with pedicle screws. *J. Bone Jt. Surg.* 81 (11), 1519–1528. doi:10.2106/00004623-199911000-00003

Lopera, J. E., Restrepo, C. S., Gonzales, A., Trimmer, C. K., and Arko, F. (2010). Aortoiliac vascular injuries after misplacement of fixation screws. *J. Trauma Inj. Infect. Crit. Care* 69 (4), 870–875. doi:10.1097/ta.0b013e3181f0bd55

Manbachi, A., Cobbold, R. S. C., and Ginsberg, H. J. (2014). Guided pedicle screw insertion: Techniques and training. *Spine J.* 14 (1), 165–179. doi:10.1016/j.spinee.2013.03.029

Maria, S., Deyanira, C., Francesca, S., Lucia, M., Alessandro, R., Silvia, T., et al. (2020). Spinal fusion surgery and local antibiotic administration A systematic review on Key points from preclinical and clinical data. *SPINE* 45 (5), 339–348. doi:10.1097/brs.0000000000003255

Mujagic, M., Ginsberg, H. J., and Cobbold, R. S. C. (2008). Development of a method for ultrasound-guided placement of pedicle screws. *IEEE Trans. Ultrason. Ferroelectr. Freq. Control* 55 (6), 1267–1276. doi:10.1109/tuffc.2008.789

Nottmeier, E. W., and Crosby, T. L. (2007). Timing of paired points and surface matching registration in three-dimensional (3D) image-guided spinal surgery. *J. SPINAL Disord. Tech.* 20 (4), 268–270. doi:10.1097/01.bsd.0000211282.06519.ab

Ovadia, D., Korn, A., Fishkin, M., Steinberg, D. M., Wientroub, S., and Ofiram, E. (2011). The contribution of an electronic conductivity device to the safety of pedicle screw insertion in scoliosis surgery. *SPINE* 36 (20), E1314–E1321. doi:10.1097/brs.0b013e31822a82ec

Sangha, G. S., and Goergen, C. J. (2016). Photoacoustic tomography: Applications for atherosclerosis imaging. *J. Opt.* 18 (8), 084005. doi:10.1088/2040-8978/18/8/084005

Shi, Q., Xi, N., Chen, Y. F., and Sheng, W. H. (2006). "Ieee. Registration of point clouds for 3D shape inspection," in IEEE/RSJ INTERNATIONAL CONFERENCE ON INTELLIGENT ROBOTS AND SYSTEMS, Beijing, China, 09-15 October 2006, 235.

Shubert, J., and Lediju Bell, M. A. (2018). Photoacoustic imaging of a human vertebra: Implications for guiding spinal fusion surgeries. *Phys. Med. Biol.* 63 (14), 144001. doi:10.1088/1361-6560/aacdd3

Steinberg, I., Huland, D. M., Vermesh, O., Frostig, H. E., Tummers, W. S., and Gambhir, S. S. (2019). Photoacoustic clinical imaging. *Photoacoustics* 14, 77–98. doi:10.1016/j.pacs.2019.05.001

Tabarestani, T. Q., Sykes, D., Murphy, K. R., Wang, T. Y., Shaffrey, C. I., Goodwin, C. R., et al. (2022). Beyond placement of pedicle screws-new applications for robotics in spine surgery: A multi-surgeon, single-institution experience. *Front. Surg.* 9, 889906. doi:10.3389/fsurg.2022.889906

Thomas, R., Rockwell, B., Marshall, W., Aldrich, R., and Zimmerman S, R., Jr (2001). A procedure for multiple-pulse maximum permissible exposure determination under the Z136.1-2000 American National Standard for Safe Use of Lasers. *J. Laser Appl.* 13, 134–140. doi:10.2351/1.1386796

Tian, N. F., Huang, Q. S., Zhou, P., Zhou, Y., Wu, R. K., Lou, Y., et al. (2011). Pedicle screw insertion accuracy with different assisted methods: A systematic review and meta-analysis of comparative studies. *Eur. Spine J.* 20 (6), 846–859. doi:10.1007/s00586-010-1577-5

Ucsb (2018). *Laser safety manual*. California, USA: UCSB Environmental Health & Safe.

Wang, Y. X. J., Che-Nordin, N., Leung, J. C. S., Yu, B. W. M., Griffith, J. F., and Kwok, T. C. Y. (2020). Elderly men have much lower vertebral fracture risk than elderly women even at advanced age: The MrOS and MsOS (Hong Kong) year 14 follow-up radiology results. *Arch. Osteoporos.* 15 (1), 176. doi:10.1007/s11657-020-00845-x

Weiss, A., Elixhauser, A., and Steiner, C. Readmissions to U.S. Hospitals by procedure, 2010: Statistical Brief #154. 2008.

Xu, M., and Wang, L. V. (2006). Photoacoustic imaging in biomedicine. *Rev. Sci. Instrum.* 77 (4), 041101. doi:10.1063/1.2195024

Yamada, T., Hasegawa, T., Yamato, Y., Yoshida, G., Banno, T., Arima, H., et al. (2022). Characteristics of pedicle screw misplacement using freehand technique in degenerative scoliosis surgery. *ARCHIVES Orthop. TRAUMA Surg.* doi:10.1007/s00402-022-04380-x

Yao, J., and Wang, L. V. (2013). Photoacoustic microscopy. *Laser Phot. Rev.* 7 (5), 758–778. doi:10.1002/lpor.201200060

Zhang, J., Li, W. S., Hu, L., Zhao, Y., and Wang, T. M. (2021). A robotic system for spine surgery positioning and pedicle screw placement. *Int. J. Med. Robot.* 17 (4), e2262. doi:10.1002/rcs.2262

Zhao, T., Desjardins, A. E., Ourselin, S., Vercauteren, T., and Xia, W. (2019). Minimally invasive photoacoustic imaging: Current status and future perspectives. *Photoacoustics* 16, 100146. doi:10.1016/j.pacs.2019.100146

Zhou, Y., Xing, W., Maslov, K. I., Cornelius, L. A., and Wang, L. V. (2014). Handheld photoacoustic microscopy to detect melanoma depth *in vivo*. *Opt. Lett.* 39 (16), 4731–4734. doi:10.1364/ol.39.004731

frontiers | Frontiers in Bioengineering and Biotechnology

TYPE Original Research
PUBLISHED 20 October 2022
DOI 10.3389/fbioe.2022.1043028

OPEN ACCESS

EDITED BY
Francis Bui,
University of Saskatchewan, Canada

REVIEWED BY
Michel Paindavoine,
Université de Bourgogne, France
Jan Kubicek,
VSB-Technical University of Ostrava, Czechia

*CORRESPONDENCE
Jiexiu Zhao,
zhaojiexiu@ciss.cn

SPECIALTY SECTION
This article was submitted to Biosensors and Biomolecular Electronics, a section of the journal Frontiers in Bioengineering and Biotechnology

RECEIVED 13 September 2022
ACCEPTED 10 October 2022
PUBLISHED 20 October 2022

CITATION
Feng Y, Fang G, Li M, Cui S, Geng X, Qu C and Zhao J (2022), Hydration monitoring and rehydration guidance system for athletes based on urine color's L*a*b* parameters. *Front. Bioeng. Biotechnol.* 10:1043028. doi: 10.3389/fbioe.2022.1043028

Hydration monitoring and rehydration guidance system for athletes based on urine color's L*a*b* parameters

Yiwei Feng[1], Guoliang Fang[1], Minghai Li[2], Shuqiang Cui[3], Xue Geng[1,4], Chaoyi Qu[1,4] and Jiexiu Zhao[1]*

[1]Exercise Biological Center, China Institute of Sport Science, Beijing, China, [2]School of Chemistry and Materials Science, Nanjing Normal University, Nanjing, China, [3]Beijing Institute of Sports Science, Beijing, China, [4]Department of Exercise Physiology, Beijing Sport University, Beijing, China

Maintaining proper hydration is essential for athletes to sustain optimal performance and preserve their physical health. Existing studies have confirmed that urine color is one of the effective indicators for the subjective evaluation of athletes' hydration through the urine color chart. However, the use of urine color charts to evaluate hydration is easily affected by the test environment, urine container and subjective feeling. At present, there are few hydration monitoring instruments based on quantitative analysis of urine color. In recent years, the L*a*b* color model has been widely used in the objective quantitative analysis of color. The L* value represents the luminance change from black to white, the a* value represents the chromaticity change from green to red, and the b* value represents the chromaticity change from blue to yellow. Our previous research has confirmed that the urine color b * value is an effective new indicator to evaluate the hydration of athletes. The research team developed a urine hydration monitoring and rehydration guidance system based on the urine color's L*a*b* parameters *via* wireless network technology and digital image technology. The hardware structure of the system is composed of a cuvette, a standard light source, a camera, an image collector, a host system, and a touch screen system. The system software is composed of functional modules, such as user information, image acquisition, image processing, and image recognition. The system operation process includes starting the system, filling in basic information, putting the sample, testing the sample, local data review, local data upload, and cloud data review. The system exhibits stable performance, a friendly operation interface, and simple and fast testing. It can objectively and accurately evaluate the hydration of athletes and provide personalized rehydration guidance. The system offers a new method for solving practical problems in sports training, and it has broad application prospects.

Abbreviations: Usg, urine specific gravity.

KEYWORDS

athletes, hydration monitoring, rehydration guidance, urine color, color space, CIE L*a*b*

1 Introduction

Water is one of the essential nutrients for the human body. For the general public, dehydration may reduce thermoregulatory capacity, increase cardiovascular stress, and raise energy expenditure (McDermott et al., 2017). Long-term chronic hypohydration may increase the risk of kidney stones, urinary tract infections, constipation, adenomatous polyps, diabetes, and cardiovascular diseases (Manz, 2007). For athletes, maintaining proper hydration is essential to sustain optimal athletic performance, physiology, and health (Volterman and Moore, 2014). Dehydration of more than 1% of body weight can impair cognitive function; dehydration of more than 2% of body weight can reduce aerobic exercise capacity (McDermott et al., 2017). Dehydration greater than 3% of body weight can lead to exertional heat illnesses, such as heat cramps, heat exhaustion, and heat stroke (Casa et al., 2000). Acute overdrinking of water after exercise may lead to hyperhydration and increase the risk of exercise-induced hyponatremia (Hew-Butler et al., 2015).

Urine testing is a common noninvasive monitoring method that is highly accepted by athletes. Urine color, urine specific gravity (Usg), and urine osmolality are effective indicators for assessing hydration in athletes (Barley et al., 2020). In 1994, Armstrong et al. first developed a urine color chart and confirmed that it was an effective tool for the subjective assessment of urine color (Armstrong et al., 1994). However, the subjective assessment of urine color by using this chart is easily affected by many confounding factors, such as the test environment, test personnel, and urine container.

Another effective method is the quantitative testing of urine color through instruments. This method can prevent the results from being affected by the external environment and the operator's subjectivity. The color space model is a mathematical model that quantitatively represents a certain color by using 1D, 2D, 3D, or even 4D model, such as the RGB, L*a*b*, and CMYK models. The L*a*b* model is a 3D color space model defined by the Commission Internationale de l′ Eclairage (CIE) in 1976. This color model has the widest color gamut that contains all the colors visible to the human eyes. L* represents the change in brightness from black (0) to white (100), a* represents the color change from green (−128) to red (+127), and b* represents the change from blue (−128) to yellow (+127) (O'Brien et al., 1990). Recent studies have found that urine color can be objectively and quantitatively assessed by analyzing its L*a*b* parameters (Belasco et al., 2020). In addition, our research team previously confirmed that the b* value of urine color is an effective indicator for assessing the hydration of athletes by collecting 803 urine samples from athletes and testing urine color's L*a*b* parameters, urine osmolality, and Usg. We found a strong correlation between urine color's b* value and Usg (r = 0.811, $p < 0.01$), and a linear regression equation exists between them (b = −1,220 + 1,220 Usg, $R^2 = 0.657$) (Feng et al., 2022). Therefore, we envisioned that an instrument can be designed to monitor hydration by testing and quantifying urine color's L*a*b* parameters.

In recent years, several research teams have developed hydration monitoring equipment based on the RGB space model of urine color through digital image technology. Digital image technology is a method that involves taking pictures with digital cameras or smartphones and then quantitatively analyzing the color information of the images to obtain the color parameters (Komatsu et al., 2016). Chin et al. designed an Internet of Things (IoT)-based pervasive body hydration tracker. This system measures the color of urine through its components, such as color sensors and urine test probes, and then uploads the results on a mobile phone. The phone infers hydration by analyzing the B value of the RGB space model of urine color (Chin and Tisan, 2015). Chew et al. (2020) evaluated hydration by taking pictures of urine with mobile phones and then verifying that the RGB values of the urine color captured by the mobile phones were highly correlated with the hydration status of dengue patients. However, urine color pictures taken with mobile phones are easily affected by the light source environment, shooting equipment, operators, and analysis software. Therefore, we envisage that developing a hydration monitoring device through digital image technology is feasible.

Currently, there are many emerging hydration monitoring devices such as patch antennas for monitoring hydration of the skin, sensors for measuring sodium ion (Na^+) concentrations in sweat, micro-osmometers for measuring plasma osmolarity in 15 μl blood samples, and ultrasound systems for assessing hydration. These hydration monitoring devices are based on different testing indicators, and their designs and principles vary (Garrett et al., 2018). However, there are few studies on the urine hydration monitoring devices based on quantitative urine color analysis. Gunawan et al. (2018) developed a urine hydration system based on urine color and support vector machine. The system uses color sensor TCS34725 to obtain urine color data. The urine test results need to be accessed by Android smartphone, and the design of the detection device seems not rigorous enough. Chin et al. proposed an IoT-based pervasive body hydration tracker that consists of a urine color measurement component to be fitted in urinals. The test results need to be viewed through the Android smartphone, and the design of the device is complex (Chin and Tisan, 2015). Chew et al. (2020) captured urine color through the camera of the mobile phone, and then used Adobe Photoshop to process the

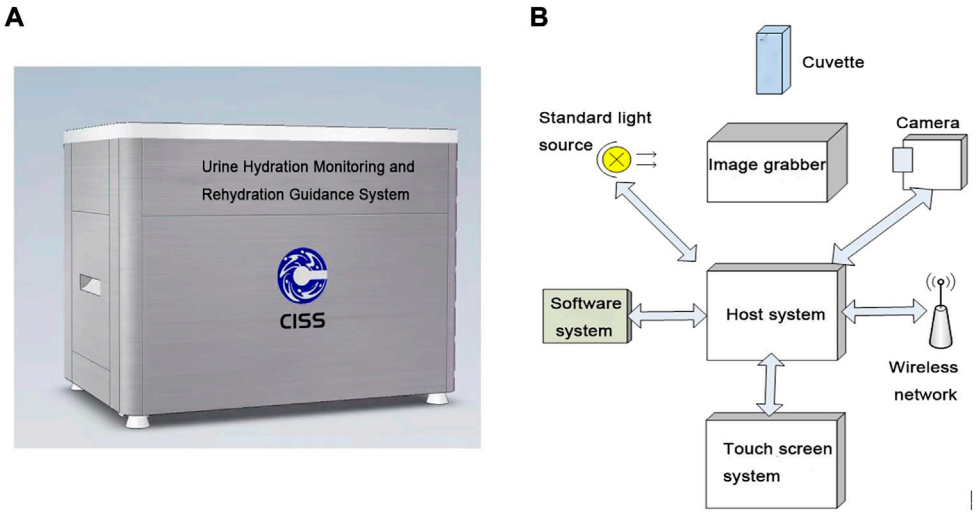

FIGURE 1
System design. **(A)** Schematic of the appearance of the system. **(B)** Schematic of system components.

picture. The study did not set test standards for mobile phone model, shooting environment and urine cup specification. The above monitoring methods are all based on RGB color space model to analyze urine color, and the practicability and accuracy of the equipment need more investigation. At present, no hydration monitoring system based on urine color's L*a*b* parameters is available.

Based on the above background, our research team developed a urine hydration monitoring and rehydration guidance system to enrich the noninvasive monitoring method of athletes' hydration and to serve during sports practice. This system combines sports nutrition, bioengineering, information technology, colorimetry, photometry, and other multidisciplinary theories. It uses urine color's parameter b* value as the evaluation index for hydration, formulates a system hydration grading standard, adopts digital image technology, uses a camera to take urine images, and is combined with digital equipment to analyze the color space L*a*b* parameters.

This paper is organized as follows: In Section 2, we introduce the appearance, hardware and software design, design principle and operation process of the urine hydration monitoring system. Then, we report the experiment result and discuss the advantages, limitations and recommendations of the system in Section 3. Finally, some conclusions and prospects are drawn in Section 4.

2 Materials and methods

2.1 System design

The design of the system is presented in Figure 1A. The hardware part of the system is composed of a cuvette, a standard light source, a camera, a host system, a touch screen system, and an image collector. The software part is composed of a software system and a wireless network (Figure 1B).

2.1.1 System hardware design

The hardware structure of this system is composed of a cuvette, a standard light source, a camera, an image collector, a host system, and a touch screen system (Figure 2). The structure and functions of the system's hardware are as follows. 1) Cuvette: It is used to hold urine samples and is equipped with a sealing cover. We use a two-pass light quartz cuvette, which exhibits the characteristics of high light transmission and high acid and alkali resistance. 2) Standard light source: We use a multi-chip white light-emitting diode (LED) surface light source that can provide a uniform lighting environment for all the samples under different test environments. 3) Camera: We use a high-definition camera (model IR500RC-14) with more than 5 million pixels and IP67 waterproof design. This camera can be used for a long time. The captured image is displayed in true color, with a maximum of 24 bit per pixel. 4) Image collector: This device is a system-integrated structural component that centrally installs standard light sources, cameras, and cuvettes. 5) Host system: The host system uses an Intel quad-core processor, 4 G memory, 32 G solid-state hard disk system, runs the general Windows system, and is equipped with a software system. 6) Touch screen system: An embedded industrial resistive touch screen that measures 7 inches (17.78 cm), with a resolution of 1,024 × 600 and a high-definition industrial screen. It exhibits the advantages of shock resistance, vibration resistance, and high and low temperature resistance.

2.1.2 System software design

The system software is composed of functional modules, such as user information, image acquisition,

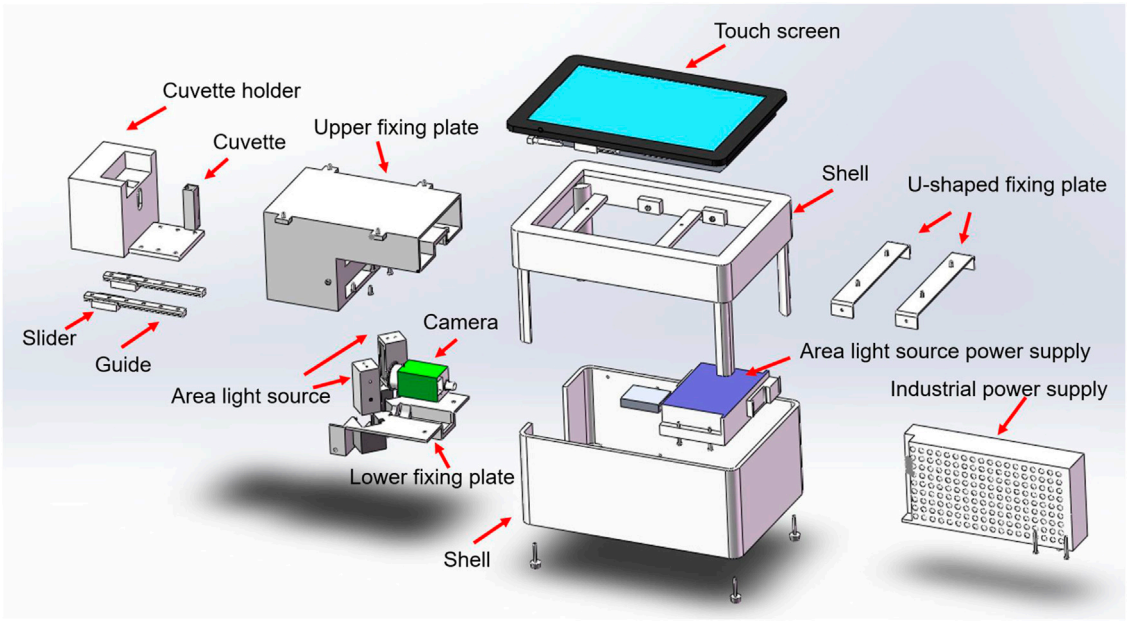

FIGURE 2
Schematic of the system hardware structure.

image processing, and image recognition. The wireless network enables the host computer to connect remotely to the server for data transmission. The system software processes and recognizes the collected images. Users can operate the software more conveniently through human–computer interaction in the touch screen system.

The functions of each module of the system software are as follows. 1) The primary function of the user information module is to record and manage the basic information of users. 2) The primary function of the image acquisition module is to transmit the image files captured by the camera to the software for real-time processing and identification. 3) The image processing module has basic image processing functions, such as region of interest extraction, smoothing denoising, bilateral denoising, and morphological processing. It can select images in key areas. It eliminates noise that may cause interference on an image while retaining the color information of the image to the greatest extent. Consequently, it improves image quality and makes an image easy to identify. 4) The image recognition module can identify the RGB value of image color in the key area and then convert the RGB color space model into the L*a*b* color space model. The hydration level that corresponds to the image is analyzed in accordance with the b* value. Then, the system provides the corresponding rehydration guidance on the basis of the hydration level.

2.2 System design principles

2.2.1 Principle of image acquisition

The system completes image acquisition through its components, including the LED standard light source, camera, and cuvette (Figure 3). The camera collects the color information of the urine in the cuvette, and the software extracts and analyzes the color information of the image. Cameras project optical signals onto an image sensor, convert the optical signals into electrical signals, and then into digital image signals. After the assembly of all hardware such as cameras and light sources, we use equipment to test standard samples to ensure that the results of multiple tests on the same sample are consistent. The standard curve is formed inside the software by determination of the standard sample. When the test sample is determined, the software can automatically correct the test value according to the standard curve.

The optical principle of liquid color imaging is based on the transmission of light. When light from a standard light source is transmitted onto urine, urine selectively absorbs light of different wavelengths. Using yellow as an example, urine selectively absorbs light of other colors, and only the yellow light is absorbed the least. Therefore, the yellow light is transmitted to the camera, and the urine appears yellow.

2.2.2 Color space model conversion algorithm

After the camera captures the image, the system software analyzes the RGB value of the image in the key area and then

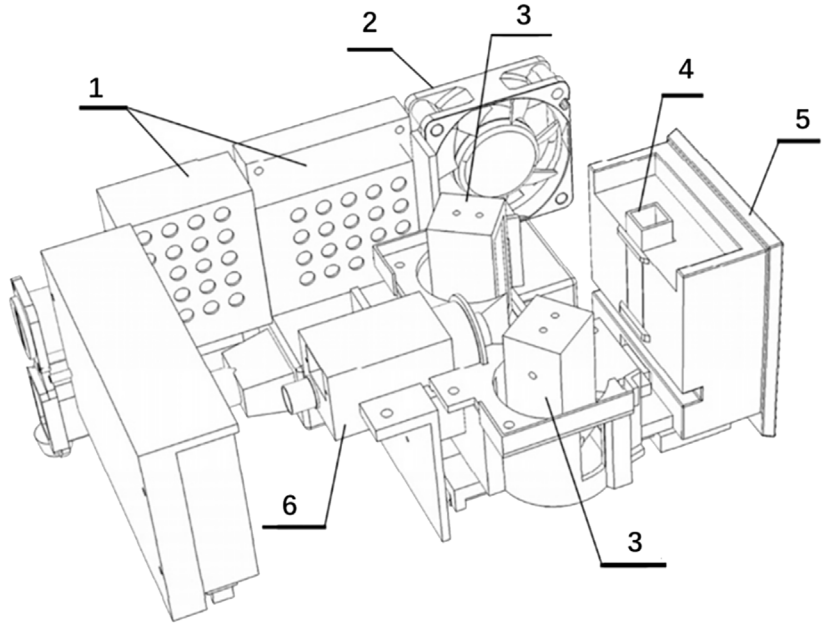

FIGURE 3
Schematic of image acquisition related structure. No. 1 refers to the industrial power supply. No. 2 refers to the cooling fan. No. 3 refers to the LED surface light source. No. 4 refers to the cuvette. No. 5 refers to the cuvette bracket. No. 6 refers to the camera.

converts the RGB color space model into the L*a*b* color space model. Then, in accordance with the b* value, the hydration level that corresponds to the urine sample is analyzed. The algorithm for converting the RGB color space model into the L*a*b* color space model is as follows (Chung et al., 2014):

(1) First, the *RGB* color space model is converted into the *XYZ* color space model:

$$\begin{bmatrix} X \\ Y \\ Z \end{bmatrix} = \begin{bmatrix} 0.4124 & 0.3575 & 0.1804 \\ 0.2126 & 0.7151 & 0.0721 \\ 0.0193 & 0.1191 & 0.9502 \end{bmatrix} \begin{bmatrix} R \\ G \\ B \end{bmatrix} \tag{1}$$

(2) Then, the *XYZ* color space model is converted into the *L*; a*b** color space model:

$$\begin{aligned} L* &= 116 f(Y/Y_n) - 16 \\ a* &= 500\left[f(X/X_n) - f(Y/Y_n)\right] \\ b* &= 200\left[f(Y/Y_n) - f(Z/Z_n)\right] \end{aligned} \tag{2}$$

Note: Xn = 95.047, Yn = 100.0, and Zn = 108.883.
Among them, the calculation formula of $f(t)$ is as follows:

$$f(t) = \begin{cases} t^{1/3} & \text{if } t > \left(\frac{6}{29}\right)^3 \\ \frac{1}{3}\left(\frac{29}{6}\right)^2 t + \frac{4}{29} & \text{elsewhere} \end{cases} \tag{3}$$

2.2.3 System hydration grading standard

We refer to the team's research base (Feng et al., 2022) and relevant high-quality literature (Armstrong et al., 1994; Casa et al., 2000; Racinais et al., 2015; Thomas et al., 2016; McDermott et al., 2017) to formulate the system's hydration grading standard in accordance with the corresponding relationship between urine color's b* value and the hydration level. We substituted the threshold values of each grade of Usg (1.000, 1.005, 1.010, 1.015, 1.020, 1.025, 1.030, and 1.035) into the linear regression equation (b = −1,220 + 1,220 Usg, R^2 = 0.657), and calculated the threshold value of each grade of urine color's b* value. The system calculates the corresponding rehydration volume on the basis of the user's weight and hydration level (Table 1). Then, the corresponding rehydration guidance is presented in the system's result report interface. For example, when a user's hydration level is 7 and his/her weight is 80 kg, the system will prompt: "You are seriously dehydrated. You are recommended to take 800 ml–1,200 ml of sports drinks. Pay attention for a short period while rehydrating. You are recommended to take 100 ml–200 ml of sports drinks every 10 min–20 min. The amount of fluid supplementation can be adjusted appropriately in accordance with the actual situation."

TABLE 1 System hydration grading standard.

Hydration level	Urine specific gravity	Hydration status	Urine color's b* value	Rehydration guidance
Level 1	1.000–1.005	Well hydrated	0–6.1	You are drinking enough.
Level 2	1.005–1.010	Well hydrated	6.1–12.2	You are drinking enough.
Level 3	1.010–1.015	Minimal dehydration	12.2–18.3	You can add up to 0.25% body weight in sports drinks.
Level 4	1.015–1.020	Minimal dehydration	18.3–24.4	You can add up to 0.25% body weight in sports drinks.
Level 5	1.020–1.025	Significant dehydration	24.4–30.5	You need to add 0.25%–0.5% body weight in sports drink.
Level 6	1.025–1.030	Significant dehydration	30.5–36.6	You need to add 0.5%–1% body weight in sports drink.
Level 7	1.030–1.035	Serious dehydration	36.6–42.7	You need to add 1%–1.5% body weight in sports drink.
Level 8	> 1.035	Serious dehydration	42.7–127	You need to add 1.5%–2% body weight in sports drink.

2.3 System operation process

The system operation process includes starting the system, filling in basic information, putting the sample, testing the sample, local data review, local data upload, and cloud data review (Figure 4).

The specific operation process of the system is as follows. 1) Start the system: The system is connected to the power data cable. The user starts the software system and enters the account number and password (Figures 4A,B). 2) Fill in the basic information: The user fills in the required information, such as "full name, height, weight, gender, date of birth, and sports events" (Figure 4C). 3) Put the sample: After the user cleans the cuvette with filter paper, a plastic straw is used to drop urine into the cuvette until about 2/3 of its capacity. The user drags out the bracket and loads the cuvette into the slot. Then, the user pushes the bracket back to its original position, seals the image acquisition system, and clicks "Place sample" (Figures 4D,E). 4) Detecting the sample: After the user puts the sample, the system's touch screen will display the image of the cuvette. Then, the user clicks "Test sample", fills in the "Location", checks the result report, and stores the test information. If the next sample still needs to be tested, then the user must clean the cuvette, reinsert the sample, and then test the sample (Figure 4F). 5) Local data review: After detection, the user can click "Data review" to view the historical test data of the system (Figure 4G). 6) Local data upload: When the system is connected to the network, users can upload local data to the cloud platform system (Figure 4G). 7) Cloud data review: The Internet cloud platform system forms a big data system by receiving detection data from each device. The user logs in to the system's website, enters his/her account number and password, and then views his/her historical data. Users can filter target data by clicking on different sports events and locations. Users can copy the data for further processing (Figure 4H).

3 Results and discussion

3.1 System testing

To test the stability and validity of the system, we collected the morning urine of 100 healthy high-level young athletes (age: 24.08 ± 3.73 years, height: 168.32 ± 13.36 cm, body mass: 61.05 ± 19.68 kg, 58 males/42 females), and used the system to determine the hydration level of the urine samples. We used IBM SPSS Statistics version 26.0 for data analysis. Statistical significance was accepted at $p < 0.05$.

3.1.1 System stability test

We repeated the detection of urine samples two times and conducted Pearson correlation analysis. Then, we found that the hydration levels of the two detection processes were highly correlated ($r = 1$, $p < 0.01$). The results suggested that system stability was high.

3.1.2 System validity test

The system is the first device used to monitor hydration level on the basis of urine color's L*a*b* parameters. Its detection principle is not the same as those of other hydration monitoring devices. At present, no "gold standard" for assessing hydration status has been accepted (Armstrong, 2007). By using Usg and urine osmolality as reference standards, we evaluated the validity of the system by analyzing the correlation between hydration level and Usg and urine osmolality. We used the system to test hydration levels, a digital refractometer (PAL-10S, Atago, Tokyo, Japan) to test Usg, and a vapor osmometer (Vapro 5,600, Wescor, United States) to test urine osmolality. Pearson correlation analysis was adopted for data. The results showed that hydration level exhibited a high correlation with Usg and urine osmolality ($r = 0.728$, 0.652, $p < 0.01$), indicating that the system had relatively high validity (Figure 5).

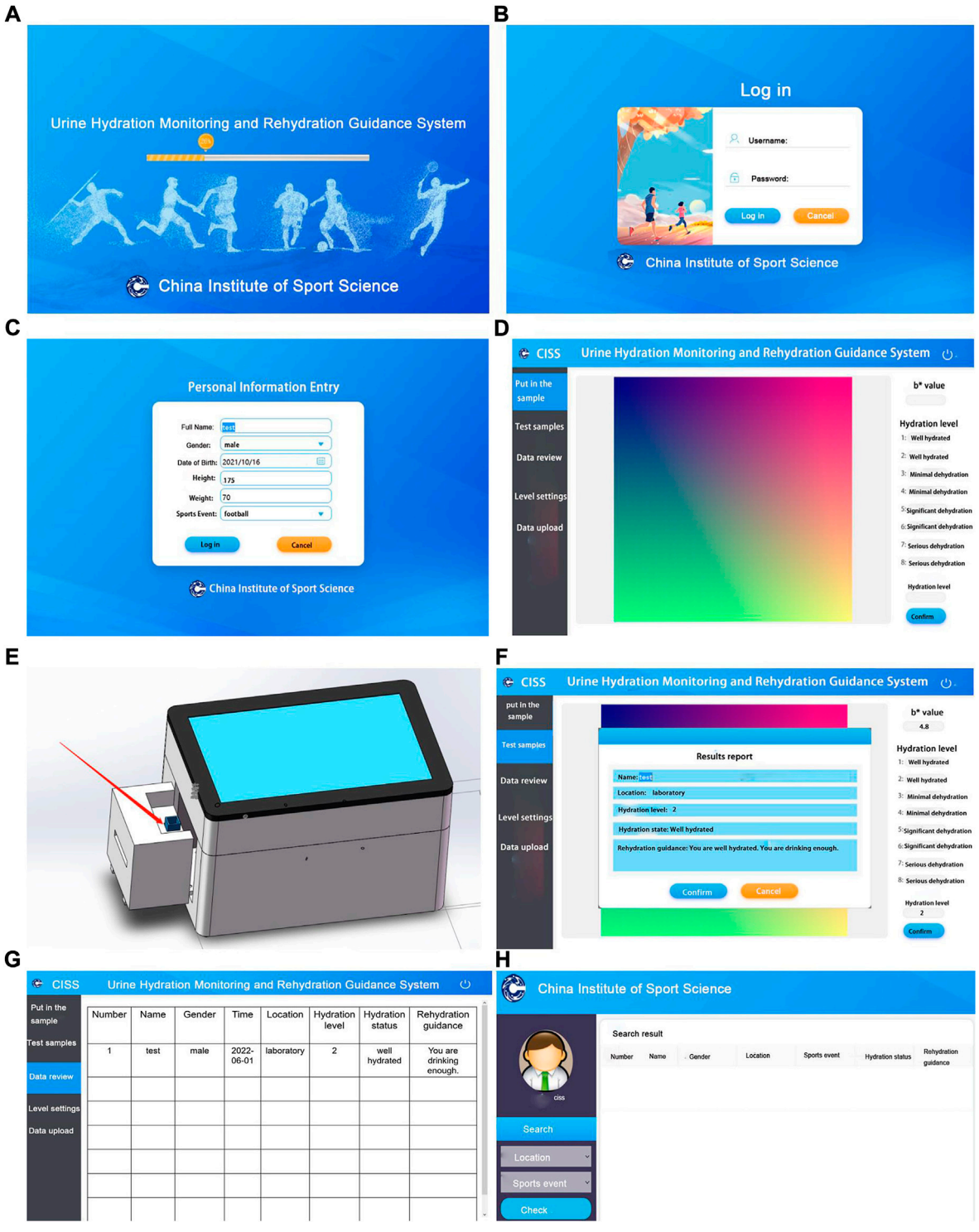

FIGURE 4
Schematic of the system interface and operation. **(A)** System entry interface, **(B)** login interface, **(C)** personal information entry interface, **(D)** sample insertion interface, **(E)** schematic of placing cuvette, **(F)** test sample and result report interface, **(G)** data upload and review interface, and **(H)** cloud data review interface.

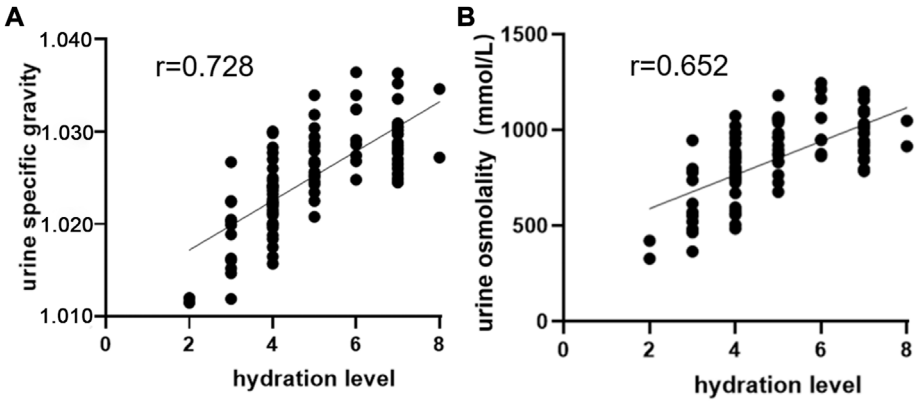

FIGURE 5
Correlation analysis of hydration level with Usg and urine osmolality. **(A)** Correlation analysis between hydration level and Usg. **(B)** Correlation analysis between hydration level and urine osmolality.

3.2 Strengths and limitations of the system

3.2.1 Strengths of the system

The strengths of the system are as follows. 1) At present, relevant hydration monitoring equipment adopts the RGB color space model. For the first time, we use the L*a*b* color space model to develop hydration monitoring and rehydration guidance equipment. The L*a*b* color space model covers all the colors that the human eyes can see, and it is currently the color space model with the widest color gamut. 2) This system uses urine color's b* value as a test index for the first time, introducing a new hydration assessment method. The detection method of this system is noninvasive and safe, and the cost is low. 3) The system strictly controls the test environment for urine color. Compared with the traditional visual urine color chart, the system's test results are unaffected by the operator's subjectivity and the external test environment. The system exhibits stable performance, high precision, a simple and friendly interface design, easy operation, and fast data analysis. It can distinguish different hydration states and provide real-time results. 4) The system is equipped with a 10 mm optical path quartz cuvette that is commonly sold in the market, and it presents good light transmittance. The amount of urine required for the system test is small. 5) The system cannot only save data locally but also transmit local data to the cloud for storage, realizing the long-term, permanent, and massive storage of test data. The system is capable of testing large sample sizes. System data can be processed and analyzed by researchers. 6) By using this system, athletes can have an intuitive visual perception of urine color and hydration level. Personalized rehydration guidance can also improve the enthusiasm and awareness of rehydration. 7) The appearance, hardware and software design of this system are unique and innovative. Compared with other urine hydration monitoring systems, this system has the function of rehydration guidance and standardized operation process.

3.2.2 Limitations of the system

The limitations and recommendations of the system are as follows. 1) The design of this system comprehensively considers factors, such as component cost, technical level, research, and development cycle, and funding. At present, the system is slightly large. In the future, the hardware can be designed to be more portable, and the system can be further updated to produce and popularize the system. 2) At present, no unified "gold standard" is available for assessing hydration (Armstrong, 2007). Therefore, we propose to integrate a variety of test indicators and methods for evaluating the hydration of athletes to achieve complementary advantages. 3) This system uses the urine color parameter as the evaluation index of hydration, and urine color may be affected by confounding factors, such as fluid intake, strenuous exercise, food, medicines, and diseases (Zubac et al., 2018). These factors may result in urine color that does not accurately identify the body's true hydration. Therefore, we recommend that athletes should minimize strenuous exercises and reduce intake of high-pigment fluids and food several hours before urine collection. 4) For the timing of urine collection, spot urine is fresh and readily available, but the test results are less accurate. Therefore, we recommend collecting morning urine sample, which is stable and the test results are easy to standardize (Baron et al., 2015; Cheuvront et al., 2015). In addition, urine hydration indicators are stable for up to 7 days in a refrigerated environment (Adams et al., 2017). If the hydration index cannot be tested immediately after collecting the urine sample, the urine sample should be stored under refrigeration and the test should be completed as soon as possible or within 1 week.

4 Conclusion

In this paper, we have successfully developed the urine hydration monitoring and rehydration guidance system for athletes based on urine color's L*a*b* parameters. The system can evaluate the hydration of athletes objectively and accurately. It provides intuitive and personalized rehydration guidance, offering a new method for solving practical problems in sports training. The system has high practical value and broad application prospects. It cannot only serve athletes in the field of competitive sports but also the general population in the fields of public health and medical care.

At present, the development of hydration monitoring system has been one of the research focuses. Athletes, soldiers, workers, children, pregnant women, the elderly, and ordinary adults all need timely hydration monitoring. For the first time, we took the L*a*b* parameters of urine color as test indicators, and successfully developed a urine hydration monitoring system. The ideal hydration monitoring equipment should be simple, fast, safe, portable, low-cost, non-invasive, cheap, easy to operate, effective, accurate and practical. In the future, we can combine multiple disciplines, adopt more new indicators and technologies, and develop various types of equipment to meet the needs of different populations and scenarios.

Data availability statement

The raw data supporting the conclusions of this article will be made available by the authors, without undue reservation.

Ethics statement

The studies involving human participants were reviewed and approved by Human Experiment Ethics Review Committee of the China Institute of Sport Science (Approval Number: 20220113). The patients/participants provided their written informed consent to participate in this study. Written informed consent was obtained from the individual(s) for the publication of any potentially identifiable images or data included in this article.

Author contributions

YF, GF, ML, and JZ contributed to the design of the system. SC, CQ, and XG assisted in completing system testing. YF performed the statistical analysis and wrote the first draft of the manuscript. GF, XG, and JZ revised the manuscript. All the authors contributed to manuscript revision. They read and approved the submitted version.

Funding

This study was supported by the National Natural Science Foundation of China (11775059), the Key Technologies of Physical Training and Training Monitoring in Winter Programs (No. 2019YFF0301600), and the Fundamental Research Foundation of the China Institute of Sport Science (19–22).

Acknowledgments

We wish to acknowledge and thank the China Institute of Sport Science for supporting us in completing the development of the system. We also thank Lanshan Yu and Xuehong Zou for their assistance with the study.

Conflict of interest

The authors declare that the research was conducted in the absence of any commercial or financial relationships that could be construed as a potential conflict of interest.

Publisher's note

References

Adams, J. D., Kavouras, S. A., Johnson, E. C., Jansen, L. T., Capitan-Jimenez, C., Robillard, J. I., et al. (2017). The effect of storing temperature and duration on urinary hydration markers. *Int. J. Sport Nutr. Exerc. Metab.* 27, 18–24. doi:10.1123/ijsnem.2016-0098

Armstrong, L. E. (2007). Assessing hydration status: The elusive gold standard. *J. Am. Coll. Nutr.* 26, 575S–584S. doi:10.1080/07315724.2007.10719661

Armstrong, L. E., Maresh, C. M., Castellani, J. W., Bergeron, M. F., Kenefick, R. W., Lagasse, K. E., et al. (1994). Urinary indices of hydration status. *Int. J. Sport Nutr.* 4, 265–279. doi:10.1123/ijsn.4.3.265

Barley, O. R., Chapman, D. W., and Abbiss, C. R. (2020). Reviewing the current methods of assessing hydration in athletes. *J. Int. Soc. Sports Nutr.* 17, 52. doi:10.1186/s12970-020-00381-6

Baron, S., Courbebaisse, M., Lepicard, E. M., and Friedlander, G. (2015). Assessment of hydration status in a large population. *Br. J. Nutr.* 113, 147–158. doi:10.1017/s0007114514003213

Belasco, R., Edwards, T., Munoz, A. J., Rayo, V., and Buono, M. J. (2020). The effect of hydration on urine color objectively evaluated in CIE L(*)a(*)b(*) color space. *Front. Nutr.* 7, 576974. doi:10.3389/fnut.2020.576974

Casa, D. J., Armstrong, L. E., Hillman, S. K., Montain, S. J., Reiff, R. V., Rich, B. S., et al. (2000). National athletic trainers' association position statement: Fluid replacement for athletes. *J. Athl. Train.* 35, 212–224.

Cheuvront, S. N., Kenefick, R. W., and Zambraski, E. J. (2015). Spot urine concentrations should not be used for hydration assessment: A methodology review. *Int. J. Sport Nutr. Exerc. Metab.* 25, 293–297. doi:10.1123/ijsnem.2014-0138

Chew, N., Noor Azhar, A. M., Bustam, A., Azanan, M. S., Wang, C., and Lum, L. C. S. (2020). Assessing dehydration status in dengue patients using urine colourimetry and mobile phone technology. *PLoS Negl. Trop. Dis.* 14, e0008562. doi:10.1371/journal.pntd.0008562

Chin, J. S.-Y., and Tisan, A. (2015). "An IoT-based pervasive body hydration tracker (PHT)," in 2015 IEEE 13th International Conference on Industrial Informatics (INDIN), Cambridge, UK, 22-24 July 2015, 437–441.

Chung, K.-L., Yang, W.-N., Lai, Y.-R., and Lin, L.-C. (2014). Novel peer group filtering method based on the CIELab color space for impulse noise reduction. *Signal Image Video process.* 8, 1691–1713. doi:10.1007/s11760-012-0403-4

Feng, Y., Fang, G., Qu, C., Cui, S., Geng, X., Gao, D., et al. (2022). Validation of urine colour L*a*b* for assessing hydration amongst athletes. *Front. Nutr.* 9, 997189. doi:10.3389/fnut.2022.997189

Garrett, D. C., Rae, N., Fletcher, J. R., Zarnke, S., Thorson, S., Hogan, D. B., et al. (2018). Engineering approaches to assessing hydration status. *IEEE Rev. Biomed. Eng.* 11, 233–248. doi:10.1109/rbme.2017.2776041

Gunawan, A., Brandon, D., Puspa, V., and Wiweko, B. (2018). Development of urine hydration system based on urine color and support vector machine. *Procedia Comput. Sci.* 135, 481–489. doi:10.1016/j.procs.2018.08.200

Hew-Butler, T., Rosner, M. H., Fowkes-Godek, S., Dugas, J. P., Hoffman, M. D., Lewis, D. P., et al. (2015). Statement of the 3rd international exercise-associated hyponatremia consensus development conference, carlsbad, California, 2015. *Br. J. Sports Med.* 49, 1432–1446. doi:10.1136/bjsports-2015-095004

Komatsu, T., Mohammadi, S., Busa, L. S., Maeki, M., Ishida, A., Tani, H., et al. (2016). Image analysis for a microfluidic paper-based analytical device using the CIE L*a*b* color system. *Analyst* 141, 6507–6509. doi:10.1039/c6an01409g

Manz, F. (2007). Hydration and disease. *J. Am. Coll. Nutr.* 26, 535s–541s. doi:10.1080/07315724.2007.10719655

Mcdermott, B. P., Anderson, S. A., Armstrong, L. E., Casa, D. J., Cheuvront, S. N., Cooper, L., et al. (2017). National athletic trainers' association position statement: Fluid replacement for the physically active. *J. Athl. Train.* 52, 877–895. doi:10.4085/1062-6050-52.9.02

O'brien, W. J., Groh, C. L., and Boenke, K. M. (1990). A new, small-color-difference equation for dental shades. *J. Dent. Res.* 69, 1762–1764. doi:10.1177/00220345900690111001

Racinais, S., Alonso, J. M., Coutts, A. J., Flouris, A. D., Girard, O., Gonzalez-Alonso, J., et al. (2015). Consensus recommendations on training and competing in the heat. *Sports Med.* 45, 925–938. doi:10.1007/s40279-015-0343-6

Thomas, D. T., Erdman, K. A., and Burke, L. M. (2016). American college of sports medicine joint position statement. Nutrition and athletic performance. *Med. Sci. Sports Exerc.* 48, 543–568. doi:10.1249/MSS.0000000000000852

Volterman, K., and Moore, D. (2014). Hydration for optimal health and performance in athletes. *Agro Food Ind. Hi Tech.* 25, 4–7.

Zubac, D., Reale, R., Karnincic, H., Sivric, A., and Jelaska, I. (2018). Urine specific gravity as an indicator of dehydration in Olympic combat sport athletes; considerations for research and practice. *Eur. J. Sport Sci.* 18, 920–929. doi:10.1080/17461391.2018.1468483

frontiers | Frontiers in Bioengineering and Biotechnology

TYPE Original Research
PUBLISHED 07 November 2022
DOI 10.3389/fbioe.2022.1025083

OPEN ACCESS

EDITED BY
Kawsar Ahmed,
Mawlana Bhashani Science and Technology University, Bangladesh

REVIEWED BY
Angel León-Buitimea,
Universidad Autonoma de Nuevo Leon, Mexico
Pedro Fernández-Soto,
University of Salamanca, Spain
Md Bellal Hossain,
The University of Sydney, Australia
Shobhitkumar Kiritkumar Patel,
Marwadi University, India

*CORRESPONDENCE
Honglan Yu,
1049251463@qq.com
Shijun Li,
zjumedjun@163.com

†These authors have contributed equally to this work

SPECIALTY SECTION
This article was submitted to Biosensors and Biomolecular Electronics, a section of the journal Frontiers in Bioengineering and Biotechnology

RECEIVED 22 August 2022
ACCEPTED 24 October 2022
PUBLISHED 07 November 2022

CITATION
Wang Y, Zhao X, Zhou Y, Lu J, Yu H and Li S (2022), Establishment and application of loop-mediated isothermal amplification coupled with nanoparticle-based lateral flow biosensor (LAMP-LFB) for visual and rapid diagnosis of Candida albicans in clinical samples.
Front. Bioeng. Biotechnol. 10:1025083. doi: 10.3389/fbioe.2022.1025083

Establishment and application of loop-mediated isothermal amplification coupled with nanoparticle-based lateral flow biosensor (LAMP-LFB) for visual and rapid diagnosis of *Candida albicans* in clinical samples

Yu Wang[1†], Xue Zhao[1†], Yuhong Zhou[2†], Jingrun Lu[1], Honglan Yu[1*] and Shijun Li[3*]

[1]Department of Clinical Laboratory, The First People's Hospital of Guiyang, Guiyang, China, [2]School of Public Health, The Key Laboratory of Environmental Pollution Monitoring and Disease Control, Ministry of Education, Guizhou Medical University, Guiyang, China, [3]Laboratory of Bacterial Infectious Disease of Experimental Center, Guizhou Provincial Centre for Disease Control and Prevention, Guiyang, China

Candida albicans is an opportunistic pathogenic yeast that predominantly causes invasive candidiasis. Conventional methods for detecting *Candida* species are costly, take 3–5 days, and require skilled technicians. Rapid pathogen identification is important in managing invasive candidiasis infection. Here, a novel molecular diagnostic assay termed loop-mediated isothermal amplification combined with nanoparticles-based lateral flow biosensor (LAMP-LFB) was developed for *C. albicans* rapid detection. A set of six primers was designed based on the *C. albicans* species-specific internal transcribed spacer 2 (ITS2) gene. The *C. albicans*-LAMP results were visually reported by LFB within 2 min. Various fungal strains representing *Candida* species, as well as several Gram-negative and Gram-positive bacterial species, were used to determine the analytical sensitivity and specificity of the assay. The optimal LAMP conditions were 64 °C for 40 min, with a sensitivity of 1 fg of genomic DNA template from *C. albicans* pure cultures. No cross-reactions were obtained with non-*albicans* strains. Thus, the analytical specificity of the LAMP-LFB assay was 100%. The entire procedure could be completed within 85 min, including specimen processing (40 min), isothermal reaction (40 min), and result reporting (within 2 min). In 330 clinical samples (including 30 whole blood, 100 middle segment urine, and 200 sputum samples), all *C. albicans*-positive (62/330) samples were identified by LAMP-LFB assay, and the diagnostic accuracy was 100% when compared to the traditional clinical cultural-based methods. Thus, this assay can be used as a diagnostic tool for the rapid, accurate, sensitive, low-cost and specific detection of *C. albicans* strains, especially in resource-limited settings.

KEYWORDS

Candida albicans, loop-mediated isothermal amplification, lateral flow biosensor, LAMP-LFB, limit of detection

Introduction

The invasive fungal disease is a neglected disease that threatens public health, is difficult to diagnose with long treatment time, costly, and poor treatment efficacy (Fisher et al., 2020; Rodrigues and Nosanchuket al., 2020). Epidemiological statistics depict that invasive fungi cause more than two million infections yearly, and the number of deaths is equivalent to tuberculosis or malaria (Schmiedel and Zimmerli, 2016). Invasive candidiasis is the most common invasive fungal disease with high morbidity and mortality. Even when the patients are treated with antifungal therapy, the mortality rate is as high as 45%, and approximately 50% of cases are attributed to *C. albicans* (Zilberberg et al., 2008; Dadar et al., 2018; Quindós et al., 2018). *C. albicans* is a symbiotic yeast on the human mucosal surface. Simultaneously, *C. albicans* is an opportunistic pathogen responsible for invasive candidiasis such as pyelonephritis, endocarditis, or candidemia (Sherry et al., 2014). According to several recent studies, biofilm formation strengthens *C. albicans* drug resistance and the immune system (Ben-Ami 2018). Additionally, the emergence of drug-resistant strains such as *Candida auris* is partially attributable to empirical treatment without an early and clear diagnosis (Adams et al., 2018; Eyre et al., 2018). Thus, patients lose the optimum time for treatment leading to increased mortality, and drug-resistant strains become prevalent (Fortún et al., 2012). Therefore, rapid and accurate *C. albicans* detection is critical in the prevention, control, and timely treatment of invasive candidiasis, and it can also prevent the emergence of drug-resistant strains.

Unfortunately, current methods for detecting *C. albicans* infections are inadequate to meet clinical requirements. The traditional culture method is the gold standard for diagnosing fungal infections, but it is time-consuming and insensitive (Pincus et al., 2007). Moreover, *C. albicans* detection is easily confused with *Candida dubliniensis* in some colorimetric methods; *C. albicans* is not always detected accurately and rapidly. Therefore, it is important to establish a rapid and effective method for *C. albicans* detection in grass-roots hospitals. Rapid detection receives considerable attention due to the high morbidity and mortality of invasive candidiasis and the increasing prevalence of drug-resistant candidiasis. In recent years, many methods that are more sensitive and faster than traditional culture have emerged for the identification of *C. albicans* have been developed, such as immunofluorescence (Gunasekera et al., 2015) and PCR-based assay (i.e., multiplex PCR and real-time PCR) (Kasai et al., 2006) and mass spectrometry (Zehm et al., 2012). These methods are unsuitable for popularization, especially in resource-poor areas, because they are complex and require expensive equipment and professionals.

In recent years, various isothermal amplification methods, including loop-mediated isothermal amplification (LAMP), multiple cross displacement amplification (MCDA), and recombinase polymerase amplification (RPA), have been designed for nucleic acid analysis to overcome the disadvantages of traditional culture and PCR-based methods and have been reported to detection of *C. albicans* (Zhao et al., 2019; Fallahi et al., 2020; Wang F. et al., 2021). Among them, loop-mediated isothermal amplification (LAMP) is a nucleic acid amplification technique under isothermal conditions that is simpler, economical, sensitive, and rapidly applied in many fields, especially in molecular medical diagnostics (Notomi et al., 2000; Dolka et al., 2019). For example, the LAMP method has been applied successfully to detect *Staphylococcus aureus*, *C. auris*, and the COVID-19 virus (Wang et al., 2017; Yamamoto et al., 2018; Zhu et al., 2020). Conventionally, LAMP amplification products can be tested using various methods, including agarose gel electrophoresis and turbidimetry changes (Hill et al., 2008; Zhao et al., 2020). However, these methods been restricted due to the need for expensive special equipment (real-time turbidimeter or fluorescence apparatus), expensive regents (calcein), and additional analysis procedure (agarose gel electrophoresis) to indicate assay's results. Therefore, an economical, rapid, simple, accurate, and suitable method for *C. albicans* detection is needed urgently.

In the past few years, nanomaterial-based biosensors have been widely used for the bioassay detection of a broad variety of targets in specimens from cancer patients (Patel et al., 2022a; Azzouz et al., 2022), cardiovascular disease (Azzouz et al., 2021), metabolites in sweat (Wang et al., 2022), proteins (Patel et al., 2022b), bacteria (Li et al., 2019) and fungi (Wang Y. et al., 2021). In the diagnosis of fungi and bacterial infections, biosensors are extremely accurate and quick (Li et al., 2019; Wang Y. et al., 2021). In the current study, we aim to combine classic Loop-mediated isothermal amplification (LAMP) with the gold nanoparticle-based lateral flow biosensors (LFB) to detect *C. albicans*, which is a new method to detect specific gene fragments of microbial with convenient and visual (Li et al., 2019). Moreover, we evaluated the ability to detect clinical samples with *C. albicans*-LAMP-LFB, to establish a fast, economical, accurate, and convenient tool for *C. albicans* detection in clinical applications.

Materials and methods

Reagents and instruments

Fungal and Bacterial genomic DNA extraction kits (Baitaike DNA mini kits, China) were obtained from Baitaike. Co., Ltd (Beijing, China). DNA Isothermal amplification kits, colorimetric indicator (Visual detection reagent, VDR), and biotin-14-dCTP were supplied by Tian-Jin HuiDeXin Biotech. Co., Ltd (Tianjin, China). The LFB materials, including the

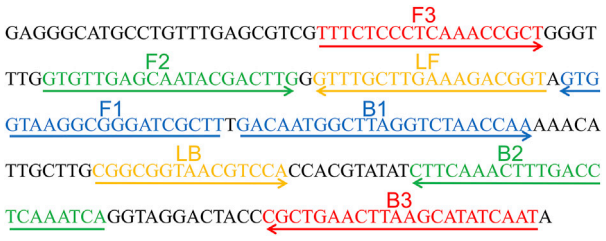

FIGURE 1
Sequence and location of ITS2 gene used to design loop-mediated isothermal amplification primers. The nucleotide sequences of the sense strand of ITS2 are listed. Right arrows and left arrows indicate sense and complementary sequences that are used.

backing card, sample pad, conjugate pad, absorbent pad, and nitrocellulose membrane (NC), were obtained from Jie-Yi Biotech. Co., Ltd (Shanghai, China). Rabbit anti-fluorescein antibody (Anti-FITC) and biotinylated bovine serum albumin (biotin-BSA) were acquired from Abcam. Co., Ltd (Shanghai, China). Dye (Crimson red) streptavidin-coated polymer nanoparticles (129 nm, 10 mg ml^{-1}; 100 mm borate, pH 8.5, with 0.1% BSA, 0.05% Tween 20 and 10 mm Ethylene Diamine Tetraacetic Acid, EDTA) were purchased from Bangs Laboratories, Inc (Indiana, United States).

LAMP assay primers design and synthesis

A set of six primes including two inner primers (FIP and BIP), two outer primers (F3 and B3), and two loop primers (LF and LB), were designed based on the reaction mechanism of LAMP to target the sequence of internal transcribed spacer 2 (ITS2) gene (Genbank accession no. AF455531.1) of *C. albicans* for the LAMP assay. All primers were designed using Primer Explorer V5 (http://primer-explorer.jp/e/; Eiken Chemical Co., Ltd, Tokyo, Japan) and validated using the basic local alignment search tool (BLAST). Figure 1 displays primer positions, while Table 1 depicts the primer sequences and modifications. In this study, all the primers were synthesized by Kunming-Tsingke Biotechnology Co., Ltd (Kunming, China) with HPLC purification grade.

Fungal and bacterial strains genomic DNA preparation

The 43 fungal and four bacterial strains were employed in the current study (Table 2), including the *C. albicans* reference strain (ATCC10231), 15 isolated *C. albicans*, and 27 non-*C. albicans* fungal strains from clinical samples. All genomic DNA templates were extracted using DNA extraction kits following the manufacturer's instructions, and the concentration and purity were measured using a Nanodrop 2000 (Thermo Fisher Scientific) at A260/280. The extracted DNA templates were stored at −20°C until further analysis. The genomic DNA of the *C. albicans* reference strain (ATCC10231) was serially diluted to concentrations ranging from 10 ng/μL to 100 ag/μL (10 ng/μL, 10 pg/μL, 1 pg/μL, 100 fg/μL, 10 fg/μL, 1 fg/μL, and 100 ag/μL), to optimize the reaction temperature, reaction time, specificity and sensitivity.

Gold nanoparticle-based lateral flow biosensor preparation

LFB was constructed and used for reporting LAMP results according to the description of a previous publication in our study (Li et al., 2019). Briefly, LFB included an absorbent pad, an immersion pad, an NC membrane, a conjugate pad, and a backing pad. Dye streptavidin-coated polymer nanoparticles (SA-PNPs) were impregnated on the conjugate pad. Then, anti-FITC and biotin-BSA were immobilized at the test line

TABLE1 Primers used in this study.

Primers name[a]	Sequences and modifications (5′-3′)[b]	Length[c]	Gene
F3	TTTCTCCCTCAAACCGCT	18 nt	ITS2
B3	ATTGATATGCTTAAGTTCAGCG	22 nt	
FIP	AAGCGATCCCGCCTTACCAC-GTGTTGAGCAATACGACTTG	41 mer	
FIP*	biotin-AAGCGATCCCGCCTTACCACGTGTTGAGCAATACGACTTG	41 mer	
BIP	GACAATGGCTTAGGTCTAACCAA-TGATTTGAGGTCAAAGTTTGAAG	47 mer	
LF	ACCGTCTTTCAAGCAAAC	18 nt	
LF*	FAM-ACCGTCTTTCAAGCAAAC	18 nt	
LB	CGGCGGTAACGTCCA	15 nt	

[a]FIP*, 5′-labeled with biotin when used in the C. albicans-LAMP-LFB, assay; LF*, 5′-labeled with FAM, when used in the C. albicans-LAMP-LFB, assay.
[b]FAM, 6-carboxy-fluorescein.
[c]Mer: monomeric; nt: nucleotide.

TABLE 2 Fungi and bacteria strains used in the study.

Strains	Strain no. (source of strain)[a]	No.of strains	*C. albicans -LAMP-LFB*[b]
Candida albicans	ATCC 10231	1	P
Candida albicans	Isolated strains (GFPH)	15	P
Candida dubliniensis	Isolated strains (GFPH)	1	N
Candida tropicalis	ATCC 13803	1	N
Candida tropicalis	Isolated strains (GFPH)	5	N
Candida krusei	Isolated strains (GFPH)	5	N
Candida glabrata	Isolated strains (GFPH)	5	N
Candida parapsilosis	Isolated strains (GFPH)	5	N
Cryptococcus neoformans	Isolated strains (GFPH)	1	N
Penicillium mameffei	Isolated strains (GFPH)	1	N
Candida stellatoidea	Isolated strains (GFPH)	1	N
Candida guilliermondi	Isolated strains (GFPH)	1	N
Aspergillus flavus	Isolated strains (GFPH)	1	N
Staphylococcus aureus	Isolated strains (GFPH)	1	N
Klebsiella pneumoniae	Isolated strains (GFPH)	1	N
Pseudomonas aeruginosa	Isolated strains (GFPH)	1	N
Acinetobacter baumannii	Isolated strains (GFPH)	1	N

[a]GFPH, The First People's Hospital of Guiyang; ATCC, american type culture collection.
[b]P, positive; N,negative. Only genomic DNA, templates from C. albicans could be detected by C. albicans-LAMP-LFB, assay, indicating the extremely high specificity of the method.

(TL) and control line (CL), respectively. According to our design, the LFB was manufactured timely by Tian-Jin HuiDeXin Biotech. Co., Ltd (Tianjin, China). The LFB was stored in a dry place away from light at a storage temperature of 2°C–25°C, valid for 18 months.

The standard *C. albicans*-LAMP assay

C. albicans-LAMP reactions were conducted per the manufacturer's instructions for the DNA Isothermal amplification kits. Each reaction mixture contained 12.5 μl of supplied buffer (2×), 0.4 μm of each outer primer, F3 and B3, 0.8 μm of each loop primer, LF* and LB, 1.6 μm of each inner primer, FIP* and BIP, 0.4 mm biotin-14-dCTP, 1 μl (8 U) 2.0 Bst DNA polymerase, and one μ1 DNA template and 1 μl VDR, and distilled water (DW) to a total volume of 25.0 μl. The reaction mixture was incubated for 40 min at 64°C. Moreover, genomic DNA from non-*C. albicans* strains, including *Candida tropicalis* and *Klebsiella pneumoniae,* were used as a negative control (NC), and blank control mixtures contained 1 μl of distilled water (DW). The *C. albicans*-LAMP products were determined and verified using two distinct techniques, including VDR and LFB methods. The color of the amplified products effectively changed from colorless to light green in the VDR assay. However, the negative and blank controls remained colorless. The strategy for visualizing LAMP products with LFB was as previously described.

Reaction temperature optimization for *C. albicans*-LAMP assay

In this study, the optimal temperature of the *C. albicans*-LAMP assay was confirmed by setting the different reaction temperatures (61–68°C, with 1°C intervals) and using *C. albicans* reference strain (ATCC10231) template DNA (10 pg/μl). Amplification mixtures containing 1 μl of *C. tropicalis* and *K. pneumoniae* template were used as NC, and 1 μl of DW was used as a blank control. The assay was performed according to the standard LAMP assay and was monitored using the Loopamp Realtime Turbidimeter LA-500 (Eiken Chemical Co., Ltd., Japan). Moreover, the threshold value (turbidity) was 0.1, and turbidity of >0.1 was considered positive amplification (Li et al., 2019).

Sensitivity of the *C. albicans*-LAMP-LFB assays

The genomic DNA templates from *C. albicans* (ATCC10231) pure culture were serially diluted 10-fold (10 ng, 10 pg, 1 pg, 100 fg, 10 fg, 1 fg, and 100 ag per microliter) to confirm the limit of detection (LoD) and to test the analytical sensitivity of LAMP-LFB assay. The LAMP-LFB reactions were carried out under the standard conditions described above, and the results were examined using a VDR and LFB. The LoD of the LAMP-LFB

assay was verified as the last dilution of each positive test. Each dilution was tested at least three times.

Reaction time optimization for *C. albicans*-LAMP assay

Four amplification reaction times (30, 40, 50, and 60 min, with 10 min intervals) were evaluated to optimize the amplification reaction time of *C. albicans*-LAMP. The *C. albicans*-LAMP reactions were performed under standard conditions, and the results were reported using LFB. Each amplification time was repeated three times.

Specificity of the *C. albicans*-LAMP-LFB assays

Genomic DNA (at least 10 ng/μl) was detected from 16 *C. albicans* strains, 27 non-*C. albicans* fungal strains and four bacterial strains according to the optimal amplification temperature and time to evaluate the specificity of *C. albicans*-LAMP-LFB assay (Table 2). All LAMP results were verified using LFB. Each sample was analyzed thrice independently.

Application of *C. albicans*-lamp-LFB assay in clinical samples

A total of 330 clinical samples (including 30 whole blood, 100 middle segment urine, and 200 sputum samples) were collected from the First People's Hospital of Guiyang suspected of having Candida infection to assess the applicability of the *C. albicans*-LAMP-LFB assay. All clinical samples were detected for *C. albicans* using traditional clinical cultural-based and *C. albicans*-LAMP-LFB methods. The routine diagnosis of *Candida* species in the laboratory was carried out using diagnostic methods such as CHROMagar *Candida* and biochemical identification. The *C. albicans*-LAMP-LFB detection was performed as described above.

Results

Detection and confirmation of *C. albicans*-LAMP products

The LAMP amplification reaction was incubated for 40 min at a constant temperature of 64°C to confirm the availability of *C. albicans*-LAMP primers. Then, the *C. albicans*-LAMP products were examined using the VDR and LFB methods. The *C. albicans*-LAMP amplified products appeared bright green under visible light, while the negative samples and blank control reactions remained colorless (Figure 2A). *C. albicans*-LAMP amplification was further confirmed by the appearance of two crimson red bands (CL and TL) in LFB, while the negatives samples and blank control only appeared as a crimson red line (CL) in LFB (Figure 2B). Therefore, the results suggested that the LAMP primer set targeting the ITS2 gene was valid for establishing the LAMP-LFB assay for *C. albicans* detection.

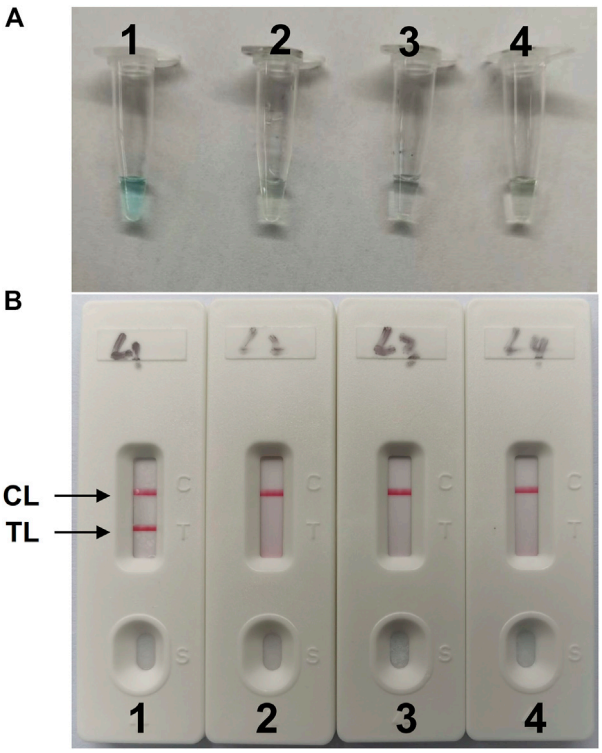

FIGURE 2
Detection and validation of (C) *albicans*-LAMP products **(A)**, Color change of *C. albicans*-LAMP tubes; **(B)**, biosensor applied for visual detection of *C. albicans*-LAMP products. Tube A1 (biosensor B1), positive amplification; tube A2 (biosensor B2), negative amplification (*Candida tropicalis*), tube A3 (biosensor B3), negative amplification (*Klebsiella pneumoniae*), tube A4 (biosensor B4), negative control (DW); TL, test line; CL, control line.

Optimal temperature of *C. albicans*-LAMP assay

The optimization test was performed to obtain the optimal reaction temperature for the *C. albicans*-LAMP experiment by setting a series of amplification temperatures (ranging from 61 to 68°C, with 1°C interval). The results were monitored using real-time turbidity measurements. The kinetics graphs were produced from the eight temperatures, with the faster reactions obtained for *C. albicans*-LAMP reactions at approach temperature of 62–65°C (Figure 3). Hence, we selected 64°C as the optimal amplification temperature for the *C. albicans*-LAMP-LFB assay.

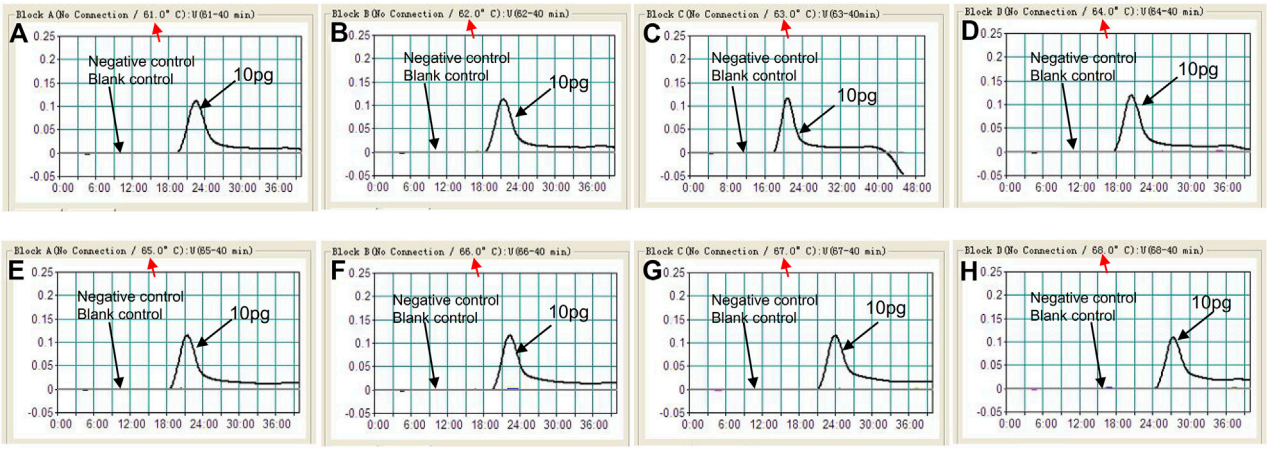

FIGURE 3
Optimization of amplification temperature for the *C. albicans*-LAMP primer set. The LAMP reactions for detection of *C. albicans* were monitored through realtime turbidity (LA-500), and the corresponding curves of concentrations of templates were marked in the figures. Eight kinetic graphs **(A–H)** were generated at various temperatures (61–68°C, 1°C intervals) with target pathogens DNA at the level of 10 pg per tube (The threshold value was 0.1 and the turbidity of >0.1 was considered to be positive). The graphs from B (62°C) to E (65°C) showed robust reaction. The optimal amplification temperature was 64°C.

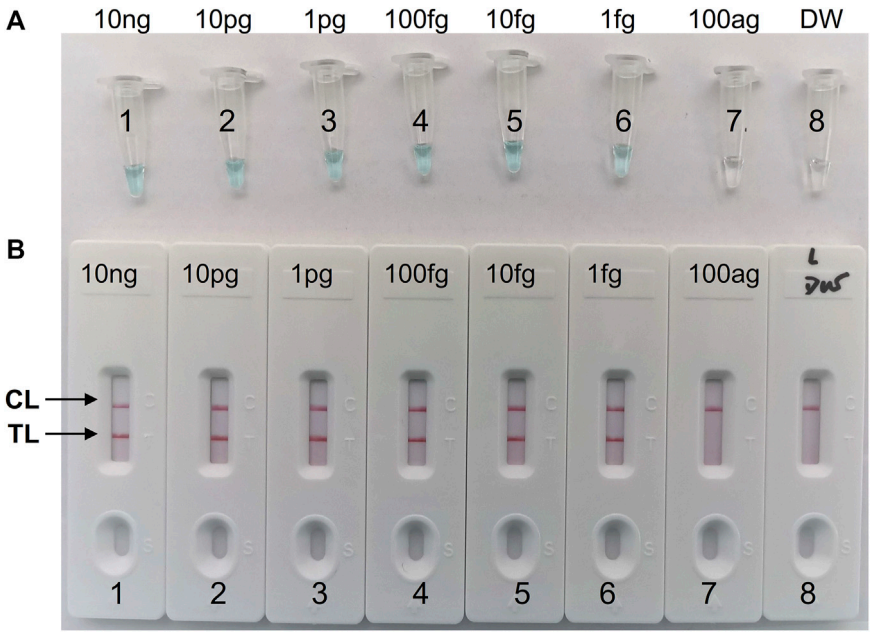

FIGURE 4
Sensitivity analysis of the *C. albicans*-LAMP-LFB assay with serial dilutions of *C. albicans* genomic DNA concentrations. Two detection methods involving a colorimetric indictor (VDR) **(A)** and LFB **(B)** were used to analyze the LAMP products. The genomic DNA was serially diluted (10 ng, 10 pg, 1 pg, 100 fg, 10 fg, 1 fg, and 100 ag per microliter) and subjected to standard LAMP. Tubes A1-7 (Biosensors B1-7), *C. albicans* strain (ATCC 10231) genomic templates (10 ng-100 ag); Tube A8 (Biosensor B8), blank control (DW), respectively. The LoD of *C. albicans*-LAMP was one fg per reaction.

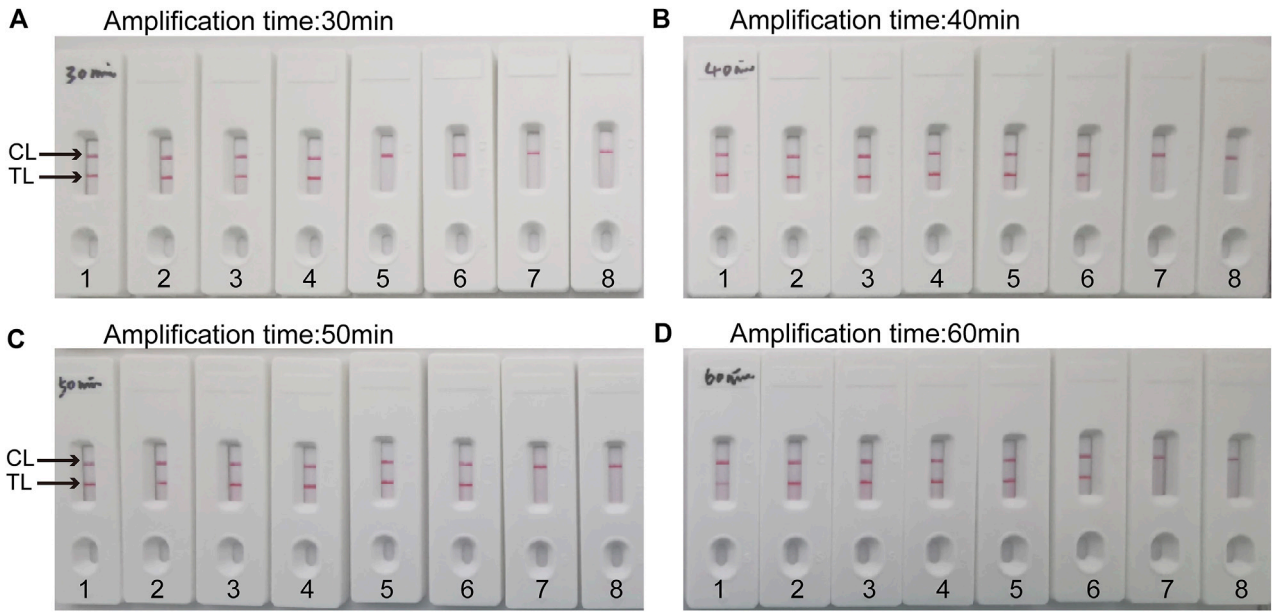

FIGURE 5
Optimal duration of time required for *C. albicans*-LAMP-LFB assay Four amplification times **(A)**, 30 min; **(B)**, 40 min; **(C)**, 50 min; **(D)**, 60 min) were evaluated at 64 °C. Biosensors 1, 2, 3, 4, 5, 6, 7, and eight represent genomic DNA (*C.albicans* (ATCC 10231)) levels of 10 ng, 10 pg, 1 pg, 100 fg, 10 fg, one fg and 100 ag target template per reaction and blank control (DW), respectively. The optimal time was showed when the amplification lasted for 40 min **(B)**.

Sensitivity of *C. albicans*-lamp-LFB detection

In our study, repeated detection of serial dilutions of *C. albicans* genomic DNA confirmed the sensitivity of the *C. albicans*-LAMP-LFB method. The *C. albicans*-LAMP-LFB assay LoD of template DNA was 1 fg/μl. Visual inspection of LAMP products with VDR reagents (Figure 4A) revealed CL and TL lines (red) on LFB, indicating positive amplification of the ITS2 gene (Figure 4B). The biosensors of the blank controls displayed only the CL line.

Optimal time of *C. albicans* -lamp-LFB assay

Four reaction time intervals (30, 40, 50, and 60 min) were tested at 64°C to obtain an optimal reaction time for *C. albicans*-LAMP-LFB. The *C. albicans*-LAMP products were identified through VDR and LFB methods. The results confirmed that the *C. albicans* (ATCC 10231) genomic DNA template was detected at the LoD level (1 fg) when the *C. albicans*-LAMP reaction lasted for 40 and 50 min at 64°C (Figure 5). There is no significant difference between the 40 min and 50 min lines. Therefore, a response time of 40 min was chosen for the LAMP-LFB test of *C. albicans*. Incubating *C. albicans*-LAMP-LFB at 64°C for 40 min was the optimal time. Thus, the whole diagnostic procedure of the *C. albicans*-LAMP-LFB assay, including Genomic DNA extraction (40 min), LAMP reaction (40 min) and result indicating (<2 min), can be completed within 85 min (Figure 6).

Specificity of *C. albicans*-lamp-LFB detection

The specificity of the *C. albicans*-LAMP-LFB assay was evaluated using DNA from 47 strains, including 1 *C. albicans* reference strain (ATCC10231), 15 *C. albicans* isolated strains, 27 non-*C. albicans* fungal strains and four bacterial strains (Table 2). Figure 7 illustrates that the *C. albicans*-LAMP-LFB assay detected all *C. albicans* strains while not detecting non-*C. albicans* fungal or bacterial strains. Hence, the *C. albicans*-LAMP-LFB assay can accurately differentiate *C. albicans* from other microbes.

Application of the LAMP-LFB assay in clinical samples for *C. albicans* detection

To verify the practical application of *C. albicans*-LAMP-LFB as a valuable tool for target pathogen detection. Traditional culture method identified *C. albicans* in 62 (18.8%) of the 330 samples (including two of the 30 whole blood, 18 of the 100 middle segment

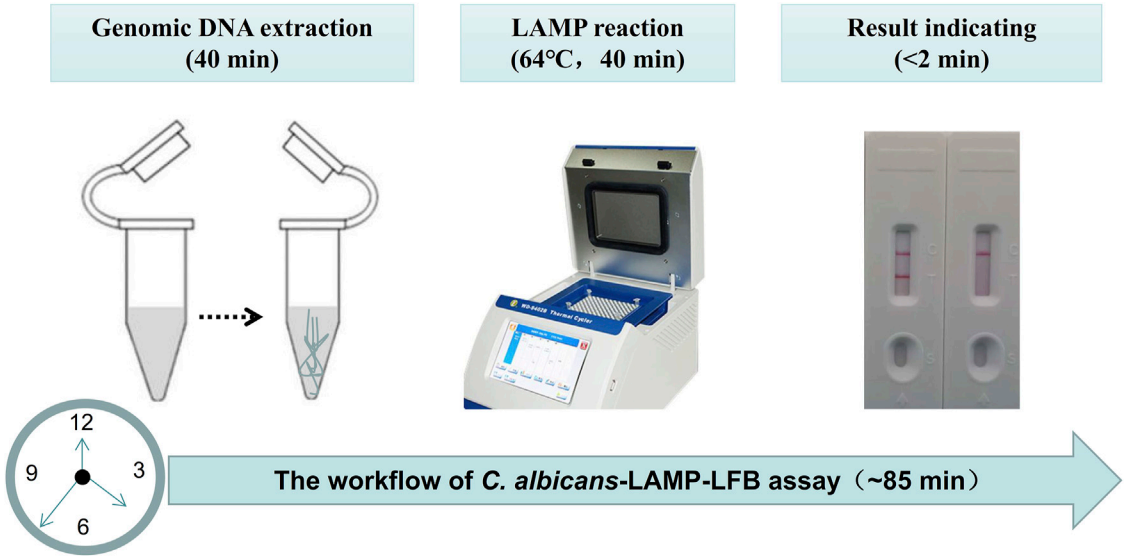

FIGURE 6
The workflow of *C. albicans*-LAMP-LFB assay. Three steps, including Genomic DNA extraction (40 min), LAMP reaction (40 min) and result reporting (<2 min), are required for the *C. albicans*-LAMP-LFB assay, and the total procedure can be completed within 85 min.

urine, and 42 of the 200 sputum samples), while the remaining 268 samples contained other bacteria or were microbe-free. The *C. albicans*-LAMP-LFB assay results were consistent with the traditional cultivation detection results. Table 3 suggests that the *C. albicans*-LAMP-LFB assay established in the current study could be used as an advanced tool to detect *C. albicans* in clinical samples.

Discussion

C. albicans is a common but important opportunistic pathogen that frequently causes superficial and deep fungal infections and is primarily responsible for invasive candidiasis such as pyelonephritis, endocarditis, and candidemia (Gow and Yadav, 2017). It is also considered the fourth leading cause of hospital bloodstream infection, with unacceptably high mortality rates (Dadar et al., 2018). Currently, invasive candidiasis is difficult to diagnose and has a poor prognosis, posing a huge burden on public health worldwide (Casadevall, 2019). However, antifungal drugs can be employed to treat fungal infections; early and accurate diagnosis results in effective treatment outcomes. Moreover, *C. albicans* has increased drug resistance by forming biofilms, making antifungal treatments more intractable (Ben-Ami, 2018). Therefore, developing a rapid and accurate diagnostic method for *C. albicans* is a high priority to improve patient quality of life, reduce patient mortality and drug resistance. Rapid pathogen identification is important in controlling and managing invasive candidiasis infection (McCarty and Pappas, 2015). However, current methods for diagnosing *C. albicans* infection are time-consuming, cumbersome, and uneconomical. Hence, an accurate, rapid, simple, and economical method for detecting *C. albicans* is urgently needed. This report combined classic LAMP with LFB to detect *C. albicans*. LAMP primer sets, including two inner primers (FIP and BIP), two outer primers (F3 and B3), and two loop primers (LF and LB), were designed per LAMP rules to recognize the sequence of the ITS2 gene of *C. albicans* with a high degree of specificity (Notomi et al., 2000). The entire procedure could be completed within 85 min, including specimen processing (40 min), isothermal reaction (40 min), and result reporting (within 2 min). Importantly, we could visually evaluate the *C. albicans*-LAMP results based on the bands on the LFB within 2 min; even non-experts can correctly interpret the results.

LAMP is more convenient and cost-effective than traditional methods such as direct microscopy, but it is not sensitive enough to distinguish all *Candida* species. Thus, the diagnosis can be ambiguous, delaying precise treatment. Although the CHROMagar *Candida* method is simple, it is time-consuming (maybe spend 3 days or more). Moreover, it is impossible to distinguish all *Candida* species, especially due to the color similarity of the colonies, such as *Candida dubliniensis* (Ells et al., 2011). Furthermore, compared to other molecular diagnostic methods that are more accurate and time efficient than traditional culture methods, real-time PCR, for example, requires professionals to operate special instruments to change the temperature to complete the experiment, making it cumbersome and uneconomical, limiting its application, especially in areas where resources are scarce (Asadzadeh et al., 2018). In this reaction system, the optimal LAMP conditions were 64°C for 40 min; a very simple and inexpensive device, such as a

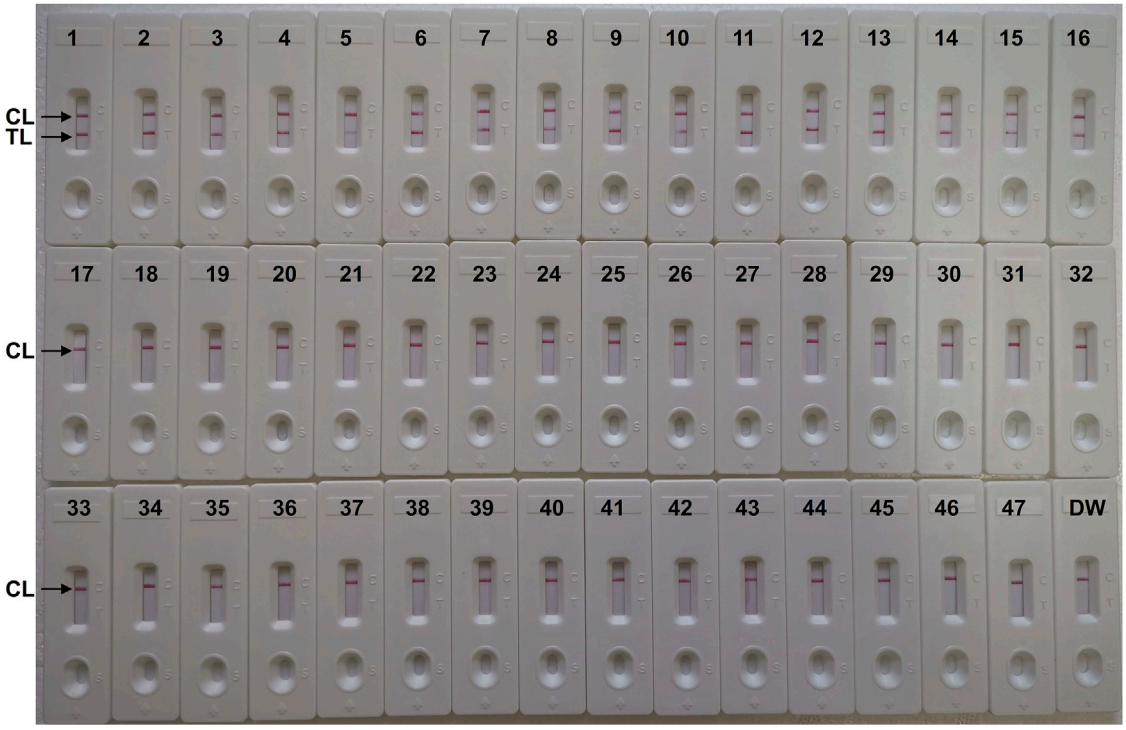

FIGURE 7
The specificity of *C. albicans*-LAMP-LFB assay for different strains. The *C. albicans*-LAMP-LFB assay was evaluated with different strains genomic DNA as templates. Two crimson lines (TL and CL) were appeared on the LFB, indicating positive results for the *C. albicans* isolates. Only a visible red line (CL) at the detection zone of LFB, reporting the negative results for non-*C. albicans* strains and blank control (DW). Biosensor1, Positive control (*C. albicans* ATCC 10231), Biosensors 2-16, isolated *C. albicans* strains; Biosensor 17, *Candida dubliniensis*; Biosensor18, *Candida tropicalis* (ATCC 13803); Biosensors19-23, isolated *Candida tropicalis* strains; Biosensors 24-28, isolated *Candida krusei* strains; Biosensors 29-33, isolated *Candida glabrata* strains; Biosensors 34-38, isolated *Candida parapsilosis* strains; Biosensor 39, *Cryptococcus neoformans*; Biosensor 40, *Penicillium mameffei*; Biosensor 41, *Candida stellatoidea*; Biosensor 42, *Candida guilliermondi*; Biosensor 43, *Aspergillus flavus*; Biosensor 44, *Staphylococcus aureus*; Biosensor 45, *Klebsiella pneumoniae*; Biosensor 46, *Pseudomonas aeruginosa*; Biosensor 47, *Acinetobacter baumannii*; Biosensor 48, blank control (DW).

TABLE 3 Comparison of conventional culture and *C. albicans*-LAMP-LFB methods to identify *C. albicans* in clinical samples.

Detection methods[a]	Blood samples (n = 30)		Middle segment urine (n = 100)		Sputum samples (n = 200)		Time consumption	Sensitivity (%)	Specificity (%)
	Positive	Negative	Positive	Negative	Positive	Negative			
Culture-based assay	2	28	18	82	42	158	At least 72 h	100	100
LAMP-LFB assay	2	28	18	82	42	158	Within 85 min	100	100

[a]LAMP, loop-mediated isothermal amplification; LFB, lateral flow biosensor.

water bath or a heater, is sufficient to keep the reaction temperature at 64°C for 40 min. It reveals that LAMP is time-saving, economical, and easy to operate. We also compared LAMP to other isothermal amplification assays, for example, Multiple cross displacement amplification (MCDA), for *C. albicans* detection (Zhao et al., 2019). In Zhao's report, the LoD to detect *C. albicans* was 200 fg, while in our study, the sensitivity was one fg of genomic DNA template from *C. albicans* pure cultures. The results demonstrated that LAMP was more sensitive than MCDA in our study. In addition, the LoD of the *C. albicans*-LAMP-LFB method developed in this report was 1 fg/μl of *C. albicans* genomic DNA, which was 10 times more sensitive that of the conventional LAMP added SYBR Green I amplification indicator to the reaction mixture in the experiment (Fallahi et al., 2020). Moreover, we demonstrated the assay specificity of the *C. albicans*-LAMP method using DNA from 47 strains, including one *C. albicans* reference strain

(ATCC10231), 15 *C. albicans* isolated strains, 27 non-*C. albicans* fungal strains and four bacterial strains. No cross-reactions to non-*albicans* strains were obtained, and the analytical specificity of the LAMP-LFB assay is 100%; therefore, the LAMP-LFB assay could be employed to detect *C. albican* with high specificity.

The LAMP assay has been used to detect various pathogens, including *C. albicans* (Wang et al., 2017; Yamamoto et al., 2018; Fallahi et al., 2020; Zhu et al., 2020). Unfortunately, traditional LAMP assay results were tedious to interpret. It requires special materials and instruments, such as agarose gel electrophoresis, real-time turbidity equipment, and an SYBR green I color indicator (Hill et al., 2018; Zhao et al., 2020). Worse, it requires a professional to operate. Hence, the factors mentioned above limited their point-of-care testing. This study used VDR and LFB methods to detect LAMP products, avoiding the shortcomings of traditional LAMP assays. The color of the amplified products effectively changed from colorless to light green in the VDR assay, while the negative and blank controls remained colorless. Moreover, CL and TL appeared on the LFB, revealing positive LAMP results for the ITS2 gene. However, only the CL line was observed on the biosensor for the blank controls. These two methods are visual and very simple; non-specialists can interpret the results accurately. Although the VDR assay can detect LAMP products, the color is fuzzy when the product concentration is low, which may lead to interpretation errors (Chen et al., 2021). So, the biosensor LFB is considered a suitable method for monitoring *C. albicans*-LAMP products due to its high sensitivity, simplicity of operation, and cost savings. The total cost of one test, including fungi genomic DNA extraction (approximately $1 USD), *C. albicans*-LAMP reaction (approximately $3.5 USD) and LFB reporting (approximately $2 USD), is estimated to be $6.5 USD, which is cheaper than conventional PCR-based methods. Combined with the elimination of labor costs because of the requirements for trained personnel in a certified laboratory, the *C. albicans*-LAMP-LFB assay becomes more cost-effective.

We evaluated the clinical application of *C. albicans*-LAMP-LFB using 330 clinical samples (including 30 whole blood, 100 middle segment urine, and 200 sputum samples); the LAMP-LFB assay identified all *C. albicans*-positive (62/330) samples. The diagnostic accuracy was 100% compared to the traditional clinical cultural-based methods. The results suggested that this assay can be used as a diagnostic tool for the rapid, accurate, sensitive, and specific detection of *C. albicans* strains. It is especially useful in implementing point-of-care testing, which is more conducive to developing resource-poor areas. Our study has some limitations LAMP-LFB assay is a qualitative test without quantitative detection. Hence, it is difficult to determine whether it is a pathogen or a colonizing bacterium. Therefore, in the future research, this method should focus on the detection of blood, middle segment urine, bronchoalveolar lavage fluid and aseptic body fluid, and try to avoid the detection of sputum samples, which is conducive to the correct use of antifungal drugs. In addition, LAMP is an isothermal amplification technique that requires multiple primer pairs; contamination can easily occur, leading to incorrect results. Therefore, we will address the above deficiencies in subsequent studies.

Conclusion

In conclusion, a visual, rapid, simple, sensitive, and cost-saving *C. albicans*-LAMP-LFB assay based on the ITS2 gene was successfully devised for identifying *C. albicans* agents in the current study. The *C. albicans*-LAMP-LFB assay showed high sensitivity and high specificity, which could successfully detect *C. albicans* isolates, and had the LoD of 1 fg genomic DNA template per tube. Besides, the clinical effectiveness of this assay was successfully upheld by clinical samples, including whole blood, middle segment urine, and sputum samples. Hence, our results indicate that *C. albicans*-LAMP-LFB strategy is an effective tool for *C. albicans* rapid detection in clinical samples, especially in resource-limited settings.

Data availability statement

The original contributions presented in the study are included in the article/Supplementary Material, further inquiries can be directed to the corresponding authors.

Ethics statement

The study was approved by the Human Ethics Committee of the First People's Hospital of Guiyang (Approval No. 2020-S025) and complied with the Declaration of Helsinki. Before our team obtained the samples/isolates and conducted the study, any personal identifiers of the suspected *C. albicans*-infected patients had been removed by the monitoring stations. So, the patient informed consent was waived by the Human Ethics Committee of the First People's Hospital of Guiyang.

Author contributions

YW, XZ, and SL conceived and designed the experiments. YW, XZ, YZ, and JL performed the experiments. YW, JL, XZ, and HL analyzed the data. YW, XZ, and SL wrote the paper.

Funding

This study was supported by the Qian Ke He Zhi Cheng [2021] Yi Ban 440 from the Science and Technology Department of Guizhou Province. Zhu Ke He Tong (2020)-10-6, Zhu Ke He Tong (2021)43-25, and (2019) Zhu Wei Jian Ke Ji He Tong Zi Di

001 from the Science and Technology Department of Guiyang city of Guizhou Province.

Conflict of interest

The authors declare that the research was conducted in the absence of any commercial or financial relationships that could be construed as a potential conflict of interest.

Publisher's note

All claims expressed in this article are solely those of the authors and do not necessarily represent those of their affiliated organizations, or those of the publisher, the editors and the reviewers. Any product that may be evaluated in this article, or claim that may be made by its manufacturer, is not guaranteed or endorsed by the publisher.

References

Adams, E., Quinn, M., Tsay, S., Poirot, E., Chaturvedi, S., Southwick, K., et al. (2018). Candida auris investigation workgroup Candida auris in healthcare facilities, New York, USA, 2013-2017. *Emerg. Infect. Dis.* 24 (10), 1816–1824. doi:10.3201/eid2410.180649

Asadzadeh, M., Ahmad, S., Al-Sweih, N., and Khan, Z. (2018). Rapid and accurate identification of Candida albicans and Candida dubliniensis by real-time PCR and melting curve analysis. *Med. Princ. Pract.* 27 (6), 543–548. doi:10.1159/000493426

Azzouz, A., Hejji, L., Kim, K. H., Kukkar, D., Souhail, B., Bhardwaj, N., et al. (2022). Advances in surface plasmon resonance-based biosensor technologies for cancer biomarker detection. *Biosens. Bioelectron. X.* 197, 113767. doi:10.1016/j.bios.2021.113767

Azzouz, A., Hejji, L., Sonne, C., Kim, K. H., Kumar, V., Bhardwaj, N., et al. (2021). Nanomaterial-based aptasensors as an efficient substitute for cardiovascular disease diagnosis: Future of smart biosensors. *Biosens. Bioelectron. X.* 193, 113767. doi:10.1016/j.bios.2021.113767

Ben-Ami, R. (2018). Treatment of invasive candidiasis: A narrative review. *J. Fungi (Basel).* 4, 97. doi:10.3390/jof4030097

Casadevall, A. (2019). Global catastrophic threats from the fungal kingdom: Fungal catastrophic threats. *Curr. Top. Microbiol. Immunol.* 424, 21–32. doi:10.1007/82_2019_161

Chen, X., Wang, S., Tan, Y., Huang, J., Yang, X., and Li, S. (2021). Nanoparticle-based lateral flow biosensors integrated with loop-mediated isothermal amplification for the rapid and visual diagnosis of hepatitis B virus in clinical application. *Front. Bioeng. Biotechnol.* 9, 731415. doi:10.3389/fbioe.2021.731415

Dadar, M., Tiwari, R., Karthik, K., Chakraborty, S., Shahali, Y., and Dhama, K. (2018). Candida albicans - biology, molecular characterization, pathogenicity, and advances in diagnosis and control - an update. *Microb. Pathog.* 117, 128–138. doi:10.1016/j.micpath.2018.02.028

Dolka, B., Cisek, A. A., and Szeleszczuk, P. (2019). The application of the loop-mediated isothermal amplification (LAMP) method for diagnosing Enterococcus hirae-associated endocarditis outbreaks in chickens. *BMC Microbiol.* 19 (1), 48. doi:10.1186/s12866-019-1420-z

Ells, R., Kock, J. L., and Pohl, C. H. (2011). Candida albicans or Candida dubliniensis. *Mycoses* 54 (1), 1–16. doi:10.1111/j.1439-0507.2009.01759.x

Eyre, D. W., Sheppard, A. E., Madder, H., Moir, I., Moroney, R., Quan, T. P., et al. (2018). A Candida auris outbreak and its control in an intensive care setting. *N. Engl. J. Med. Overseas. Ed.* 379 (14), 1322–1331. doi:10.1056/NEJMoa1714373

Fallahi, S., Babaei, M., Rostami, A., Rostami, A., Mirahmadi, H., Arab-Mazar, Z., et al. (2020). Diagnosis of Candida albicans: Conventional diagnostic methods compared to the loop-mediated isothermal amplification (lamp) assay. *Arch. Microbiol.* 202 (17), 275–282. doi:10.1007/s00203-019-01736-7

Fisher, M. C., Gurr, S. J., Cuomo, C. A., Blehert, D. S., Jin, H., Stukenbrock, E. H., et al. (2020). Threats posed by the fungal kingdom to humans, wildlife, and agriculture. *mBio* 11 (3), e00449-20. doi:10.1128/mBio.00449-20

Fortún, J., Martín-Dávila, P., Gómez-García, d., Pedrosa, E., Pintado, V., Cobo, J., et al. (2012). Emerging trends in candidemia: A higher incidence but a similar outcome. *J. Infect.* 65 (1), 64–70. doi:10.1016/j.jinf.2012.02.011

Gow, N. A. R., and Yadav, B. (2017). Microbe profile: Candida albicans: A shape-changing, opportunistic pathogenic fungus of humans. *Microbiol. Read.* 163 (8), 1145–1147. doi:10.1099/mic.0.000499

Gunasekera, M., Narine, M., Ashton, M., and Esfandiari, J. (2015). Development of a dual path platform (DPP®) immunoassay for rapid detection of Candida albicans in human whole blood and serum. *J. Immunol. Methods* 424, 7–13. doi:10.1016/j.jim.2015.04.014

Hill, J., Beriwal, S., Chandra, I., Paul, V. K., Kapil, A., Singh, T., et al. (2008). Loop-mediated isothermal amplification assay for rapid detection of common strains of *Escherichia coli*. *J. Clin. Microbiol.* 46 (8), 2800–2804. doi:10.1128/JCM.00152-08

Kasai, M., Francesconi, A., Petraitiene, R., Petraitis, V., Kelaher, A. M., Kim, H. S., et al. (2006). Use of quantitative real-time PCR to study the kinetics of extracellular DNA released from Candida albicans, with implications for diagnosis of invasive candidiasis. *J. Clin. Microbiol.* 44 (1), 143–150. doi:10.1128/JCM.44.1.143-150.2006

Li, S., Liu, Y., Wang, Y., Chen, H., Liu, C., and Wang, Y. (2019). Lateral flow biosensor combined with loop-mediated isothermal amplification for simple, rapid, sensitive, and reliable detection of *Brucella* spp. *Infect. Drug Resist.* 30 (12), 2343–2353. doi:10.2147/IDR.S211644

McCarty, T. P., and Pappas, P. G. (2015). Invasive candidiasis. *Infect. Dis. Clin. North Am.* 30, 103–124. doi:10.1016/j.idc.2015.10.013

Notomi, T., Okayama, H., Masubuchi, H., Yonekawa, T., Watanabe, K., Amino, N., et al. (2000). Loop-mediated isothermal amplification of DNA. *Nucleic Acids Res.* 28 (12), E63–E63. doi:10.1093/nar/28.12.e63

Patel, S. K., Surve, J., and Parmar, J. (2022a). Detection of cancer with graphene metasurface-based highly efficient sensors. *Diam. Relat. Mat.* 129, 109367. doi:10.1016/j.diamond.2022.109367

Patel, S. K., Surve, J., Parmar, J., Natesan, A., and Katkar, V. (2022b). Graphene-based metasurface refractive index biosensor for hemoglobin detection: Machine learning assisted optimization. *IEEE Trans. Nanobioscience*, 1. doi:10.1109/TNB.2022.3201237

Pincus, D. H., Orenga, S., and Chatellier, S. (2007). Yeast identification-past, present, and future methods. *Med. Mycol.* 45 (2), 97–121. doi:10.1080/13693780601059936

Quindós, G., Marcos-Arias, C., San-Millán, R., Mateo, E., and Eraso, E. (2018). The continuous changes in the aetiology and epidemiology of invasive candidiasis: From familiar Candida albicans to multiresistant Candida auris. *Int. Microbiol.* 21 (3), 107–119. doi:10.1007/s10123-018-0014-1

Rodrigues, M. L., and Nosanchuk, J. D. (2020). Fungal diseases as neglected pathogens: A wake-up call to public health officials. *PLoS Negl. Trop. Dis.* 14 (2), e0007964. doi:10.1371/journal.pntd.0007964

Schmiedel, Y., and Zimmerli, S. (2016). Common invasive fungal diseases: An overview of invasive candidiasis, aspergillosis, cryptococcosis, and pneumocystis pneumonia. *Swiss Med. Wkly.* 146, w14281. doi:10.4414/smw.2016.14281

Sherry, L., Rajendran, R., Lappin, D. F., Borghi, E., Perdoni, F., Falleni, M., et al. (2014). Biofilms formed by Candida albicans bloodstream isolates display phenotypic and transcriptional heterogeneity that are associated with resistance and pathogenicity. *BMC Microbiol.* 14, 182. doi:10.1186/1471-2180-14-182

Wang, F., Ge, D. B., Wang, L., Li, N., Chen, H. M., Zhang, Z. X., et al. (2021a). Rapid and sensitive recombinase polymerase amplification combined with lateral flow strips for detecting Candida albicans. *Anal. Biochem.* 15 (633), 114428. doi:10.1016/j.ab.2021.114428

Wang, M., Yang, Y., Min, J., Song, Y., Tu, J. B., Mukasa, D., et al. (2022). A wearable electrochemical biosensor for the monitoring of metabolites and nutrients. *Nat. Biomed. Eng.* doi:10.1038/s41551-022-00916-z

Wang, Y., Li, H., Wang, Y., Zhang, L., Xu, J., and Ye, C. (2017). Loop-mediated isothermal amplification label-based gold nanoparticles lateral flow biosensor for detection of *Enterococcus faecalis* and *Staphylococcus aureus*. *Front. Microbiol.* 8, 192. doi:10.3389/fmicb.2017.00192

Wang, Y., Zhao, X., Cheng, J., Tang, X., Chen, X., Yu, H. L., et al. (2021b). Development and application of a multiple cross displacement amplification combined with nanoparticle-based lateral flow biosensor assay to detect *Candida tropicalis*. *Front. Microbiol.* 12, 681488. doi:10.3389/fmicb.2021.681488

Yamamoto, M., Alshahni, M. M., Tamura, T., Satoh, K., Iguchi, S., Kikuchi, K., et al. (2018). Rapid detection of Candida auris based on loop-mediated isothermal amplification (LAMP). *J. Clin. Microbiol.* 56 (9), e00591-18. doi:10.1128/JCM.00591-18

Zehm, S., Schweinitz, S., Würzner, R., Colvin, H. P., and Rieder, J. (2012). Detection of Candida albicans by mass spectrometric fingerprinting. *Curr. Microbiol.* 64 (3), 271–275. doi:10.1007/s00284-011-0064-5

Zhao, F., Niu, L., Yan, L., Nong, J., Wang, C., Wang, J., et al. (2019). Establishment and application of multiple cross displacement amplification coupled with lateral flow biosensor (MCDA-LFB) for visual and rapid detection of *Candida albicans* in clinical samples. *Front. Cell. Infect. Microbiol.* 9, 102. doi:10.3389/fcimb.2019.00102

Zhao, V. X. T., Wong, T. I., Zheng, X. T., Tan, Y. N., and Zhou, X. (2020). Colorimetric biosensors for point-of-care virus detections. *Mat. Sci. Energy Technol.* 3, 237–249. doi:10.1016/j.mset.2019.10.002

Zhu, X., Wang, X., Han, L., Chen, T., Wang, L., Li, H., et al. (2020). Multiplex reverse transcription loop-mediated isothermal amplification combined with nanoparticle-based lateral flow biosensor for the diagnosis of COVID-19. *Biosens. Bioelectron. X.* 166, 112437. doi:10.1016/j.bios.2020.112437

Zilberberg, M. D., Shorr, A. F., and Kollef, M. H. (2008). Secular trends in candidemia-related hospitalization in the United States, 2000-2005. *Infect. Control Hosp. Epidemiol.* 29 (10), 978–980. doi:10.1086/591033

frontiers | Frontiers in Bioengineering and Biotechnology

TYPE Original Research
PUBLISHED 24 April 2023
DOI 10.3389/fbioe.2023.1085976

OPEN ACCESS

EDITED BY
Tatiana Fiordelisio,
National Autonomous University of Mexico, Mexico

REVIEWED BY
Abdollah Derakhshandeh,
Shiraz University, Iran
Susana De La Torre-Zavala,
Autonomous University of Nuevo León, Mexico

*CORRESPONDENCE
María Leticia Arena-Ortiz,
leticia.arena@ciencias.unam.mx

SPECIALTY SECTION
This article was submitted to Biosensors and Biomolecular Electronics, a section of the journal Frontiers in Bioengineering and Biotechnology

RECEIVED 31 October 2022
ACCEPTED 28 March 2023
PUBLISHED 24 April 2023

CITATION
Arena-Ortiz ML, Sánchez-Rodríguez EC, Apodaca-Hernández JE, Ortiz-Alcántara JM, Ríos-Contreras K and Chiappa-Carrara X (2023), DNA microarrays to identify etiological agents, as sensors of environmental wellbeing. *Front. Bioeng. Biotechnol.* 11:1085976. doi: 10.3389/fbioe.2023.1085976

DNA microarrays to identify etiological agents, as sensors of environmental wellbeing

María Leticia Arena-Ortiz[1]*, Ernesto Cuauhtemoc Sánchez-Rodríguez[2], Javier Eduardo Apodaca-Hernández[3], Joanna María Ortiz-Alcántara[1], Karen Ríos-Contreras[1] and Xavier Chiappa-Carrara[4]

[1]Ecogenomics Laboratory, National Autonomous University of Mexico (UNAM), Yucatan, Mexico, [2]Hyperbaric Medicine Department at Hospital Agustín O'Horan, Health Ministry of Yucatán, Postgraduate Department of Faculty of Medicine of National Autonomous University of Mexico (UNAM), and Global Health Institute, Michigan State University (MSU), Mérida, Mexico, [3]Bibliotecas Genómicas S.A, Merida, Mexico, [4]Conservation Biology Laboratory, National Autonomous University of Mexico (UNAM), Yucatan, Mexico

Background: The epidemiologic transition in Mexico has generated a change of paradigm in public health. Morbidity is characterized by infectious diseases and the mortality is due to chronic degenerative diseases. The three most important infectious diseases in the country are: respiratory infections, diarrhea, and urinary tract infections.

Method: The objective of this work was to build a tool to monitor the presence of health risks in the environment in a timely manner and to demonstrate its application in different sicknesses, especially those that are water related. In this study, we analyzed water samples from five cenotes with high tourist flow in the State of Yucatan. We developed a DNA microarray for the adequate and prompt detection of viruses, bacteria, fungi, and parasites. This microarray could be used in samples of different origin including air, water (fresh, brackish and saltwater), food, inert surfaces or wounds. Clinically, it would allow prompt and precise detection of etiological agents of infectious diseases to prevent outbreaks. It would also be useful for the identification of those agents that cannot be detected in our laboratories with the traditional methods. It includes 38,000 probes that detect 252 etiological agents of diseases in humans and antimicrobial resistance genes. Results from DNA samples can be obtained in 24 h, which would be difficult or impossible using other technologies.

Results: The results are readily available within 24 h. Samples from five cenotes (sinkholes) with high flow of people, were analyzed with the microarray. The water samples analyzed detected 228 different bacteria, viruses, fungi, and protozoa. They are amongst the most important etiological agents for infectious diseases in Mexico.

Conclusions: The microarray provides the opportunity for precise and early detection of various infectious agents in individuals, hospitals and natural environments. This could help reduce the global burden of diseases, the severity of outbreaks, and reduce antibiotic resistance.

KEYWORDS
biosensor, etiological agents, environmental wellbeing, public health, dnamicroarray

1 Introduction

There is a great need to address the growing impact of the environmental conditions on public health. Some examples are environmental pathogens that cause respiratory infections, diarrhea, hospital infections, and bacterial resistance to antibiotics.

Using information from a data bank of diseases that are monitored monthly in health institutions in Mexico, we developed a DNA biosensor for the early and prompt detection of these pathogens in air, water (fresh, salt, and brackish), food, inert surfaces, and also in wounds. This could become a key monitoring device for health institutions, in case of outbreaks and other infectious risks.

Microarray technology was developed to analyze thousands of genetic sequences at once and is used for its sensibility and for the great amount of information that can be obtained from a single chip in short times, using laboratory resources more efficiently. Results can be obtained in 24 h from DNA sample collection, without the need of cultivating or amplifying the targets, task that would be difficult or impossible using other technologies. Probes of DNA or RNA are attached to a solid surface. Then, the sample of genetic material is hybridized with the probes in the device and the pairing of complementary bases can be detected using fluorescence that is quantified by the reader, allowing the identification of the target genes (Boussioutas and Haviv, 2003; Dudda-Subramanya et al., 2003).

Our biosensor called "Yucateco" contains 38,000 probes that are species-specific for a set of organisms that were selected due to their public health importance, since they directly cause multiple infections. It allowed the detection of 1 arthropod, 112 bacteria, 29 fungi and yeasts, 31 microalgae, 8 nematodes, 8 flatworms, 11 protozoa, 40 viruses that cause diseases in humans and 12 antimicrobial resistance genes to betalactam agents, fluroquinolones, newer generation of cephalosporins and carbapenems genes (Supplementary Table S1). Eighty-five percent of them are identified to the species level and the rest to the level of genus. In the case of viruses and bacteria where all the species included in the same genus are considered pathogenic, it would be enough to detect potential risks to human health identifying organisms to the taxonomic level of genus.

The design and specificity of the probes was validated through bioinformatic challenges by our team and by Affymetrix, now part of Thermo Fisher Scientific that manufactured the array for the GeneChip® system. Furthermore, the microarray was tested using a control sample prepared with bacterial DNA in different concentrations to simulate the behavior of environmental samples.

The objective of this work was to use this biosensor to evaluate the water quality in five sinkholes (cenotes) of the Yucatan Peninsula. They have a vital importance as a water source but could also become a reservoir of infectious diseases. The Yucatan peninsula holds 85% of the underground water reserve of the country and cenotes are not only part of it but they have great cultural, religious, ecological, and touristic importance. Anthropogenic contaminants in water are a major issue in the area. Human contact with contaminated water for recreational use in natural environments could become a public health issue (Hoogesteijn-Reul et al., 2015; Aguilar-Duarte et al., 2016; Batllori and Chávez-Guzmán, 2016; Chávez-Guzmán, 2016; Hernández Flores, 2018).

2 Materials and methods

2.1 Sample collection

Water samples were collected from five cenotes with high tourist activity in the State of Yucatan, Mexico, including: Pájaros (in the natural protected area of El Corchito), Xlacah (in the Archeological zone of Dzibilchaltún), X´batun (San Antonio Mulix municipality), and Yaxbacaltun and Santa María (Homún municipality) (Figure 1). Physicochemical parameters of the water were measured *in situ*, with a multiparameter meter (YSI, OH, United States). These included: temperature, pH, salinity, conductivity, dissolved oxygen, total dissolved solids, and redox potential. Water samples were collected in polyethylene containers of 4 L in triplicates and transported in an ice cooler to the Ecogenomics laboratory to be stored at 4°C for up to 24 h. Four liters of water were filtered on a sterile nitrocellulose membrane of 0.45 µm pore size (Millipore, Darmstadt, Germany). The filters were stored at −20°C until DNA extraction.

2.2 DNA extraction

Metagenomic DNA was extracted from the filters according to a silica-based protocol previously reported (Rojas-Herrera et al., 2008). The DNA integrity was checked on a 1% agarose gel. dsDNA concentration and purity were determined using the QuantiFluor® dsDNA kit in a Quantus Fluorometer (Promega Corporation, Madison, WI, United States) and the Multiskan Go Spectrophotometer (Thermo Scientific Waltham, MA, United States), respectively, following the manufacturer's protocols. The DNA obtained from the filters of each sampling site was pulled to be analyzed in a single chip. The total amount of DNA used as input for each array was 3.01 ng from X´batun, 178.8 ng from Santa María and Yaxbacaltun, 269.5 ng from Xlacah, and 490 ng from Pájaros cenote.

2.3 Control sample preparation

To simulate the behavior of environmental samples where a complex mixture of genomes is present, a control sample was prepared including 1 µL of DNA of each of the following species, in different quantities: *Acinetobacter baumannii*, 22 ng; *Bordetella pertussis*, 0.27 ng; *Bordetella parapertussis*, 18 ng; *Enterobacter cloacae*, 46 ng; *Escherichia coli* (enteropathogenic), 191 ng; enteroaggregative, 166 ng; enteroinvasive, 95 ng; enterotoxigenic, 200 ng; diffusely-adherent, 154 ng; adherent-invasive, 160 ng; *Helicobacter pylori*, 60 ng; *Klebsiella pneumoniae*, 125.0 ng;

FIGURE 1
Map of the Yucatan peninsula with the location of sampled cenotes including Pájaros (Reserva Ecológica El Corchito), Xlacah (Zona Arqueológica de Dzibilchaltún), X´batun (San Antonio Mulix), Yaxbacaltun and Santa María (Homún).

Klebsiella oxytoca, 28.0 ng; *Mycobacterium tuberculosis*, 7.5 ng; *Mycobacterium avium*, 1.53 ng; *Mycobacterium kansasii*, 1.25 ng; *Neisseria meningitidis*, 0.09 ng; *Pseudomonas aeruginosa*, 48 ng; *Shigella* sp., 27 ng; *Staphylococcus aureus*, 2.6 ng; *Vibrio cholerae*, 1.44 ng; *Vibrio parahaemolyticus*, 4.83 ng; antimicrobial resistance genes (QniA, 23 ng; Qni B, 9 ng; VIM, 24 ng; TLA, 33 ng; IMP, 30 ng; SHV, 14 ng; NDM, 31 ng; CTXM, 25 ng; GES, 19 ng; aac, 19 ng).

2.4 DNA microarrays

A customized microarray was designed containing 38,000 specific probes (patent application MX/a/2018/014650) to detect 269 pathogens and antimicrobial resistance genes in a single chip. The chip was manufactured for the GeneChip® platform by Affymetrix (Applied Biosystems Microarrays, Thermo Fisher Scientific, Waltham, MA, United States). The metagenomic DNA was processed following a protocol optimized for a complex mixture of genetic materials, using the Affymetrix® SNP 6.0 Core Reagent Kit (Thermo Fisher Scientific, Waltham, MA, United States). Briefly, end-labeled fragments of DNA were generated with DNase I, biotin-labeled nucleotides and a deoxy terminal transferase (TdT). Labeled DNA was hybridized to the chip at 49 °C for 16 h in a GeneChip® 645 oven (Thermo Fisher Scientific, Waltham, MA, United States), then washed and dyed in the GeneChip® Fluidics Station 450 (Thermo Fisher Scientific, Waltham, MA, United States), and scanned in a GeneChip® Scanner 3,000 7G (Thermo Fisher Scientific, Waltham, MA, United States). The etiological agents in each sample were determined according to the pixel intensity data in each cell at the specific probe locations in the microarray.

2.5 Data analysis

The analysis of the CDF files generated after scanning the chip was performed with a pipeline using the Bioconductor package (https://www.bioconductor.org/) and R programming language (https://cran.r-project.org/). Specific libraries include *makecdfenv* to build the work environment; *affxparser* to delimit data from plain text and define working columns; and *affy* to manage specific data from Affymetrix. The values referring to the grid were customized for this "Yucateco" microarray. From the raw data file, the pixel intensity values were obtained, the values from a blank sample not containing DNA were subtracted and considered a negative control. Additionally, by convention, a cut-off point was determined for the assignment of a positive sample, thus all those values below 30% of pixel intensity were considered as negative. A list of etiological agents was created based on this criterion for each sample. Subsequently, using the *batch blast entrez* algorithm (https://www.ncbi.nlm.nih.gov/sites/batchentrez) the complete genetic annotation was retrieved from the databases corresponding to the access numbers of each pathogen, to assign the names including genus, species and, in some cases, genotype. The etiological agents were classified according to the systems that they can affect in the following categories: gastrointestinal, respiratory, nervous system, muscle and soft tissue, immunological, ophthalmological, cardiovascular, urinary and other, including otic, congenital and bones. A cluster analysis constructed using the Euclidean distance as a measure of association, allowed to obtain a dendrogram in which a cut-off value equal to 5 was used to determine the degree of dissimilarity between the sites sampled with relation to the presence or absence of the targeted species was carried out with the Primer 6 software (Villardón, 2007).

10.3389/fbioe.2023.1085976

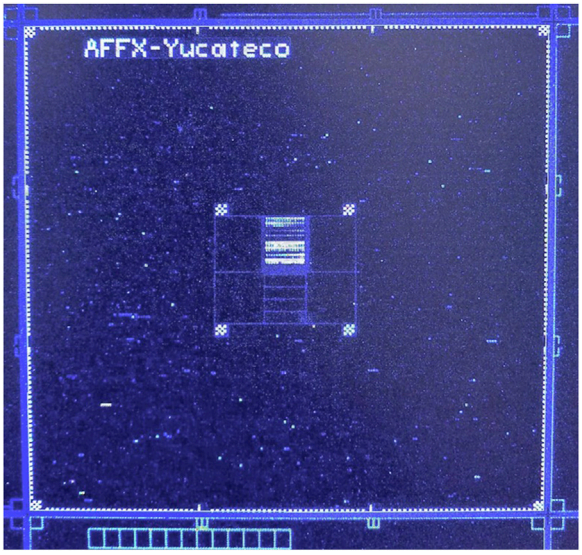

FIGURE 2
Image of the Yucateco array hybridized with the water sample from the Pájaros cenote in Reserva Ecológica El Corchito. Pixels where DNA fragments hybridized at the specific probes in the microarray appear in blue and hybridization controls in white.

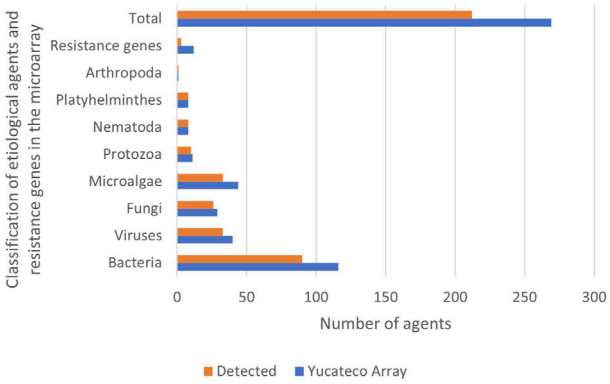

FIGURE 3
Etiological agents and resistence genes included in the microarray and detected in cenotes by classification.

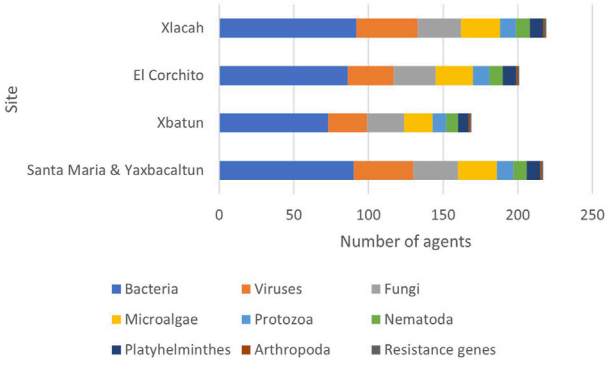

FIGURE 4
Etiological agents detected by cenote. The number of agents detected in each cenote according to its classification are presented, a total of 228 agents were detected in the samples.

3 Results

The DNA concentration obtained from environmental samples is directly related to several factors, therefore it is not feasible to set a constant number of liters of water required per analysis. A control sample was prepared to mock an environmental sample, where a complex mixture of genomes can be found, including purified DNA from 22 bacterial species and 10 antimicrobial resistance genes. The amount of DNA spiked in the control sample ranged from 0.09 to 200 ng, corresponding to *Neisseria meningitidis* and enterotoxigenic *E. coli,* respectively, both being detected by the array. A total of 18 out of 22 species were detected by the microarray. However, some species such as *Mycobacterium kansassi* (1.25 ng), *M. avium* (1.53 ng), *S. aureus* (2.6 ng) and *Acinetobacter baumanii* (22 ng) were not detected by the array in the control sample. In the case of resistance genes, 6 out of 10 were detected, the amount of DNA used as input ranged from 14 to 31 ng. In this study, it was necessary to filter up to 12 L of water from each cenote to obtain at least 0.1 ng/μL of DNA to be able to have reading results in the array. The total DNA used as input for each array was in the range of 3.01 ng from X′batun to 490 ng from Pájaros cenote, while 178.8 ng from Santa María and Yaxbacaltun, and 269.5 ng of DNA from Xlacah.

The presence or absence of etiological agents in the samples were determined according to the pixel intensity in each area of the array defined as a cell. Detection of the fluorescence emitted by the DNA fragments hybridized at the specific probes in the microarray, resulted in an image of points called pixels, with coordinates and values of fluorescence intensity (Figure 2).

The etiological agents found in the water samples included pathogens that represent a threat to humans as well as other microorganisms that are not harmful but could cause diseases to other species. Some species of microalgae and other microorganisms were included in the microarray due to their potential biotechnological use, and not because they represent a health risk. With the use of the "Yucateco" array a total of 209 agents were detected from the 269 targeted, including 90 bacteria, 33 viruses, 26 fungi and yeasts, 33 microalgae, 10 protozoa, 8 nematodes, 8 platyhelminthes, 1 arthropod, and some resistance genes (Figure 3).

In some cases, more than one species was detected with a total of 228 species found in the samples. The number of species detected in each cenote according to its classification are presented in Figure 4. Results show that Xlacah is the cenote where the highest number of species were identified, with 218 species. Both, Santa Maria and Yaxbacaltun cenotes presented a total of 216 species, followed by the Pájaros cenote, with 200 species. In the X′batun cenote, 168 species of human pathogens were found.

The diseases associated with the pathogens detected in the cenotes were classified according to the affected system (Figure 5). Gastrointestinal and respiratory etiological agents

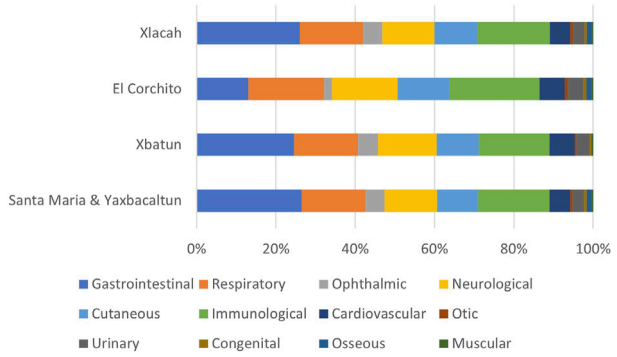

FIGURE 5
Human systems affected by diseases caused by etiological agents detected in cenotes. Etiological agents were classified according to the systems that can affect in the following categories: gastrointestinal, respiratory, nervous system, muscle and soft tissue, immunological, ophthalmological, cardiovascular, urinary and other, including otic, congenital and bones.

were the most commonly identified species, while species that affect the muscular and osseous systems, were the least common. It is important to consider that a single etiological agent can affect more than one system at the same time.

The cluster analysis allowed cenotes to be assembled in two groups (Figure 6). The first was formed only by the X′batun cenote, and the second group which includes similar cenotes based on the species detected is formed by Xlacah, Santa Maria and Yaxbacaltun, and El Pájaro. Xlacah, and Santa Maria and Yaxbacaltun cenotes formed a subgroup within the second cluster.

4 Discussion

It is considered that in developing countries around 70% of the diseases are transmitted by water. In Yucatán, the three most common infectious diseases are respiratory, gastrointestinal, and urinary, reaching 88.88% of reported infections (Servicios de Salud de Yucatán Dirección General de Epidemiología, 2021). In these countries, gastroenteritis is responsible for many deaths in the first year of age. Later in life, there is a predisposition to acquire respiratory disease that compromise the immune system, already affected by malnourishment. Detection of all the etiological agents is difficult since it is presumed that we can only culture between 10% and 15% of all the infectious pathogens reported by health services. The early identification of these pathogens could improve the results of the treatment and reduce the resistance generated by these agents.

Microarrays are a sensitive tool that can be used for quick detection of viruses and bacteria from complex clinical samples, that are key for public and veterinary health, as well as food safety (Gardner et al., 2010; Thissen et al., 2019). The "Yucateco" microarray is a biosensor designed to detect pathogens of indirect transmission reported in the epidemiological surveillance conducted yearly in the Yucatán peninsula by the Ministry of Health. Early *in situ* detection of these pathogens with the "Yucateco" array could be a useful tool for governments to prevent epidemiological outbreaks. The detectable etiological agents include many microorganisms that are not only found in Yucatán. The array also contains probes for detecting other agents not yet reported in the region, which could even represent health risks globally, such as Ebola virus. Therefore, the "Yucateco" microarray can be used to analyze samples worldwide, in any laboratory where the GeneChip® system is available. It could be helpful to identify local or global health risks, from different samples, including soil, water, food, inert surfaces, and wounds. The input sample analyzed by the "Yucateco" array was DNA purified directly from environmental samples without the need of cultivating the microorganisms. The GeneChip® high-density microarrays as the Yucateco offer several advantages. They include multiple 25-mer probe sets of each target, allowing multiple independent measurements, for an accurate evaluation that balances sensitivity and specificity. They also provide high resolution scans and simplified sample preparation, then the results are obtained using time and resources more efficiently than with other technologies. Most of the pathogens included in the probes of the device were

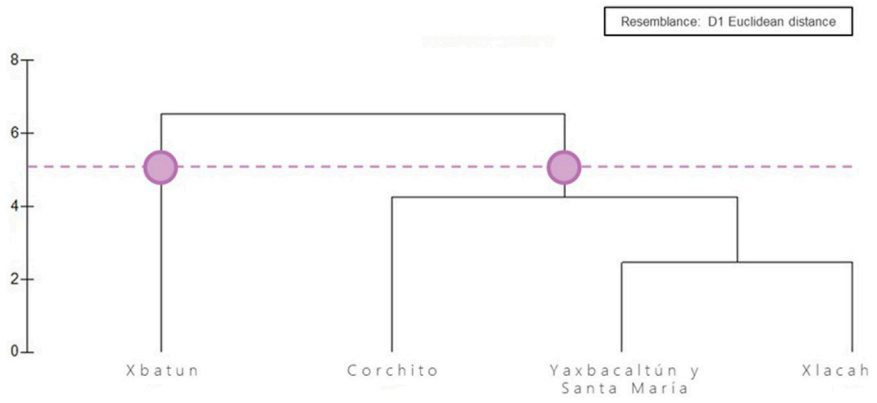

FIGURE 6
Cluster analysis. A cut-off value of 5 was used to determine the degree of dissimilarity between the sites with relation to the presence or absence of the detected species. The Euclidean distance was chosen as a measure of association..

detected in cenotes. However, some microorganisms were not found. The genus *Vibrio* contains 66 species, 12 are pathogenic (Franco-Monsreal et al., 2014), 10 of them are included in the microarray but 5 were not detected. For example, *Vibrio fluvialis* is more abundant in the marine environment and was not found in sweet water from the cenotes. Another marine species that was not detected by the array was *Prorocentrum minimum* (Saburova and Chomérat, 2016). Other microorganisms not detected are scarce in nature, such as *Tsukamurella* mostly reported in soil and mud samples (Bratcher, 2018).

Etiological agents of zoonotic diseases were detected, including *Coxiella burnetti,* bacteria of the genera *Leptospira*, *Ehrlichia*, *Borrelia*, *Rickettsia*, viruses such as Hantavirus, rabies virus and Influenza, and the protozoa *Trypanosoma cruzi.* This could be expected since many wild animals such as rodents and bats, are reservoirs of zoonotic diseases in the Yucatán peninsula (Reyes-Novelo and Ruiz-Piña, 2011).

Gastrointestinal pathogens which are amongst the most abundant fecal bacteria, having humans as the sole reservoir and transmitted by the ingestion of contaminated water, including *Shigella sonnei* and *dysenteriae*, and *V. cholerae* (World Health Organization, 2005; Azman et al., 2013), were detected in all cenotes studied.

Additionally, our biosensor has detected some resistance genes in samples of the localities, Corchito (*Raoultella planticola* strain RP01 plasmid pRP01 metallo-beta-lactamase blaNDM-1 gene), Santa María (*K. pneumoniae* strain 1121740 class B beta-lactamase blaNDM-16 gene), Xbatún (*Proteus mirabilis* strain AMP_C_M_3829_10 AmpC bla gene), and Xlacah (*A. baumannii* carbapenem-hydrolyzing beta-lactamase OXA-58 bla-oxa-58 gene). This is crucial information for the implementation of sanitation programs. Therefore, the microarray also could be applied for monitoring hospital environments.

Data generated using the "Yucateco" array can be used to better understand the health status of the ecosystems and the impact of anthropogenic disturbances in the environment. Other technologies to detect etiological agents, such as microbiology techniques, or those derived from molecular biology, such as PCR, have been widely used. However, in all the alternatives it is necessary to carry out an analysis for each of the pathogen species. The innovative element of this biosensor is its capacity to detect up to 269 pathogens in a single experiment. This translates into an efficient use of financial and human resources, and particularly shortening detection times. Early detection can make the difference between an epidemiological outbreak or that it does not occur by applying the appropriate control measures.

Data availability statement

The raw data supporting the conclusion of this article will be made available by the authors, without undue reservation.

Author contributions

MA-O, conceptualization, funding acquisition, project administration, supervision, writing-review and editing. ES-R, conceptualization, supervising, writing-review and editing. JA-H, conceptualization, founding acquisition, formal analysis. JO-A, methodology, formal analysis, investigation, writing and editing. KR-C, Methodology Formal analysis, writing. XC-C, Formal analysis, founding acquisition, investigation, writing and editing.

Funding

This Proyect was founded by the Mexican National Council of Science and Technology with the grant Problemas Nacionales "Diseño y construcción de una herramienta prototipo basada en tecnología de ADN de detección de agentes de riesgo para la salud en muestras ambientales y de alimentos" CONACyT 212745.

Acknowledgments

The authors wish to acknowledge: M. Sc. Karla Martinez Escalente of the Central Laboratory UMDI-Sisal UNAM for the faccilities and techical assistance, and Dr. Jesús Silva Sánchez of the Epidemiological Diagnosis Department, Infectious Diseases Research Center in the Mexican Public Health National Institute for their input on the resistance genes.

Conflict of interest

The authors declare that the research was conducted in the absence of any commercial or financial relationships that could be construed as a potential conflict of interest.

The handling editor TF declared a shared affiliation with the authors MO, JA, KR and XC at the time of the review.

Publisher's note

Supplementary material

The Supplementary Material for this article can be found online at: https://www.frontiersin.org/articles/10.3389/fbioe.2023.1085976/full#supplementary-material

References

Aguilar-Duarte, Y., Bautista, F., Mendoza, M., Frausto, O., Ihl, Y., and Delgado, D. (2016). Ivaky: Índice de la vulnerabilidad del acuífero kárstico Yucateco a la contaminación. *Rev. Mex. Ing. Quím.* 15, 913–933. doi:10.24275/rmiq/ia1081

Azman, A. S., Rudolph, K. E., Cummings, D. A., and Lessler, J. (2013). The incubation period of cholera: A systematic review. *J. Infect.* 66, 432–438. doi:10.1016/j.jinf.2012.11.013

Batllori, E. (2016). "Condiciones actuales del agua subterránea en la península de Yucatán," in *El manejo del agua a través del tiempo en la península de Yucatán. Yucatán, méxico: UADY, fgra*. Editor M. Chávez-Guzmán (Yucatán, México: CCPY), 201–227.

Boussioutas, A., and Haviv, I. (2003). Current and potential uses for DNA microarrays in transplantation medicine: Lessons from other disciplines. *Tissue Antigens* 62, 93–103. Tissue antigens. doi:10.1034/j.1399-0039.2003.00109.x

Bratcher, D. (2018). *Principles and practice of pediatric infectious diseases book*. Fifth Edition. Amsterdam: Elsevier, 786–790. doi:10.1016/C2013-0-19020-4

Chávez-Guzmán, M. (2016). *El manejo del agua a través del tiempo en la península de Yucatán. Yucatán: UADY, UCS, CCPY*. Orlando, FL: FGRA.

Dudda-Subramanya, R., Lucchese, G., Kanduc, D., and Sinha, A. A. (2003). Clinical applications of DNA microarray analysis. *J. Exp. Ther. Oncol.* 3, 297–304. doi:10.1111/j.1533-869x.2003.01104.x

Franco-Monsreal, J., Lara-Zaragoza, E., Villa-Ruano, N., Mota-Magaña, L., Serralta-Peraza, L., Cuevas-Albarrán, V., et al. (2014). Especies de importancia clínica del género Vibrio en alimentos marinos de origen animal de establecimientos de Puerto Ángel, Oaxaca, México. *Cienc. Mar* 52, 3–30.

Gardner, S. N., Jaing, C. J., McLoughlin, K. S., and Slezak, T. R. (2010). A microbial detection array (MDA) for viral and bacterial detection. *BMC Genomics* 11, 668. doi:10.1186/1471-2164-11-668

Hernández Flores, C. (2018). *Ocurrencia de norovirus, virus de hepatitis A y reovirus en cuerpos de agua del norte de Quintana roo: Predicciones de riesgos para la salud. Cancún, quintana roo*. Mexico: Centro de Investigación Científica de Yucatán, A.C.

Hoogesteijn-Reul, A. L., Febles-Patrón, J. L., and Nava-Galindo, V. A. (2015). La contaminación fecal en cenotes de interés turístico y recreacional del estado de Yucatán. *Ingeniería* 19, 169–175.

Reyes-Novelo, E., and Ruiz-Piña, H. (2011). Escobedo-Ortegón J, Rodríguez-Vivas I, Bolio-Gonzalez M, Polanco-Rodriguez A, Manrique-Saide P. Situación actual y perspectivas para el estudio de las enfermedades zoonóticas emergentes, reemergentes y olvidadas en la península de Yucatán, México. *Trop. Subtrop. Agroecosyst.* 14, 35–54.

Rojas-Herrera, R., Narvaez-Zapata, J., Zamudio-Maya, M., and Mena-Martinez, M. E. (2008). A simple silica-based method for metagenomic DNA extraction from soil and sediments. *Mol. Biotechnol.* 40, 13–17. doi:10.1007/s12033-008-9061-8

Saburova, M., and Chomérat, N. (2016). An emended description and phylogeny of the little-known Prorocentrum sipadanense mohammad-noor, daugbjerg and moestrup (prorocentrales, dinophyceae) from the Indian ocean, Oman. *Eur. J. Phycol.* 51, 270–281. doi:10.1080/09670262.2015.1134815

Thissen, J. B., Be, N. A., McLoughlin, K., Gardner, S., Rack, P. G., Shapero, M. H., et al. (2019). Axiom Microbiome Array, the next generation microarray for high-throughput pathogen and microbiome analysis. *PLoS ONE* 14, e0212045. doi:10.1371/journal.pone.0212045

Villardón, V. (2007). *Introducción al análisis de cluster*. España: Universidad de Salamanca.

World Health Organization (2005). *Guidelines for the control of shigellosis, including epidemics due to* Shigella dysenteriae *1*. Geneva, Switzerland: WHO Press, 3.

frontiers | Frontiers in Bioengineering and Biotechnology

TYPE Original Research
PUBLISHED 06 July 2023
DOI 10.3389/fbioe.2023.1202126

OPEN ACCESS

EDITED BY
Noureddine Raouafi,
Tunis El Manar University, Tunisia

REVIEWED BY
Sumit Ghosh,
The Research Institute at Nationwide Children's Hospital, United States
Riham Zayani,
Tunis El Manar University, Tunisia

*CORRESPONDENCE
Tatiana Fiordelisio,
tfiorde@ciencias.unam.mx

RECEIVED 07 April 2023
ACCEPTED 22 June 2023
PUBLISHED 06 July 2023

CITATION
Nelson-Mora J, Rubio D, Ventura-Martínez A, González LA, Del-Rio D, Aranda-López Y, Jiménez-Díaz E, Zamarrón-Hernández D, Ríos-López DG, Aguirre S, Ruiz-Hernandez Y, Cruz-Ramírez A, Barjau JS, Jáurez MA, Lopez-Aparicio J, Campa-Higareda A and Fiordelisio T (2023), New detection method of SARS-CoV-2 antibodies toward a point-of-care biosensor. *Front. Bioeng. Biotechnol.* 11:1202126. doi: 10.3389/fbioe.2023.1202126

New detection method of SARS-CoV-2 antibodies toward a point-of-care biosensor

Janikua Nelson-Mora[1], Diana Rubio[1], Amairani Ventura-Martínez[1], Luis A. González[1], Diana Del-Rio[1,2], Yuli Aranda-López[1], Edgar Jiménez-Díaz[2,3], Diego Zamarrón-Hernández[1], Diana G. Ríos-López[1], Stephanie Aguirre[1], Yasab Ruiz-Hernandez[1], Aarón Cruz-Ramírez[1], Jonás S. Barjau[1], Miguel A. Jáurez[1], Jehú Lopez-Aparicio[1], Andrea Campa-Higareda[1] and Tatiana Fiordelisio[1,2,3]*

[1]Unidad de Biología Molecular y Diagnóstico, Laboratorio Nacional de Soluciones Biomiméticas para Diagnóstico y Terapia LaNSBioDyT, Facultad de Ciencias, Universidad Nacional Autónoma de México, Mexico City, Mexico, [2]Laboratorio de Neuroendocrinología Comparada-LaNSBioDyT, Facultad de Ciencias, Universidad Nacional Autónoma de México, Mexico City, Mexico, [3]Unidad de Imagenología Cuantitativa, Laboratorio Nacional de Soluciones Biomiméticas para Diagnóstico y Terapia LaNSBioDyT, Facultad de Ciencias, Universidad Nacional Autónoma de México, Mexico City, Mexico

The outbreak of COVID-19, a disease caused by severe acute respiratory syndrome coronavirus 2 (SARS-CoV-2) infection, is regarded as the most severe of the documented coronavirus pandemics. The measurement and monitoring of SARS-CoV-2 antibody levels by serological tests are relevant for a better epidemiological and clinical understanding of COVID-19. The aim of this work was to design a method called the SARS-CoV-2 antibody detection method (SARS-CoV-2 AbDM) for fluorescence immunodetection of anti-SARS-CoV-2 IgG and IgM on both plate and microfluidic chip. For this purpose, a system with magnetic beads that immobilize the antigen (S protein and RBD) on its surface was used to determine the presence and quantity of antibodies in a sample in a single reaction. The SARS-CoV-2 AbDM led to several advantages in the performance of the tests, such as reduced cost, possibility of performing isolated or multiple samples, potential of multiplex detection, and capacity to detect whole blood samples without losing resolution. In addition, due to the microfluidic chip in conjunction with the motorized actuated platform, the time, sample quantity, and operator intervention during the process were reduced. All these advantages suggest that the SARS-CoV-2 AbDM has the potential to be developed as a PoC that can be used as a tool for seroprevalence monitoring, allowing a better understanding of the epidemiological and clinical characteristics of COVID-19 and contributing to more effective and ethical decision-making in strategies to fight against the COVID-19 pandemic.

KEYWORDS

fluorescence, immunodetection, microfluidic chip, COVID-19, magnetic beads

1 Introduction

The current pandemic of coronavirus disease 19 (COVID-19), due to infection with severe acute respiratory syndrome coronavirus 2 (SARS-CoV-2), is considered the most severe of the documented coronavirus outbreaks and one of the most complex, multifaceted, and devastating challenges humanity has faced in the 21st century. Although the fatality rate is lower than that of other highly pathogenic beta coronaviruses, such as severe acute respiratory syndrome virus (SARS-CoV) and middle east respiratory syndrome virus (MERS-CoV), its spread has been such that the number of affected countries (228), cases (>617 million), and associated deaths (>6.5 millions), from its origin in December 2019 (Wu et al., 2020) to date, is overwhelmingly higher (Shi et al., 2020; Osuchowski et al., 2021; Worldometers.info, 2022).

Although SARS-CoV-2 and SARS-CoV have many similarities, present structural genomic and phenotypic differences influence pathogenesis (Mousavizadeh and Ghasemi, 2021; Osuchowski et al., 2021). These viruses share high genomic homology (79.6%) and, in general, have a high amino acid identity (>90%) in their structural proteins, except the spike protein (S), whose similarity is lower (76.7%–77.0%), especially in the S1 domain (64%) (Lu et al., 2020; Shi et al., 2020; Zhou et al., 2020; Hu et al., 2021). Both beta coronaviruses recognize angiotensin-converting enzyme 2 (ACE2) as its receptor.

S protein plays a crucial role in the infection process by mediating viral entry into cells through binding of the RBD in the S1 subunit to the ACE2 receptor and subsequently with membrane fusion through the S2 subunit (Harrison et al., 2020; Tai et al., 2020). Structural and biophysical evidence points to amino acid sequence changes in critical motifs of the S1/RBD and that SARS-CoV-2 binding through this domain to the ACE2 receptor is 10- to 20-fold more cognate than that of SARS-CoV RBD (Wrapp et al., 2020). This may influence the high transmissibility of SARS-CoV-2 and the fact that approximately 90% of the activity of neutralizing IgG antibodies is precisely directed toward RBD (Piccoli et al., 2020; Bachmann et al., 2021).

Likewise, the differences between SARS-CoV and SARS-CoV-2 RBD are sufficiently important that there is no cross binding of specific monoclonal antibodies (Wrapp et al., 2020). Consequently, it is pertinent to define S protein, particularly the RBD, in SARS-CoV-2 as both a therapeutic and diagnostic target (Shi et al., 2020; Tai et al., 2020; Wrapp et al., 2020; Zhao et al., 2020; Emeribe et al., 2022).

During viral infections, innate and adaptive immune responses are triggered (Abdulamir and Hafidh, 2020; Prompetchara et al., 2020; Sette and Crotty, 2021). In the particular case of SARS-CoV-2, it is reported that the virus is effective in evading the triggering of early innate immune responses (Sette and Crotty, 2021), delaying the adaptive response onset while the infection progresses (Cevik et al., 2020; Sette and Crotty, 2021). Multiple classes of immunoglobulins, especially IgM and IgG, are involved in the adaptive immune response. In COVID-19, the cumulative seroconversion rate increases rapidly during the first 2 weeks of the onset of SARS-CoV-2 infection, exceeding 50% (Zhao et al., 2020). The adaptive response begins during the ongoing infection (between 1 week and 2 weeks), with the increase of IgM levels until reaching a maximum (in 3 weeks) and then decreasing in an inverse relationship with the concomitant increase of IgG levels (3 weeks–7 weeks), whose affinity for the antigen and neutralization capacity is greater (Galipeau et al., 2020; Guo et al., 2020; Post et al., 2020; Sette and Crotty, 2021; Emeribe et al., 2022).

Notwithstanding these generalities and given the differences observed in the profile of the immune response in the general population (Emeribe et al., 2022), the measurement and monitoring of IgM and IgG levels by serological tests are relevant to characterize the responses, complement the diagnosis in patients with COVID-19 at different stages, and contribute to a better understanding of the pathogenesis of this disease (Azkur et al., 2020).

Given the global spread and prevalence of SARS-CoV-2, this virus is expected to become endemic. However, many elements of COVID-19 immunity are still unknown, including the duration of immunity, medium- and long-term immunologic effect of the vaccines used, and response to future vaccines developed (Galipeau et al., 2020; Goel et al., 2021; Huggett et al., 2021). The usefulness of serological assays in COVID-19 is, therefore, multiple and consequent in decision-making. From an epidemiological perspective, a serological assay could be used to identify the proportion of individuals exposed to the virus in various populations so that the evolution of disease incidence and the acquisition of social immunity can be closely monitored (Galipeau et al., 2020; Ravi et al., 2020).

Serological tests used for the detection of SARS-CoV-2-specific antibodies (mainly IgM and IgG) include the enzyme-linked immunosorbent assay (ELISA), chemiluminescent immunoassay (CLIA), and rapid diagnostic tests (RDTs) (Prazuck et al., 2020; Ravi et al., 2020). ELISA, considered the gold standard, is a quantitative test in which antibody titration can be performed; its basic process involves coating the plate with a known capture antigen that binds to the antibody present in the sample (usually serum or plasma), and these react with secondary antibodies bound to enzymes to produce a chromogenic reaction (Lin, 2015; Ravi et al., 2020). However, the protocol is relatively complex and long (2–8 h), of medium cost, and requires specialized personnel, instrumentation, and laboratories (Yüce et al., 2021).

The most common RDTs are those employing lateral flow chromatographic immunoassays (LFIAs) (Prazuck et al., 2020; Ravi et al., 2020). In this case, the treated sample migrates by capillary action and, if it contains viral antibodies, reacts with immobilized recognition antibodies conjugated with colloidal gold or colored latex particles. The result of these tests is binary (absence or presence). They are of low cost, require a small amount of sample (often a finger prick blood drop), simple and rapid (3–30 min), and usually consist of a portable point-of-care (PoC) device and paper analysis (Carrio et al., 2015; Koczula and Gallotta, 2016; Moreno et al., 2017; Kubina and Dziedzic, 2020; Ravi et al., 2020). However, in addition to being less specific and sensitive than ELISA, they do not quantify antibody titer (Yüce et al., 2021).

The COVID-19 pandemic caused an abrupt and unprecedented increase in the demand for antibody-based tests for healthcare or research purposes. This generated a resource-limited setting for tests and laboratory supplies, not just in managing COVID-19 patients but also for those with many other major medical conditions, with low-income and middle-income countries (LMICs) being the most

affected (Bong et al., 2020). Thus, in response to the needs arising from this pandemic, which is expected to recur in the future, a call has been made to evaluate and create new detection methods that allow the constant monitoring of biomarkers of individual relevance not only for the health of the person but also for the population, as is the case of antibodies (Hallal et al., 2020; Vengesai et al., 2021; Emeribe et al., 2022).

PoCs, such as microfluidic chips, have become an important diagnostic tool in medicine. Their main advantage is to speed up diagnosis and allow the monitoring of diseases, mainly in non-urban areas or areas with limited access to medicine in LMICs, and are characterized by their low cost and high efficiency (Wieland et al., 2020). Therefore, the objective of this work is designing a method for the detection of IgG and IgM anti-SARS-COV-2 antibodies and implementing it in a microfluidic chip.

The method, hereinafter called the SARS-CoV-2 antibody detection method (SARS-CoV-2 AbDM), employs a magnetic bead system that immobilizes the antigen (S protein or RBD) on its surface and allows determining the presence and quantity of both antibodies in a serum or whole blood sample in a single reaction. Our working group has already implemented this technology for the detection of hypersensitivity pneumonitis antibodies (Fiordelisio et al., 2021), where it was observed that the use of magnetic beads, due to their small size and spherical geometry, allows for maximizing the number of immobilized biomolecules and increasing the sensitivity of the immunoassays besides reducing the reaction times and volumes of solutions and antibodies.

2 Materials and methods

2.1 Sample collection

The experimental protocol complies with all UNAM ethical guidelines for work in humans and was approved by the Commission of Academic Ethics and Scientific Responsibility of the Faculty of Sciences of UNAM (Folio: PI_2020_-2_003). All participating volunteers gave and signed informed consent.

Blood samples (n = 50) were obtained from adults between 21 and 86 years, without sex distinction, and residents of the metropolitan area of Mexico City, with 3–4 weeks of previous positive diagnosis of SARS-CoV-2 by RT-qPCR or who had been vaccinated for COVID-19. The inclusion criterion was that the sample had been previously determined as positive or negative by the ELISA method. Samples were identified as positive if they showed an absorbance with a cut-off greater than 0.4. Whole blood was obtained by venipuncture into collection tubes with a coagulation activator and separator gel (BDN-368159, BD Vacutainer, New Jersey, United States); after leaving them for 30 min at room temperature to clot, the samples were centrifuged at 1350 RCF for 15 min (5430-R, Eppendorf, Hamburg, Germany), and the resulting supernatant was collected as serum and stored at −70°C until used. For assays in which blood serum and whole blood samples were compared, these were obtained on the same day of the assay. Whole blood samples were collected in heparin tubes (BDN-367878, BD Vacutainer, New Jersey, United States).

2.2 SARS-CoV-2 antibody detection method

The SARS-CoV-2 AbDM is based on the one presented by Fiordelisio et al. (2021), where magnetic beads functionalized with an antigen react with a serum sample (with an unknown concentration of primary antibodies to be detected) and subsequently with a fluorescent conjugated secondary antibody to detect the emitted signal.

2.2.1 Functionalization

Assays were performed with two different SARS-CoV-2 antigens: S protein and RBD. The protocol for coupling the antigen to the magnetic beads (Dynabeads™ Tosylactivated M-450, Invitrogen, Carlsbad, California, United States) followed the manufacturer's instructions. These magnetic beads bind covalently to primary amino and sulfhydryl groups present in proteins such as RBD and S-protein.

For IgM and IgGS protein antibodies detection assays (C.V S-Protein Construct 6, LakePharma, California, United States), 240K magnetic beads were used per reaction, while for anti-RBD (S protein RBD (319-591-His10) LakePharma, 46438, Belmont, California, United States), 360K beads were used. To select the concentration of S protein and RBD, the theoretical antigen binding capacity of the beads established by the manufacturer was used as indicative and determined experimentally. A dilution curve containing at least one point with excess antigen was selected from these values. The tested antigen concentrations for the S protein were 0, 30, 60, 120, 240, 360, 480, and 600 ng/240K beads, and for RBD, it was 0, 240, 360, 360, 480, and 720 ng/360K beads.

To functionalize the magnetic beads, they were transferred to 500 µL of buffer 1 solution (B1; NaH_2PO_4 0.1 M, Na_2HPO_4 0.1 M pH = 8, S0751 and S0876, Sigma-Aldrich, Darmstadt, Germany) in 1.5 mL tubes (MCT-150-C, Axygen no pyrogenic and RNase/DNase-free, Corning, New York, United States), resuspended by 30 s vortexing. Beads were pooled using a magnet, the supernatant was discarded, and the antigen solution was subsequently added.

The total volume in each tube was 500 µL of functionalization solution (B1 added with antigen at corresponding concentration). The mixture was incubated for 24 h at room temperature (RT) under constant agitation in HulaMixer (HulaMixer Sample Mixer, Invitrogen, Carlsbad, United States). Subsequently, two washes were performed with buffer 2 solution (B2; Dulbecco's PBS, 10 mM EDTA, supplemented with 0.2% BSA pH 7.4; D5652, E9884, and A2156, Sigma-Aldrich, Darmstadt, Germany).

To block the remaining tosyl groups, 500 µL of buffer 3 solution (B3; tris base 0.2 M supplemented with 1% BSA pH = 8.5; T1503 Sigma-Aldrich, Darmstadt, Germany) was added. The mixture was incubated for 16 h in HulaMixer at 37°C in a benchtop incubator (New Brunswick™ Innova® 40/40R, Eppendorf, Hamburg, Germany). Two washes were performed with B2 and finally resuspended in buffer 4 (B4: Dulbecco's PBS, D5652, Sigma-Aldrich, Darmstadt, Germany) to seed 50 µL a in 96-well plate (previously blocked with 0.05% BSA) and in buffer 4T (B4T: Dulbecco's PBS, supplemented with 0.01% Tween 20; P1379, Sigma-Aldrich, Darmstadt, Germany) to load 15 µL on the microfluidic chip, at the appropriate concentration of beads according to the antigen. In this way, they were ready for the

uptake of anti-SARS-COV-2 IgG and IgM antibodies in the serum sample and their subsequent detection with the secondary antibody.

Serum samples with the highest ELISA-confirmed titer (8100) and a secondary antibody saturating condition were used to standardize the functionalization parameters. To verify whether there was a non-specific binding of serum or secondary antibody, beads functionalized without antigen, i.e., without RBD (woRBD) or S (woS), were used as controls, using B1 added with 1% BSA as the functionalization solution. The washing and blocking processes were performed under the same conditions as the antigen-functionalized beads.

2.2.2 Detection reaction

For detection of the anti-SARS-CoV-2 antibodies present in the serum samples, anti-IgG (αHIgG-647) conjugated with Alexa Fluor® 647 AffiniPure Donkey Anti-Human IgG H + L (RRID: AB_2340578; Jackson ImmunoResearch Labs Cat# 709-605-149, 1.25 mg/mL, West Grove, United States) and anti-IgM (αHIgM-488) conjugated to Alexa Fluor® 488 AffiniPure Donkey Anti-Human IgM Fc Fragment specific (RRID: AB_2340564; Jackson InmunoResearch Labs Cat# 709-545-073, 1.33 mg/mL, West Grove, United States) were used.

For antibody recognition assays, a dose–response curve was performed to determine the saturation point for RBD antigen (0.018, 0.036, 0.054, 0.072, and 0.09 μg/μL) and S protein antigen (0.012, 0.024, 0.036, 0.048, and 0.06 μg/μL) recognition in a 96-well plate (Costar 3915, Corning, Maine, United States). This parameter was also determined for the microfluidic chip reaction (0.012, 0.024, 0.036, 0.048, 0.06, 0.08, and 0.093 μg/μL) with S protein as antigen.

A final volume of 50 μL of secondary antibody solution in B4 was used for IgG and IgM plate recognition, and a final volume of 15 μL prepared with B4T was used for the microfluidic chip. For the plate detection reactions, incubation was performed at RT with shaking (250 rpm) for 2 h; finally, three washes were performed with B4 and resuspended in 50 μL of the same buffer. On the other hand, in the microfluidic chip, the incubation was 45 min at RT, with agitation by transverse magnet movement (TMM) (Fiordelisio et al., 2021). Subsequently, a wash was performed by transiting the beads through B4T and resuspending them in the same buffer for reading. For both platforms, a serum sample with ELISA titer of 8100 was used.

2.2.3 Measurement of anti-RBD and anti-S antibodies

The optimal amount of serum sample was determined by a dilution curve. Serum samples were prepared for both antigens according to the reaction platform: 50 μL of a B4-diluted serum sample (1:20, 1:10, 1:5, and 3:10) was used for the plate reactions, while 15 μL of the B4T-diluted serum sample (1:6, 1:3, and 2:3) was used for the chip.

For the measurement of antiSARS-CoV-2 antibodies on a plate, the serum sample solution was added to the functionalized beads and incubated at RT under agitation (250 rpm, 2 h). Then, two washes were performed (50 μL B4, 250 rpm, RT, 5 min). On the chip, incubation was performed for 45 min at RT with TMM agitation; a wash was performed by transiting the beads through B4T. In both cases, the detection reaction with the secondary antibody was performed as described previously.

2.2.4 Fluorescent detection analysis

Upon completion of the detection reaction with the secondary antibodies, the plates and microfluidic chips were analyzed with a Cytation 5 multi-mode cell imager (CYT5MW BioTek, Winooski, Vermont, United States). Three representative images were captured at ×20 magnification using a CY5 filter cube (EX/EM 628/685) for IgG and a GFP filter cube (EX/EM 469/525) for IgM, and the following acquisition parameters were set: led intensity of 1, gain of 9, and integration of 100 ms (RBD and microfluidic chip) or 150 ms (S protein). The images were saved in tiff format and analyzed with *ad hoc* software designed to obtain the average fluorescence intensity and the standard deviation associated with each of the images obtained.

The designed software determines the fluorescence intensity per sample by calculating the fluorescence intensity at three different levels: bead, image, and sample. At the bead level, a Laplacian Gaussian filter (LoG filter) was used for segmentation and detection of beads in the images. After precise spatial localization, the fluorescence intensity of each bead was calculated by averaging the values of the set of pixels that constitute it. The minimum and maximum intensity levels, the number of identified beads, and the average fluorescence intensity per image were obtained. In addition to the average, two additional values were calculated: the 75th percentile and the sum of all N values above the 25th percentile divided by N (the weighted sum). Finally, the fluorescence intensity values of all images related to a single sample were used to calculate the same values (average fluorescence intensity, 75th percentile average, and weighted sum). In all cases, the average and associated standard deviation were calculated as well as the data used for the weighted sum.

To obtain a better resolution of the magnetic beads, the images presented in this work were obtained with an upright confocal microscope (TCS-SP8, LEICA, Wetzlar, Germany). For this purpose, an aliquot (10 μL) was placed on a slide, taking care to arrange the beads in a single focal plane using a magnet, and a slide was placed on the top. The magnetic beads were excited with a laser at 488 nm (IgM) or 638 nm (IgG). Emission was detected with a hybrid detector and collected at 493–570 nm and 646–708 nm, respectively. Samples were observed with a ×40/0.80 objective. Three photos of each well were taken and exported in tiff format for analysis.

2.2.5 Microfluidic chip

The SARS-CoV-2 AbDM was implemented on a microfluidic chip making use of an automated platform, both designed by Fiordelisio et al. (2021). The chip consists of a series of six wells (I–VI) with different reagents connected by microchannels with mineral oil (M5904, Sigma-Aldrich, Steinheim, Germany) (Figure 1A) to prevent mixing of the different solutions. The chip is placed on the automated platform (Figure 1B) whose magnets move the functionalized beads along the series of wells where the different reactions and washes are carried out keeping them in agitation, during each reaction process.

As an alternative to the process of hermetically sealing the chip with polymethyl methacrylate (PMMA) and absolute ethanol (Fiordelisio et al., 2021), adhesion was performed with a 60 × 24 mm glass coverslip (2980-246, Corning, New York, United States) and polydimethylsiloxane (PDMS; SYLGARD™ 184 Silicone Elastomer Base and SYLGARD™ 184 Silicone Elastomer Curing Agent Kit, DOW, Michigan, United States) (Figure 1C) by thermal

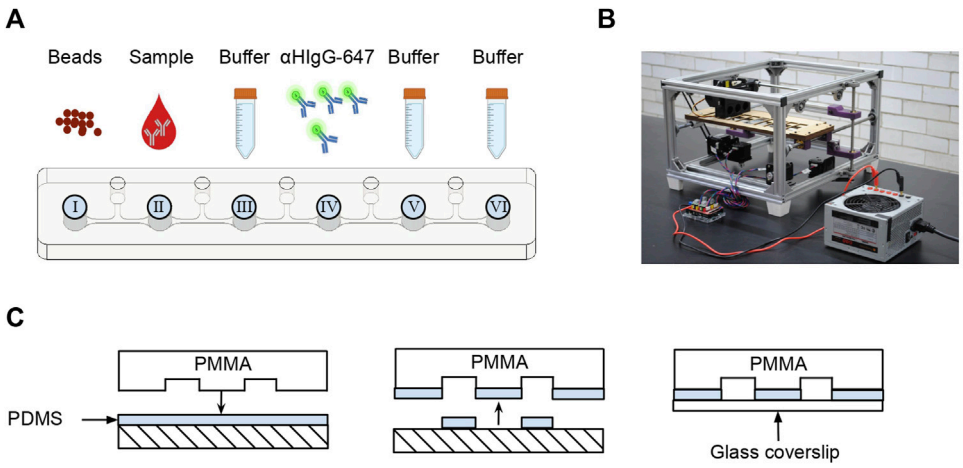

FIGURE 1
Microfluidic chip for SARS-CoV-2 AbDM. **(A)** Schema of the sequence of microchannel and the contents of each well. **(B)** Photograph of the automated platform used to move the magnetic beads in the microfluidic chip. **(C)** Sealing of the microfluidic chip. The microstructured PMMA is coated in uncured PDMS and then sealed with a coverslip.

polymerization (60°C, 1 h) in an incubator (SI-950 Ultraviolet Incubator, Analytik Jena, California, United States).

Chip loading consisted of filling each well with the solutions in the following order: I, functionalized magnetic beads; II, serum sample solution; III, B4T as a wash solution; IV, secondary antibody solution; V, B4T for the wash; and VI, B4T for readout. After filling all wells, to avoid well contamination, a clean glass coverslip was placed on top and mounted on the platform for the execution of the programmed routine.

2.3 ELISA

For the detection of anti-S IgG/IgM and anti-RBD IgG/IgM, a screening ELISA was performed to determine positive and negative serum samples, and, subsequently, an ELISA for titer determination was performed for positive serum samples (Amanat et al., 2020; Martínez-Barnetche et al., 2022). In both protocols, a 96-well high-affinity plate (82.1581.200, SARSTEDT, Nümbrecht, Germany) was coated with S protein (C.V.S Protein RBD Construct 6, LakePharma, California, United States) or with RBD (S Protein, RBD (319-591)-His10, LakePharma, California, United States) and incubated at 4°C overnight. Subsequently, three washes with PBS containing 0.1% Tween 20 (PBS-T; Dulbecco's PBS; Tween 20; D5652 and P1379, Sigma-Aldrich, Darmstadt, Germany) and a block with PBS-T supplemented with 3% milk (Svelty low fat, Nestlé S.A de C.V, CDMX, Mexico) were performed for 3 h at RT.

Briefly, serum samples were pre-diluted 1:5 in PBS for subsequent dilutions in PBS-T supplemented with 1% milk in a 96-well low affinity plate (Costar 9017, Corning, Maine, United States), both for screening ELISA (1:50) and for ELISA for titer determination of IgG (1:100, 1:300, 1:900, 1:2700, and 1:8100) and IgM (1:100, 1:200, 1:400, 1:800, and 1:1600) antibodies. These dilutions were transferred (50 µL) to the plate coated with S protein (80 ng/well) or RBD (100 ng/well), incubated (2 h at RT), and then extensively washed with PBS-T.

Next, goat anti-human IgG:HRP (RRID:AB_619881, Cat# 204005, Bio-Rad, California, United States; αHIgG-HRP) and goat F (ab')2 anti-human IgM-HRP (MBS675102, MyBioSource, California, United States; αHIgM-HRP) secondary antibody solution was added 1:3000 in PBS-T supplemented with 1% milk (50 µL) and incubated (50 min at RT). Next, three washes were performed with PBS T and incubated in 100 µL OPD solution (0.402 mg/mL OPD; o-phenylenediamine dihydrochloride: P1526, Sigma-Aldrich, Missouri, United States; and 0.02 mg/mL H_2O_2; 10 min, TA and in the dark), and 3N HCl was used as a stop solution (50 µL). Finally, OD_{492nm} was determined on the Cytation 5 reader.

2.4 Statistical analysis

One-way ANOVA with *post hoc* Tukey or Z test was used for the differences between the means of the assays. An α of 0.05 was set for significant differences. All statistical analyses were performed with GraphPad Prism software (v. 9, GraphPad Software, Greenville, Columbia, United States).

To determine the limit of the detection (LoD) of the SARS-CoV-2 AbDM, the definition by Mac Dougall and co. (1980) was used: the detection limit signal of an analytical method should be greater than three times the standard deviation of the blank measurement. In this case, the control functionalized without antigen was used as blank. This LoD is presented as the lower limit of the detection range.

ROC analysis was performed in PSPP statistics separately for RBD and S protein (v. 1.4, GNU Software, Boston, Massachusetts, United States).

3 Results

3.1 SARS-CoV-2 AbDM standardization

To optimize the SARS-CoV-2 AbDM, before its validation and application on microfluidic chips, several parameters were

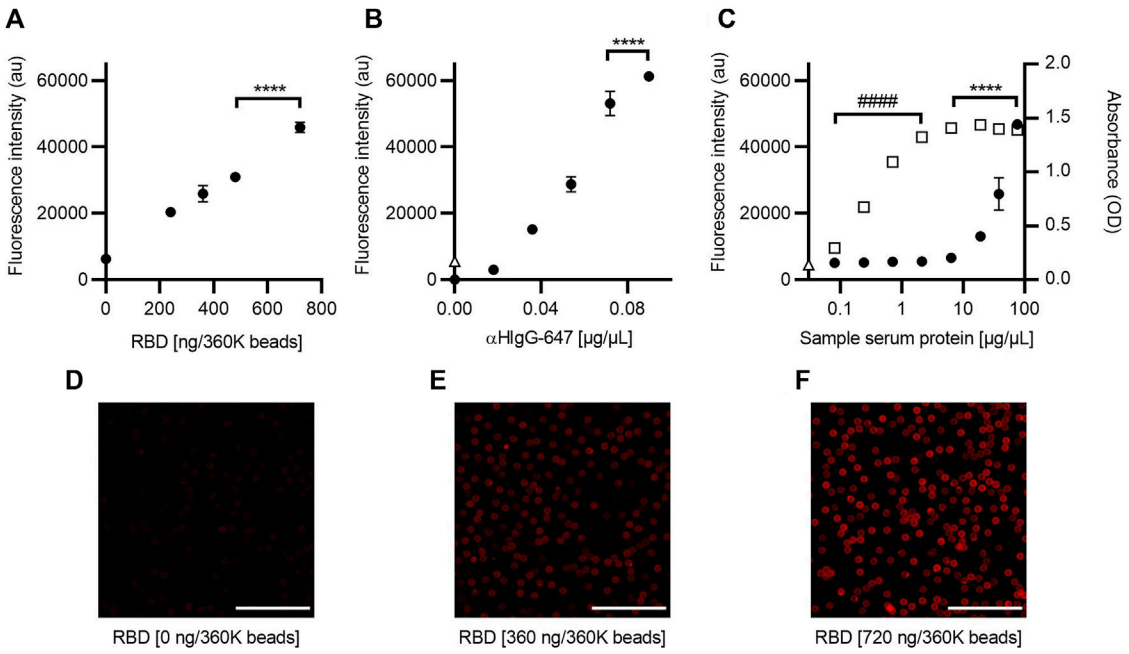

FIGURE 2
Optimization of the SARS-CoV-2 AbDM for IgG-RBD detection. **(A)** Plot of the fluorescence intensity obtained for different concentrations of RBD, used in the functionalization of the beads (360K beads), and **(B)** for different concentrations of αHIgG-647. **(C)** Comparative plot of the fluorescence and absorbance measurement obtained for IgG-RBD with the SARS-CoV-2 AbDM and with ELISA, respectively. Plotted (●) is the result of SARS-CoV-2 AbDM and (□) is the values obtained by ELISA. In **(B)** and **(C)**, Δ represents the fluorescence value of the control beads functionalized without RBD (woRBD). In all plots, symbols represent the mean of three replicates ± SD. Statistically significant differences are shown with **** ($p < 0.0001$) for SARS-CoV-2 AbDM and with #### ($p < 0.0001$) for ELISA. **(D–F)** Representative confocal microscopy images of **(A)**. Scales: 50 μm.

standardized using the RBD or S protein as antigen. These parameters included the optimal amount of antigen to functionalize the magnetic beads, the amount of secondary antibody to obtain the highest possible detection of anti-SARS-CoV-2 antibodies in the sample, and the ratio of serum sample dilution.

3.1.1 RBD as antigen

A direct relationship between fluorescence intensity and the amount of RBD was observed when determining the optimal amount of RBD antigen to functionalize the beads (Figure 2A). Based on these results, it was decided to use 720 ng/360K beads, as this condition showed a 1.5-fold increase in fluorescence intensity compared to the lowest concentration (ANOVA, $F = 271.4$, $p < 0.0001$, and Tukey, $p < 0.0001$) and homogeneous labeling in the bead population (Figures 2D–F).

In the determination of the optimal concentration of secondary antibody (αHIgG-647) for the anti-RBD antibodies detection carried out in the SARS-CoV-2 AbDM plate-based method, a tendency of saturation of the fluorescence signal was observed after 0.072 μg/μL, with the difference being significant at 0.09 μg/μL (ANOVA $F = 653.4$, $p < 0.0001$, and Tukey $p < 0.001$) (Figure 2B). Therefore, the concentration of αHIgG-64 to be used was determined to be 0.09 μg/μL.

The fluorescence intensity of a series of dilutions (0.08, 0.24, 0.71, 2.13, 6.40, 19.20, 38.41, and 76.81 μg/μL total protein) of an ELISA-confirmed serum titer of 8100 was analyzed to determine the optimal sample concentration for detection and to compare the measurement of IgG anti-RBD antibodies between the ELISA and the SARS-CoV-2 AbDM plate-based method. In all cases, the volume of serum added to the reaction was 2.5 μL (Figure 2C). It was observed that the SARS-CoV-2 AbDM allows discriminating differences from 19.20 μg/μL (ANOVA, $F = 209$, $p < 0.0001$, and Tukey, $p < 0.0001$) and that the saturation point is not reached with the concentrations evaluated. On the other hand, with the ELISA method, the positive sample can be distinguished from 0.08 μg/μL and saturates from 6.40 μg/μL (ANOVA, $F = 993$, $p < 0.0001$, and Tukey, $p > 0.05$).

3.1.2 S protein as antigen

The same assay strategy as for the RBD was used to standardize the SARS-CoV-2 AbDM using S protein as antigen. The saturation concentration to functionalize was estimated at 360 ng/240K beads (ANOVA, $F = 137.3$, $p < 0.0001$, and Tukey, $p < 0.001$), and adequate labeling is observed (Figure 3A, Figures 3D–F). Therefore, this value was selected for the other assays. As for the concentration of αHIgG-647 for plate detection (Figure 3B), 0.036 μg/μL was chosen because, from this condition, it does not increase fluorescence significantly.

Comparison of IgG-S measurement by ELISA and the SARS-CoV-2 AbDM plate-based method (Figure 3C) was also evaluated in the same way as for IgG-RBD; it was observed that, in this case, the SARS-CoV-2 AbDM discriminates from 0.71 μg/μL (ANOVA, $F = 279$, $p < 0.0001$, and Tukey, $p < 0.05$) and does not reach saturation in the conditions evaluated. On the other hand, the ELISA

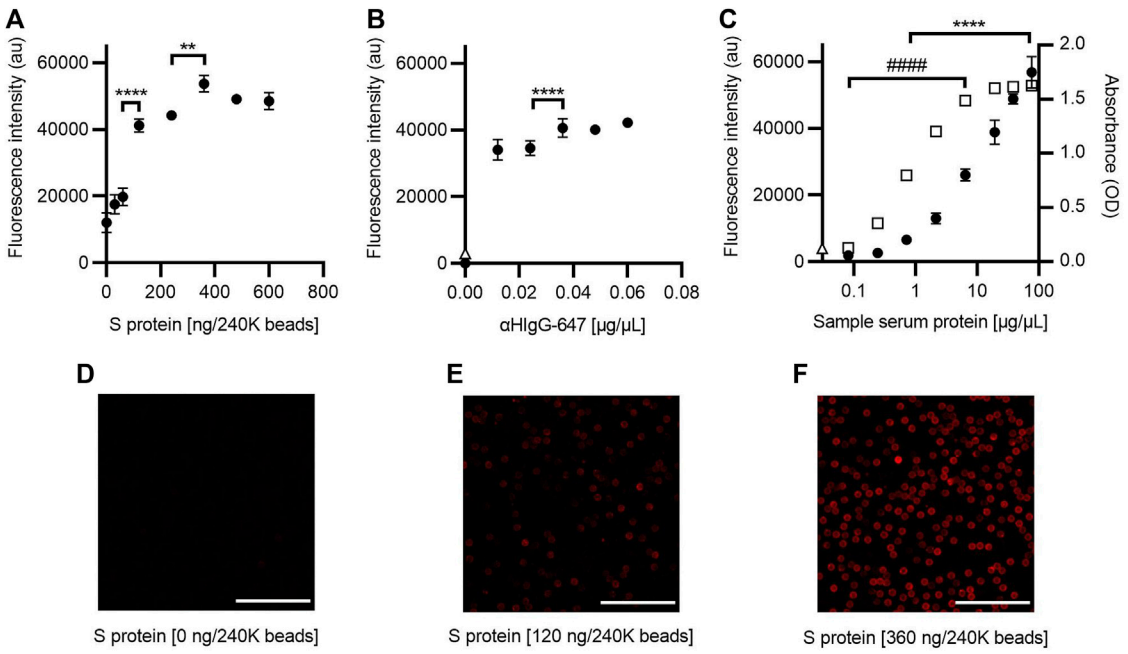

FIGURE 3
Optimization of the SARS-CoV-2 AbDM for IgG-S detection. **(A)** Plot of the fluorescence intensity obtained for beads (240K beads) functionalized with different concentrations of S protein and **(B)** for different concentrations of αHIgG-647. **(C)** Comparison of the fluorescence and absorbance measured for IgG-S using the SARS-CoV-2 AbDM and ELISA, respectively. Plot shows (●) the SARS-CoV-2 AbDM results and (□) the ELISA values. In **(B)** and **(C)**, Δ represents the fluorescence intensity of the control beads functionalized without S protein (woS). In all plots, symbols represent the mean of three replicates ± SD. Statistically significant differences are shown with ** ($p < 0.01$) and **** ($p < 0.0001$) for SARS-CoV-2 AbDM and with ####, ($p < 0.0001$) for ELISA. **(D–F)** Representative confocal microscopy images of **(A)**. Scales: 50 μm.

discriminates at 0.08 μg/μL, and the signal saturates at 19.20 μg/μL (ANOVA, $F = 4084$, $p < 0.0001$, and Tukey, $p > 0.05$).

3.2 Validation of the SARS-CoV-2 AbDM

To validate the SARS-CoV-2 AbDM, a selection of an equal number of serum samples from the different ELISA titer groups was tested for IgG-RBD ($n = 50$), and a different selection of samples was tested for IgG-S ($n = 31$) and compared with the ELISA. Each serum sample was determined in duplicate (four plates for RBD and three for S protein). In order to compare the results of each set of experiments, the values obtained were normalized, in each case, to the average value of the fluorescence intensity of the samples with the highest titer (8100). The normalized fluorescence intensity was compared against ELISA titers (Figures 4A, D). For both antigens, an increasing trend in the average normalized fluorescence intensity is observed in accordance with the increase in the ELISA titer. In addition, the dispersion in the populations of each titer is smaller in the detection of IgG-S (Figures 4D–F).

A receiver operating characteristic (ROC) curve was executed to assess the area under the curve (AUC) for the normalized fluorescence intensity of SARS-CoV-2 AbDM as a detection tool for IgG-RBD and IgG-S (Figures 4B, E). The AUC for RBD was 0.84, and the cutoff point of 0.23 is related to the highest specificity (71%) and sensitivity (84%) for the SARS-CoV-2 AbDM variable. On the other hand, the AUC for S protein was 1, and the cutoff point of 0.15 is related to the highest specificity (100%) and sensitivity (100%) for the SARS-CoV-2 AbDM variable.

To make the comparison between the two methods more direct, the cutoff points for each titer were determined from the normalized fluorescence intensity values. For this purpose, a ROC analysis was performed by changing the state variable for each titer, and the cut-off point at which sensitivity and specificity were optimal was extracted. Thus, the simile of the ELISA titer applied to the SARS-CoV-2 AbDM was obtained. To compare both methods, a bubble plot was constructed with the values obtained with SARS-CoV-2 AbDM against the ELISA titers represented in groups with incidences equivalent to the bubble size (Figures 4C, F). It was thus observed that there is a greater coincidence in the titers obtained by both methods in the detection of IgG-S, especially in titers greater than 900.

3.3 Detection in whole blood

The process of obtaining serum from a blood sample, as indicated in the methods, requires at least 45 min, special equipment, and tubing, so it is possible to facilitate the detection process if the sample used is whole blood instead of serum. Therefore, the ability of the SARS-CoV-2 AbDM to detect IgG-RBD and IgG-S using whole blood was evaluated. For this purpose,

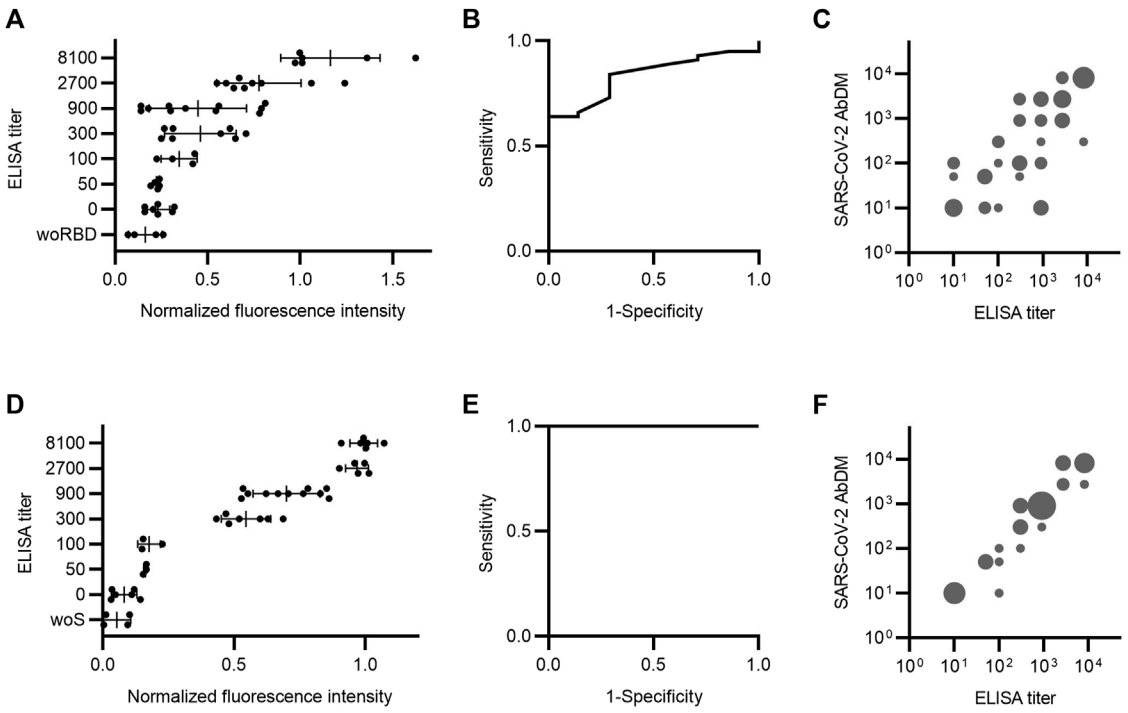

FIGURE 4
Serum antibody detection comparison between SARS-CoV-2 AbDM and ELISA. Samples were analyzed by both methods to detect **(A–C)** IgG-RBD (n = 50) and **(D–F)** IgG-S (n = 31). **(A** and **D)** ELISA titer versus SARS-CoV-2 AbDM normalized fluorescence intensity. The mean (●) of the SARS-CoV-2 AbDM result for each sample and the mean and deviation of each ELISA titer population are shown. woRBD and woS correspond to control beads functionalized without antigen. **(B** and **E)** Receiver operating characteristic (ROC) curve for SARS-CoV-2 AbDM, with an area under the curve of 0.84 for IgG-RBD and 1 for IgG-S. **(C** and **F)** SARS-CoV-2 AbDM titer versus ELISA titer. Cut-off points of the normalized fluorescence intensity were determined for each titer using ROC analysis. The size of the bubble is proportional to the number of incidences (1–10) in each range. All negative cases were plotted with the value of 10, as the scale is logarithmic.

IgG detection with SARS-CoV-2 AbDM was performed on both antigens in serum and whole blood samples (Figure 5), with ELISA titers determined in serum (50, 2700, and 8100). As shown in Figure 5, it is possible to measure the presence of antibodies in whole blood as well as in serum, showing significant differences in fluorescence intensity with respect to the controls (an increase in signal of 0.71 fold for RBD and 1.40 fold for S protein), both for the detection of IgG-RBD (Z test, Z = 4.7, $p < 0.00001$) and IgG-S (Z test, Z = 5.6, $p < 0.00001$), and it was possible to distinguish all the titers (RBD: ANOVA, $F = 155.6$, $p < 0.0001$; S: ANOVA, $F = 265$, $p <$ 0.0001a 900).

3.4 Co-detection of IgG and IgM

The ability of SARS-CoV-2 AbDM to co-detect IgG and IgM of both antigens was evaluated in two serum samples, one positive only for IgG (+IgG/-IgM) and the other positive for both immunoglobulins (+IgG/+IgM), determined by ELISA (Figure 6). For this, the results obtained with SARS-CoV-2 AbDM were consistent because in the fluorescence intensity of the +IgG/-IgM sample in both antigens, significant differences were only observed for IgG (RBD: ANOVA, $F = 946.1$, $p < 0.0001$; Tukey, $p < 0.0001$; S: ANOVA, $F = 310.9$, $p < 0.0001$; Tukey, $p < 0.001$) with respect to the control, while for the +IgG/+IgM sample, it was significant for both IgG (RBD: ANOVA, $F = 946.1$, $p < 0.0001$; Tukey, $p < 0.001$; S: ANOVA $F = 310.9$, $p < 0.0001$; Tukey, $p < 0.001$) and for IgM (RBD: ANOVA, $F = 31.23$, $p < 0.001$; Tukey, $p < 0.0001$; S: ANOVA, $F =$ 43.02, $p < 0.001$; Tukey, $p < 0.0001$).

3.5 Microfluidic chip implementation

The next step in the development of the SARS-CoV-2 AbDM was its implementation on a microfluidic chip for the detection of IgG-S toward a PoC device. For this purpose, it was necessary to optimize the secondary antibody concentration parameters and the serum sample dilution ratio; it is worth mentioning that the established functionalization parameters were maintained as this process is independent of the device. Thus, for the determination of αHIgG-647 concentration for on-chip detection (Figure 7A), 0.08 μg/μL was chosen, as, from this condition, it does not increase fluorescence significantly.

Regarding the comparison of IgG-S measurement between ELISA and on-chip SARS-CoV-2 AbDM (Figure 7B), this was performed in the same way as described for the plate and considering the concentration of αHIgG-647 established for the chip; consistent results were obtained with those presented

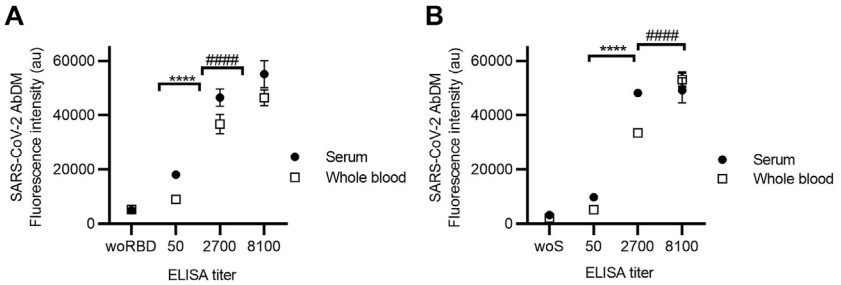

FIGURE 5
Detection of **(A)** IgG-RBD and **(B)** IgG-S in serum and whole blood using SARS-CoV-2 AbDM in ELISA-titrated samples. Mean of three replicates ± SD of (●) serum and (□) whole blood fluorescence intensity values are plotted. woRBD and woS correspond to control beads functionalized without antigen and reacted with the highest titered sample. Statistically significant differences are shown with **** ($p < 0.0001$) for serum and with #### ($p < 0.0001$) for whole blood.

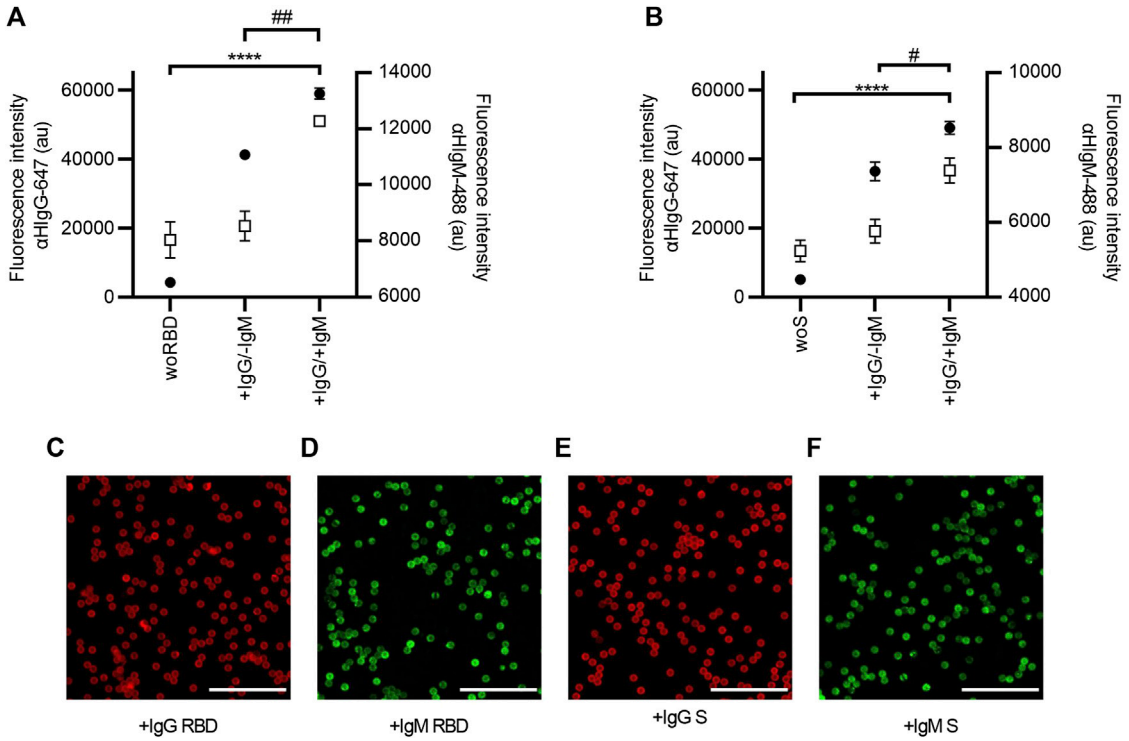

FIGURE 6
Co-detection of IgG and IgM in serum samples with SARS-CoV-2 AbDM, using **(A)** RBD and **(B)** S protein as antigen. Mean of three replicates ± SD of (●) IgG (αHIgG-647) and (□) IgM (αHIgM-488) fluorescence intensity values are plotted. Two serum samples previously analyzed by ELISA were tested: a serum sample positive only for IgG (+IgG/-IgM) and a serum sample positive for both antibodies (+IgG/+IgM); woRBD and woS correspond to control beads functionalized without antigen and reacted with the +IgG/+IgM sample. Statistically significant differences by ANOVA are shown for IgG **** ($p < 0.0001$) and for IgM ## ($p < 0.001$) and # ($p < 0.01$). **(C–F)** Representative confocal microscopy images of IgG and IgM detection with both antigens. Scales: 50 μm.

for IgG-S on the plate (Figure 3C), resolving in SARS-CoV-2 AbDM on the chip from 2.13 μg/μL (ANOVA F = 139, $p < 0.0001$, and Tukey $p < 0.0001$) without reaching the saturation point at the concentrations used. Likewise, to evaluate the sample ratio to be used in the on-chip SARS-CoV-2 AbDM, serum samples of different ELISA titers (negative, 50, and 8100) diluted at 1:6, 1:3, and 2:3 ratios were analyzed (Figure 7C). We established 2:3 as the sample dilution ratio to be used in the chip as it presents the maximum fluorescence in both positive samples. In addition, in this ratio, the sample with the lowest titer (50) is significantly different from the negative one (ANOVA, $F = 105.1$, $p < 0.0001$; Tukey, $p < 0.01$).

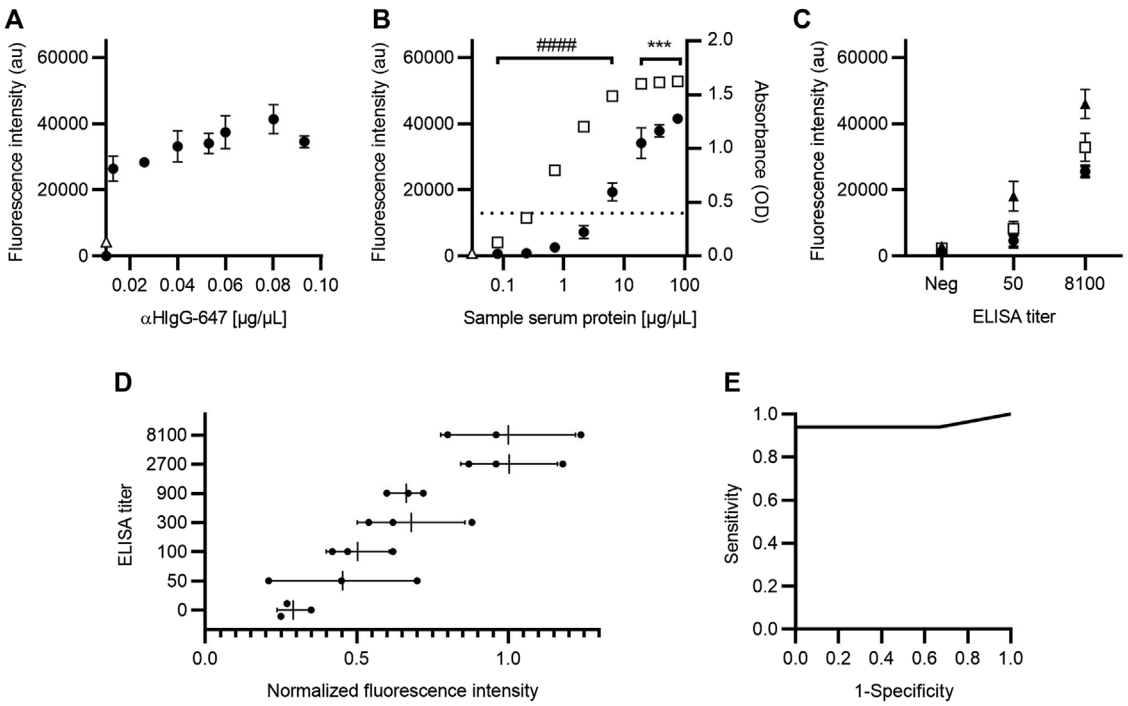

FIGURE 7
Optimization of IgG-S detection with SARS-CoV-2 AbDM for on-chip microfluidic implementation. **(A)** Fluorescence intensity plot for different secondary antibody (αHIgG-647) concentrations on-chip. **(B)** Comparison of fluorescence and absorbance measurements for IgG-S with SARS-CoV-2 AbDM on-chip and with ELISA, respectively. The SARS-CoV-2 AbDM results are shown with (●), and the ELISA values are shown with (□). In **(A)** and **(B)**, (Δ) represents the fluorescence intensity of the control beads functionalized without S protein (woS). **(C)** Determination of serum sample dilution ratio. Fluorescence intensity of samples with different ELISA titers (negative; 50; 8100) are shown with (●) for 1:6, with (□) for 1:3, and with (▲) for 2:3. **(D)** ELISA titer versus normalized fluorescence intensity of SARS-CoV-2 AbDM on-chip. The mean (●) of the SARS-CoV-2 AbDM result on chip for each sample (n = 21) and the mean and deviation of each ELISA titer population are shown. **(E)** ROC curve for SARS-CoV-2 AbDM on chip, with an area under the curve of 0.94 for IgG-S. Symbols represent the mean of three **(A–C)** or two **(D)** replicates ± SD. Statistically significant differences are shown with *** ($p < 0.001$) for SARS-CoV-2 AbDM and with #### ($p < 0.0001$) for ELISA.

As in the SARS-CoV-2 plate-based AbDM, the chip method was validated by analyzing serum samples for IgG-S detection (n = 21) and compared with ELISA. Each sample was determined in duplicate, the results were normalized to the average fluorescence intensity of 8100 titer samples, and the normalized fluorescence intensity was compared against ELISA titers (Figure 7D). As in the plate validation, an increasing trend in the average fluorescence intensity was observed as the ELISA titer increased. A ROC curve was executed for the fluorescence intensity of IgG-S, with SARS-CoV-2 AbDM on-chip as a detection tool (Figure 7E). The AUC was 0.94, and the cutoff point of 0.40 is related to the highest specificity (100%) and sensitivity (94%) for the SARS-CoV-2 AbDM variable.

4 Discussion

In order to design a method for the detection of anti-SARS-COV-2 IgG and IgM antibodies in human samples, we present the SARS-CoV-2 AbDM, which was implemented both in a multiwell plate and in a microfluidic chip. This method is based on fluorescence immunodetection of such immunoglobulins using magnetic beads with the viral antigen immobilized on their surface (Fiordelisio et al., 2021).

Tests were carried out to determine the standardization parameters of the SARS-CoV-2 AbDM implemented both in a multiwell plate and in a microfluidic chip, such as the concentration of antigen (RBD or S protein) to functionalize the magnetic beads, the concentration of secondary antibody, the detection limit, and the proportion of the serum sample dilution to be used. Validation of the SARS-CoV-2 AbDM was performed with different samples, using ELISA as a reference method. Likewise, assays were performed with the SARS-CoV-2 AbDM for the detection of whole blood as a sample and the co-detection of both IgG and IgM in the same serum sample.

Based on the results obtained, the ELISA method appears to be more sensitive than the SARS-CoV-2 AbDM for both RBD and S protein (Figure 2C; Figure 3C; Figure 7B), reaching a plateau in absorbance at high serum protein concentration values. On the other hand, the SARS-CoV-2 AbDM did not reach saturation, which indicates that it has a greater range in its ability to determine higher values than the ELISA. In addition, it should be noted that, in the detection of antibodies by ELISA, the first step is to determine whether the sample is positive or negative, and then, a titration process is performed to determine the concentration of the sample within a range, which is dependent on the color generated by an enzymatic reaction. This process can easily vary depending on the time and temperature. In the case of SARS-CoV-2 AbDM, this

TABLE 1 Comparison of the main serological detection methods for antibodies against SARS-CoV-2.

	Fast test	ELISA	SARS-CoV-2 AbDM
Sensitivity	54.3%–99%	65%–100%	84%–100%[a]
Specificity	94.1%–100%	84.4%–100%	71%–100%[b]
Cost	10.22–28.33 USD[†]	53.87–113.54 USD[†]	6 USD
Simplicity	Capillary blood auto test	Trained personnel and requires multiple assays	Automated with chip
Time for result	10–20 min	16 h	1.5 h
Response type	Binary +/−	Semi-quantitative	Quantitative
Co-detection	Yes	No	Yes
Sample type	Blood	Serum	Blood/serum

[a]Sensitivity for RBD in plate is 84%, S protein in plate is 100%, and S protein on chip is 94%.
[b]Specificity for RBD in plate is 81%, S protein in plate is 100%, and S protein on chip is 100%.
[†]The costs of the tests are from the main clinical laboratories in Mexico.
Adapted from Gong et al.

variation does not exist since there is no such process, and the detection is performed directly.

Although the performance of the ELISA, determined by a dilution curve, shows high sensibility compared to the SARS-CoV-2 AbDM when used as a diagnosis with patient samples, the first value is that of a titer of 50 (0.4 OD), corresponding to 0.71 μg/μL. In this sense, the diagnosis by ELISA is not only done in two steps with six analyses that consume twice the time and supplies, but its first level of detection is also closer to that of the SARS-CoV-2 AbDM. Thus, the developed method would allow a quantitative measurement of the antibody concentration in a single assay with a higher dynamic range and a similar detection limit (2.13 μg/μL).

As for the comparison of the normalized fluorescence intensity obtained with SARS-CoV-2 AbDM in serum samples, an upward trend is observed with respect to the ELISA titers, which is the expected behavior, since the higher the ELISA titer, the higher the fluorescence intensity should be (Figures 4A, D). When using S protein as antigen, a better resolution was observed among the ELISA titers than with RBD, which coincides with the data obtained and previously discussed from the standardization process. It is evident that, for each ELISA titer, a great variability is reflected in the fluorescence intensity values since a limitation of the ELISA is that it groups the determinations in ranges, i.e., the absorbance value obtained is classified according to the last dilution of the sample that exceeds the cut-off point threshold. In contrast, with the SARS-CoV-2 AbDM, the fluorescence intensity value is continuous, thus giving a spectrum of fluorescence values for a single ELISA titer value, providing greater resolution.

Regarding the validation of the SARS-CoV-2 AbDM on a plate for the detection of anti-SARS-CoV-2 IgG, and based on the ROC analysis performed, we consider the specificity (RBD, 71%; S protein, 100%) and sensitivity (RBD, 84%; S protein, 100%) values to be excellent for S protein as antigen, RBD less so. This difference observed between RBD and S protein may be due to the inherent properties of these proteins; for example, since S protein is larger (1273 aa vs. 319-541 aa) and has more antibody binding sites than RBD, the stoichiometry with the antibody is more favorable. Therefore, the orientation of RBD in the bead attachment or on the reaction surface could compromise the exposure of the antibody binding site and, therefore, contributes to the variability observed with this protein as antigen. Nevertheless, the evaluation of specificity would benefit greatly from more negative samples, but we had no serum samples from before the pandemic began.

In common practice, in order to avoid high background signal, when making immunoglobulin determinations in blood by ELISA, serum samples are usually used instead of whole blood (Kovac et al., 2020); the main problem of the background is that it makes it difficult to differentiate low values. We demonstrated that, with the SARS-CoV-2 AbDM, the reaction is specific, and the reaction surface is clean to such a degree that we can use whole blood or serum without modifying the value obtained. This raises the possibility of developing a PoC-type device that uses whole blood as a sample, like the rapid LFIAs, but with a quantitative result and greater sensitivity and specificity. However, it is important to note that for this evaluation, three samples were used.

Another attribute of the SARS-CoV-2 AbDM is that, by using fluorescence as the marker signal instead of a colorimetric enzymatic reaction, such as ELISA, it can be used to perform multiple detections with the same sample. Thus, with the proposed method, we achieve the co-detection of IgG and IgM anti-SARS-COV-2 antibodies in a single sample simultaneously. This represents a great advantage over ELISA since it saves resources in terms of time and consumables by not needing to carry out independent determinations.

The versatility of the SARS-CoV-2 AbDM allowed it to be implemented for IgG-S detection on a microfluidic chip toward a PoC, with a motorized platform (Fiordelisio et al., 2021) that allowed for a precise reaction and manipulation of the samples up to the optical detection stage. As with the plate-based version of the method, an upward trend of fluorescence intensity with respect to the ELISA titers and variation in their respective ranges was observed on the chip, as expected. Furthermore, the specificity

(100%) and sensitivity (94%) values after ROC analysis are adequate and promising for future development as a PoC device (Figure 7). In addition, another great advantage of using the SARS-CoV-2 AbDM on the microfluidic chip is that the operator only needs to place the sample in the well of the chip since the platform automates the reaction process up to the use of the detection device. This reduces the human error associated with handling and frees up the user's time for other matters.

The cost of performing SARS-CoV-2 AbDM in American dollars was 6 USD for the 96-wells plate and microfluidic chip compared to the ELISA's 13 USD cost. Since ELISA requires a series of dilutions in several wells to perform the titration of the samples, the space available on a single plate is limited to a few samples (approximately eight, including controls), so a strategy is usually followed, as the one we follow, where first an ELISA is performed only for screening of positives or negatives and then selecting only the positives to determine the titer (Stadlbauer et al., 2020; Martínez-Barnetche et al., 2022), thus doubling the time to 16 h, resources and cost invested. In contrast, with the SARS-CoV-2 AbDM, by not requiring serial dilutions, with a single sample in a reaction well, the result can be obtained in 5 h on a plate or 1.5 h on a chip, without the need for prior scanning, with the possibility of multiple detections.

Since the reaction surface of the SARS-CoV-2 AbDM does not depend on a fixed area but on the number of beads, an advantage of this method is the ability to modify the dynamic range; for example, by increasing the number of beads, the reaction surface area is increased, thus allowing more antibodies to be captured. Another possibility is to reduce the dilution of the serum sample, which increases the number of antibodies available for detection, resulting in a higher detection signal. All these are opportunities to settle parameters depending on antibodies and antigens used to measure.

In short, we have presented a quantitative method with similar sensitivity to an ELISA, in less time, and with a cost comparable to that of a LFIA test, with a high potential to be developed as a PoC and thus be an alternative tool for monitoring seroprevalence of SARS-CoV-2 antibodies (Table 1). Both the present work and the one previously reported by our group (Fiordelisio et al., 2021) demonstrate the versatility of the method based on the bead system as a reaction surface and allow us to believe in a wide range of applications in other biomolecules.

The SARS-CoV-2 AbDM designed to detect IgG and IgM antibodies against SARS-CoV-2 S protein and RBD in human serum samples (assayed in well plates and microfluidic chip) proved to be comparable to conventional ELISA assays, especially for S protein as antigen. The SARS-CoV-2 AbDM provided several advantages in testing, such as cost reduction, the possibility of performing single or multiplex assays, the possibility of multiplex detection, and the ability to detect whole blood samples without loss of resolution. In addition, with the microfluidic chip in conjunction with the motorized actuated platform, there is the advantage of automation, reduction of time, sample quantity, and operator intervention during the process. All these advantages suggest that the SARS-CoV-2 AbDM can be used as a tool for seroprevalence monitoring, allowing a better understanding of the epidemiological and clinical characteristics of COVID-19 and contributing to more effective and ethical decision-making in strategies to combat the COVID-19 pandemic. The demonstrated versatility of the method and its eventual implementation in PoC made it possible to offer greater availability of analytical tests for other biomolecules, whether of health or non-health interest, in places where the use of expensive and complex instruments is not an option.

Data availability statement

The original contributions presented in the study are included in the article/supplementary material, further inquiries can be directed to the corresponding author/s.

Ethics statement

The studies involving human participants were reviewed and approved by the Commission of Academic Ethics and Scientific Responsibility of the Faculty of Sciences of UNAM (Folio: PI_2020_-2_003). The patients/participants provided their written informed consent to participate in this study.

Author contributions

TF and JN-M contributed to the conception and design of the project. JN-M, DR, AV-M, and LG performed experiments on both plates and microfluidic chips. DR-L, YA-L, SA, AC-H, and DD-R collected samples. YA-L, AC-H, and DD-R performed ELISA. YR-H, AC-R, DZ-H, and DR designed and manufactured microfluidic chips. JB, MJ, and JL-A were involved in design, construction, and operation of the automated platform for on-chip determinations. EJ-D acquired confocal microscope and analyzed data. TF, JN-M, DR, AV-M, LG, and DZ-H were involved in analysis or interpretation of data. TF, JN-M, DD-R, DZ-H, LG, YA-L, AV-M, and DR drafted the manuscript. D-RL, EJ-D, SA, AC-H, and AC-R revised the draft for important intellectual content. TF was involved in supervision and funding acquisition. All authors contributed to the article and approved the submitted version.

Funding

This work was funded by UNAM-PAPIIT BV-200820, CONACYT CY-313005, CONACYT CY-315805, Liomont Labs, Kaluz Foundation, Casa Cordoba, Sertull Foundation, Roberto Hernandez R Foundation, and Ph.D. Armando Jinich Ripstein.

Acknowledgments

The authors are grateful to Laura Palomares, Claudia Segal, Daniel Ochoa, Catalina Stern, Mathieu Hautefeuille, and Sergio

Valentinoti for insightful comments and support; Luis Fernando Losoya Uribe, Daniel Barreto Cabrera, and Ma. Paz Rodríguez for technical assistance in ELISA performance; Regina Zamora for helpful management of sample database and subjects; Samuel Amat for technical assistance in chip performance; Facultad de Ciencias UNAM for facilities; CVTT-UNAM for its consultancy on the cost calculation; CIC-UNAM for its support of the continuous operation of LaNSBioDyT; Raúl Caudillo Viurquez, Luz Mendoza Sanlúcar, and Flor Mónica Gutierrez Alcántara for their support with the quality management system; and to all the people who voluntarily donated blood. JN-M is grateful for the postdoctoral grant by Programa de Becas Posdoctorales de la UNAM, Dirección General de Asuntos del Personal Académico, UNAM.

Conflict of interest

The authors declare that the research was conducted in the absence of any commercial or financial relationships that could be construed as a potential conflict of interest.

Publisher's note

References

Abdulamir, A. S., and Hafidh, R. R. (2020). The possible immunological pathways for the variable immunopathogenesis of COVID—19 infections among healthy adults, elderly and children. *Electron. J. Gen. Med.* 17, em202. doi:10.29333/ejgm/7850

Amanat, F., Stadlbauer, D., Strohmeier, S., Nguyen, T. H. O., Chromikova, V., McMahon, M., et al. (2020). A serological assay to detect SARS-CoV-2 seroconversion in humans. *Nat. Med.* 26, 1033–1036. doi:10.1038/s41591-020-0913-5

Azkur, A. K., Akdis, M., Azkur, D., Sokolowska, M., van de Veen, W., Brüggen, M.-C., et al. (2020). Immune response to SARS-CoV-2 and mechanisms of immunopathological changes in COVID-19. *Allergy* 75, 1564–1581. doi:10.1111/all.14364

Bachmann, M. F., Mohsen, M. O., Zha, L., Vogel, M., and Speiser, D. E. (2021). SARS-CoV-2 structural features may explain limited neutralizing-antibody responses. *NPJ Vaccines* 6, 2. doi:10.1038/s41541-020-00264-6

Bong, C.-L., Brasher, C., Chikumba, E., McDougall, R., Mellin-Olsen, J., and Enright, A. (2020). The COVID-19 pandemic: Effects on low- and middle-income countries. *Anesth. Analg.* 131, 86–92. doi:10.1213/ane.0000000000004846

Carrio, A., Sampedro, C., Sanchez-Lopez, J. L., Pimienta, M., and Campoy, P. (2015). Automated low-cost smartphone-based lateral flow saliva test reader for drugs-of-abuse detection. *Sensors* 15, 29569–29593. doi:10.3390/s151129569

Cevik, M., Kuppalli, K., Kindrachuk, J., and Peiris, M. (2020). Virology, transmission, and pathogenesis of SARS-CoV-2. *BMJ* 371, m3862. doi:10.1136/bmj.m3862

Emeribe, A. U., Abdullahi, I. N., Shuwa, H. A., Uzairue, L., Musa, S., Anka, A. U., et al. (2022). Humoral immunological kinetics of severe acute respiratory syndrome coronavirus 2 infection and diagnostic performance of serological assays for coronavirus disease 2019: An analysis of global reports. *Int. Health* 14, 18–52. doi:10.1093/inthealth/ihab005

Fiordelisio, T., Buendia-Roldan, I., Hautefeuille, M., Del-Rio, D., Ríos-López, D. G., Zamarrón-Hernández, D., et al. (2021). Development of a diagnostic biosensor method of hypersensitivity pneumonitis towards a point-of-care biosensor. *Biosensors* 11, 196. doi:10.3390/bios11060196

Galipeau, Y., Greig, M., Liu, G., Driedger, M., and Langlois, M.-A. (2020). Humoral responses and serological assays in SARS-CoV-2 infections. *Front. Immunol.* 11, 610688. doi:10.3389/fimmu.2020.610688

Goel, R. R., Painter, M. M., Apostolidis, S. A., Mathew, D., Meng, W., Rosenfeld, A. M., et al. (2021). mRNA vaccines induce durable immune memory to SARS-CoV-2 and variants of concern. *Science* 374, abm0829. doi:10.1126/science.abm0829

Guo, L., Ren, L., Yang, S., Xiao, M., Chang, D., Yang, F., et al. (2020). Profiling early humoral response to diagnose novel coronavirus disease (COVID-19). *Clin. Infect. Dis.* 71, 778–785. doi:10.1093/cid/ciaa310

Hallal, P. C., Hartwig, F. P., Horta, B. L., Silveira, M. F., Struchiner, C. J., Vidaletti, L. P., et al. (2020). SARS-CoV-2 antibody prevalence in Brazil: Results from two successive nationwide serological household surveys. *Lancet Glob. Health* 8, e1390–e1398. doi:10.1016/s2214-109x(20)30387-9

Harrison, A. G., Lin, T., and Wang, P. (2020). Mechanisms of SARS-CoV-2 transmission and pathogenesis. *Trends Immunol.* 41, 1100–1115. doi:10.1016/j.it.2020.10.004

Huggett, J. F., Moran-Gilad, J., and Lee, J. E. (2021). COVID-19 new diagnostics development: Novel detection methods for SARS-CoV-2 infection and considerations for their translation to routine use. *Curr. Opin. Pulm. Med.* 27, 155–162. doi:10.1097/mcp.0000000000000768

Koczula, K. M., and Gallotta, A. (2016). Lateral flow assays. *Essays Biochem.* 60, 111–120. doi:10.1042/ebc20150012

Kovac, M., Risch, L., Thiel, S., Weber, M., Grossmann, K., Wohlwend, N., et al. (2020). EDTA-anticoagulated whole blood for SARS-CoV-2 antibody testing by electrochemiluminescence immunoassay (ECLIA) and enzyme-linked immunosorbent assay (ELISA). *Diagnostics* 10, 593. doi:10.3390/diagnostics10080593

Kubina, R., and Dziedzic, A. (2020). Molecular and serological tests for COVID-19 a comparative review of SARS-CoV-2 coronavirus laboratory and point-of-care diagnostics. *Diagn. (Basel)* 10, 434. doi:10.3390/diagnostics10060434

Lin, A. V. (2015). Indirect ELISA. *Methods Mol. Biol.* 1318, 51–59. doi:10.1007/978-1-4939-2742-5_5

MacDougall, D., Crummett, W. B., Amore, F. J., Cox, G. V., Freeman, D. H., Crosby, D. G., et al. (1980). Guidelines for data acquisition and data quality evaluation in environmental chemistry. *Anal. Chem.* 52, 2242–2249. doi:10.1021/ac50064a004

Martínez-Barnetche, J., Carnalla, M., Gaspar-Castillo, C., Basto-Abreu, A., Lizardi, R., Antonio, R. A., et al. (2022). Comparable diagnostic accuracy of SARS-CoV-2 Spike RBD and N-specific IgG tests to determine pre-vaccination nation-wide baseline seroprevalence in Mexico. *Sci. Rep.* 12, 18014. doi:10.1038/s41598-022-22146-8

Moreno, M. de L., Cebolla, Á., Muñoz-Suano, A., Carrillo-Carrion, C., Comino, I., Pizarro, Á., et al. (2017). Detection of gluten immunogenic peptides in the urine of patients with coeliac disease reveals transgressions in the gluten-free diet and incomplete mucosal healing. *Gut* 66, 250–257. doi:10.1136/gutjnl-2015-310148

Mousavizadeh, L., and Ghasemi, S. (2021). Genotype and phenotype of COVID-19: Their roles in pathogenesis. *J. Microbiol. Immunol. Infect.* 54, 159–163. doi:10.1016/j.jmii.2020.03.022

Osuchowski, M. F., Winkler, M. S., Skirecki, T., Cajander, S., Shankar-Hari, M., Lachmann, G., et al. (2021). The COVID-19 puzzle: Deciphering pathophysiology and phenotypes of a new disease entity. *Lancet Respir. Med.* 9, 622–642. doi:10.1016/s2213-2600(21)00218-6

Piccoli, L., Park, Y.-J., Tortorici, M. A., Czudnochowski, N., Walls, A. C., Beltramello, M., et al. (2020). Mapping neutralizing and immunodominant sites on the SARS-CoV-2 spike receptor-binding domain by structure-guided high-resolution serology. *Cell* 183, 1024–1042.e21. doi:10.1016/j.cell.2020.09.037

Post, N., Eddy, D., Huntley, C., van Schalkwyk, M. C. I., Shrotri, M., Leeman, D., et al. (2020). Antibody response to SARS-CoV-2 infection in humans: A systematic review. *PLoS One* 15, e0244126. doi:10.1371/journal.pone.0244126

Prazuck, T., Colin, M., Giachè, S., Gubavu, C., Seve, A., Rzepecki, V., et al. (2020). Evaluation of performance of two SARS-CoV-2 Rapid IgM-IgG combined antibody tests on capillary whole blood samples from the fingertip. *PLoS One* 15, e0237694. doi:10.1371/journal.pone.0237694

Prompetchara, E., Ketloy, C., and Palaga, T. (2020). Immune responses in COVID-19 and potential vaccines: Lessons learned from SARS and MERS epidemic. *Asian pac. J. Allergy Immunol.* 38, 1–9. doi:10.12932/AP-200220-0772

Ravi, N., Cortade, D. L., Ng, E., and Wang, S. X. (2020). Diagnostics for SARS-CoV-2 detection: A comprehensive review of the FDA-EUA COVID-19 testing landscape. *Biosens. Bioelectron.* 165, 112454. doi:10.1016/j.bios.2020.112454

Sette, A., and Crotty, S. (2021). Adaptive immunity to SARS-CoV-2 and COVID-19. *Cell* 184, 861–880. doi:10.1016/j.cell.2021.01.007

Shi, Y., Wang, G., Cai, X.-P., Deng, J.-W., Zheng, L., Zhu, H.-H., et al. (2020). An overview of COVID-19. *J. Zhejiang Univ. Sci. B* 21, 343–360. doi:10.1631/jzus.b2000083

Stadlbauer, D., Amanat, F., Chromikova, V., Jiang, K., Strohmeier, S., Arunkumar, G. A., et al. (2020). SARS-CoV-2 seroconversion in humans: A detailed protocol for a serological assay, antigen production, and test setup. *Curr. Protoc. Microbiol.* 57, e100. doi:10.1002/cpmc.100

Tai, W., He, L., Zhang, X., Pu, J., Voronin, D., Jiang, S., et al. (2020). Characterization of the receptor-binding domain (RBD) of 2019 novel coronavirus: Implication for development of RBD protein as a viral attachment inhibitor and vaccine. *Cell. Mol. Immunol.* 17, 613–620. doi:10.1038/s41423-020-0400-4

Vengesai, A., Midzi, H., Kasambala, M., Mutandadzi, H., Mduluza-Jokonya, T. L., Rusakaniko, S., et al. (2021). A systematic and meta-analysis review on the diagnostic accuracy of antibodies in the serological diagnosis of COVID-19. *Syst. Rev.* 10, 155. doi:10.1186/s13643-021-01689-3

Wieland, F., Bruch, R., Bergmann, M., Partel, S., Urban, G. A., and Dincer, C. (2020). Enhanced protein immobilization on polymers-A plasma surface activation study. *Polymers* 12, 104. doi:10.3390/polym12010104

Worldometers.info (2022). COVID-19 coronavirus pandemic. Worldometer. Available at: https://www.worldometers.info/coronavirus/ (Accessed September 20, 2022).

Wrapp, D., Wang, N., Corbett, K. S., Goldsmith, J. A., Hsieh, C.-L., Abiona, O., et al. (2020). Cryo-EM structure of the 2019-nCoV spike in the prefusion conformation. *Science* 367, 1260–1263. doi:10.1126/science.abb2507

Wu, F., Zhao, S., Yu, B., Chen, Y.-M., Wang, W., Song, Z.-G., et al. (2020). A new coronavirus associated with human respiratory disease in China. *Nature* 579, 265–269. doi:10.1038/s41586-020-2008-3

Yüce, M., Filiztekin, E., and Özkaya, K. G. (2021). COVID-19 diagnosis -A review of current methods. *Biosens. Bioelectron.* 172, 112752. doi:10.1016/j.bios.2020.112752

Zhao, J., Yuan, Q., Wang, H., Liu, W., Liao, X., Su, Y., et al. (2020). Antibody responses to SARS-CoV-2 in patients with novel coronavirus disease 2019. *Clin. Infect. Dis.* 71, 2027–2034. doi:10.1093/cid/ciaa344

Frontiers in
Bioengineering and Biotechnology

Accelerates the development of therapies, devices, and technologies to improve our lives

A multidisciplinary journal that accelerates the development of biological therapies, devices, processes and technologies to improve our lives by bridging the gap between discoveries and their application.

Discover the latest Research Topics

See more →

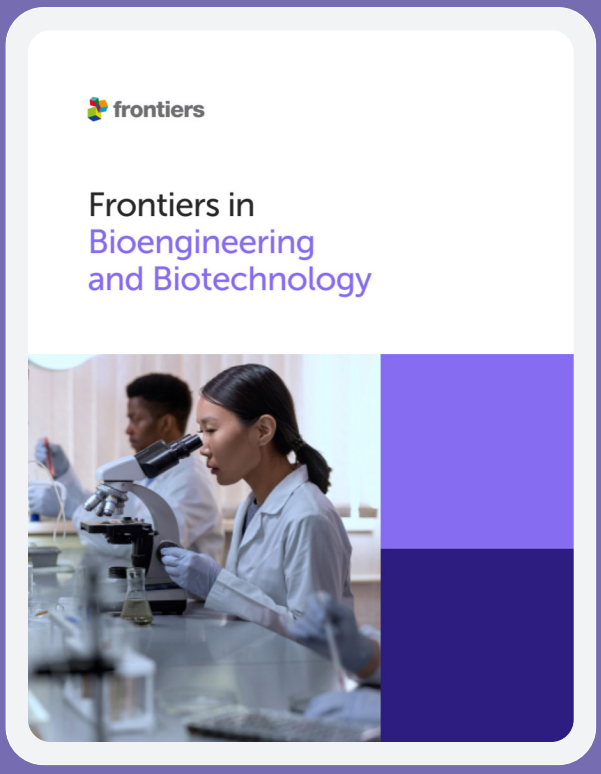

Frontiers

Avenue du Tribunal-Fédéral 34
1005 Lausanne, Switzerland
frontiersin.org

Contact us

+41 (0)21 510 17 00
frontiersin.org/about/contact